

INFORMATION TO USERS

This manuscript has been reproduced from the microfilm master. UMI films the text directly from the original or copy submitted. Thus, some thesis and dissertation copies are in typewriter face, while others may be from any type of computer printer.

The quality of this reproduction is dependent upon the quality of the copy submitted. Broken or indistinct print, colored or poor quality illustrations and photographs, print bleedthrough, substandard margins, and improper alignment can adversely affect reproduction.

In the unlikely event that the author did not send UMI a complete manuscript and there are missing pages, these will be noted. Also, if unauthorized copyright material had to be removed, a note will indicate the deletion.

Oversize materials (e.g., maps, drawings, charts) are reproduced by sectioning the original, beginning at the upper left-hand corner and continuing from left to right in equal sections with small overlaps. Each original is also photographed in one exposure and is included in reduced form at the back of the book.

Photographs included in the original manuscript have been reproduced xerographically in this copy. Higher quality 6" x 9" black and white photographic prints are available for any photographs or illustrations appearing in this copy for an additional charge. Contact UMI directly to order.

UMI

A Bell & Howell Information Company
300 North Zeeb Road, Ann Arbor MI 48106-1346 USA
313/761-4700 800/521-0600

**MICROSTRUCTURAL DEVELOPMENT DURING THE DIRECTIONAL
SOLIDIFICATION OF MERCURY ZINC SELENIDE ALLOYS**

By

SHARON D. COBB

**A DISSERTATION PRESENTED TO THE GRADUATE SCHOOL
OF THE UNIVERSITY OF FLORIDA IN PARTIAL FULFILLMENT
OF THE REQUIREMENTS FOR THE DEGREE OF
DOCTOR OF PHILOSOPHY**

UNIVERSITY OF FLORIDA

1998

UMI Number: 9905931

UMI Microform 9905931
Copyright 1998, by UMI Company. All rights reserved.

**This microform edition is protected against unauthorized
copying under Title 17, United States Code.**

UMI
300 North Zeeb Road
Ann Arbor, MI 48103

This work is dedicated to my parents, Kenneth and Nell Cobb, for giving me the opportunity to start this journey and the moral support to finish it.

ACKNOWLEDGMENTS

The author wishes to thank Curtis Bahr and Rens Ross for technical hardware assistance, Helga Alexander for assistance with microprobe measurements, Allison Yu and Prof. Michael Dudley for x-ray topography analysis, and Dr. Kevin Jones for his support. The author is indebted to Drs. Frank Szofran, Ching-Hua, Donald Gillies, and especially Sandor Lehoczy for many enlightening discussions and to the Microgravity Science and Applications Division of the Microgravity Research Program at the National Aeronautics and Space Administration for its continued support.

TABLE OF CONTENTS

	<u>page</u>
ACKNOWLEDGMENTS	iii
ABSTRACT	vi
 CHAPTERS	
1 INTRODUCTION AND MOTIVATION	1
Historical Review of the $\text{Hg}_{1-x}\text{Zn}_x\text{Se}$ Alloy System	6
Motivation and Objectives	15
Experimental Approach	17
2 PSEUDOBINARY HgSe-ZnSe PHASE DIAGRAM	21
Alloy Synthesis and Sample Preparation	21
Procedure for Differential Thermal Analyses	24
Results and Discussion	28
Calculation of the $\text{Hg}_{1-x}\text{Zn}_x\text{Se}$ Pseudobinary Phase Diagram	43
3 ALLOY SYNTHESIS AND CRYSTAL GROWTH	48
Ampoule Preparation	48
Preparation of Charge for Synthesis	49
Alloy Synthesis	50
Crystal Growth	51
4 BASIC MACROSCOPIC DEVELOPMENT DURING DIRECTIONAL SOLIDIFICATION	61
Surface Analysis	61
Development of Grain Structure	77
Crystallographic Orientation	78
Crystal Quality by Synchrotron Radiation	79

5	COMPOSITIONAL VARIATIONS DURING DIRECTIONAL SOLIDIFICATION.....	85
	Axial Compositional Variations.....	85
	Radial Compositional Variations.....	87
6	DISLOCATION GENERATION DURING DIRECTIONAL SOLIDIFICATION.....	109
	Surface Preparation for Etch Pit Study.....	110
	Selection of Appropriate Etchant.....	111
	Method for Determining Etch Pit Density.....	112
	Origin of Dislocations during Directional Solidification.....	135
	Effect of Ampoule Wall on Etch Pit Density.....	137
	Effect of Magnetic Field on Dislocation Density.....	142
	Other Considerations.....	144
	Comparison of Dislocation Densities in $\text{Hg}_{1-x}\text{Zn}_x\text{Se}$ Alloys with Similar Materials.....	146
7	CONCLUSIONS.....	148
APPENDIX		
A	COLLAGES OF INGOT SURFACE FEATURES.....	153
B	COLLAGES OF GRAIN STRUCTURE.....	186
	LIST OF REFERENCES.....	193
	BIOGRAPHICAL SKETCH.....	198

Abstract of Dissertation Presented to the Graduate School
of the University of Florida in Partial Fulfillment of the
Requirements for the Degree of Doctor of Philosophy

**MICROSTRUCTURAL DEVELOPMENT DURING THE DIRECTIONAL
SOLIDIFICATION OF MERCURY ZINC SELENIDE ALLOYS**

By

Sharon D. Cobb

August 1998

Chairman: Professor Kevin S. Jones
Major Department: Materials Science and Engineering

Mercury zinc selenide alloys have potential for the detection electromagnetic radiation over a wide wavelength range, because their energy gap varies with the alloy composition. Compositional variations and distribution of defects, however, must be understood to ensure the desired electrical response. The primary objectives of this investigation were to characterize the basic structural properties of bulk material, and determine whether the addition of Zn to the HgSe lattice reduced the potential for defect formation.

In order to determine optimum growth conditions, the liquidus and solidus temperatures of select compositions were measured, and the phase diagram was calculated using a regular solution model. Using this information, $\text{Hg}_{0.9}\text{Zn}_{0.1}\text{Se}$ alloys were synthesized, then remelted and directionally solidified. One ingot was solidified in a magnetic field to reduce radial compositional variations. Surface features of each ingot

were documented after growth, and the composition distribution was determined in the radial and axial directions. Development of the grain structure was investigated along the centerline of each crystal. Each ingot was oriented to a specific crystallographic orientation and wafers were removed. Wafers were polished and chemically etched to reveal the densities of dislocation etch pits.

Liquidus temperatures were difficult to determine for low ZnSe concentration, however, results were sufficient to determine proper growth conditions. Axial compositional variations indicated diffusion controlled solidification. Radial compositional variations were greatly reduced when solidification occurred in an applied magnetic field. Features observed on the as-grown ingot surface indicated that very little wetting occurred between the alloy and ampoule, especially when a graphite getter was incorporated into the ampoule. The combination of convex interface shape and reduced wetting was favorable for single crystal growth and reduced dislocation densities. A change in the thermal gradient during processing was responsible for generating more dislocations than any other experimental parameter. Overall, however, the $\text{Hg}_{1-x}\text{Zn}_x\text{Se}$ system had etch pit densities one to two orders of magnitude less than HgTe based alloys. The results of this investigation indicate this alloy has improved resistance to dislocation formation, compared with similar II-VI alloys, and should be further investigated for the detection of electromagnetic radiation.

CHAPTER 1 INTRODUCTION AND MOTIVATION

It is well documented that semiconductor alloys of the II-VI type, such as the widely used mercury cadmium telluride ($\text{Hg}_{1-x}\text{Cd}_x\text{Te}$) alloy, possess appropriate electrical and optical properties for use in electro-optical devices. These alloys behave as pseudobinary alloys whose end points are binary alloys. The technological importance of this class of materials is derived from the almost linear variation of the band gap with alloy composition. This property allows detectors with specific spectral response to be tailor made by appropriate selection of composition. This feature however, can also be detrimental to device performance if compositional variations are induced during the growth process.

Inherent in the nature of the growth process of alloys such as $\text{Hg}_{1-x}\text{Cd}_x\text{Te}$ are a multitude of factors that can lead to compositional variations. The wide separation of the liquidus and solidus curves on the phase diagram results in a large segregation coefficient, and thus a large difference in the composition of the solid and liquid in equilibrium at the interface. As solidification progresses, a diffusion boundary layer is established in the liquid ahead of the interface. If the interface is not flat, the difference in density of the liquid immediately ahead of the interface, depleted of solute, and the liquid of nominal composition farther into the melt leads to buoyancy effects that result in convective flow in the melt. Once established, these flow fields lead to increased curvature in the interface,

which causes radial variations in composition. In addition to solutally generated convection, fluid motion is also caused by radial thermal gradients arising from differences in thermal conductivity in the solid and liquid near the solid/liquid interface region that are caused by transverse heat flow into and out of the sample. Variations in thermal and compositional uniformity also lead to defects in the crystal structural that influence the structural and electrical properties of the material.

In addition to problems created by the nature of the growth process, the application of the $\text{Hg}_{1-x}\text{Cd}_x\text{Te}$ system, in particular, has also been hindered by the destabilization of the lattice that results from the weakening of the Hg-Te bonds caused by Cd alloying. A number of theories have been proposed to explain this phenomenon.

The primary contribution to structural instability is thought to be related to the atomic structure and bonding characteristics of these alloys. Chen et al. (1983) postulated that during the formation of the $\text{Hg}_{1-x}\text{Cd}_x\text{Te}$ tetrahedron, there is a net transfer of electrons from the Cd to the Hg. These electrons are thought to occupy anti-bonding states, since the bonding states on the HgTe bond are full, thus causing a destabilization of the HgTe bond. This reduces the bond strength which explains the increase in dislocation formation, vacancies and other defects which contribute to the mobility of Hg through the lattice (Spicer et al., 1983).

Spicer et al. (1983) also attributed the ease of defect formation and movement to the atomic structure and bonding characteristics of Hg in these alloys. They considered the change in binding energy of the s^2 electrons when they are transferred from the lighter group II (Cd) to the heavier group VI (Hg) elements to be important. Experimental measurements showed the Hg ionization energy of the $6s^2$ valence electrons is 1.4 eV

greater than the $5s^2$ Cd valence electrons. Photoemission studies showed that Hg 5d levels rise to lower binding energies with the addition of Cd to the HgTe bond. The weakened Hg-Te bond explains the high susceptibility of $\text{Hg}_{1-x}\text{Cd}_x\text{Te}$ alloys to mechanical damage. Hg was shown to be extremely mobile in $\text{Hg}_{1-x}\text{Cd}_x\text{Te}$ alloys, moving via vacancies, interstitials or along dislocations, grain and sub-grain boundaries.

It has been shown theoretically (Sher et al., 1985) and experimentally (Triboulet, 1988) that the HgTe bond can be strengthened by alloying with ZnTe. Several previous investigations have proposed explanations for the origin of this increased lattice stability.

Sher et al. (1985) suggested that there is no net transfer of electrons to anti-bonding states when Zn is added to HgTe, contrary to the behavior of HgTe alloyed with Cd. An additional benefit of the HgTe system is the presence of the shorter, stronger ZnTe bond, which increases the stability of the alloy.

Triboulet (1988) explained that the shorter bond length of ZnTe, and thus increased lattice stability in mercury zinc telluride ($\text{Hg}_{1-x}\text{Zn}_x\text{Te}$) alloys, is due to the smaller screening effect of the electrons in alloys composed of Zn rather than Cd. The atomic binding energy of ZnTe is also higher than CdTe as shown in Table 1.

The contribution of ionicity to the overall bond characteristics is also known to be a predictor of bond strength. It has been suggested (Phillips, 1982) that there is a value

Table 1-1. Properties of binary II-VI semiconductors.

Property	HgTe	CdTe	ZnTe	HgSe	CdSe	ZnSe
Bond Length (Å)*	2.797	2.805	2.643	2.635	2.62	2.455
Binding Energy (eV)**	-2.85	-4.3	-4.7			
Bonding Energy (eV)*				-0.909**	-1.45**	-1.51**
Ionicity Parameter***	65.2%	67.5%	59.9%	68.0%	68.4%	62.3%

*(Sher et al., 1985), **(Triboulet, 1988), *** (Phillips, 1982)

for ionicity of 0.78 above which the zinc blende crystal structure is predicted to be unstable. Hall and Vander Sande (1978) found an inverse relationship between ionicity and stacking fault energy. The addition of Zn decreases the ionicity statistically, consequently making the lattice more stable and the energy of formation of dislocations higher. Sher et al. (1985) found interaction dislocation energies are proportional to d^{-5} to d^{-11} (where d is the bond length), the former value applying to purely covalent materials, thus, the shorter and less ionic the bond, the more stable the lattice against line defect formation.

Mechanical strengthening mechanisms have also been suggested as an explanation for increased lattice strength and reduction in dislocation formation. Ehrenreich and Hirth (1985) proposed that in GaAs, the addition of In caused solution hardening with the surrounding atoms, and that this strain field contributed to a pinning force that inhibited dislocation motion. For $\text{Hg}_{1-x}\text{Zn}_x\text{Te}$ and $\text{Hg}_{1-x}\text{Cd}_x\text{Te}$ alloys, Guergouri and Triboulet (1988) calculated the critical resolved shear stress (CRSS) to show the effect of Zn in strengthening the lattice. Micro-hardness measurements as a function of composition followed the trends of calculated CRSS values. Higher values occurred when there was a greater bond length difference between AC and BC, and when there was a weak BC bond length variation as a function of composition (Guergouri et al., 1988). This model, however, neglects electronic contributions.

The mercury cadmium selenide ($\text{Hg}_{1-x}\text{Cd}_x\text{Se}$) system, another II-VI alloy system, has also been investigated for electro-optical applications. Sher's calculation of bond length and strength suggests that the HgSe bond is more stable than the HgTe bond.

Bond energy for HgSe is predicted to be -0.909 eV, compared with -0.480 eV for HgTe (Sher et al., 1985). The $\text{Hg}_{1-x}\text{Cd}_x\text{Se}$ alloy system has received little commercial attention, however, primarily because its electrical properties are not stable with time (Nelson et al., 1978). The same mechanisms responsible for the destabilization of HgTe with Cd additions are thought to apply to the addition of Cd to HgSe.

The mercury zinc selenide ($\text{Hg}_{1-x}\text{Zn}_x\text{Se}$) alloy system has also been shown to have appropriate response in a range of specific wavelengths that are of technological interest for infrared radiation imaging and detection. The widely investigated $\text{Hg}_{1-x}\text{Cd}_x\text{Te}$ and $\text{Hg}_{1-x}\text{Zn}_x\text{Te}$ alloys systems are electrically p-type. The $\text{Hg}_{1-x}\text{Zn}_x\text{Se}$ system, however, forms with a stoichiometric excess of Hg atoms, which results in n-type material. This could be beneficial for detector applications mounted in a vacuum environment. $\text{Hg}_{1-x}\text{Cd}_x\text{Te}$ and $\text{Hg}_{1-x}\text{Zn}_x\text{Te}$ alloys that have been annealed in Hg vapor can revert back to their natural state when exposed to a vacuum environment at temperatures above 200 °C. $\text{Hg}_{1-x}\text{Zn}_x\text{Se}$ and $\text{Hg}_{1-x}\text{Cd}_x\text{Se}$ alloys are often annealed in a vacuum to reduce the number of intrinsic charge carriers. Therefore, the use of a material with a natural Hg excess should be an advantage for applications requiring devices to operate in a vacuum environment.

Sher et al. (1985) showed theoretically that the addition of Zn to HgSe should have a stabilizing effect on the HgSe bond as opposed to the destabilizing effects caused by Cd additions. It was shown by Cobb et al. (1991), through periodic measurement of transmission properties as a function of time, that the addition of Zn to the basic HgSe zinc blende structure improved the stability of the properties compared with the behavior in HgSe. Andrews et al. (1990) investigated the micro-hardness of HgSe and HgTe based

alloys with Zn and Cd additions. Their results showed, qualitatively, the correlation between the relative bond energy contribution and increased lattice stability as manifested through mechanical strength. They found that alloys based on the HgSe bond had higher hardness values than HgTe based alloys for similar percentage of alloy element, and that alloys with Zn additions had a higher micro-hardness than those compounds alloyed with Cd. This is another indication that the addition of Zn increased the bond stability in these alloys.

In addition to the potential application of $\text{Hg}_{1-x}\text{Zn}_x\text{Se}$ as substrate materials for infrared detectors, Ren et al. (1993) described a combination of a light emission multi-layered structure with a graded heterostructure of HgSe-HgZnSe layers to improve ohmic contact to the upper p-type layer of the light emitting structure. The reduction in valence band offset provided a stable low resistance ohmic contact for ZnSe based light emitting and laser diodes.

Historical Review of the $\text{Hg}_{1-x}\text{Zn}_x\text{Se}$ Alloy System

$\text{Hg}_{1-x}\text{Zn}_x\text{Se}$ is a pseudobinary alloy between HgSe and ZnSe whose band gap can be compositionally tuned for specific wave length response from -0.06 eV for $x = 0$ (Lehoczky et al., 1974) to 2.6 eV for $x = 1.0$ (Kot et al., 1964). HgSe has a negative direct-energy band gap and is a perfect semi-metal, while ZnSe has a large energy gap and is a semiconductor. Research, to date, on the $\text{Hg}_{1-x}\text{Zn}_x\text{Se}$ system has been primarily focused on the electrical characteristics of the system.

The first investigation of this system was published over thirty years ago by Kot and Simashkevich (1964). It included information on the synthesis, structural and

electrical properties of $\text{Hg}_{1-x}\text{Zn}_x\text{Se}$ alloys. The structure of all samples was face-centered-cubic. The variation of lattice constant with composition, as deduced from x-ray diffraction measurements, was linear from 6.07 Å to 5.66 Å, for HgSe and ZnSe, respectively. For most samples, electron concentration varied from 3×10^{18} to $2 \times 10^{17} \text{ cm}^{-3}$. In bulk samples, Hall mobility at room temperature varied from 22,000 cm^2/V for HgSe to a few thousand cm^2/V for 75% ZnSe.

Investigations into the band structure of this material to explain the differences between this system and other II-VI semiconductor materials began a decade later. Leibler et al. (1973) established that there was a fundamental difference in the spectra for $\text{Hg}_{1-x}\text{Zn}_x\text{Se}$ and $\text{Hg}_{1-x}\text{Zn}_x\text{Te}$ alloys compared with CdZnTe and ZnSSe alloys. They postulated that these differences were due to changes in band structure. Gavaleshko and Khomyak (1976) found that a strong interaction between bands caused the dispersion relationship of these narrow-gap semiconductors to be very non-parabolic. The non-linear dependence of the energy gap on composition in the investigated composition range indicated that the bowing parameter had a sign opposite of that typically found in zinc blende alloys. Gavaleshko et al. (1984b) determined the energy band parameters from plasma reflection minima. Infrared reflection spectra showed that the conduction band could be described by the Kane three-band model and that Γ_6 and Γ_8 energy band inversion occurred.

Gavaleshko et al. (1977) studied the band structure in the vicinity of the semi-metal/semiconductor transition composition, and determined the transition point to be at about $x = 0.03$. Later, the measurements of the effective mass and energy gap as a function of composition and temperature predicted the inversion point of the Γ_6 and Γ_8

bands to be in the range of $0.02 \leq x \leq 0.06$ (Gavaleshko et al., 1980; Potapov et al., 1980). Miller and Koh (1994) attributed the large axial crystal field interaction parameter they observed in Hg based II-VI alloys, to the change in band gap that occurred as these alloys changed from negative or zero band gap to the normal positive semiconductor band gap structure as alloying was increased.

Gavaleshko and Khomyak (1976) initially noted the strong non-linear dependence of the energy gap on composition in the investigated composition range. This non-linear behavior was also observed in thin layers grown by flash evaporation, electrochemical deposition and molecular beam epitaxy (Kashyap et al., 1990; Natarajan et al., 1995; Behr et al, 1996). Kumazaki et al. (1988) found that valence band to conduction band transitions were quadratically dependent on composition, while the Δ_1 spin-orbit splitting dependence was almost linear. They also found that the coefficients in the equation for the compositional dependence of energy splittings were considerably different than in $\text{Hg}_{1-x}\text{Cd}_x\text{Te}$ alloys. In films prepared by flash evaporation technique, Kashyap et al. (1990) observed a direct optical energy gap. They were also expecting, based on the calculations of Sher et al. (1985), that the Hg-Se bond would produce more stable materials than $\text{Hg}_{1-x}\text{Zn}_x\text{Te}$ alloys. They also observed the typical bowing observed in other pseudobinary compounds, but the larger bowing in $\text{Hg}_{1-x}\text{Zn}_x\text{Se}$ alloys resulted in a reduction in the slope of dE_g/dx (energy gap change per change in composition), making it easier to achieve a homogeneous single crystal with $E_g \leq 0.1$ eV. The larger bowing was possibly, because HgSe is less ionic than HgTe.

Scattering mechanisms were investigated to explain electrical property measurements, particularly the temperature and compositional dependence of the charge carrier mobility. One investigation (Gavaleshko and Khomyak, 1976) found scattering was dominated by optical and piezoacoustic phonons at liquid nitrogen temperatures for alloys with $x = 0.10$. Kumazaki and Nishiguchi (1986) observed two transverse optical (TO) modes, TO_1 and TO_2 , in far-infrared reflection spectra due to native defects or compositional inhomogeneity. Longitudinal optical (LO) peaks were dependent on composition and temperature. Potapov et al. (1979) explored a wider temperature range and found by Shubnikov-de Haas oscillations that the dominant scattering mechanism was ionized impurities in the 4.2 - 30°K temperature range. In the 30-90°K range, electron scattering was by acoustic phonons. For $T > 90^\circ\text{K}$, the temperature dependence of oscillations indicated considerable scattering by optical phonons. Scattering mechanisms were also determined by studying the temperature and concentration dependence of mobility in degenerate $\text{Hg}_{1-x}\text{Zn}_x\text{Se}$ samples (Gavaleshko et al., 1980; Gavaleshko et al., 1986b). They found the dominant scattering mechanisms were impurity ions and polar optical phonons. They found that carrier mobility was a function of electron carrier concentration and was limited by impurity and optical scattering at 77 and 300K, respectively. Scattering by optical phonons was weakly dependent on electron density, but the reduction in mobility due to scattering by impurities decreased greatly with increasing carrier density.

Several investigators have explored the contribution of defect mechanisms to the electrical properties of $\text{Hg}_{1-x}\text{Zn}_x\text{Se}$ alloys. Applying Hagemark's theory (Hagemark, 1976) to $\text{Hg}_{1-x}\text{Zn}_x\text{Se}$ alloys, Ekbote and Zope (1978) postulated that as the alloy cooled from

1200°C, Hg atoms became immobile first, since they were the largest and heaviest. As annealing continued at 600°C, the Hg remained frozen in at interstitial sites. The Zn was still mobile at this temperature, so it occupied the vacant Hg sites. The requirement for charge neutrality required the creation of increased Se vacancy concentration, leaving the alloy n-type. For higher concentrations of Zn, there was more Zn to fill the Hg vacancies, resulting in a more stoichiometric (HgZn)Se system with less Hg interstitials. The electrical conductivity, which was due mainly to ionized Hg interstitials, decreased as the amount of HgSe in the solution was reduced. The higher ionicity of the ZnSe also decreased the Hall mobility with increasing ZnSe. This theory implies that Hg interstitials remain frozen in even after moderate heat treatment temperatures. Ekbote and Zope used this theory to explain the electrical properties of $\text{Hg}_{1-x}\text{Zn}_x\text{Se}$ alloys. Gavaleshko et al. (1986a) questioned this theory because of their observations during annealing experiments. They suggested that during annealing in Se vapor, Se atoms were absorbed on the surface, which annihilated surface vacancies, thereby reducing the vacancy concentration. During Hg annealing, they believed that Se atoms migrated to the surface and formed stable HgSe dimers at the Hg site. A new layer was formed on the surface causing a net increase in the number of Se vacancies in the bulk. This scenario is likely during crystal growth in a sealed ampoule, due to the high Hg vapor pressure at elevated temperatures.

Deep defect level energy calculations were performed (Li and Patterson, 1994; Li and Patterson, 1996; Patterson and Li, 1996) to predict the type and characteristics of defects in the II-VI Hg chalcogenides. The predicted location of interstitial impurities was similar in the $\text{Hg}_{1-x}\text{Cd}_x\text{Te}$, and $\text{Hg}_{1-x}\text{Zn}_x\text{Te}$ systems. Chemical trends of deep levels in

$\text{Hg}_{1-x}\text{Zn}_x\text{Se}$ were different from the other two systems. Little explanation was given due to the lack of experimental data to compare with predictions. A Green's function technique was used to calculate defect formation energies. They found the formation energy of nominal impurities was similar for all alloys. The formation energy of a negative impurity was larger than for a positive one and the formation energy of charged states varied widely. They found that the lowest formation energy occurred for self-interstitials, while the energies for antisites and vacancies were almost the same. For $\text{Hg}_{0.92}\text{Zn}_{0.08}\text{Se}$, the formation energy of vacancies was 1.75 eV and the deep level was calculated to be 0.06 eV. Their calculations predicted more vacancies in $\text{Hg}_{1-x}\text{Zn}_x\text{Se}$ than in $\text{Hg}_{1-x}\text{Cd}_x\text{Te}$ or $\text{Hg}_{1-x}\text{Zn}_x\text{Te}$.

The effect of dopants on the electrical properties of the system was also explored. Alloys ($x \leq 0.072$ and $0 \leq x \leq 0.14$) highly doped with Fe had an improved carrier mobility (Dobrowolski et al., 1992; Dobrowolski et al., 1993a; Dobrowolski et al, 1993b) due to reduced scattering. Electron concentration and mobility improved with increasing Fe concentrations. For high doping levels, their calculations agreed well with experimental mobility values, leading them to concluded that scattering was due to ionized impurities and alloying. Experimental mobility was lower than predicted for low dopant concentrations, so they concluded that other scattering mechanisms were operative. They concluded that the improvement in electron mobility with increasing Fe doping had a healing effect on the electrical properties, probably by making defect formation less likely (Sher et al., 1985).

No information has been published on device production in $\text{Hg}_{1-x}\text{Zn}_x\text{Se}$ alloys, however, Ren et al. (1993) described an idea for a new integrated heterostructure device

composed of a wide band gap light emission multilayered structure with a narrow band gap HgSe-HgZnSe graded heterostructure to improve ohmic contact to the upper p-type structure. The graded HgZnSe would reduce the valence offset between the ZnSe and the HgSe contact and provide a stable low resistivity ohmic contact.

Another potential application was to use wide band gap $\text{Hg}_{1-x}\text{Zn}_x\text{Se}$ ($0.86 \leq x \leq 1.0$) to replace ZnCdSe in quantum-well blue-green lasers (ZnCdSe/ZnSSe/ZnMgSSe) because there was less lattice mismatch (Hara et al., 1995). Samples consisted of a ZnSe buffer layer on a GaAs substrate followed by $\text{Hg}_{1-x}\text{Zn}_x\text{Se}$ layers grown by molecular beam epitaxy. Their observations were consistent with the non-linear relationship between band gap energy and composition previously observed for $\text{Hg}_{1-x}\text{Zn}_x\text{Se}$ bulk alloys. X-ray diffraction measurements showed a lattice mismatch of 0.04% for $x = .015$. The band gap at this composition corresponds to the band gap of $\text{Zn}_{0.8}\text{Cd}_{0.2}\text{Se}$ used in blue-green lasers, making $\text{Hg}_{1-x}\text{Zn}_x\text{Se}$ an attractive alternative for this application.

The potential advantage of these II-VI semiconductors for photoconductive infrared detectors is related to the variation of the energy band gap with composition. On the other hand, in order for production to be economically advantageous and device performance to be reliable at the desired wavelength, wafers from bulk grown materials must be compositionally uniform. Cobb et al. (1991) investigated the effects of growth rate on compositional variations in Bridgman grown crystals. They found that for fast growth rates the average axial composition was constant in the steady state growth region; however, there were radial compositional variations. For slow growth rates, radial compositional variations were reduced, but the average axial composition varied.

The advantage of the Zn based HgSe alloys over Cd based alloys is thought to be related to the higher ionicity of the ZnSe bond compared to the CdSe bond. The stronger ZnSe bond also increases the bond strength of the system, which should improve the stability of electrical properties with time. The micro-hardness of HgSe and HgTe based alloys with Zn and Cd additions was compared, (Andrews et al., 1990) and it was found that alloys with Zn additions had a higher micro-hardness than those compounds alloyed with Cd. This supports the supposition that the addition of Zn increases bond stability in the alloy. The optical and electrical properties were measured for the as-grown crystals and for crystals annealed in selenium vapor (Cobb et al., 1991). Optical transmission properties were improved by this annealing which caused a reduction in charge carrier concentration. This improvement was stable with time. They concluded that the addition of Zn to the basic HgSe zinc blende structure improved the stability of electrical properties compared with similar results for HgSe (Nelson et al., 1978).

The microstructural characteristics of the $\text{Hg}_{1-x}\text{Zn}_x\text{Se}$ system have been reported only for thin layers. Natarajan et al. (1995) produced films of composition $0.20 \leq x \leq 1.0$ by electrochemical deposition from aqueous baths. They found the $\text{Hg}_{1-x}\text{Zn}_x\text{Se}$ films were n-type, naturally, with no excess, and the Hg rich films had larger crystallite size. Einfeldt et al. (1995) reported on molecular beam epitaxial growth and the microstructural characteristics of the $\text{Hg}_{1-x}\text{Zn}_x\text{Se}$ system as a way to produce the device described by Ren et al. (1993). The layers they produced never became polycrystalline, however, x-ray rocking curves could not be obtained on all samples. They concluded that the poor quality was related to neither growth conditions or substrate lattice mismatch. They postulated it might be due to a miscibility gap below 443°C , because similar predictions were made in

$\text{Hg}_{1-x}\text{Zn}_x\text{SeS}$ alloys (Leute and Plate, 1989). Gavaleshko et al. (1984a) had already modeled the alloy phase diagram using the regular associated solution theory. Experimental values were obtained from differential thermal analysis (DTA) to within $\pm 2^\circ\text{C}$ for $0 \leq x \leq 0.2$. A rather large variation between experiment and both the ideal and regular solution theories was observed, but a miscibility gap was not detected. Subsequent studies (Behr et al., 1996) using cross-sectional transmission electron microscopy (TEM), high resolution TEM (HRTEM), and transmission electron diffraction failed to confirm their prediction. They eliminated spinodal demixing, atomic ordering, or embedded hexagonal crystallites as possible sources of the two different microstructures they observed. A larger deviation from the linear composition versus energy gap relationship was observed in samples containing a large number of microtwins, stacking faults and twins, however, a correlation between growth conditions, development of twins, and the relationship to energy gap was not found. They concluded that the $\text{Hg}_{1-x}\text{Zn}_x\text{Se}$ was not suitable for molecular beam epitaxy and that the formation of a graded gap between HgSe and p-ZnSe, described by Ren, was not possible.

In summary, the $\text{Hg}_{1-x}\text{Zn}_x\text{Se}$ system has been well characterized in terms of electrical properties. It is a viable candidate for the detection of infrared radiation and other electro-optical applications. It has been shown, theoretically, that the greater bond strength and shorter bond length should lead to a more stable lattice which is less susceptible to defect generation than the Cd based alloys. Micro-hardness, electrical and optical measurements clearly indicate increased lattice stability, however, to date there has been no characterization of the grain structure or crystalline quality for crystals grown from the melt. The primary objectives of this study were to determine the nature of grain

development in this alloy and to determine whether the strong bonding characteristics of this system resulted in lower dislocation densities.

Motivation and Objectives

Previous studies on this system have been primarily focused on the electrical properties of the alloy. Predictions of increased lattice stability for HgSe alloyed with Zn have been substantiated with optical property measurements and micro-hardness measurements as a function of composition. However, because grain boundaries and other structural defects can lead to current leakage in devices, a basic understanding of the microstructural properties must be developed before this system can be considered as a viable substrate material.

It has been shown (Mikkelsen and Boyce, 1982) by extended x-ray absorption fine structure (EXAFS) measurements on GaInAs alloys that while the average lattice parameter obeys Vegard's rule, varying linearly between the values of the binary endpoints, the actual bond lengths between individual elements (GaAs and InAs) are about the same as observed in the binary compounds. The bonds shrink and stretch by about 4% to accommodate the impurity. Only local arrangement is disturbed. Dislocation energies are dominated by long range bond angle distortions (Hirth and Lothe, 1982), and influenced by the shear coefficients which scale with bond length as d^{-7} (Harrison, 1980), consequently, a lower number of dislocations are expected in materials with shorter bond lengths. A supersaturated vacancy concentration often exists just behind the growth front because the equilibrium number of vacancies is less in the solid than at the elevated temperature of the liquid (Sher et al., 1985). These excess vacancies can come together to

form dislocation loops at the growth interface. If the loop continues to absorb vacancies, it can climb toward the growth interface and become incorporated into the growing crystal. For compounds with higher bond strength, vacancy formation is more difficult and thus, the dislocation energies will be higher, making climb less favorable. Based on this logic and the values shown in Table 1-1, the $\text{Hg}_{1-x}\text{Zn}_x\text{Se}$ alloy system should certainly exhibit greater resistance to dislocation formation than $\text{Hg}_{1-x}\text{Cd}_x\text{Se}$ alloys, and possibly even show a reduction compared to $\text{Hg}_{1-x}\text{Cd}_x\text{Te}$ and $\text{Hg}_{1-x}\text{Zn}_x\text{Te}$ alloys. In addition to dislocations, stacking faults and tellurium inclusions have also been observed in $\text{Hg}_{1-x}\text{Cd}_x\text{Te}$ alloys, which tend to limit the usefulness of these alloys for certain types of electro-optical applications.

Although the more favorable bonding characteristics of the $\text{Hg}_{1-x}\text{Zn}_x\text{Se}$ system should result in lower dislocation densities, selection of proper growth conditions are also important in controlling dislocations generated from thermal stresses induced during solidification. Previous work on the $\text{Hg}_{1-x}\text{Cd}_x\text{Te}$ system (Bornykh et al., 1974) indicates a higher dislocation density in alloys solidified at higher rates. At the highest growth rates employed, solidification was unstable due to variations in vapor pressure. This resulted in the formation of dislocations around Te precipitates. Although not stated, different dislocation densities would be expected for different growth rates because steeper thermal gradients are required to maintain stable growth conditions at slower rates. Slower growth rates produced relatively large crystals with a subgrain misorientation of 0.3-1.5 arc-sec. It was also reported that dislocation density was 1-2 orders of magnitude higher at the crystal circumference than in the central portion. This is thought to be due, in part, to the differences in the thermal expansion coefficient between the alloy and the fused

silica ampoules used for containment. Genzel et al. (1990) reported similar behavior for $\text{Hg}_{1-x}\text{Cd}_x\text{Te}$ crystals grown by the traveling heater process. For the slowest growth rates, they reported lowest dislocation densities at the leading edge of the crystal, with an increase in density at the tail end.

The relationship between solidification rate and defect generation is also effected by radial temperature gradients that cause convective cells in the melt ahead of the interface. The interaction of these cells with the diffusion boundary layer contribute to the shape of the interface shape, causing compositional variations. Since the lattice constant varies with composition, dislocations can be produced to accommodate these strains.

It is generally accepted that the presence of the stronger, shorter ZnSe bond results in a more stable lattice and should therefore result in an improvement in the electrical and mechanical properties of related pseudobinary alloys. The goal of this research study was to investigate the predicted improved resistance to defect generation related to this increased lattice stability in $\text{Hg}_{1-x}\text{Zn}_x\text{Se}$ alloys. Initially, the macroscopic structural properties of the alloy were investigated. The influences of processing parameters, such as ampoule wall preparation, and ampoule diameter, on defect generation were determined.

Experimental Approach

The emphasis of this study was to investigate the basic structural characteristics of $\text{Hg}_{1-x}\text{Zn}_x\text{Se}$ alloys. In order to evaluate the viability of this alloy for device applications it is important to understand the grain structure, and tendency toward formation of structural defects, such as twins and inclusions, in this material. Although many studies

have suggested explanations for the role Zn plays in the electrical properties of this system based on the results of electrical property measurement and modeling, there is no documentation of the structural characteristics of bulk material. The first portion of this study focused on determining the proper thermal environment for growing these alloys from the melt. The investigation then examined the basic microstructural characteristics of this material compared with other Hg based alloys to determine the effects of Zn on dislocation formation in this alloy system.

Phase Diagram

It is well known that interface shape, convection in the melt ahead of the interface, and the temperature gradient near the interface play substantial roles in crystal quality. Each of these are influenced by the thermal profile employed during solidification. The initial goal of this investigation was to determine the liquidus and solidus temperatures for low ZnSe mole fractions for this system, so that optimum experimental conditions were employed during growth of samples used for microstructural analysis. Several investigations have successfully used Bridgman type solidification techniques to grow bulk $\text{Hg}_{1-x}\text{Zn}_x\text{Se}$ alloy crystals, however, little is known about the thermophysical properties or the liquidus and solidus temperatures of the system. Gavaleshko et al. (1984a) performed DTA on $\text{Hg}_{1-x}\text{Zn}_x\text{Se}$ alloys with $x \leq 0.20$, but little is known about sample preparation, experimental setup or the thermal arrest curves.

For this investigation, samples were prepared for compositions ranging from $x = 0$ to at least $x = 0.2$. These HgSe-ZnSe alloys were synthesized by reacting high purity elemental constituents in fused silica ampoules. DTA measurements were taken to determine the phase equilibria temperatures.

Alloy Synthesis and Crystal Growth

Previously developed procedures (Cobb et al., 1991) were used to homogenize samples for directional solidification. The synthesized alloys were melted and directionally solidified in a Bridgman-Stockbarger type furnace.

The first series of experiments was to determine the effect of interface shape during solidification on microstructural characteristic in $\text{Hg}_{1-x}\text{Zn}_x\text{Se}$ alloys. The second set of experiments was to determine the effects of ampoule preparation on microstructural development.

Effect of Interface Shape on Defect Generation

The shape of the interface is known to influence radial compositional variations as well as the generation of thermal stresses at the solidification front that lead to dislocation formation. The direction of curvature is also known to effect grain selection and twin generation (Chang and Wilcox, 1974). Phase diagram data and previous data available for this alloy were used to select the proper growth rate to prevent constitutional supercooling.

Ampoule Preparation

Previous studies indicated that wetting between the molten alloy and the fused silica ampoule caused sticking along the ingot surface during solidification. This results in nucleation sites for grains and imposes stresses on the surface that can generate dislocations. Shetty et al. (1995) investigated the relative effectiveness of graphite and boron nitride coated ampoules. They found that less wetting occurred with the boron nitride coating. Another way to reduce wetting is the addition of a piece of high density

graphite to an ampoule prior to synthesis which acts as a getter for oxygen. Oxygen present in the elemental components can react with Si in the ampoule, causing wetting.

The objective of this phase of the study was to reduce wetting between the alloy and ampoule which can be a source for generating dislocations and nucleating grains. Crystals were grown in standard fused silica ampoules, ampoules with graphite plugs, and in an ampoule coated with a thin film of boron nitride. Microstructural characteristics and etch pit densities were compared.

Microstructural Characterization

Due to lack of previous microstructural work in this system, initially the basic characteristics of the crystal were documented. Images of the variations in as-grown surfaces were recorded. Compositional variations in the axial direction were determined along the surface of each ingot. Axial and radial composition was determined along the internal centerline of each crystal. Grain development was observed along the crystal centerlines using electron backscattered images

Two quenched crystals were sectioned in the region of the growth interface, parallel to the growth direction. The shape of the interface was determined.

Oriented samples from the steady state portion of each ingot were cut. These samples were chemically treated to reveal etch pits. These samples were used to compare relative etch pit densities for different growth conditions.

Results of this study were compared with previous investigations on similar the HgCdTe and HgZnTe alloy systems to determine if the bonding properties of the HgZnSe system improved the alloy's resistance to dislocation formation as predicted.

CHAPTER 2

PSEUDOBINARY HgSe-ZnSe PHASE DIAGRAM

Alloy Synthesis and Sample Preparation

Ampoules used for differential thermal analysis (DTA) measurements were produced using fused silica from National Scientific. Ampoules were formed by tapering the end of 15 mm-o.d. x 9 mm-i.d. tubing. The 3 mm wall thickness was required to contain the high Hg vapor pressure that developed in $\text{Hg}_{1-x}\text{Zn}_x\text{Se}$ alloys at temperatures close to the softening point of fused silica. Ampoules were cleaned with hydrofluoric acid, then triple rinsed, alternating between methanol and distilled water. Each ampoule was annealed by heating slowly to 1140°C, held for two hours, then slowly cooled to remove any strain induced during ampoule shaping. After this procedure, the ampoule was loaded with five-nines grade Zn and Se and triply distilled Hg in the quantity required to produce a sample approximately 5 cm long of the desired composition. The exact weights for each sample are shown in Table 2-1.

An 8 mm diameter by 10 mm length piece of graphite was added to two of the samples to help reduce wetting and prevent ampoules from cracking. The graphite plugs were outgassed under vacuum prior to loading. The graphite was expected to be a getter for oxygen, reducing the reaction between the small amounts of oxygen in the alloy and the fused silica ampoule. A reference sample, with similar mass of six-nines pure Sb, was heated in a rocking furnace to 650 °C, and then cast by removing power from the furnace.

Table 2-1. Composition of DTA samples.

Sample # - Composition	Hg (grams)	Se (grams)	Zn (grams)	Total	Result
DTA-1.0	37.5807	14.793 2		52.3739	Ampoule failed
DTA-2.0	37.5809	14.793 5		52.3744	Considerable wetting
DTA-3.1	17.2733	7.5551	0.6255	25.4539	Resealed to reduce open volume, used for DTA
DTA-4.08	17.5891	7.5225	0.4984	25.6100	Used for DTA
DTA-5.06 w/graphite	17.8915	7.4905	0.3725	25.755	Composition too low to measure transition, wetting reduced
DTA-6.15	16.4889	7.6361	0.9488	25.0738	Ampoule failed
DTA-7.15	16.5023	7.6361	0.9488	25.0872	Resealed to reduce open volume, ampoule failed during DTA
DTA 8.15 w/graphite	16.4910	7.6357	0.9487	25.0754	Ampoule failed
DTA 9.20	15.6878	7.7173	1.2777	24.6828	Used for DTA
DTA 10.15	16.4902	7.6357	0.9483	25.0742	Resealed to reduce open volume, used for DTA

Each sample was heated according to the schedule, shown in Figure 2-1, which was developed for this alloy system based on the method described by Cobb et al. (1991) and private communications related to measurements of the thermal arrest curves for the $\text{Hg}_{1-x}\text{Zn}_x\text{Te}$ system (Su et al., 1996). The samples were heated in a rocking furnace that was equipped with gimbals, allowing the furnace to be slowly tilted to $\pm 60^\circ$ along the horizontal axis. Arrows in Figure 2-1 indicate the duration of the rocking motion.

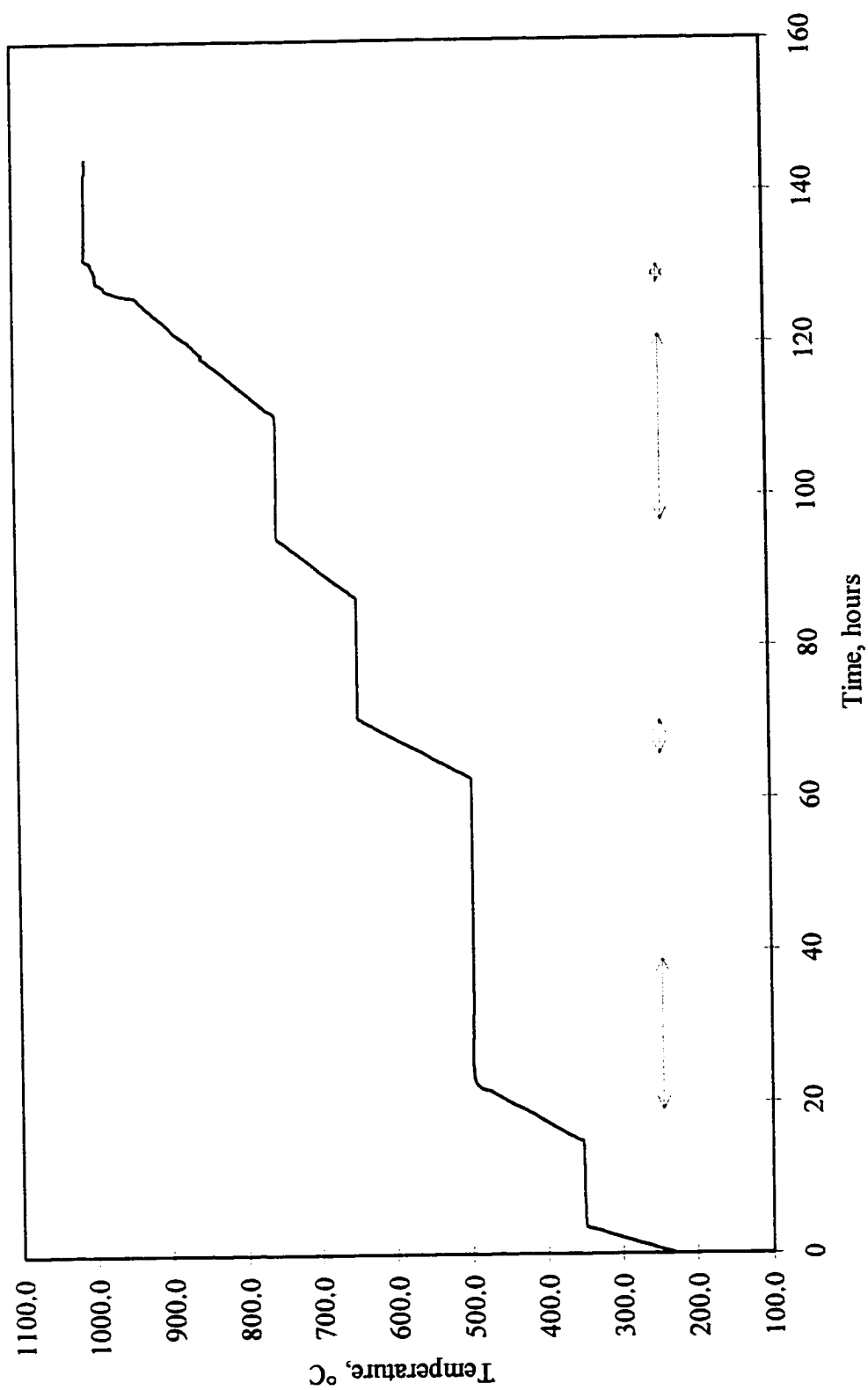


Figure 2-1. Heating schedule for synthesis of Hg_{1-x}Zn_xSe alloys.

Procedure for Differential Thermal Analyses

The phase equilibria temperatures were determined for $\text{Hg}_{1-x}\text{Zn}_x\text{Se}$ alloys with compositions $x = 0.08, 0.10, 0.15,$ and 0.20 by DTA measurements. The furnace configuration and arrangement of samples are shown in Figure 2-2.

Heating was accomplished with a Mellen, single-zone, resistively-heated, tubular furnace and a LFE Instruments temperature controller. The bore of the furnace was lined with a sodium heat pipe to improve isothermality. A reference sample of antimony was used as an internal calibration point for each experiment run. The second sample contained the alloy.

The two ampoules were loaded end-to-end in a quartz tube and then loaded into an Inconel tube to protect the furnace and heat pipe if the ampoule failed. A type R thermocouple was attached to each ampoule with a platinum foil band. The negative lead was connected to both bands. The differential signal was measured between the positive leads of each thermocouple. At a junction outside the furnace, the Pt lead on each thermocouple was attached to a Cu extension lead, and the Pt-13Rh lead to a Cu27 extension lead. A junction to pure Cu extensions was made at a Kaye Instrument Ice Point Reference. Two thermocouple signals and the differential signal were monitored by a Keithly 705 scanner. They were read by a Keithly 181 nanovoltmeter and recorded on a 486 personal computer. A schematic of the signal acquisition configuration is shown in Figure 2-3.

The initial scheme was to perform DTA inside a pressurized cartridge in order to provide a pressure balance as the internal Hg vapor pressure inside the ampoule increased

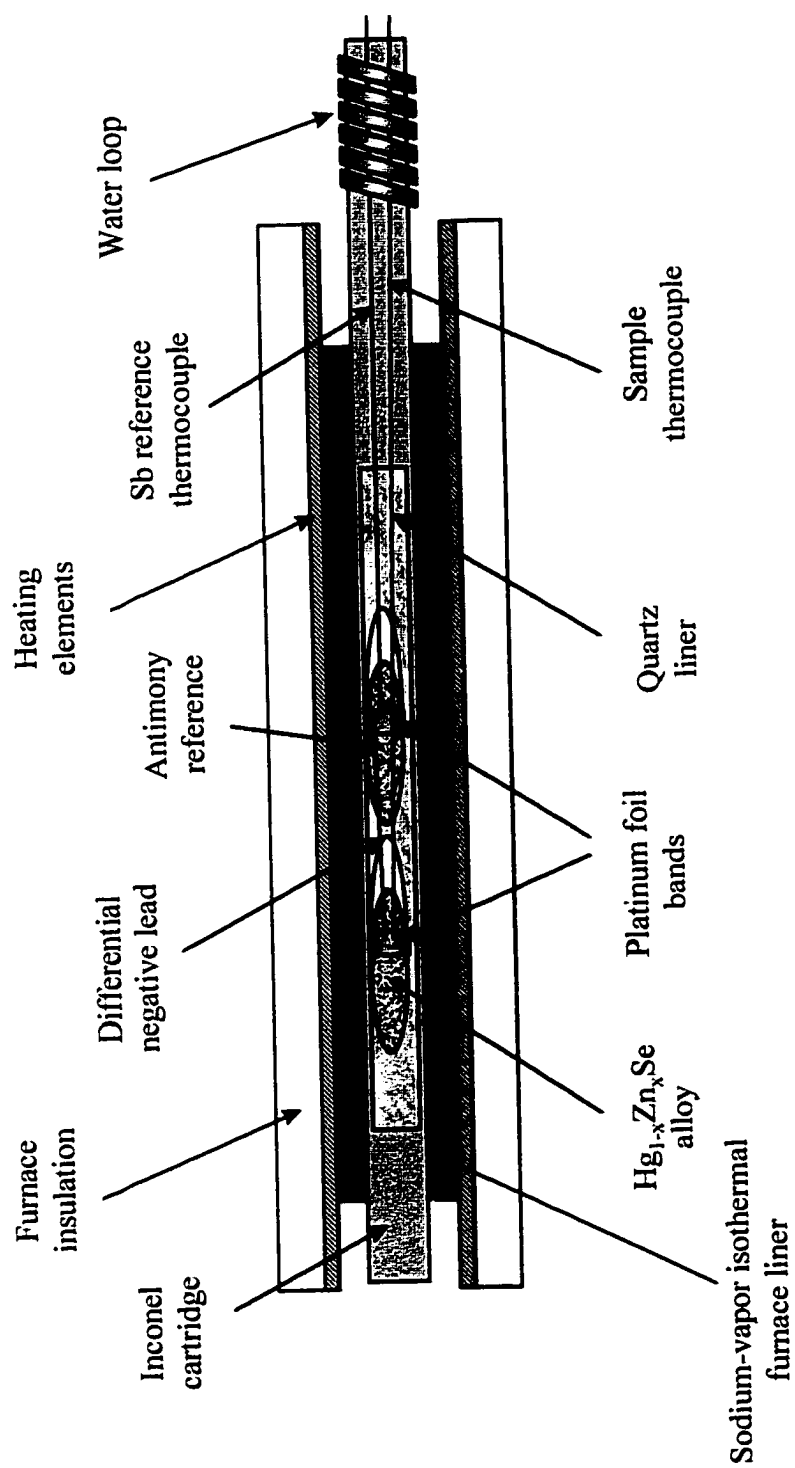


Figure 2-2. Experiment configuration for differential thermal analyses.

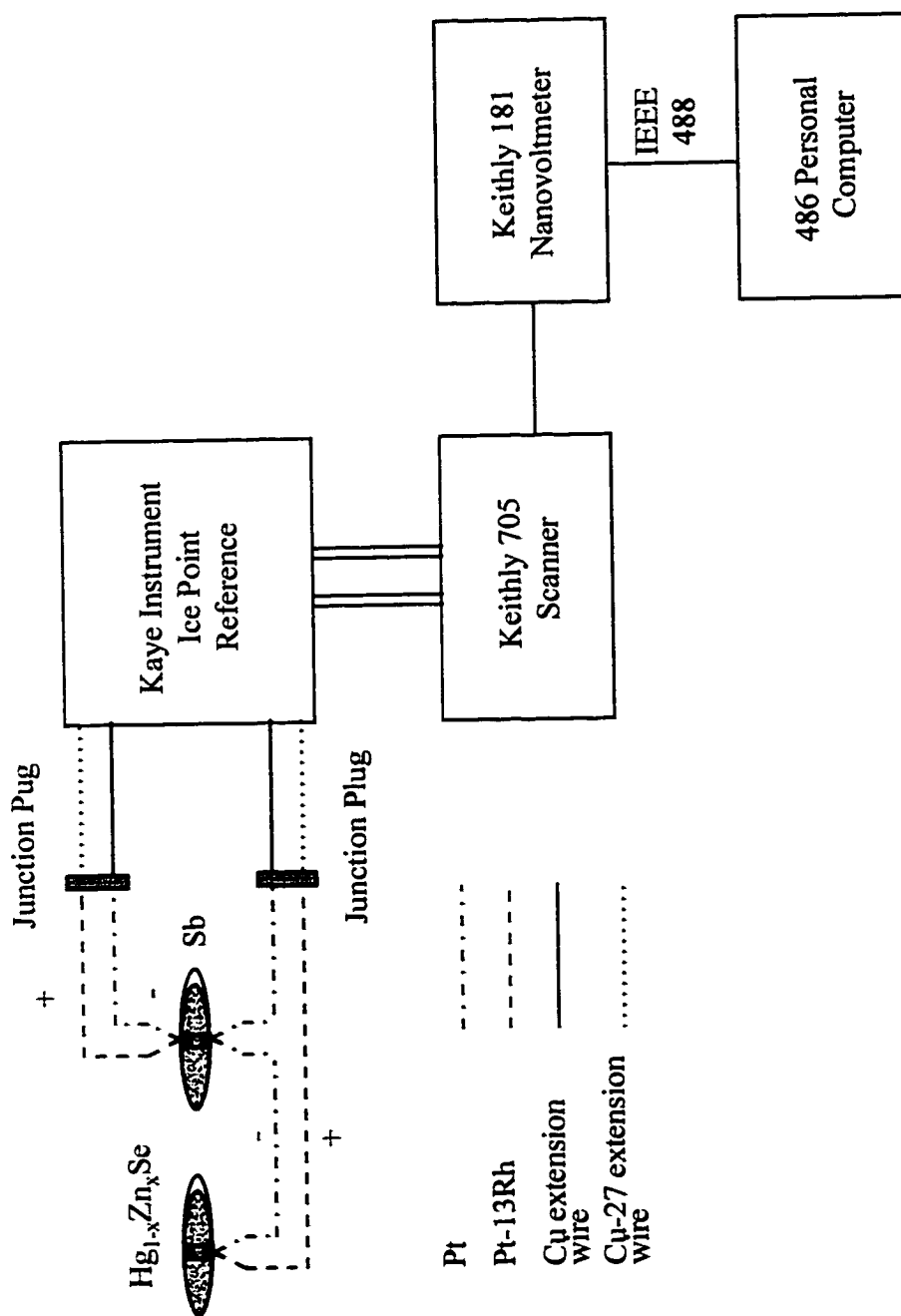


Figure 2-3. Configuration of electronics used for differential thermal analyses.

with temperature. It was hoped that by balancing the internal pressure, it would be possible to test samples with melting points close to the softening point of the fused silica ampoules. Several runs were performed at a pressure of 310-345 N/cm². This effort was eventually abandoned for two reasons: the thermal environment induced by the presence of a high density gaseous medium made it impossible to achieve isothermality between the reference and alloy samples; the high pressure environment made the thermal response time inadequate for determination of phase transition temperatures. It was, therefore, not possible to make measurements on alloys with $x > 0.20$.

HgSe and Hg_{1-x}Cd_xTe samples were used to verify the functionality of the system configuration. Calibration runs were also performed to determine the proper heating and cooling rate. The heating and cooling rates have a significant effect on the magnitude of the differential signal output. Experimental runs on HgSe at heating rates of 1.0, 1.9, and 5.0°C were used to determine the optimum rate. The thermal arrest curves for these runs are shown in Figure 2-4.

The solid and liquid transformation temperatures are broad when samples are not compositionally homogenous. To eliminate radial variations, all samples were annealed at 700-750°C for 14-75 hours. Samples were cooled at a uniform rate after each DTA run to reduce preferential segregation in the axial direction. The effects of annealing on the sharpness of the transition temperatures are shown in Figure 2-5.

The thermal arrest curves for each alloy composition were measured by heating the furnace from 550°C to temperatures between 1000 and 1100°C at a rate of 2°C/min. Cooling curves were also recorded as the furnace cooled at the same rate. As was observed in other II-VI systems (Lehoczky and Szofran, 1980; Su et al., 1996), thermal

hysteresis occurred upon cooling. This is attributed to undercooling, and occurs on both the Sb reference sample and the alloy sample. An example of this phenomenon is shown in Figure 2-6 for $x = 0.10$. For this reason, only heating curves were used to determine solidus and liquidus temperatures.

The solidus temperature was determined from the point where the initial melting curve intersected an extension of the baseline. The liquidus temperature was determined to be the point where the heating curve suddenly changed slope increasing back toward the baseline. This represented the point where the alloy absorbed the full heat of fusion for the phase change and the temperature of the liquid alloy increased. The Sb reference sample was used to correct the measured solidus and liquidus temperatures for thermocouple calibration error. The measured liquidus and solidus temperatures were corrected by adding or subtracting the amount that the Sb measured melting point deviated from 630.5°C (Su et al., 1996).

Results and Discussion

The experimental conditions employed for each test are summarized in Table 2-2. The thermal arrest curves measured during heating are shown for one experiment run of each alloy composition in Figures 2-7 through 2-11. The solidus and liquidus temperatures determined from the thermal arrest heating curves are shown in Table 2-3. Solidus temperatures for each alloy composition were easily determined after sufficient annealing. Determination of the liquidus temperatures was much more difficult. The measurement of the liquidus temperature was also problematic in DTA measurements on the $\text{Hg}_{1-x}\text{Cd}_x\text{Te}$ (Lehoczky and Szofran, 1980) and $\text{Hg}_{1-x}\text{Zn}_x\text{Te}$ (Su et al., 1996) alloy systems for $x < 0.20$.

The change in slope used to determine liquidus transition temperatures was undetectable in alloy compositions below $x = 0.1$. For low compositions, the heat of fusion of the last solid to melt is not largely different from that of the starting composition, because both the overall composition and the last solid to melt contain a relatively small amount of ZnSe. Therefore, the change in slope as the last solid melts is not well pronounced. For alloys with higher overall composition (i.e. $x > 0.3$) the last solid to melt contains a large mole fraction of ZnSe, which has a heat of fusion two times that of HgSe. This results in a more rapid change in energy absorbed per degree change in temperature. The situation is complicated by the fact that the high vapor pressure of this system prevents the incorporation of thermocouples directly into the sample. For low compositions, the thermal contact is probably not sufficient to detect the small change in slope at the transition from solid plus liquid to liquid.

For any composition, the final transition to the liquid phase in the thermal arrest curve is less clear when compositional inhomogeneities are present. For the $\text{Hg}_{1-x}\text{Zn}_x\text{Te}$ alloy system, density and viscosity measurements were performed at high temperature (Su et al., 1996). These measurements showed a temperature dependent hysteresis similar to what is observed in the melting and cooling curves. This led to the conclusion that regions or pockets of different composition were developing in the liquid plus solid region as well as in the liquid. These compositional variations could be a result of insufficient mixing during synthesis, small gas bubbles that develop in the melt, evaporation and condensation of Hg vapor into the ampoule free volume, development of subcritical clusters of a second phase (Yukalov, 1991) or formation of associated molecular species (Brebrick et al., 1983; Yu and Brebrick, 1992). Regions of various compositions would be expected to

round the slope change at the phase transition. For low compositions where the slope change is already small, compositional variations could totally mask this transition.

For compositions $0.1 \leq x \leq 0.2$, a slope change was often detectable, but did not occur at the same temperature for repeated tests on each composition. The thermal arrest curves for the repeated tests were measured on samples that had been heated and cooled several times with as short as 14 hours annealing at 750°C between runs. Almost all of the tests were run on samples that had not been remelted and rocked prior to retesting. It is very likely that the phase change did not occur at the same temperature each time because of compositional inhomogeneities caused by heating and cooling the samples. Samples were annealed between each run, however, annealing times used in this study were based on times used for the measurement of the $\text{Hg}_{1-x}\text{Cd}_x\text{Te}$ phase diagram (Lehoczky and Szofran, 1980). Since the diffusion coefficient of Zn in solid $\text{Hg}_{1-x}\text{Zn}_x\text{Se}$ is an order of magnitude smaller than for Cd in the $\text{Hg}_{1-x}\text{Cd}_x\text{Te}$ system, significantly longer annealing times will be required to obtain compositionally homogeneous samples.

Experimental solidus and liquidus points from these experiments, as well as those previously reported, are plotted in Figure 2-12. No information is available on sample preparation, annealing, or thermal arrest curves for the previously reported measurements. It is assumed that the difference in liquidus values reported is due the difficulty in determining liquidus temperatures for low x values as discussed above. Calculation of the HgSe-ZnSe pseudobinary phase diagram is discussed in the next section. The slope of the liquidus curve and the melting temperature for $x = 0.10$ were used to estimate the critical gradient/growth rate (G/R) ratio needed to prevent constitutional supercooling during subsequent directional solidification of $\text{Hg}_{1-x}\text{Zn}_x\text{Se}$ ingots.

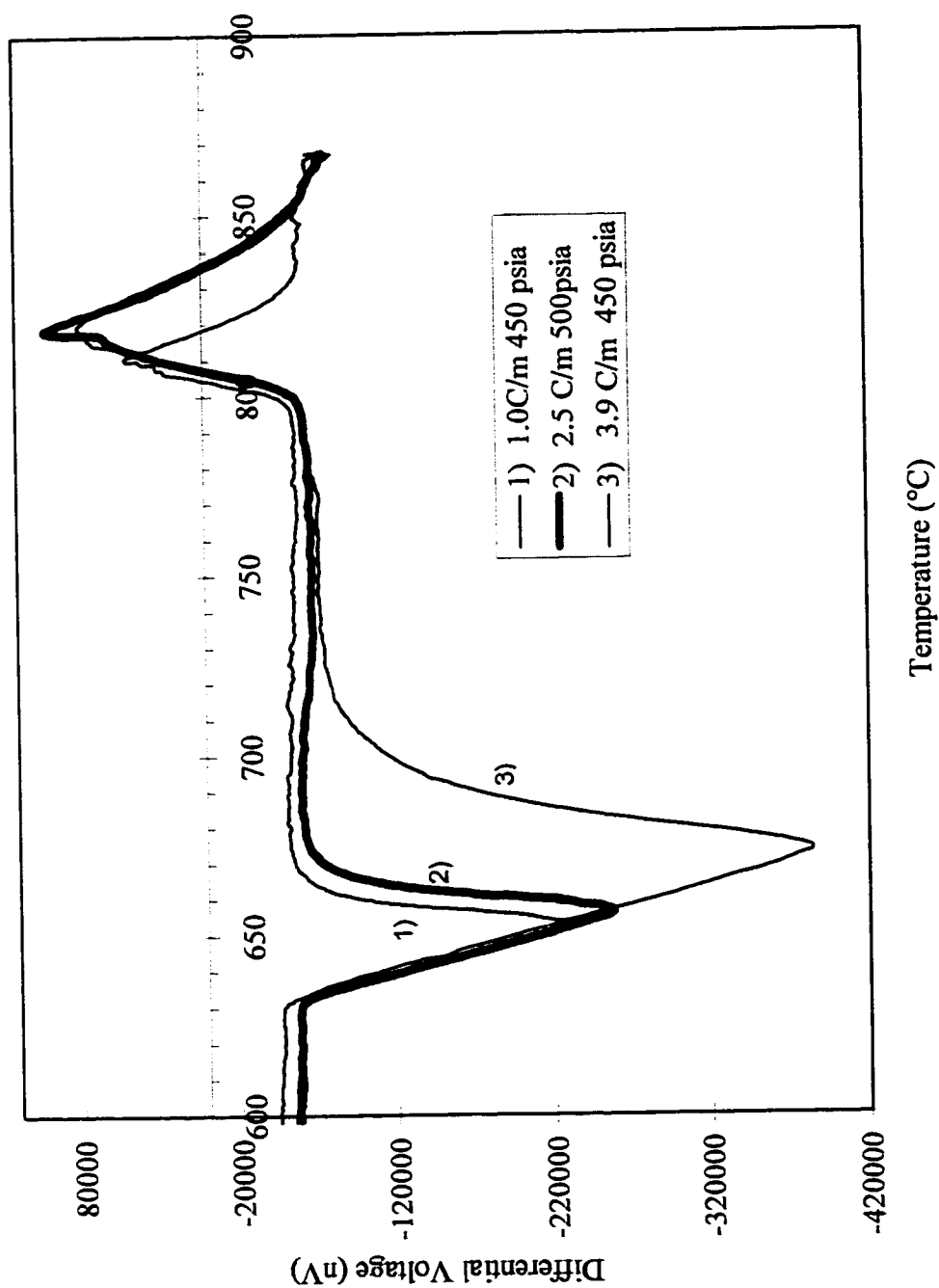


Figure 2-4. Effect of heating rate on transition temperature for HgSe ($x = 0$).

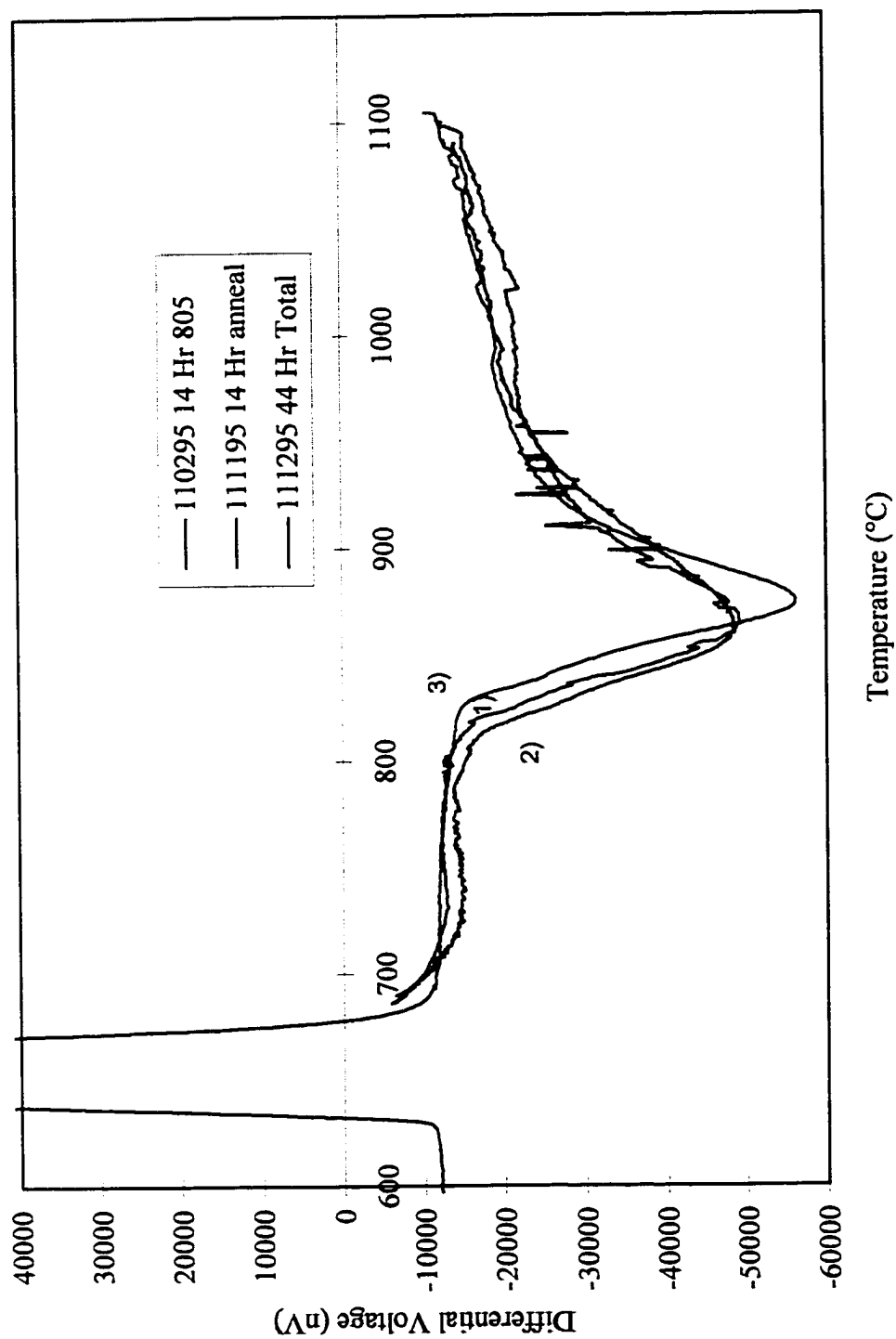


Figure 2-5. Effect of annealing time on transition temperature for $\text{Hg}_{1-x}\text{Zn}_x\text{Se}$ ($x = 0.20$).

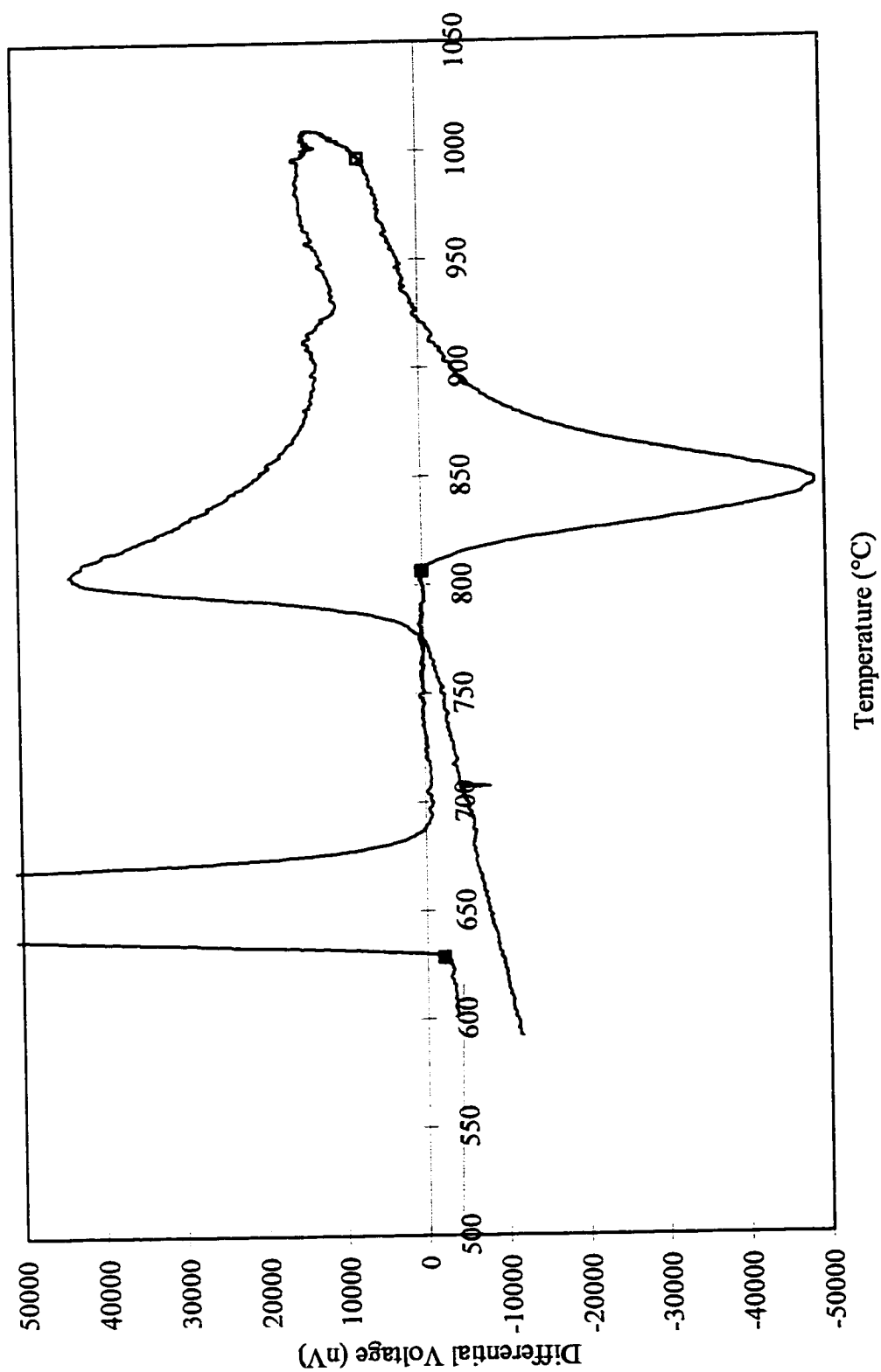


Figure 2-6. Transition temperature hysteresis during cooling in $\text{Hg}_{1-x}\text{Zn}_x\text{Se}$ ($x = 0.10$).

Table 2-2. Differential thermal analysis conditions.

File Name	Date	Start Timecode	% Zn	Ramp Rate (°C/min)	Pressure (psia)	Time Line (°C)	Notes
MSa	41495	8811014	0	2.5	14.7	500-860-25	
MSb	41795		0	5	450	500-860-500	Thermocouple data was noisy.
MSc	41895	9174340	0	1	450	500-860-500 1hr hold at 860	
MZS08a	71395	16661277	0.08	2.5	14.7	500-900-500	Maximum temperature was too low.
MZS08b	71495	16801389	0.08	5	14.7	500-968-500 1 hr at 950	
MZS08c	72695	17849264	0.08	2.5	14.7	500-968-500	Wide spaced ampoules without extra dirt insulation.
MZS08d	80195	18365766	0.08	2.1	14.7	460-1012-600	
MZS08e	8195	18396554	0.08	2	14.7	550-1004	
MZS10a	61595	14161691	0.1	2.1		500-955-750 held 1hr @950	Held for 15 hrs after run.
MZS10a	61595	14237100	0.1			750-955-500	
MZS10b	61695	14335678	0.1	2.5	450	750-950-500 held for 12 hr- after run	Very round transition.
MZS10c	616a95	14260370	0.1	2.5	450	14 hr anneal at 750	Very round transition.
MZS10d	61995	14596612	0.1	5	14.7	500-960-500	Maximum temperature was too low.
MZS10e	82295	20169200	0.1	2.5	14.7	500-1009-500	Detectable transition.
MZS10f	100997		0.1	2	14.7		First run, no anneal
MZS10g	101597		0.1	2	14.7		Annealed at 755 for 120 hour.
MZS10h	101597		0.1	2	14.7	rerun	

Table 2-2. Continued.

File Name	Date	Start Timecode	% Zn	Ramp Rate (°C/min)	Pressure (psia)	Time Line (°C)	Notes
MZS10f	100997		0.1	2	14.7		First run, no anneal.
MZS10g	101597		0.1	2	14.7		Annealed at 755 for 120 hours.
MZS10h	101597		0.1	2	14.7	rerun	
MZS15a	82395	20256459	0.15	2.5	14.7	560-1035	Wrong thermocouple conversion coefficients.
MZS15b	101895	25105013	0.15	2.5	14.7	500-1050-500	New Sb. Used type S t/c. Conversion error.
MZS15c	102495	25520178	0.15	2.5	14.7	500-1100-500	Used type S t/c. Conversion error.
MZS15d	102695	25720491	0.15	2.5	14.7	700-1100-700	Run ends with 12 hour hold until 10/27/95.
MZS15e	102795	25793151	0.15	2.5	14.7	700-1100-700	After 12 hour hold at 700.
MZS15f			0.15	2	14.7		
MZS15g	102897		0.15	2	14.7		After 192 hour hold.
MZS20a	102895?	25888403	0.2	2.5	14.7	800-1100-800 14 hr hold 800-1100-2.5	4.5 empty volume, 4 cm sample
MZS20b	103195	26155500	0.2	2.5	14.7	500-1100-800 14 hr 1100-800	Very rounded transition.
MZS20c	110295	26156106	0.2	2.5	14.7	500-1100-800-14 hr	
MZS20d	110395	26403006	0.2	2.5	14.7	800-1100-800	After 14 hour hold.
MZS20e	110495	26502477	0.2	2.5	14.7	800-1100-off	After 14 hour hold.
MZS20f	110795	26768927	0.2	2.5	14.7	500-1100-off	
MZS20g	111195	27011803	0.2	2.5	14.7	690-1100-690	After 30 hour hold at 690.
MZS20h	111295	27249174	0.2	2.5	14.7	687-1100-687	After 30 hour hold.

Table 2-3. Differential thermal analysis results.

File Name	Date	Start Timecode	% Zn	T(melt) Sb	T(sol.)	T(liq.)	T(s) corrected	T(l) corrected
MSa	41495	8811014	0	628.26	798.02		800.26	
MSb	41795		0	632.87	799.86		797.49	
MSc	41895	9174340	0	631.16	799.15		798.49	
MS Average							798.75	
MZS08a	71395	16661277	0.08	627.10	810.60		814.00	
MZS08b	71495	16801389	0.08	627.52	813.95	904.43	816.93	907.41
MZS08c	72695	17849264	0.08	627.21	808.46	878.49	811.75	881.78
MZS08d	80195	18365766	0.08	626.89	808.73	892.78	812.34	896.39
MZS08e	81695	18396554	0.08	628.27	815.53	889.63	817.76	891.86
MZS08 Avg							814.56	894.36
MZS10a	61595	14161691	0.1	632.20	825.12	900.00	823.42	898.30
MZS10b	61595	14237100	0.1	632.20	824.60	901.70	822.90	900.00
MZS10c	61695	14335678	0.1	632.20	819.00	902.00	817.30	900.30
MZS10d	616a95	14260370	0.1					
MZS10e	61995	14596612	0.1	635.56	820.88		815.82	
MZS10f	82295	20169200	0.1	628.70	814.53		816.33	
MZS10g	100897		0.1	628.34	814.54		816.70	
MZS10h	100997		0.1	629.29	814.81	907.08	816.02	908.29
MZS10i	101597		0.1	632.22	819.43		817.71	
MZS10j	101597		0.1	627.63	812.99	937.78	815.86	
MZS10k	121397		0.1	627.15	818.00	889.43	821.35	892.78
MZS10 Avg					818.39		818.34	899.93

Table 2-3, Continued.

File Name	Date	Start Timecode	% Zn	T(melt) Sb	T(sol.)	T(liq.)	T(s) corrected	T(l) corrected
MZS15a	82395	20256459	0.15					
MZS15b	101895	25105013	0.15					
MZS15c	102495	25520178	0.15					
MZS15d	102695	25720491	0.15	632.77	822.07		819.80	
MZS15g	102897	25877831	0.15	626.44	834.27		838.33	
MZS15 Avg							829.07	
MZS20a	102895	25888403	0.2					
MZS20b	103195	26156106	0.2	626.97				
MZS20c	110295	26156106	0.2	628.37	814.58		816.71	
MZS20d	110395	26403006	0.2	628.37	833.31	1076.16	835.44	1078.29
MZS20e	110495	26526086	0.2	628.37	829.50		831.63	
MZS20f	110795	26768927	0.2					
MZS20g	111195	27011803	0.2	628.37	808.69	1020.60	810.82	1022.73
MZS20h	111295	27249174	0.2	628.37	823.74		825.87	
MZS20 Avg							824.09	1050.51
MCT20a	82195	20083695	0.2	628.53	699.10	784.90	701.07	786.87

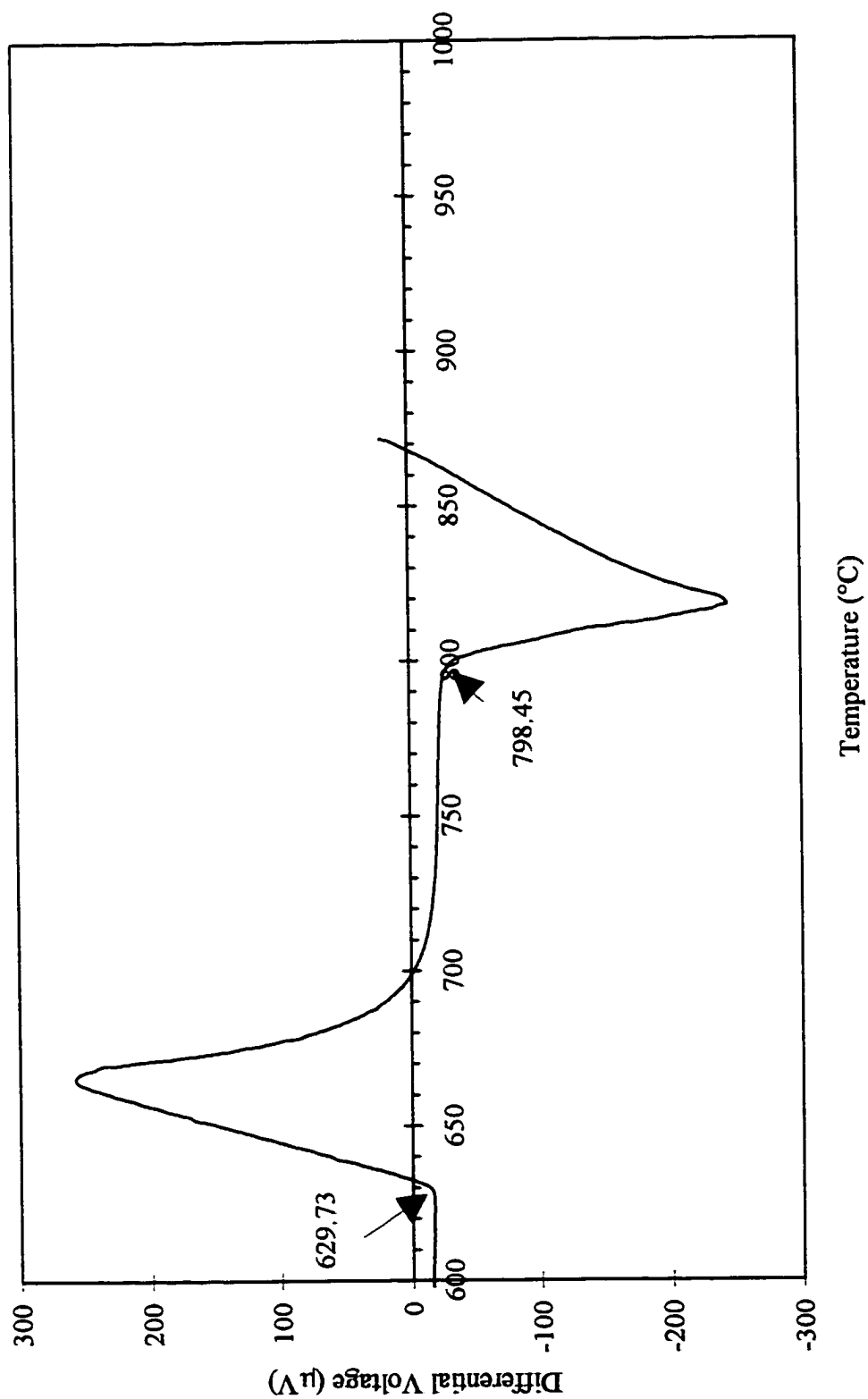


Figure 2-7. Thermal arrest heating curve for $x = 0.0$.

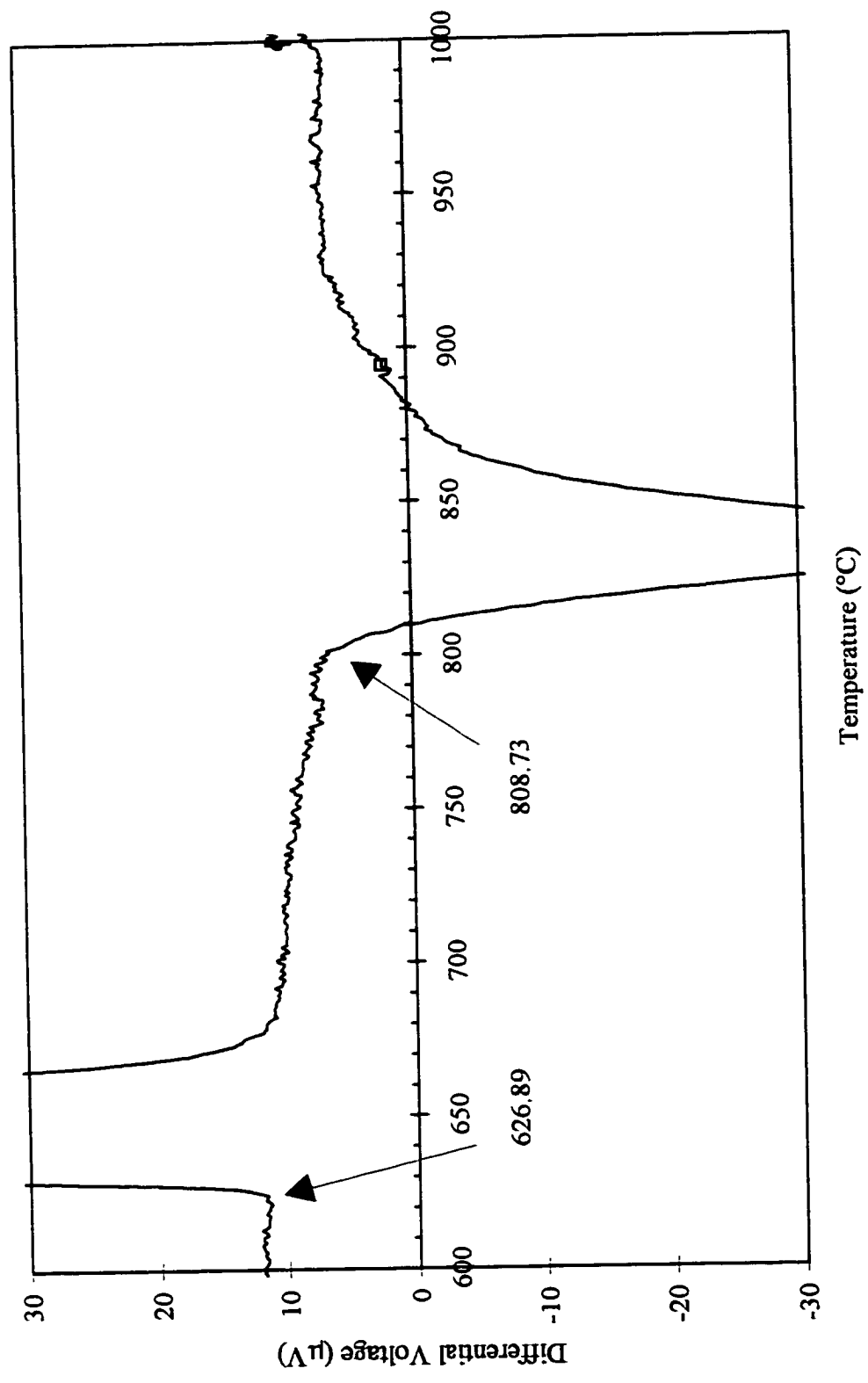


Figure 2-8. Thermal arrest heating curve for $x = 0.08$.

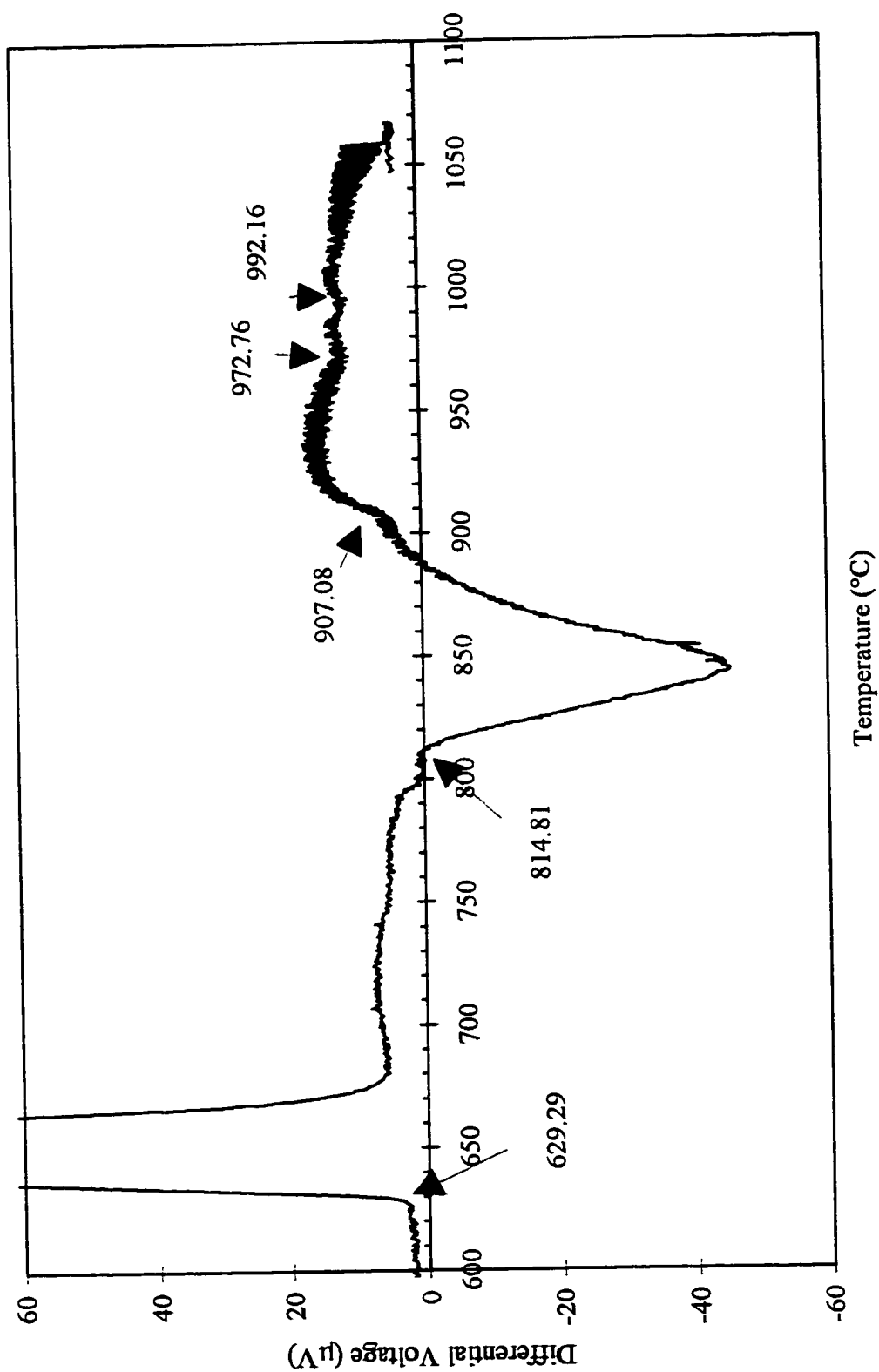


Figure 2-9. Thermal arrest heating curve for $x = 0.10$.

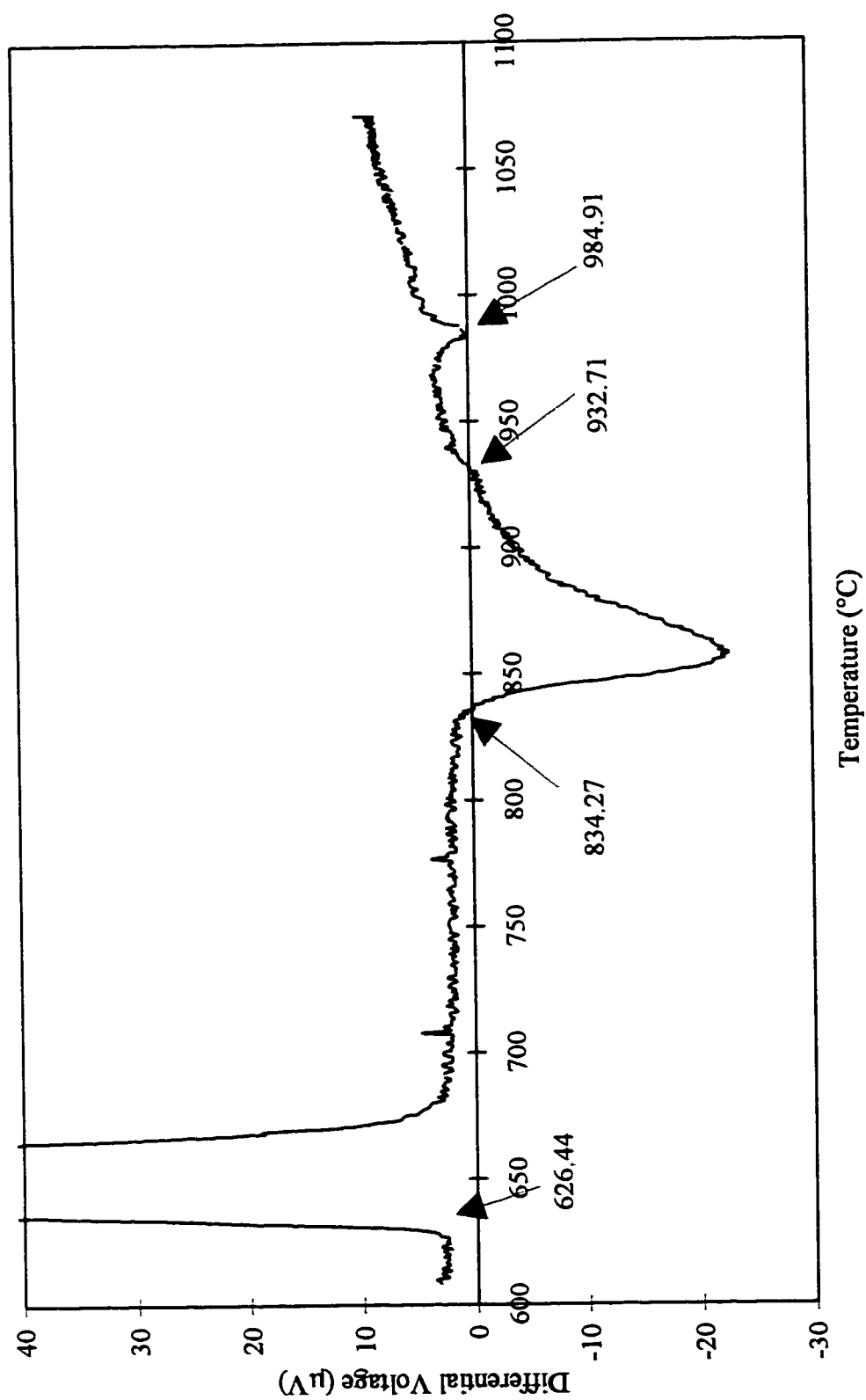


Figure 2-10. Thermal arrest heating curve for $x = 0.15$.

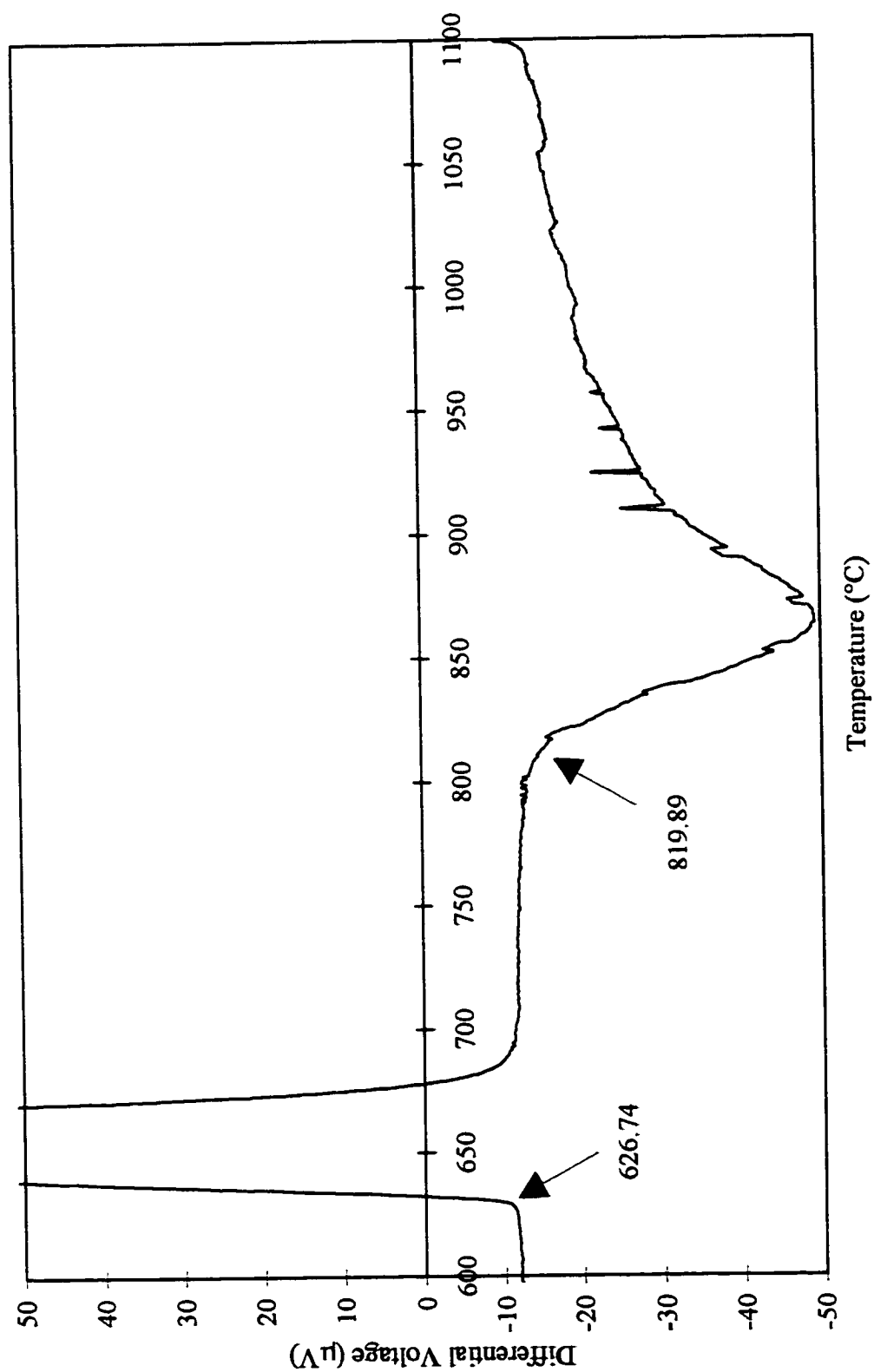


Figure 2-11. Thermal arrest heating curve for $x = 0.20$.

Calculation of the $\text{Hg}_{1-x}\text{Zn}_x\text{Se}$ Pseudobinary Phase Diagram

The Hg-Zn-Se pseudobinary can be assumed to be a binary system with no intermediate compounds and complete solubility in both the solid and liquid phases. The binary AC, or HgSe, will be treated as element A and binary BC, or ZnSe, as element B. Using these assumptions, the thermodynamic equilibrium between the solid and the liquid phases are given by:

$$\mu_A^l(X_B^l, T) = \mu_A^s(X_B^s, T) \quad (2-1)$$

$$\mu_B^l(X_B^l, T) = \mu_B^s(X_B^s, T), \quad (2-2)$$

where $\mu_A^l(X_B^l, T)$ and $\mu_B^l(X_B^l, T)$ are the chemical potential of A and B, respectively, in the liquid (2-1) at composition X_B^l and temperature T, whereas $\mu_A^s(X_B^s, T)$ and $\mu_B^s(X_B^s, T)$ are the chemical potential of A and B, respectively, in the solid(s) at composition X_B^s and temperature T. From the expression for chemical potential one can write:

$$\mu_i^j(X_B^j, T) = H_i^j - TS_i^j + RT \ln X_B^j + \mu_i^{j,0}(T), \quad (2-3)$$

where H_i^j and S_i^j are the partial molar enthalpy and excess entropy for component i in phase j, and $\mu_i^{j,0}(T)$ is the chemical potential for pure component i in phase j at temperature T. By setting $X_B^l = x$ and $X_B^s = y$ and realizing that

$$\mu_i^{s,0}(T) - \mu_i^{l,0}(T) = \Delta H_i(T/T_i - 1), \quad (2-4)$$

where ΔH_i and T_i are the heat of fusion and melting point for component i, respectively,

equations (2-1 to 2-3) can be rewritten as:

$$H_A^l - TS_A^l + RT \ln (1-x) = H_A^s - TS_A^s + RT \ln (1-y) + \Delta H_A(T/T_A - 1) \quad (2-5)$$

$$H_B^l - TS_B^l + RT \ln x = H_B^s - TS_B^s + RT \ln y + \Delta H_B(T/T_B - 1). \quad (2-6)$$

Once the enthalpy and excess entropy for each component in each phase are known as functions of composition and temperature, liquidus and solidus curves can be generated using equations (2-5) and (2-6) with the thermophysical properties, heat of fusion and melting point for each component as inputs.

A simple solution model that leads to good fits to the liquidus and solidus lines and is capable of representing a number of liquid and solid phases in metallic system is the cubic Margules model and is defined by writing the excess Gibbs energy of mixing as:

$$\Delta G_M^e = WX(1 - X) [1 + A (X - \frac{1}{2})] - VTX(1 - X) [1 + C (X - \frac{1}{2})], \quad (2-7)$$

where W, V, A and C are the adjustable interaction parameters that are independent of T and X. The total Gibbs energy of mixing is the sum of this excess part and the contribution from ideal mixing:

$$\Delta G_M = \Delta G_M^e + RT [X \ln x + (1-X) \ln (1-X)]. \quad (2-8)$$

It can be deduced that

$$\Delta H_M = WX(1 - X) [1 + A (X - \frac{1}{2})] \quad (2-9)$$

$$\Delta S_M = VX(1 - X) [1 + C (X - \frac{1}{2})] - R [X \ln x + (1-X) \ln (1-X)]. \quad (2-10)$$

The partial molar enthalpies and excess partial molar entropies obtained for the components are:

$$H_A = X^2W [1 + A(2X - 3/2)] \quad (2-11)$$

$$H_B = (1 - X)^2W [1 + A(2X - \frac{1}{2})] \quad (2-12)$$

$$S_A = X^2V [1 + C(2X - 3/2)] \quad (2-13)$$

$$S_B = (1 - X)^2V [1 + C(2X - 1/2)]. \quad (2-14)$$

Commonly used solution models such as the ideal, strictly regular, athermal, quasi-regular and cubic models can be adopted by setting all or none of the adjustable interaction parameters to zero as shown in Table 2-4.

Table 2-4. Adjustable parameter values used in phase diagram calculations.

	W	A	V	C
ideal	0	0	0	0
strictly regular	$\neq 0$	0	0	0
athermal	0	0	$\neq 0$	0
quasi-regular	$\neq 0$	0	$\neq 0$	0
cubic	$\neq 0$	$\neq 0$	$\neq 0$	$\neq 0$

The $\text{Hg}_{1-x}\text{Zn}_x\text{Se}$ phase diagram was calculated by assuming the cubic Margules model for the solid and liquid phases of HgSe-ZnSe pseudobinary with interaction parameters W_s , A_s , V_s and C_s for the solid and W_L , A_L , V_L and C_L for the liquid. The literature values for the melting points of HgSe (Strauss and Farell, 1962) and ZnSe (Sysoev et al., 1967), 799 and 1526.1°C, respectively, were employed as input parameters. The value of 66.944 kJ/mole was used as the heat of fusion for ZnSe (Brebrick and Haochieh, 1996) and a value of 30.7 kJ/mole, for HgSe (Steininger 1970).

The calculated results are plotted in Figure 2-12 together with the experimental data. The solid curves (number 2 in legend) were calculated assuming an ideal solution model for both the liquid and solid phases, i.e. all the interaction parameters were set to zero. The dashed curves (number 3 in legend) were calculated assuming a strictly regular solution model for the liquid with $W_L = -10000$ J/mole and an ideal solution for the solid. The dotted lines (number 4 in legend) were calculated assuming an ideal solution model

for the liquid and a strictly regular model for the solid with $W_s = 10000$ J/mole. Both the dashed and dotted curves have better fits to the experimental data than the curves of the ideal solution model. This suggests that there is strong association in both the solid and liquid. The dashed curve fits the liquidus data slightly better than the dotted curve while the dotted curve showed a better agreement and trend with the experimental solidus data. Because the experimental data was scattered and only available for mole fractions of ZnSe less than 0.25, both the dashed and dotted curves were considered to be satisfactory and no other calculations were performed. At present, more data in the region of high ZnSe content are needed to better define the solid and liquid phases. In addition, the absence of information concerning species interaction parameters further limits refinement of calculations.

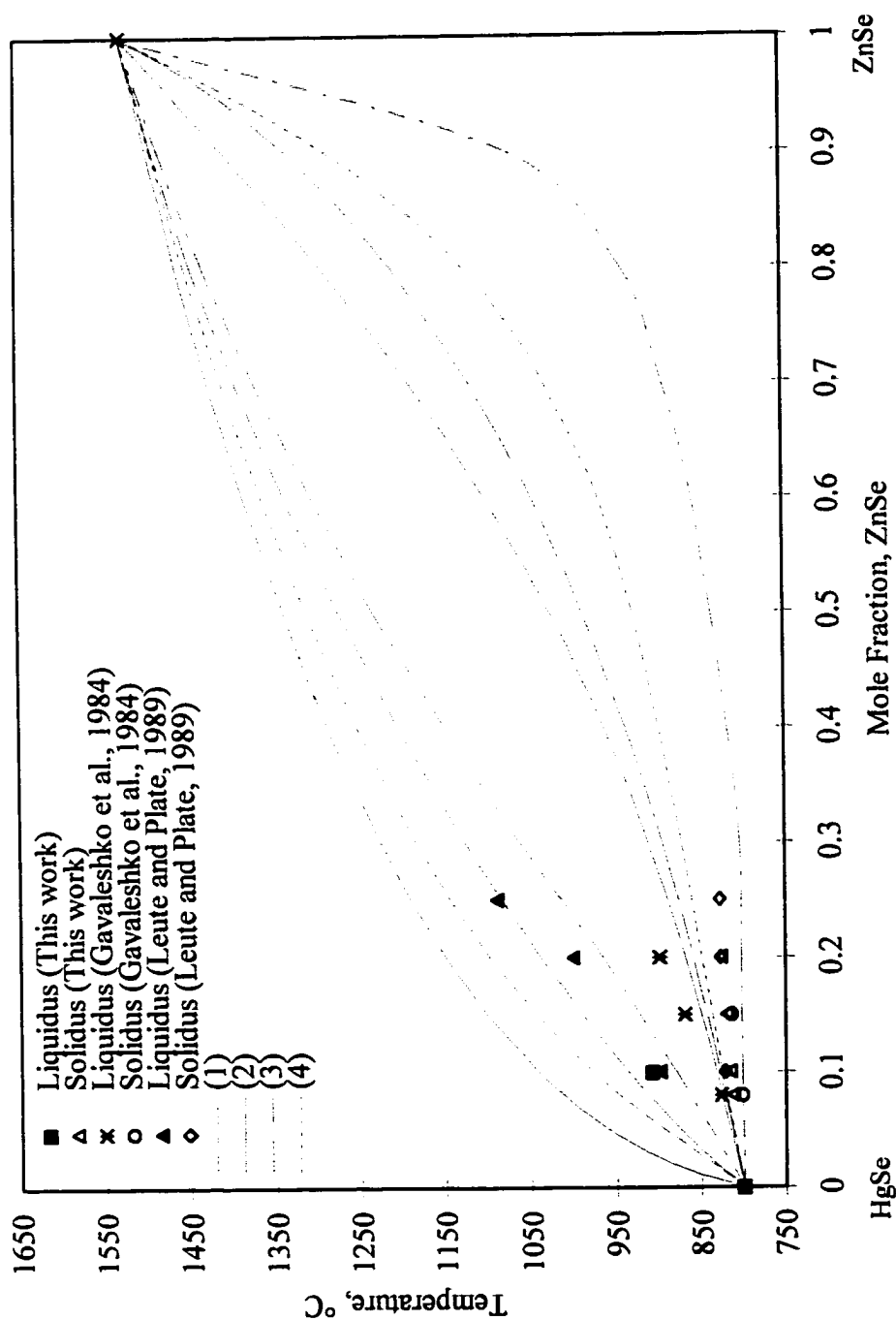


Figure 2-12. Solid points are experimental liquidus and solidus temperatures for $\text{Hg}_{1-x}\text{Zn}_x\text{Se}$. Lines represent the following calculated solidus and liquidus curves: (1) regular solution approximation (Gavaleshko et al., 1984a), (2) ideal solution (L, and S), (3) regular solution (L) $W_L = -10000$, ideal solution (S), (4) regular solution (S) $W_S = 10000$, ideal solution (L).

CHAPTER 3

ALLOY SYNTHESIS AND CRYSTAL GROWTH

The synthesis and subsequent directional solidification of Hg based II-VI alloys is complicated by the requirement for a container capable of withstanding the high temperature required for melting the alloy and the high vapor pressure that develops as a result of heating the Hg constituent. Fused silica with a wall thickness of at least 2.5 mm was used for both alloy synthesis and subsequent growth experiments.

Ampoule Preparation

Ampoules were constructed from fused silica tubing with 10 mm outer diameter and 5 mm inner diameter. One experiment utilized an ampoule with 12 mm outer diameter and 7.3 mm inner diameter. One end of each ampoule was tapered to encourage solidification from the tip. The first two ampoules were produced at the same time and had a taper length of 1.5 cm. The remaining ampoules had a taper length of 0.9 cm. A 0.3 cm diameter solid quartz rod was attached to the tapered end of the ampoule to provide support during subsequent directional solidification. Each ampoule was cleaned with hydrofluoric acid, then rinsed three times with methanol followed by distilled water. Ampoules were slowly heated to a maximum temperature of 1140°C, then cooled, slowly, to remove strain which was introduced during fabrication of the ampoule.

Preparation of Charge for Synthesis

The ratio of Hg, Zn, and Se components required to produce a $\text{Hg}_{1-x}\text{Zn}_x\text{Se}$ alloy of composition $x=0.10$ and approximately 15 cm in length was determined. Elemental constituents were 99.999% pure zinc shot from Cerac, 99.999% pure selenium shot purchased from Aesar, and triple distilled mercury from Bethlehem Instrument. Elements were weighed to an accuracy of ± 0.0004 grams. Selenium and zinc shot were loaded into the ampoules in a layered pattern to aid in mixing during synthesis. The mercury was then introduced into the ampoule.

The open end of the ampoule was attached to a vacuum system with an o-ring fitting and evacuated to approximately 1.3×10^{-4} N/cm². The ampoule remained under vacuum for 30-45 minutes, and was then sealed 2-3 cm above the charge using an oxygen-hydrogen torch. Strain from the sealing process was removed by slowly heating and cooling the seal in a low temperature torch flame.

Additional procedures were performed on various samples to determine the effect of alloy-ampoule interactions on defect generation. One sample, MZS-2, was prepared as described above. The next ampoule, MZS-5, was produced from 12 mm outer diameter by 7.3 mm inner diameter fused silica tubing to determine the effect of sample diameter on grain development and dislocation density. A piece of outgassed graphite slightly smaller in diameter than the quartz ampoule and one centimeter long was placed into the ampoule prior to sealing. The graphite was expected to act as a getter for oxygen, reducing the wetting between the alloy and the fused silica ampoule. An additional ampoule, for sample MZS-8, was prepared with a boron nitride (BN) coating. A HCM grade powder

of boron nitride from Advanced Ceramics was loaded into a clean ampoule and then fire annealed with an oxygen-hydrogen torch to bond a BN film to the inner surface of the ampoule. This procedure has been used (Shetty et al., 1995) to reduce wetting of the ampoule wall. All ampoules included a graphite piece, except for MZS-2 and MZS-8.

Alloy Synthesis

The sealed ampoules were cleaned and wrapped in fiber insulation to improve uniform heating and protect the ampoule from abrasion during alloy synthesis. The ampoule was packed into a quartz tube and loaded into an Inconel furnace liner that was capped on both ends. The furnace consisted of three zones and was mounted on single axis gimbals which allowed the furnace to rotate about the horizontal axis. The rocking action facilitated complete mixing of the alloy. The heating procedure described earlier (Cobb et al., 1991) was successfully modified to reduce the amount of time required for synthesis. All three furnace zones were raised to 500°C at a rate of 1.4°C/minute, the sample was held at 500°C for 20 hours. The sample was rocked during the first 8 hours then held horizontally for 8 hours. The temperature was increased to 800°C at a rate of 0.3°C/minute. The sample was rocked during heat-up to reduce the chance of breaking the ampoule due to sudden melting of intermediate compounds formed during heating. The alloy was held stationary at 800°C for 38 hours to facilitate homogenization by diffusion. The sample was heated to 1010°C at a rate of 0.35°C/minute while being rocked, then held stationary at 1010°C for 8 hours. The alloy was rocked for 30 minutes for a final mixing and then rotated 60 degrees with the tapered tip pointing downward. The controller for the lower zone was turned off, and to encourage solidification from the

tapered end, the lower endcap was opened slightly to accelerate heat removal from the tip of the sample. Power was then removed from the middle and upper zone controllers after one hour. After sufficient cooling, all samples were removed from the insulation and cleaned with methanol prior to remelting and directional solidification.

Crystal Growth

All samples were remelted and directionally solidified by a modified Bridgman-Stockbarger technique. Four of the samples, MZS-2, MZS-5, MZS-7, and MZS-8 were grown in the same furnace with the same furnace profiles. Samples MZS-10 and MZS-11 were melted and solidified in a furnace that was inserted into the bore of a superconducting magnet. The purpose of the magnet was to reduce convective fluid flow in the molten alloy.

Modified Bridgman-Stockbarger Crystal Growth

The furnace configuration used to grow the four samples processed by standard directional solidification is shown schematically in Figure 3-1. The furnace consisted of two resistively heated zones, each lined with sodium heat pipes to provide well defined isothermal regions. The upper and lower zone settings were 1010°C and 630°C, respectively. The two heated zones were separated by a 2.5 cm thick alumina barrier. The width of this barrier resulted in a temperature gradient of 65°C/cm. The temperature gradient influences the maximum growth rate that can be maintained while avoiding constitutional supercooling. The general criteria for constitutional supercooling during plane front solidification is given by

$$\frac{G_L}{R} = \frac{m_L C_0 (1 - k)}{k D_L} \quad (3-1)$$

where G_L is the temperature gradient in the liquid at the interface, R is the growth rate, m_L is the slope of the liquidus line, C_0 is the alloy melt composition, k is the interface segregation coefficient, and D_L is the diffusion coefficient in the liquid. A thermocouple attached to a quartz rod was used to measure the temperature profile in the furnace with an upper zone temperature setting of 1010°C and a lower zone setting of 630°C. The furnace profile for samples MZS-2, MZS-5, MZS-7, and MZS-8 is shown in Figure 3-2.

The synthesized sample was held stationary in a quartz rod attached to a base plate during the melting and growth process. The sample was centered in the insulation barrier and aligned vertically by adjusting set screws in the base plate. To reduce radial compositional variations, the samples had to be aligned parallel to the growth direction to prevent fluid flow generated by non-symmetric radial thermal fields.

The aligned sample was placed so the entire sample was in the upper temperature zone. Both zones were increased to their respective set points over a period of 8 hours. The molten sample was held at temperature in the upper zone for 12 hours. The furnace was then translated at a rate of 0.10 $\mu\text{m}/\text{sec}$ upward, moving the sample slowly through the gradient zone and into the lower zone.

The optimum growth rate chosen for this study was 0.10 $\mu\text{m}/\text{sec}$. This growth rate produced a fairly flat steady state axial growth region while preventing constitutional supercooling (Cobb et al., 1991). A summary of growth conditions for all samples is shown in Table 3-1. All samples were prepared with a nominal composition of $x = 0.10$.

For samples MZS-7 and MZS-8, the furnace controllers were powered off and the furnace was allowed to cool naturally after the furnace had translated the entire length of the sample. Sample MZS-2 was intentionally quenched after 8 cm of growth to study the shape of the solid-liquid interface. Sample MZS-5 was quenched, unintentionally, when the upper zone heating element failed.

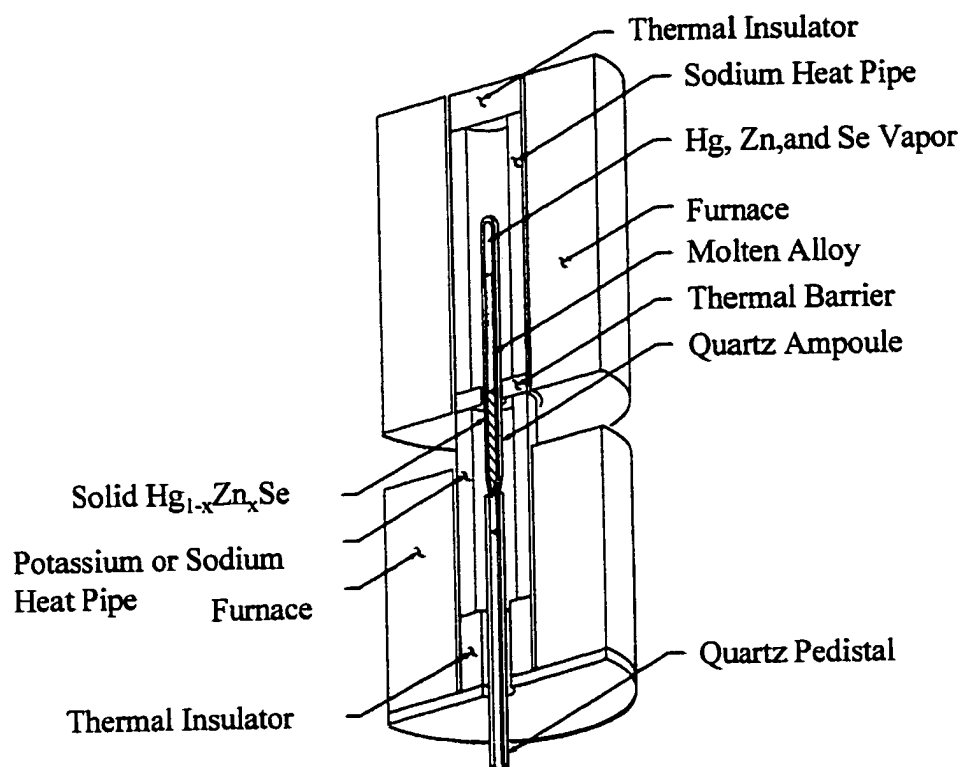


Figure 3-1. Bridgman-Stockbarger furnace configuration used for ingots MZS-2, MZS-5, MZS-7, and MZS-8.

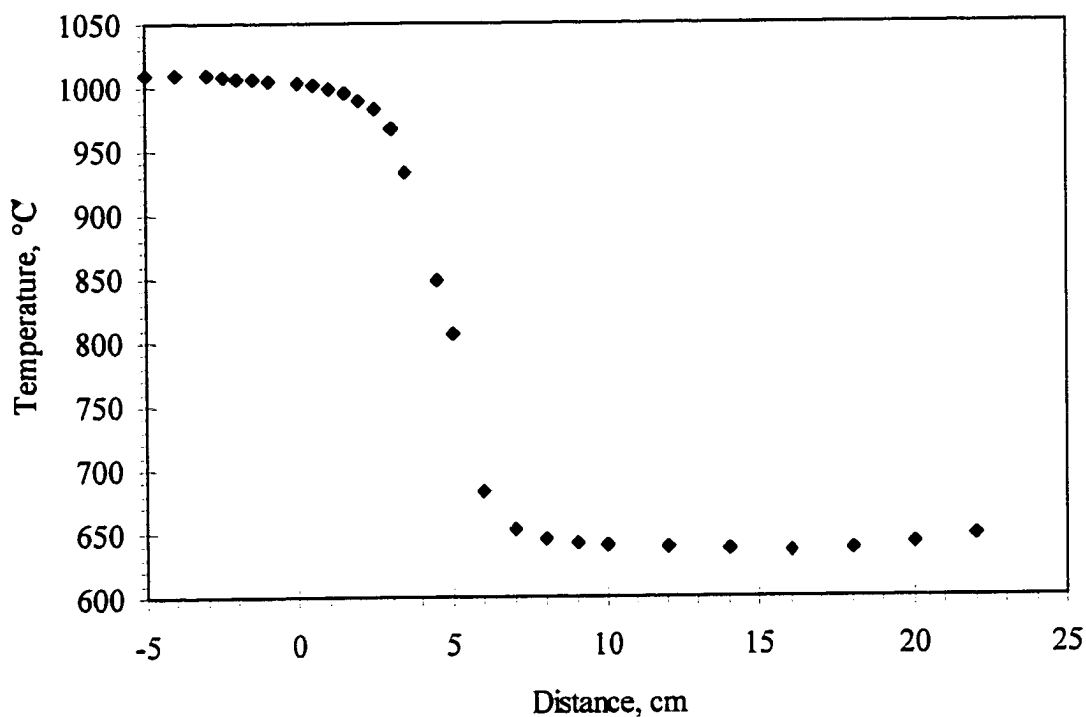


Figure 3-2. Thermal profile in Bridgman-Stockbarger furnace for ingots MZS-2, MZS-5, MZS-7, and MZS-8.

Table 3-1: Summary of sample growth conditions.

Sample Designation	Diameter (mm)	Growth Rate ($\mu\text{m}/\text{sec}$)	Ampoule Preparation	Magnetic Field Strength (Tesla)
MZS-2	5.41-5.57	0.10	Basic	0
MZS-5	7.01-7.25	0.10	Graphite Plug	0
MZS-7	5.41-5.48	0.10	Graphite Plug	0
MZS-8	4.95-5.23	0.10	BN Coating	0
MZS-10	5.51-5.61	0.10	Graphite Plug	5
MZS-11	5.16-5.28	0.10	Graphite Plug	0

Crystal Growth in an Applied Magnetic Field

The presence of a magnetic field surrounding the growth furnace has been shown to reduce the amount of convective turbulent fluid flow in electrically conductive molten alloys (Fowles, 1987; Series and Hurle, 1990; Hurle and Hunt, 1968; Kim, 1982; Matthiesen et al., 1987). The reduction in convection leads to a more planar interface shape by reducing radial temperature differences, and therefore diminishes the extent of radial compositional variations. The magnetic field induced by the superconducting magnet interacts with fluid motion in the molten alloy. The result of the interaction is to increase the viscosity of the melt and reduce convection. This technique has proven very successful in reducing radial compositional variations in II-VI systems including $\text{Hg}_{1-x}\text{Cd}_x\text{Te}$ (Watring and Lehoczy, 1996) and $\text{Hg}_{1-x}\text{Zn}_x\text{Te}$ (Sha et al., 1997) alloys which have properties similar to the $\text{Hg}_{1-x}\text{Zn}_x\text{Se}$ system.

One sample, MZS-10, was remelted and directionally solidified in a Bridgman-Stockbarger furnace in the presence of a five Tesla magnetic field. A second sample was processed in the same furnace without the magnetic field for comparison. The furnace configuration is shown in Figure 3-3. This furnace utilized five heated zones to achieve uniform hot and cold zone temperatures, since it was not lined with heat pipes. The temperature settings for MZS-10 and MZS-11 are shown in Table 3-2. The combined furnace and magnet configuration is shown in Figure 3-4.

The sample, contained in the fused silica ampoule had to be loaded into an Inconel cartridge for processing, to protect the furnace and magnet components. Three Type S thermocouples were wire wrapped to the outside of the ampoule and then inserted into the cartridge. This allowed the temperature profile to be monitored while directional

solidification proceeded. The temperature profile during growth for MZS-10 is shown in Figure 3-4. The guard heater was turned off during the growth of MZS-11 because of extremely high noise interference that could not be immediately corrected. As a result there were several differences in the thermal profiles for the two samples. The gradient was constant over a smaller temperature range. The lower zone temperature was less isothermal than for the growth of MZS-10 and the lower zone temperature was 200°C lower in some regions than for MZS-10. The thermal profile for MZS-11 is shown in Figure 3-5.

The sample, contained in the fused silica ampoule had to be loaded into an Inconel cartridge for processing, to protect the furnace and magnet components. Three Type S thermocouples were attached to the outside of the ampoule with wire before it was inserted into the cartridge. This allowed the temperature profile to be monitored while directional solidification proceeded. The temperature profile during growth for MZS-10 is shown in Figure 3-5. The guard heater was turned off during the growth of MZS-11 because of extremely high noise interference that could not be immediately corrected. As a result there were several differences in the thermal profiles for the two samples. The gradient was constant over a smaller temperature range. The lower zone temperature was less isothermal than for the growth of MZS-10 and the lower zone temperature was 200°C lower in some regions than for MZS-10. The thermal profile for MZS-11 is shown in Figure 3-6.

Table 3-2. Heater zone settings for samples grown in magnet furnace.

Heater	MZS-10 (5 Tesla Field)	MZS-11 (0 Tesla Field)
	(°C)	(°C)
Hot Guard	1026	1026
Hot Main	990	990
Booster	1150	1150
Cold Main	650	650
Cold Guard	650	Powered Off

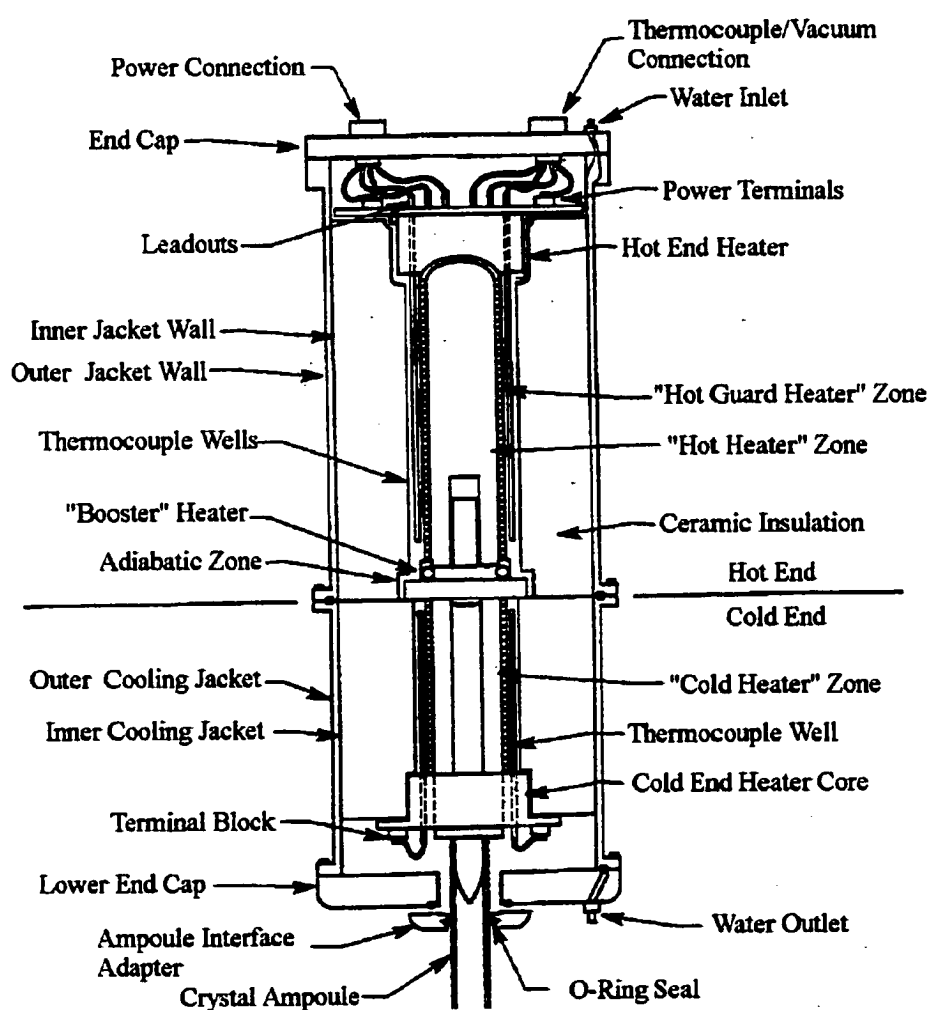


Figure 3-3. Bridgman-Stockbarger furnace configuration inside superconducting magnet used for ingots MZS-10 and MZS-11.

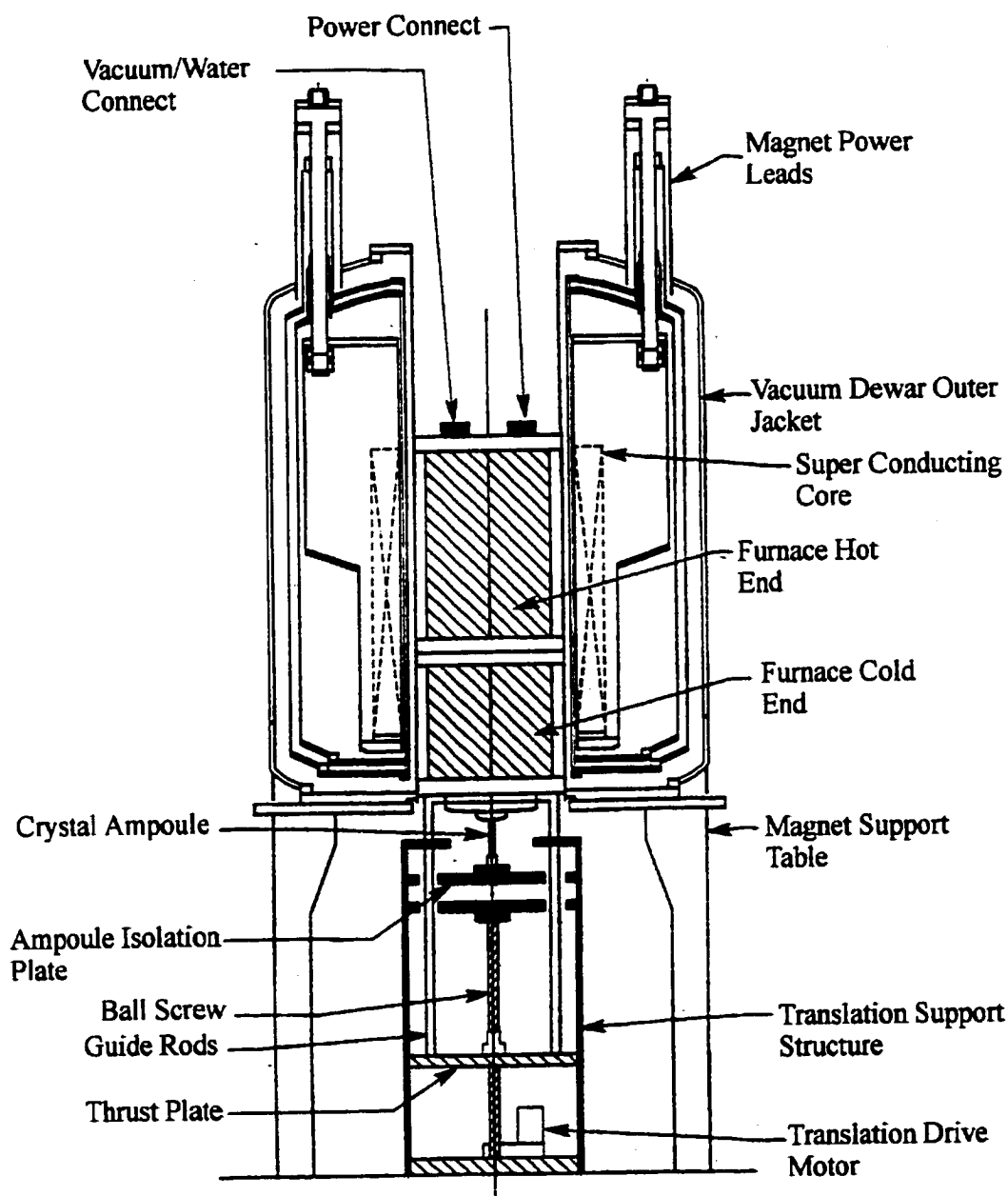


Figure 3-4. Magnet/furnace configuration used for ingots MZS-10 and MZS-11.

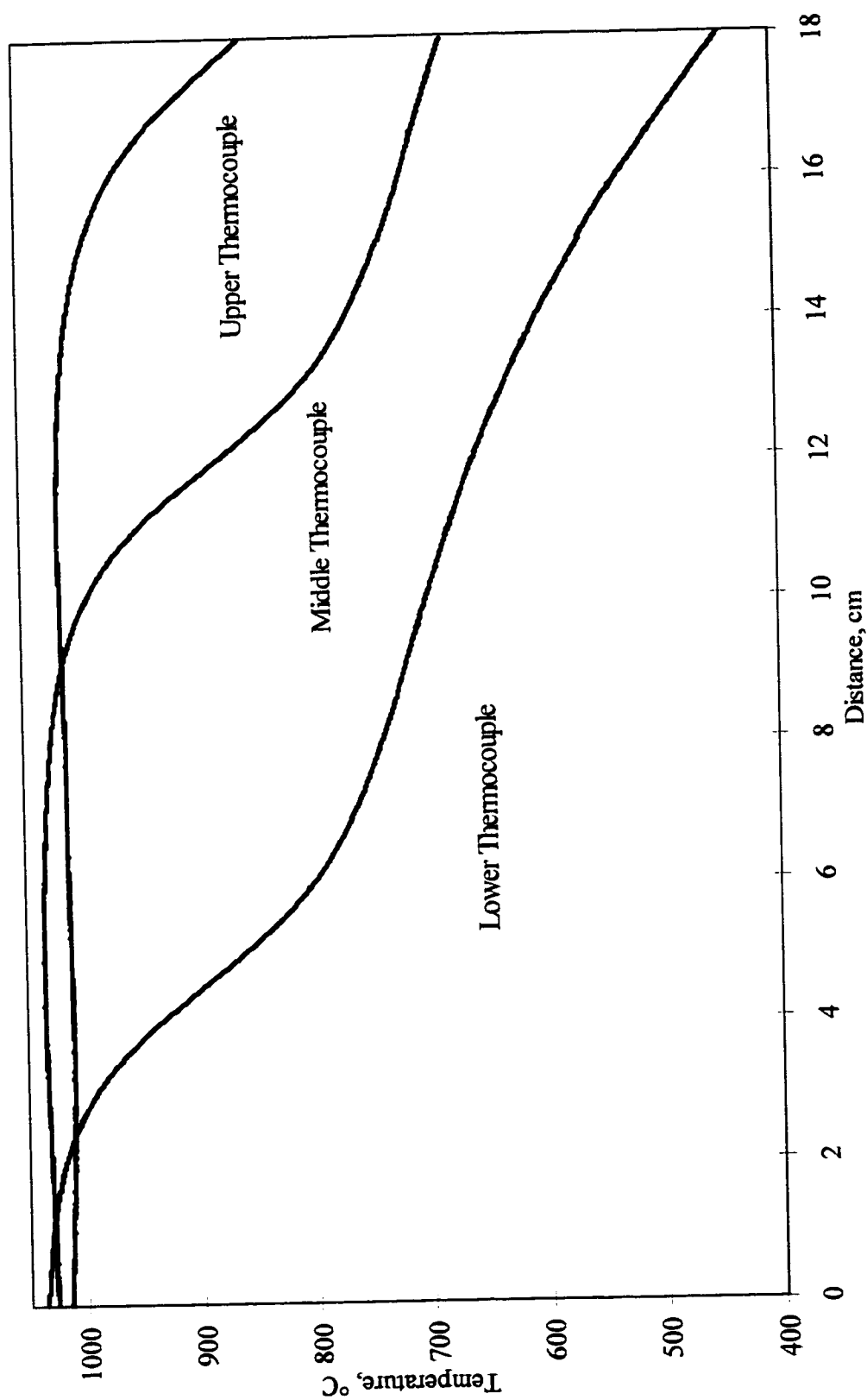


Figure 3-5. Temperature profile for MZS-10 with 5 Tesla magnetic field.

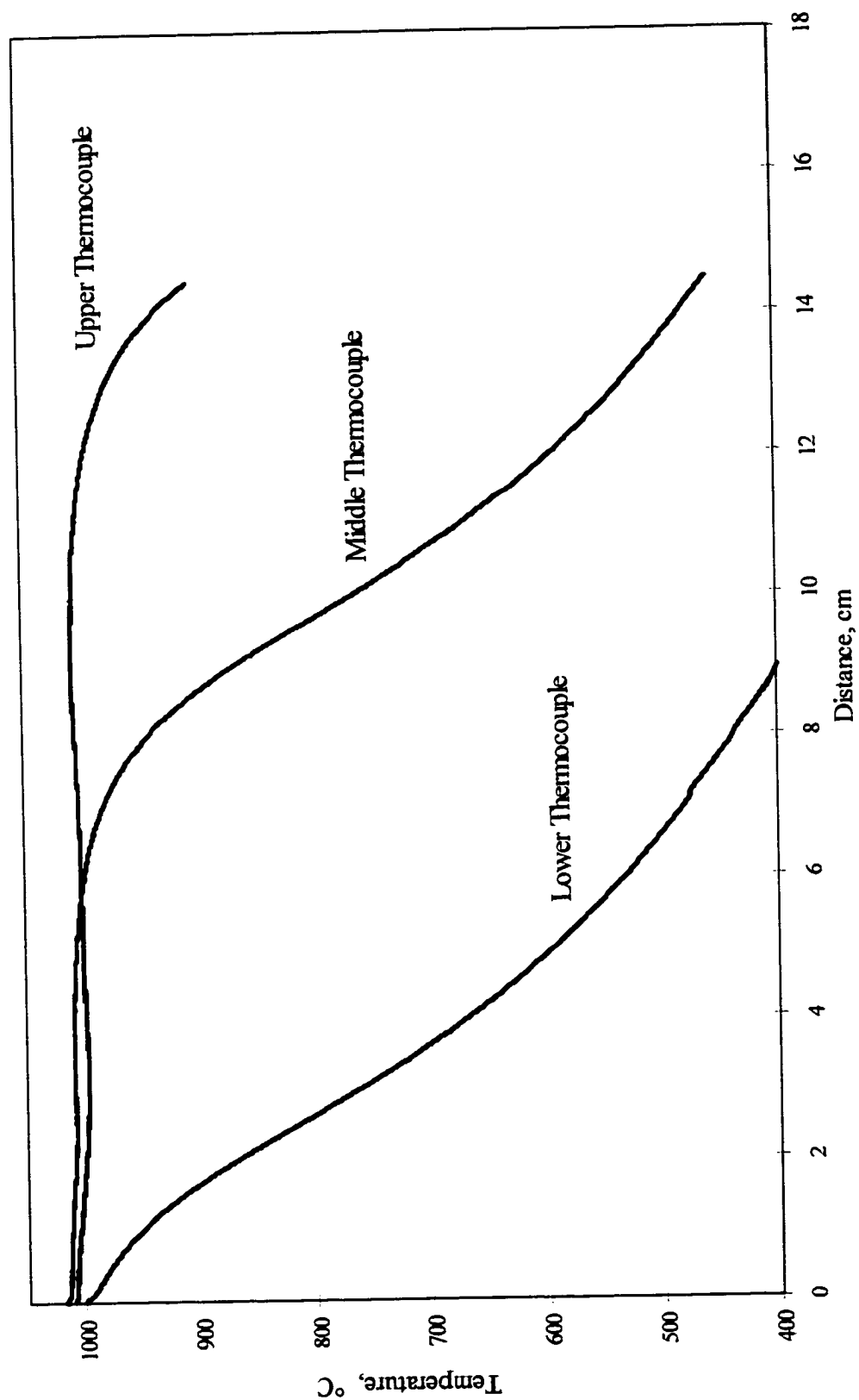


Figure 3-6. Temperature profile for MZS-11 without magnetic field.

CHAPTER 4 BASIC MACROSCOPIC DEVELOPMENT DURING DIRECTIONAL SOLIDIFICATION

Samples were synthesized and directionally solidified as described in Chapter 3.

After the entire length of the sample had passed through the gradient zone of the furnace, power to the heated zones was terminated, and the furnace was allowed to cool naturally. Each sample was removed from the furnace and placed into concentrated hydrofluoric acid to remove the fused silica ampoule except for MZS-7 which moved freely in the ampoule and slid out when the end of the ampoule was removed. All samples were broken in several places prior to ampoule removal. The location of these breaks is shown in Figure 4-1. Each sample was pieced together and mounted onto a graphite holder.

This chapter describes the effects of ampoule treatments, ampoule diameter, and solidification in a magnetic field on the development of surface features, grain structure, and compositional distribution. Surface features and compositional distribution were observed on a Zeiss scanning electron microscope (SEM). Grain structure was observed by a backscatter detector. Crystallographic orientation was determined by back reflection Laue x-ray diffraction.

Surface Analysis

The surface of the first sample grown, MZS-2, was sandblasted, a common way to observe the distribution of grains along the ingot surface. However, examination with a

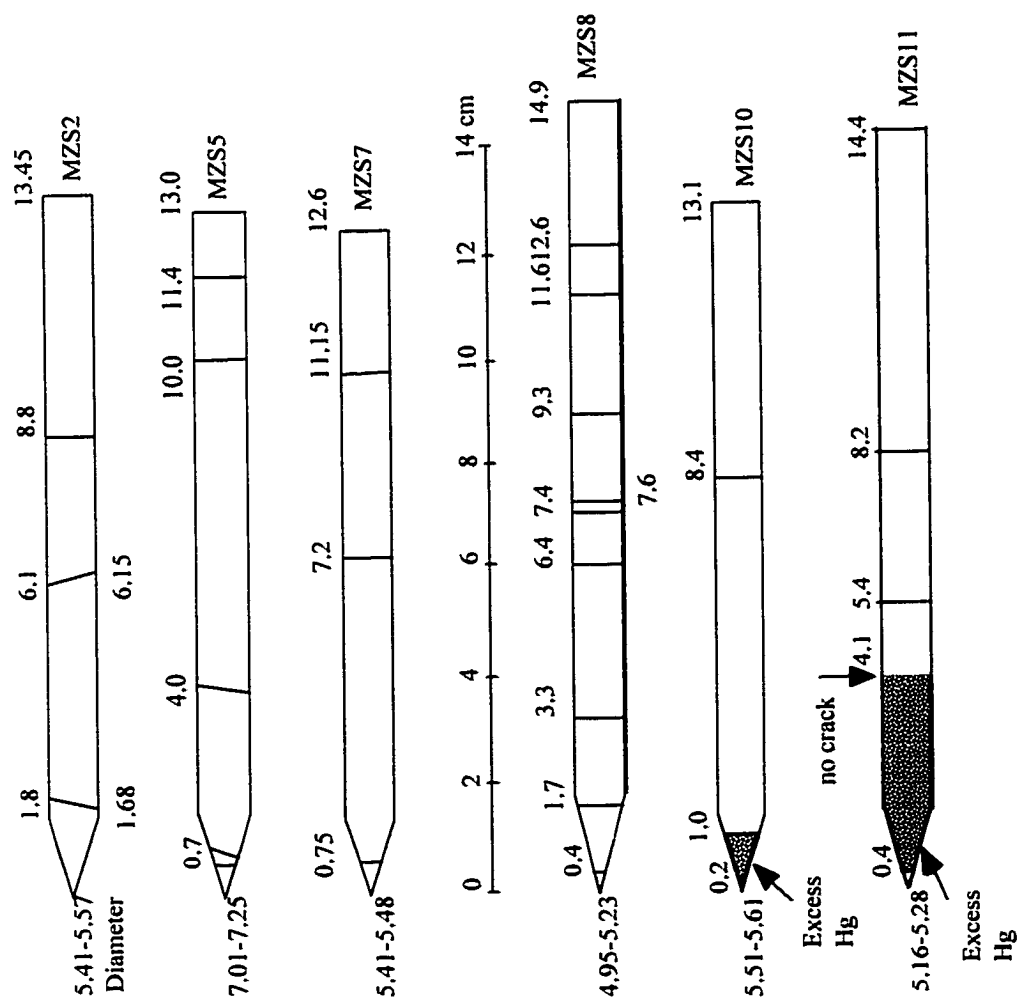


Figure 4-1. Illustration of external dimensions and location of breaks in each sample. All dimensions in centimeters.

SEM of the surface of the second sample, MZS-5, revealed interesting features. The surface features were recorded for all remaining samples. Collages of ingot surfaces are shown in Appendix A.

The surface of sample MZS-2 that was attached to the graphite holder was masked from the sandblasting treatment and was later examined for comparison. The surface of MZS-2, whose ampoule received no surface preparation other than cleaning, contained regions of raised height, observed in only one region on only one other sample. These regions had very few surface features, in contrast to areas where the surface is not raised. Both of these type regions are shown in Figure 4-2. These raised regions were observed only in the first 3.5 cm of the sample to freeze. Typical surface features from this region of MZS-2 are documented in Figure 4-3. After observing the surface of the other samples, it was determined that these regions of raised height were areas where the molten alloy wetted the containment ampoule. As solidification progressed, there were regions where the molten alloy appeared to have pulled away from the ampoule. Figure 4-4 shows an interface between these two regions. The small pits are believed to be thermal etch pits. Thermal etch pits have been observed where dislocations intersect the surface in the presence of an appropriate vapor. Angular pits observed on the as-grown surface are shown at 2000 times magnification in Figure 4-5. The solidification direction on all pictures is from the bottom of the figure toward the top.

Sample MZS-5 was solidified in an ampoule with a 7.3 mm inner diameter compared with a 5.28 ± 0.33 mm inner diameter for all other samples. This sample was loaded with a piece of graphite at the top of the ampoule. This sample was quenched, unintentionally, when the upper zone of the furnace failed. The quenched interface is

located 8.3 cm from the first to freeze tip. The surface of MZS-5 is covered with thermal etch pits. Figure 4-6 shows thermal etch pits in an array of lines, indicating a grain boundary. The location of the region is consistent with the observation of grain boundaries by other techniques. These arrays occurs in only the first 1.8 cm of the surface. The only evidence of the alloy adhering to the ampoule is in the regions where the grain boundary terminates. This region is shown at 20x in Figure 4-7 and magnified 200 times in Figure 4-8. As was observed for MZS-2, thermal etch pits were observed on the surface in the regions where there was a gap between the solidified ingot and the ampoule wall.

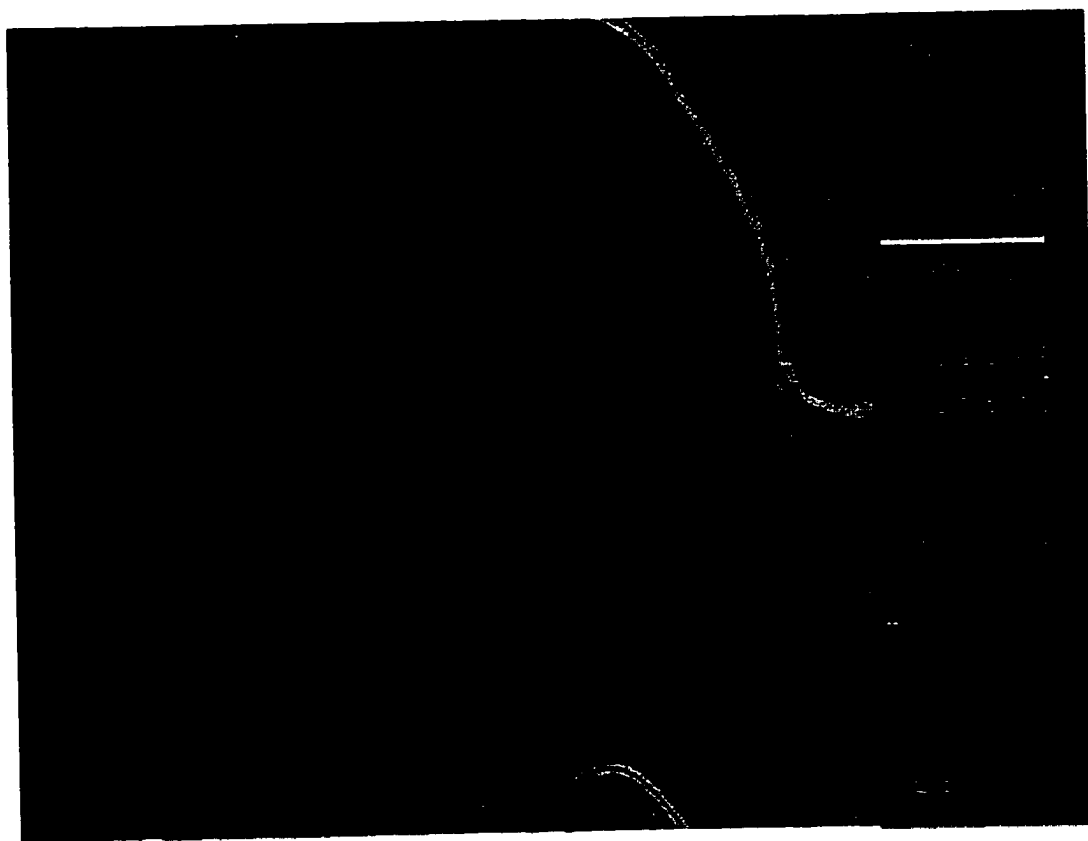


Figure 4-2. Region of as-grown surface of MZS-2 at a magnification of 94x showing raised surface regions.

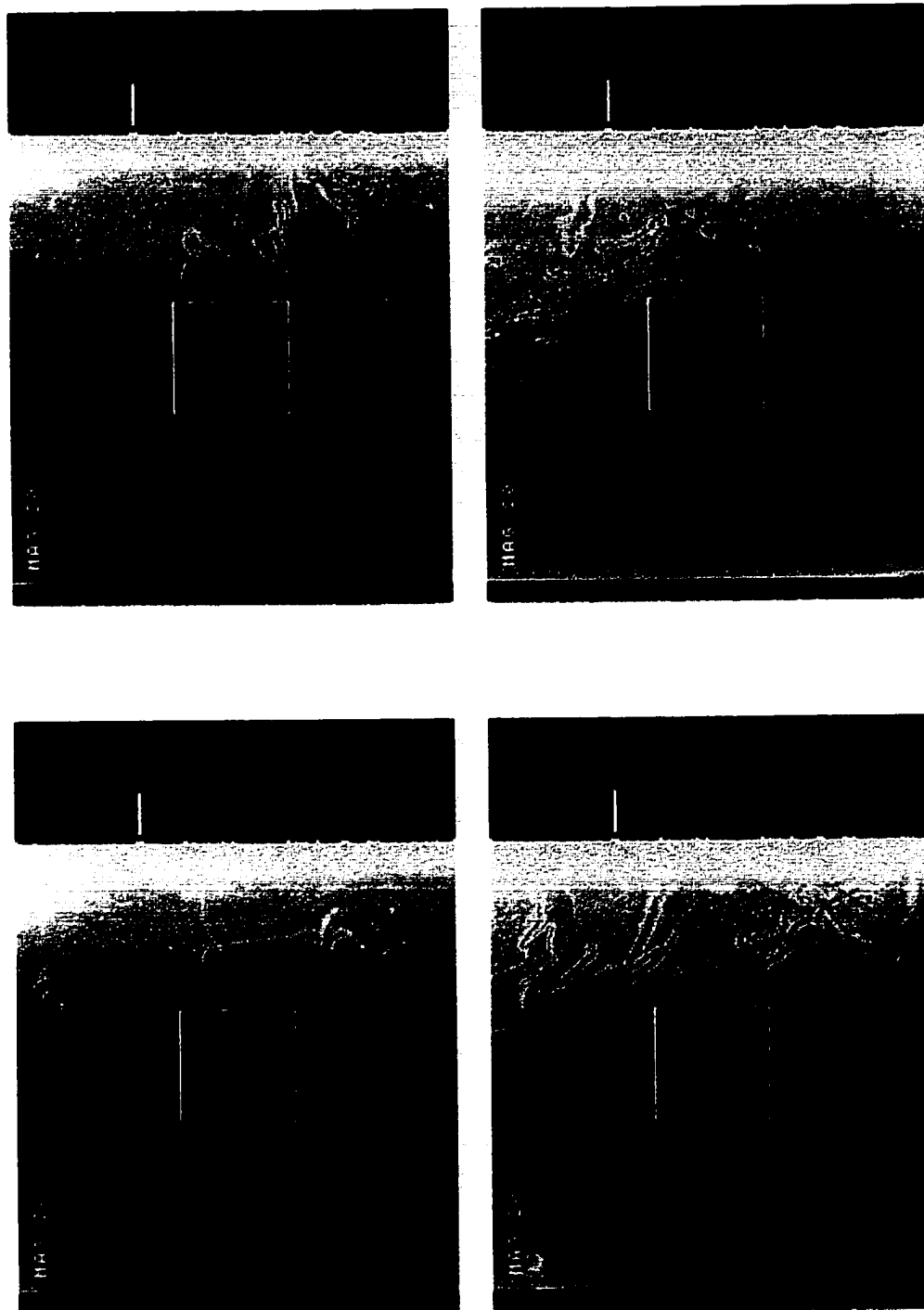


Figure 4-3. Surface features observed in the first third of the as-grown surface of MZS-2.

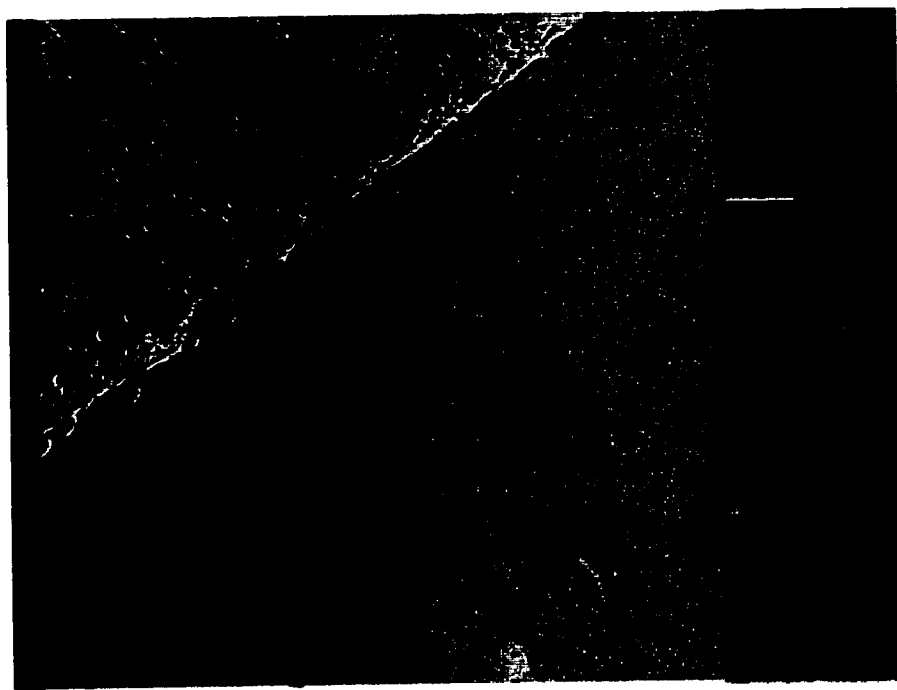


Figure 4-4. Interface between attached and detached growth on the as-grown surface of MZS-2. Solidification direction is from bottom to top.

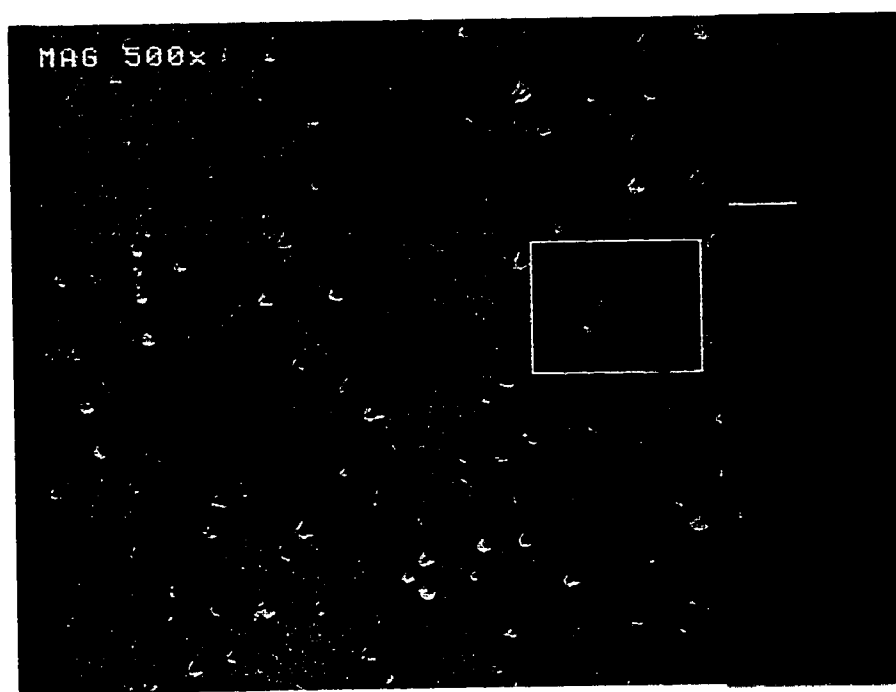


Figure 4-5. Thermal etch pits observed on the as-grown surface of MZS-2 at 500x.

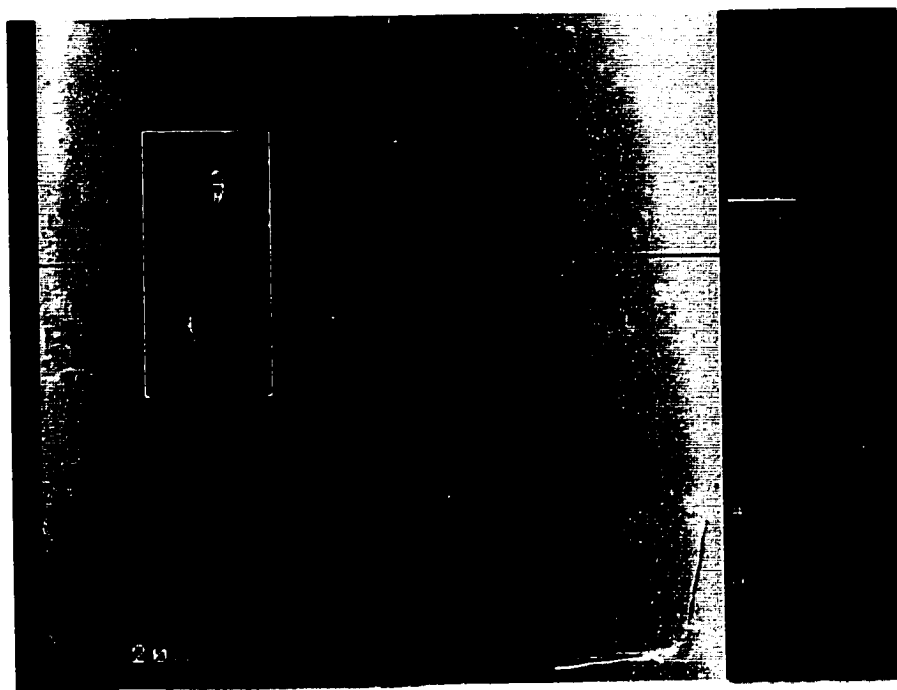


Figure 4-6. Surface of MZS-5 showing pile up of thermal etch pits at grain boundaries.

Thermal etch pits on the surface of MZS-5 were more rounded than those observed on MZS-2. This is due to the difference in orientation of the surface being examined. As with chemical etching, the sharpness of the etch pit depends on the ratio of dissolution rates in the lateral and vertical directions. When the dislocation exits the surface of the ingot along a major crystallographic orientation such as the (1,1,1) and the vertical dissolution rate is larger than the lateral rate, geometric angular pits are produced. When a dislocation exits the ingot at a surface from a different angle, the dissolution rates are different and the surface edge of the pit becomes rounded. Unusual surface features were observed in the region where the upper furnace zone failed. Just before total power failure in the zone, the temperatures fluctuated, falling below the desired temperature, then increasing back to the set point. These features are related to the localized remelting that occurred during these temperature fluctuations. The composition also fluctuated in these

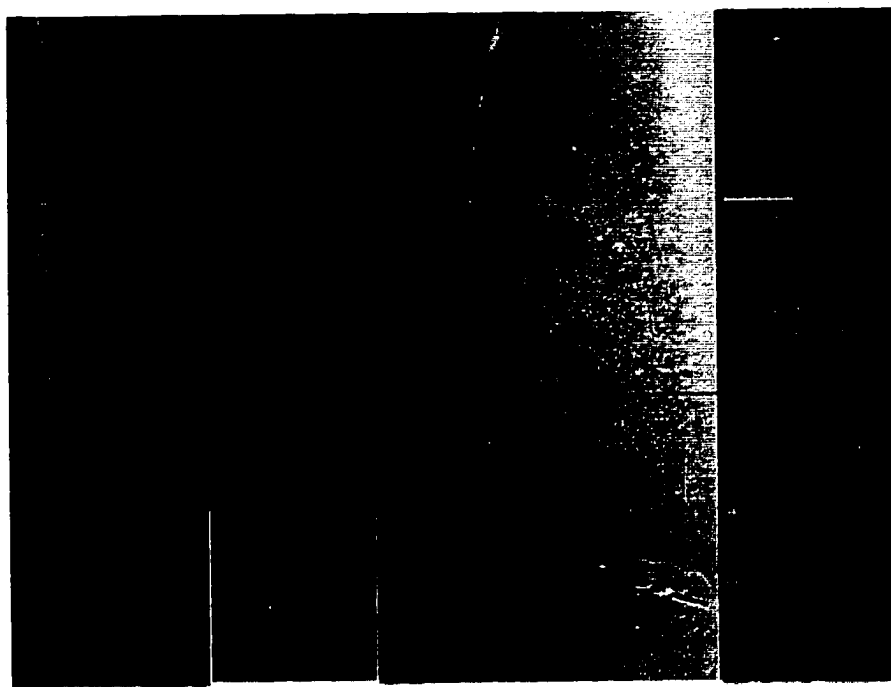


Figure 4-7. Surface of MZS-5 showing grain boundary and region where alloy was attached to ampoule during solidification.



Figure 4-8. Surface of MZS-5 showing grain boundary magnified 200 times at region where alloy was attached to ampoule during solidification.

regions as discussed in the next chapter, corroborating this relationship. These features, shown in Figure 4-9, were not observed in any other samples.

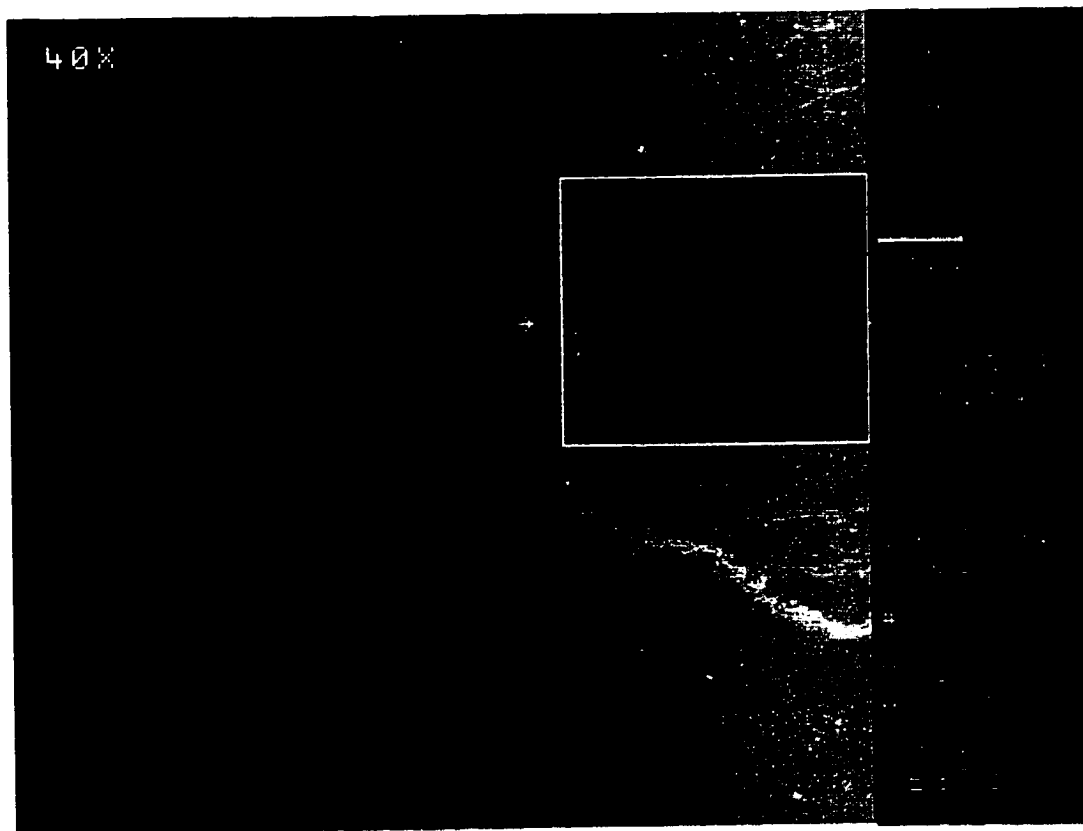


Figure 4-9. Surface of MZS-5 showing features in region of furnace failure approximately 8.2 cm from tip of ingot.

Ingot MZS-7 was processed in a 5.5 mm inner diameter ampoule with a graphite piece on top of the melt. Globular features, shown in Figure 4-10, were observed in the first 1.6 cm of this ingot. The remainder of the surface was covered only with thermal etch pits as shown in Figure 4-11. The density of etch pits appears to increase at about two thirds the length of the ingot and then decreases again in the last 1.0 cm. This ingot moved freely in the ampoule after processing. This is another indication that the solid alloy did not stick to the ampoule wall.

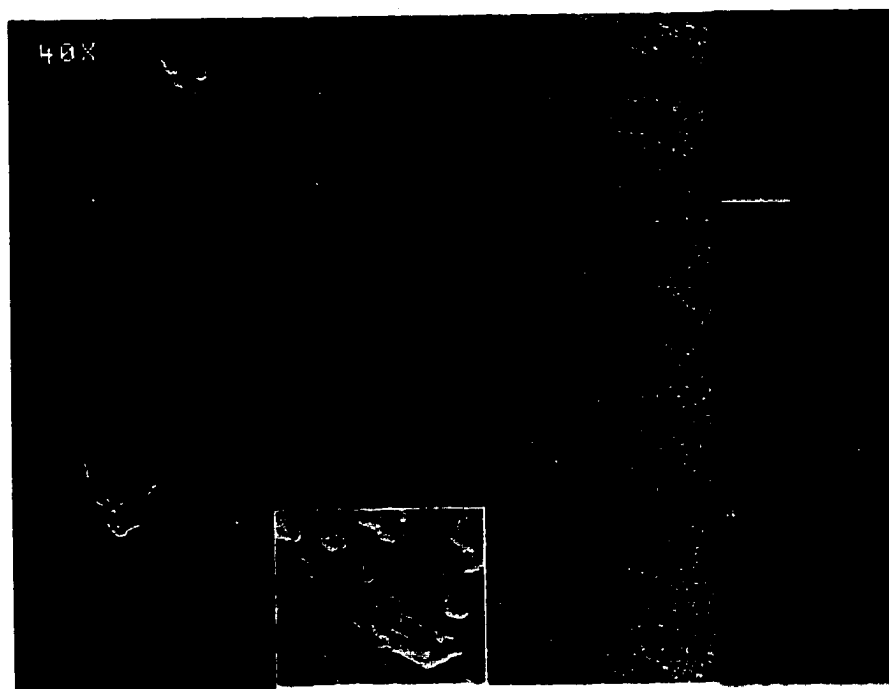


Figure 4-10. Surface of MZS-7 showing typical globular features observed in the first 1.6 cm of the ingot.

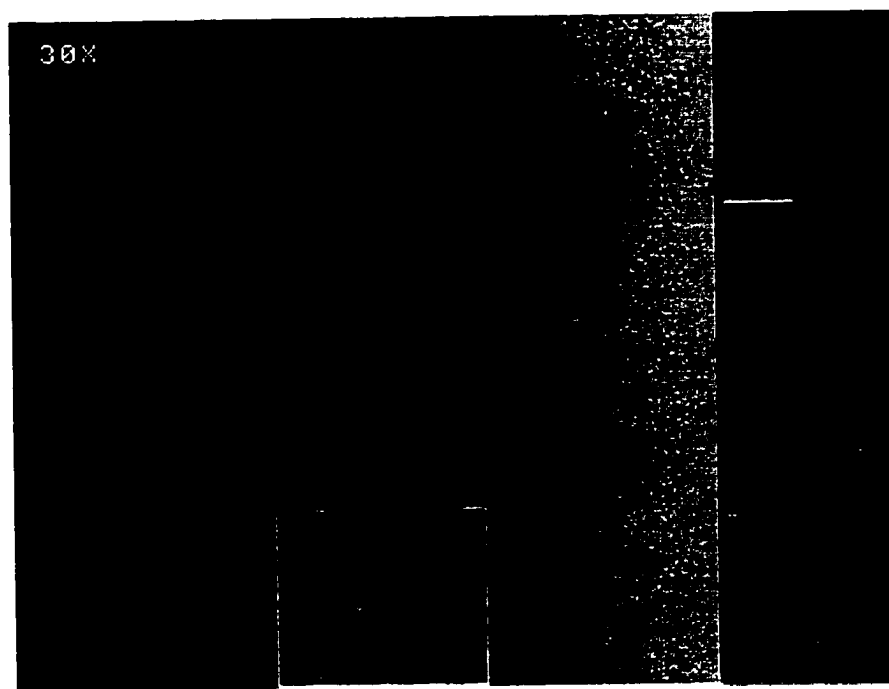


Figure 4-11. Surface of MZS-7 showing typical thermal etch pits observed over the entire ingot surface.

Sample MZS-8 was processed in a 5.0 mm inner diameter ampoule that had a coating of boron nitride applied to the inner surface. Regions were observed on the first 1.9 cm of the surface that appeared to have pulled away from the surface, as shown in Figure 4-12. The fracture surface is shown, magnified, in Figure 4-13. Thermal etch pits were observed around the edge of the fracture surface, but not on the surface. This led to the conclusion that this surface was not exposed to Hg vapor at elevated temperatures, and that the molten alloy wetted the boron nitride coating in some areas. The solidified alloy apparently pulled away from the ampoule during handling after removal from the furnace. The ingot was broken in eight places when removed from the ampoule, twice as many as any other ingot. This is another indication that the alloy stuck to the ampoule wall in many places. Some wetting was also observed on the tip of MZS-2 which had no surface treatment. It is likely that residual oxygen trapped in the tip increased the reactivity between the alloy and ampoule in this region. Yasuda et al.(1990) found that TeO_2 in the starting charge of CdTe ingots reacted with the quartz ampoule, causing adhesion. When oxygen was removed by annealing the charge in hydrogen before evacuating and sealing the ampoule, adhesion was eliminated. The same situation is likely to occur with ZnO_2 and SeO_2 in this alloy.

Sample MZS-10 was processed in a 5.5 cm diameter ampoule with a graphite piece at the top of the alloy. This ingot was processed in a furnace placed into the bore of a superconducting magnet operated at five Tesla. The first 0.9 cm of the ingot had an unusual texture, shown in Figure 4-14, that appeared to be chemically etched. The etching was caused by condensed Hg in the tip of both of the samples processed in the magnet furnace. The temperature at the very bottom of the thermal profile for samples MZS-10

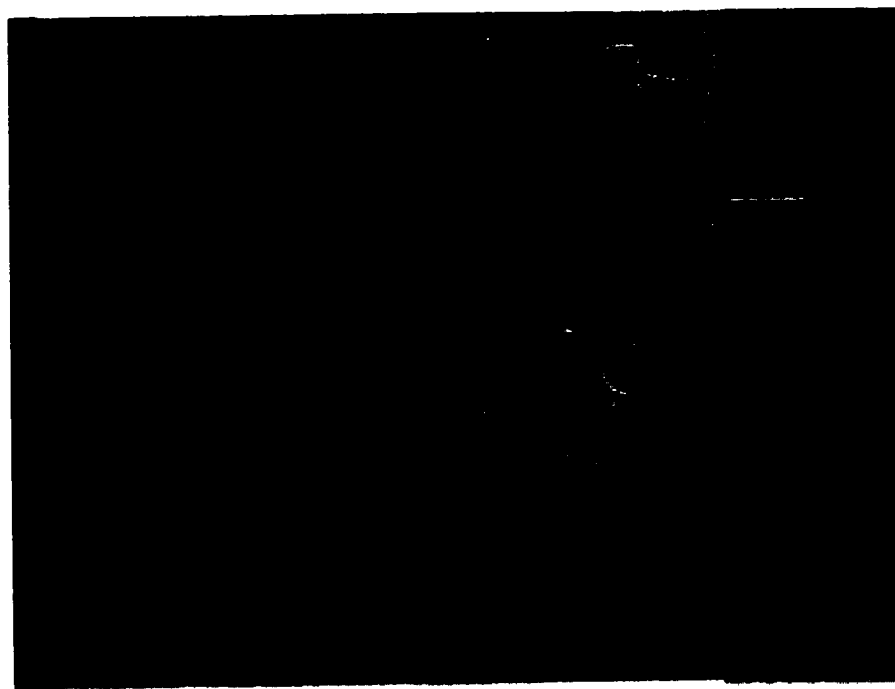


Figure 4-12. Surface of MZS-8 showing fracture surface observed in the first 1.9 cm of the ingot.

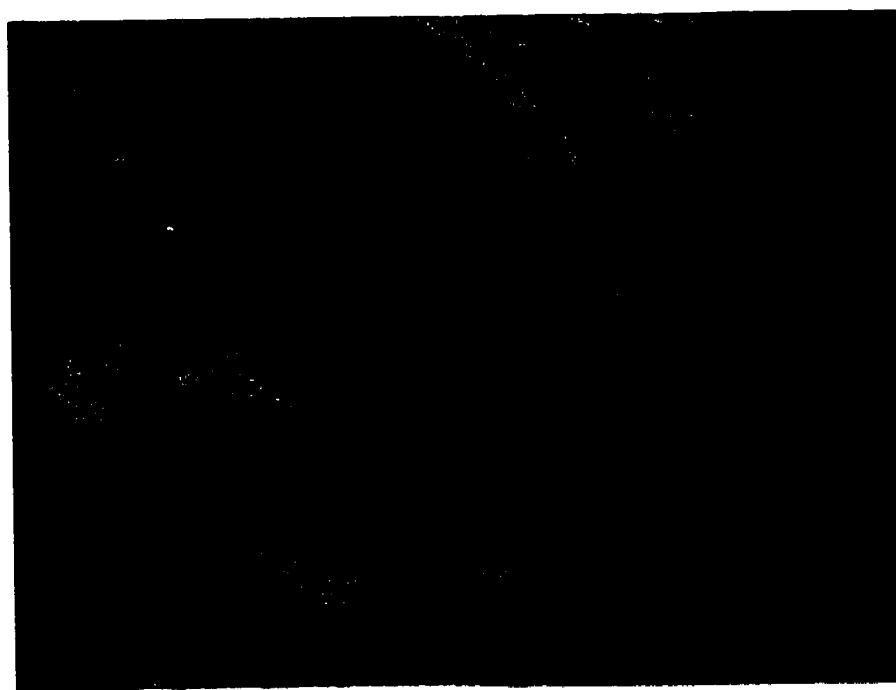


Figure 4-13. Surface of MZS-8, magnified by 200x, showing thermal etch pits surrounding the fracture surface.

and MZS-11 was 300°C below that of the samples grown in the Bridgman-Stockbarger configuration because heat pipes were not utilized. This temperature was low enough for the Hg vapor present in the ampoule to condense at the ingot tip. Thermal etch pits were observed (Figure 4-15) along grain boundaries in the first 3.4 cm of this ingot. The remainder of the ingot's surface was covered with thermal etch pits. No evidence of alloy wetting was observed on this ingot as with the other samples containing the graphite getter.

Sample MZS-11 was processed in a 5.2 mm inner diameter ampoule with a graphite piece. It was processed in the same furnace as MZS-10, but with no magnetic field. The guard heater in the lower furnace zone had to be turned off during this run because of erratic power fluctuations, so the lower zone temperature was 300° C below normal processing conditions. When this ingot was removed from the furnace, it was noted that Hg had condensed between the sample and the ampoule wall for the first 4.1 cm. Cellular type patterns of etch pits shown in Figure 4-16 were observed on the surface in the region where the Hg was in contact with the ingot. Very few thermal etch pits were observed between the cell boundaries. The cellular pattern terminated at 4.1 cm, where the condensed Hg ended. This interface is shown in Figure 4-17. Very few thermal etch pits were observed for the next 3.3 cm, as shown in Figure 4-18. The density of thermal etch pits gradually increased as solidification proceeded toward the end of the ingot (Figure 4-19). No evidence of wetting was observed on the surface of this ingot which also contained a graphite getter.

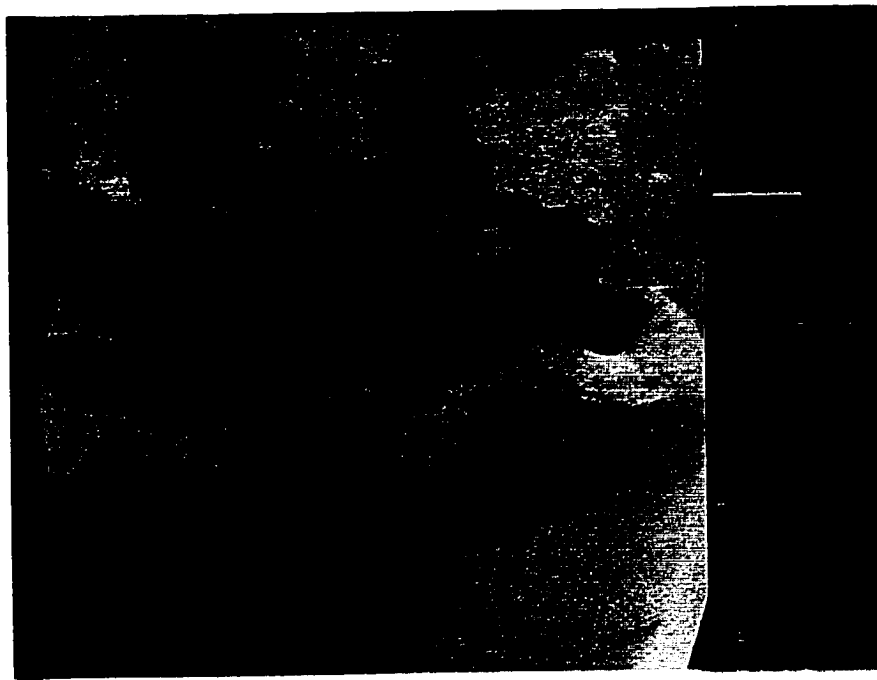


Figure 4-14. Surface of MZS-10, 1.0 cm from first to freeze tip. Tip appears to be chemically etched.

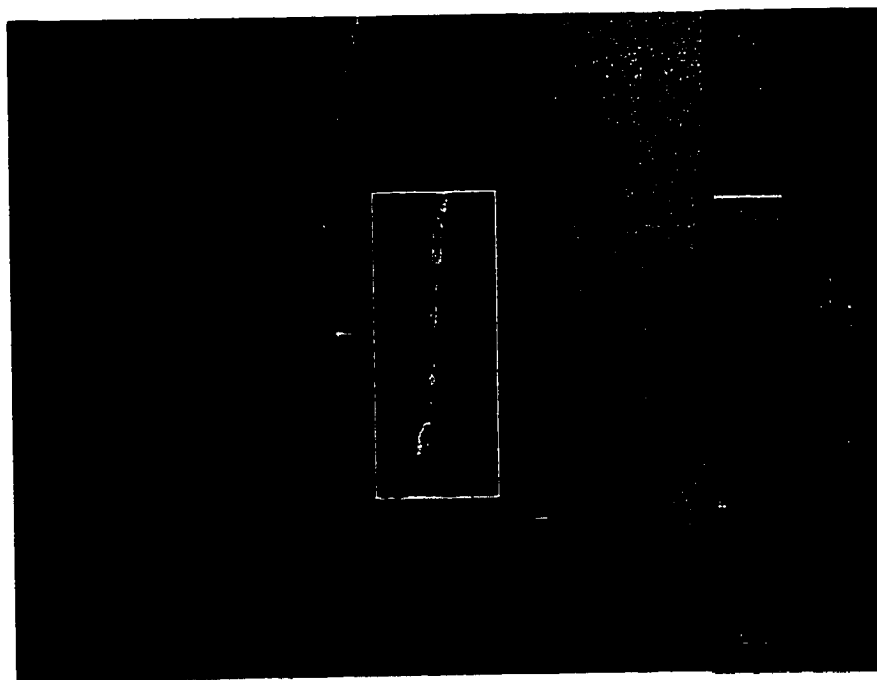


Figure 4-15. Surface of MZS-10 magnified at 26x, approximately 3.0 cm from first to freeze tip showing thermal etching at a grain boundary. Insert magnified at 100x.

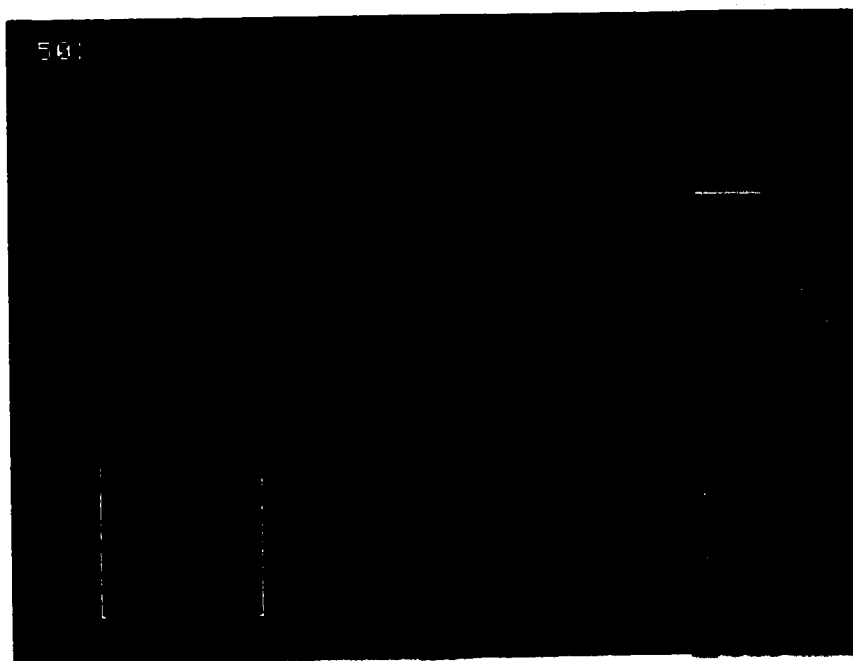


Figure 4-16. Surface of MZS-11, taken from the region where condensed Hg was in contact with the ingot surface.

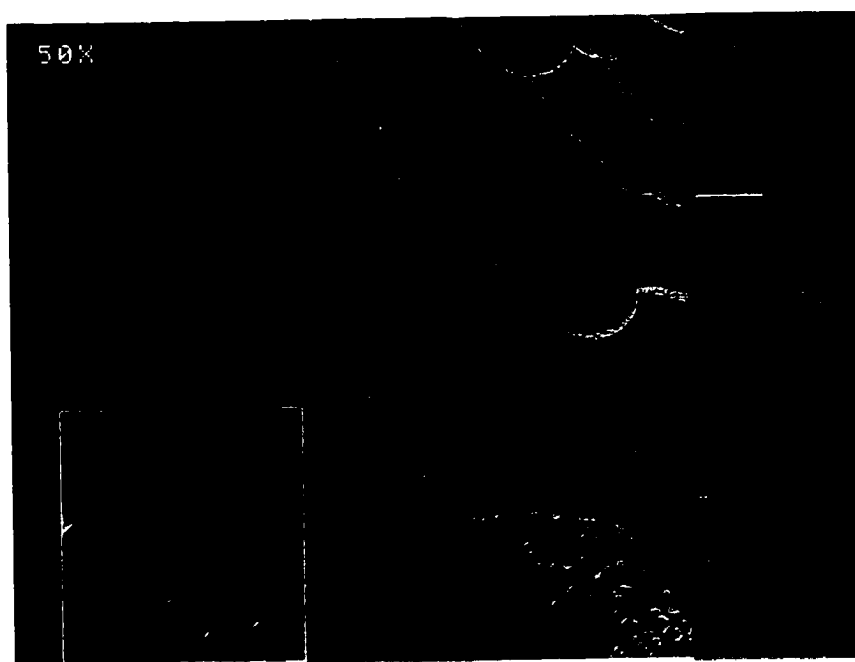


Figure 4-17. Surface of MZS-11 at the interface where the condensed Hg ended.

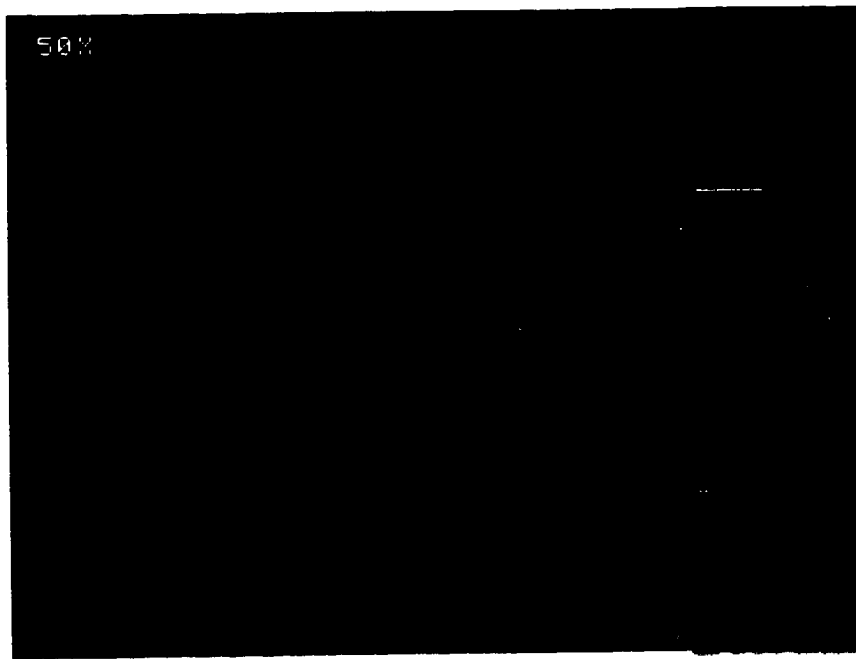


Figure 4-18. Surface of MZS-11, approximately 6.0 cm from the first to freeze tip, showing low thermal etch pit density.

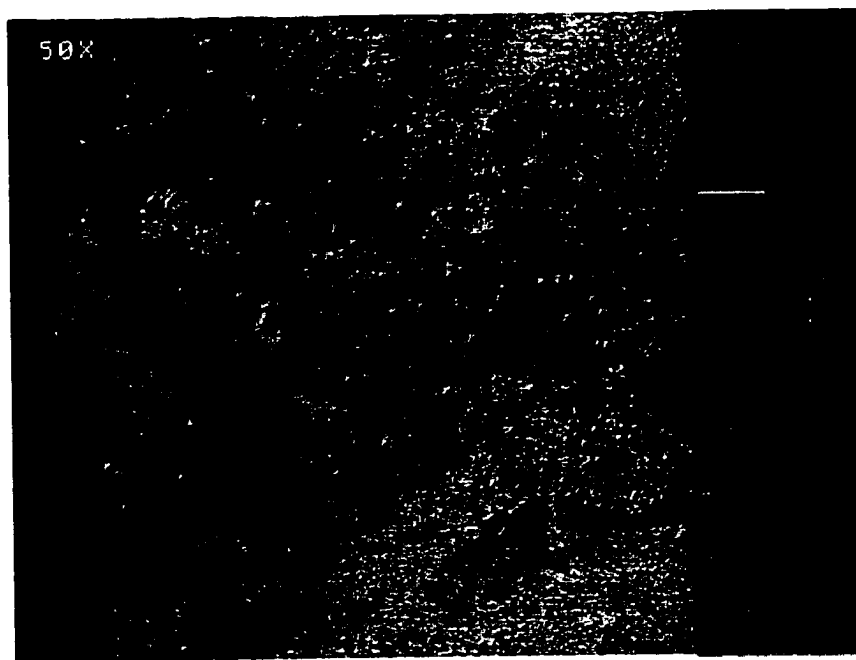


Figure 4-19. Surface of MZS-11, approximately 12.5 cm from tip showing increased etch pit density.

Development of Grain Structure

Each of the six ingots were mounted on a graphite holder and cut along the centerline of the growth axis. One half of each ingot was rough polished by hand on alumina grit papers, starting with 240, then 360 and finishing with 600. Fine polishing was performed on medium nap nylon felt with 6 μm , 1 μm , then 0.25 μm diamond paste. The inner surface of each ingot was observed in a JEOL microprobe with the backscatter detector. A difference in contrast was observed in the backscattered image for regions of different orientation. This method was used to delineate grain boundaries because an etchant appropriate for this material was not found.

Sample MZS-2 had a more elongated tip than the other samples due to the shape of the ampoule. The sample did not reach full diameter until approximately 2.7 cm from the first to freeze tip. The majority of this tip was intact when removed from the ampoule, allowing the development of grain structure to be examined. A large number of grains were observed in the tapered portion of the tip. One major grain prevailed after 3.8 cm had solidified. However, examination of the quenched interface (at 8.0 cm) revealed a second grain along the outer edge of the sample. This grain was either not visible along the entire centerline plane being examined or it nucleated from the ampoule wall at a location close to the quenched interface.

Sample MZS-5 initially contained several grains that merged into three at about 1.3 cm. One grain remained after 2.1 cm.

Sample MZS-7 contained three primary grains initially. One orientation dominated after 1.8 cm.

Sample MZS-8 contained the largest number of grains. Only two grains were present at 4.5 cm. One grain had prevailed after 6.4 cm.

Sample MZS-10 was grown in the presence of a magnetic field. Initially several small grains immersed from the tip, merging into a few larger grains. Only one grain was observed after the first 3.15 cm of the sample.

Ingot MZS-11 contained three main grains that grew toward the ampoule wall. After 1.05 cm, a singular grain had developed and remained throughout the length of the sample. A twin appeared 1.0 cm from the tip, and ended at the ingot surface 2.2 cm from the tip. This was the only twin observed and was probably a result of the large thermal gradient in the solid.

Crystallographic Orientation

Laue backscatter x-ray diffraction was used to determine the crystallographic orientation of three sectioned samples at various distances from the tapered tip, along the centerline. Results are summarized in Tables 4-1 through 4-3. Since each ingot was in several pieces, actual angular variations could only be compared within each piece. A single line in a table signifies the start of a different piece of the sample. Since each diffraction pattern was taken from the surface of the bisected ingot, the crystallographic orientation stated is normal to the crystal growth direction. The tabulated angles, δ and γ , are the angles measured in the horizontal and vertical directions, respectively, from a Geringer chart. For ingot MZS-10, diffraction patterns were taken across the radius, to verify that the ingot was a single grain across the radius. Radial displacement, in Table 4-3, is distance from centerline of ingot. These results verify the grain structure observed in

backscattered images from the microprobe. The tip regions contained several grains which grew out toward the ampoule wall, resulting in a single dominant grain orientation.

Crystal Quality By Synchrotron Radiation

The following information was observed using Beamline X-19C at the National Synchrotron Light Source, Brookhaven National Laboratory, Upton, NY. Samples MZS-7 and MZS-10 were found to be basically single crystals. All sample contained subgrain boundaries. Figure 4-20 is a topograph taken from a slice of MZS-7, 7.2 to 11.5 cm (MZS7a) from the tip. The topograph shown, is a magnification of one diffraction spot. Almost the entire crystal diffracted to one spot indicating that the entire region was essentially one crystal. Figure 4-21 is the topograph from MZS-7, 11.5 to 12.6 cm (MZS7b) from the tip. Figure 4-22 is the topograph from sample MZS-10, 8.3 to 9.5 cm from the tip. Lattice distortion was observed in the region closest to the ampoule wall in all three samples. Sample MZS7a showed larger distortion, due to strain, than the other two samples. Streaking and stray spots observed in the topographs were caused by the presence of inhomogeneous strain in the sample. The lattice parameter varied in these regions, causing diffraction to different spots. Subgrain misorientations observed were considered rather large, but were similar to values observed in HgCdTe and HgZnTe alloys produced by the same method. A summary of subgrain size and misorientation is given in Table 4-4. Subgrain averages were obtained on approximately 20 points per sample.

Table 4-1. Crystallographic displacement from (111) for MZS-2.

Distance from tip (cm)	δ (Degrees Vertical)	γ (Degrees Horizontal)
2	-12	9.5
2.5	-12	9.5
3	-12	9
3.5	-12	9
4	-12	8.5
4.5	-12 & -12.5	9 & 9.5
5	-12	9
5.5	-13	8
6	-13	8

Table 4-2. Crystallographic displacement from (111) for MZS-5.

Distance from tip (cm)	δ (Degrees Vertical)	γ (Degrees Horizontal)
1	-27 to -26	-16.2 to -17
1.5	-24	-17
2	-22.5	-17.5
2.5	-23	-17
3	-22	-17
3.5	-22.5	17.2
4.5	-20	-18
5.5	-19	-17.8
6.5	-20	-18
7.5	-20	-17.5
8.5	-19	-17
9	-19.5	-18
9.5	-19	-18

Table 4-3. Crystallographic displacement from (111) for MZS-10.

Distance from tip (cm)	δ (Degrees Vertical)	γ (Degrees Horizontal)	Radial Distance (cm)
0.5	17	-9	-0.2
0.5	17	-9	0.0
1.0	12	-7	-0.2
1.5	14	-6	-0.2
1.5	-17	-5	0.0
2.2	30	-18	0
3.2	30	-18	0
4.2	29.8	-17.5	0
4.6	12	-9	-0.2
4.6	-6	25	0.0
4.8	12	-9.5	-0.2
5.6	12	-9.5	-0.2
6.6	12	-9.0	-0.2
7.6	12	-9.5	0.0
7.6	-7	25	+0.2
8.4	no data	no data	+.02 (sample edge)
8.4	20	4.0	0.0
8.4	13	-8	-0.2
8.5	23	-17.5	0
9.5	23	-17.2	0
10.5	22.7	-17.2	0
11.5	22.2	-18	0
12.5	22.2	-18	0

Table 4-4. Summary of subgrain calculations from Synchrotron White Beam X-ray Topography.

Sample Number	Average Subgrain Size (mm)	Largest Subgrain Size (mm)	Average Subgrain Misorientation	Largest Subgrain Misorientation
MZS-7a	0.55	1.0	46''	2'20''
MZS-7b	0.35	0.5	2'	4'41''
MZS-10	0.50	1.1	3'	4'41''



Figure 4-20. X-ray topograph of MZS-7a, 7.2 to 11.5 cm from tip.



Figure 4-21. X-ray topograph of MZS-7b, 11.5 to 12.6 cm from tip.

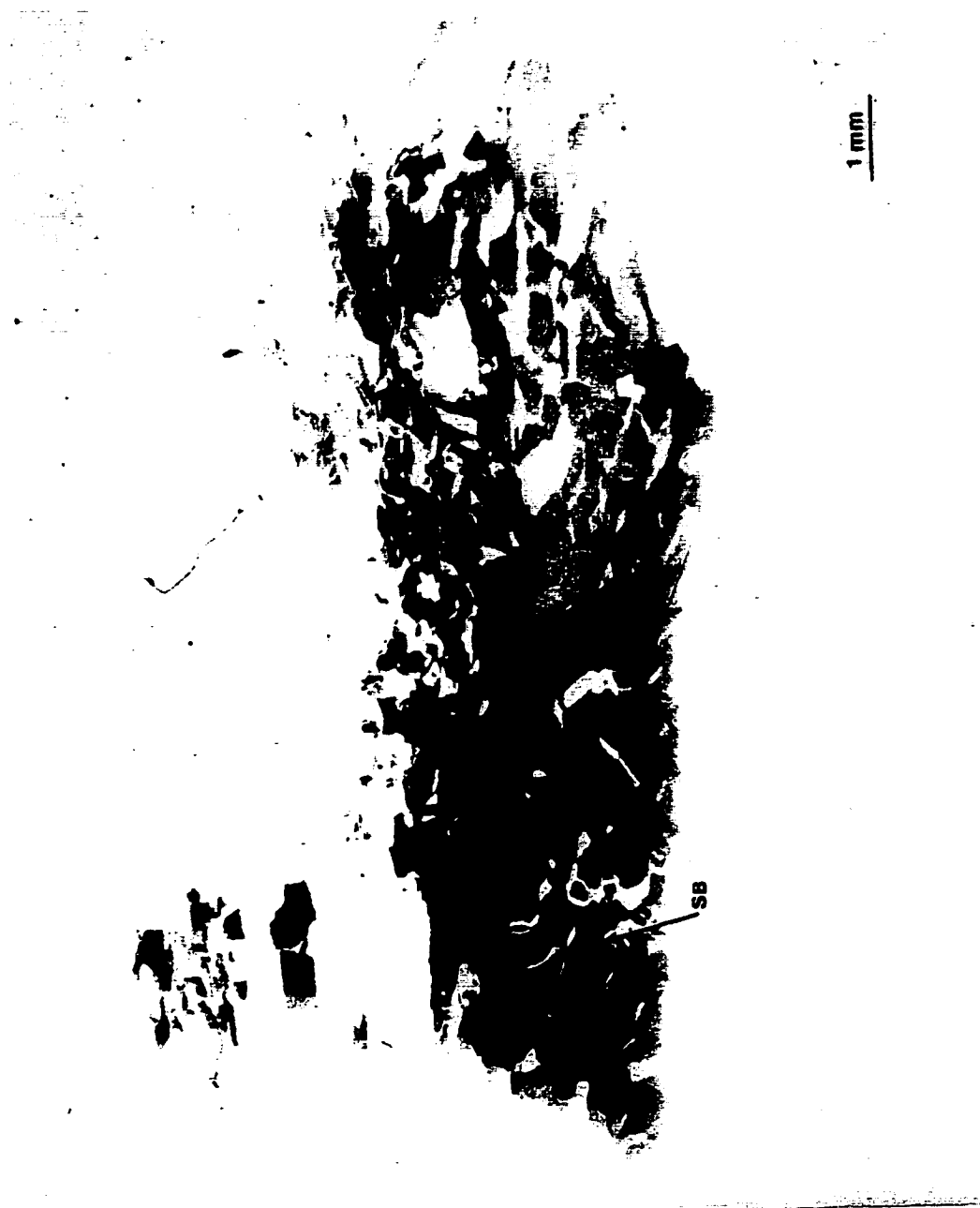


Figure 4-22. X-ray topograph of MZS-10, 8.3 to 9.5 cm from tip.

CHAPTER 5

COMPOSITIONAL VARIATIONS DURING DIRECTIONAL SOLIDIFICATION

This chapter describes the compositional distribution observed in each sample after solidification. Compositional variations were measured on the surface and through the sample centerline by energy dispersive x-ray spectroscopy (EDS) on a Zeiss scanning electron microscope (SEM) and for one sample, wavelength dispersive x-ray spectroscopy (WDS) on a JEOL microprobe. Radial compositional variations were measured by either EDS or WDS across the diameter of each crystal. Radial line scans were taken at various distances from the tip of each crystal. Radial composition variations indicated the curvature of the interface between the liquid charge and the solid crystal.

Axial Compositional Variations

In a previous study, Cobb et al. (1991) determined the average composition of slices of $\text{Hg}_{1-x}\text{Zn}_x\text{Se}$ crystals cut perpendicular to the growth direction by precision density measurements. They compared the axial composition profile with a one-dimensional diffusion calculation to determine the effective diffusion coefficient. For this study, it was important to understand small radial compositional variations as opposed to the average composition. For these materials to be viable substrate candidates, it is important to obtain both radial and axial compositional homogeneity.

Initially EDS measurements, using a SEM, were performed on the outer surface of each crystal. For one crystal, MZS-5, the composition was measured on the surface along

three lines the axial direction, each separated by 90 degrees. Figure 5-1 shows the results of three axial compositional profiles measured on the surface of this sample. This sample was quenched, unintentionally, after approximately 9 cm of growth due to failure of the upper zone heater. The differences in composition for the three rotations are within experimental error, indicating that the shape of the interface is symmetric with respect to the walls of the ampoule. This test was not repeated on other samples.

To further investigate compositional variations, each crystal was mounted in a graphite fixture and bisected along the centerline. The center plane of each sample was polished and the sample was mounted to a graphite block with conductive carbon paste or tape. The composition of each crystal along the centerline was determined by EDS. Measurements were made every millimeter through the initial composition transient. The remaining measurements were made every two millimeters.

The surface and centerline axial compositions for each crystal are plotted as a function of distance from the first-to-freeze tip in Figures 5-2 through 5-7. The axial centerline compositional profile for MZS-5 was also measured by WDS for comparison, and is included in Figure 5-3. The tips of the ampoules used for MZS-2 and MZS-5 had a longer taper than the other ampoules. This explains why there is a difference in the onset of the steady state growth region. The other ampoules were all constructed with the same taper dimensions.

Large scatter was noticed in the axial profile from MZS-5 at a position of approximately 6 cm. Compositional analysis was performed by WDS in a microprobe to verify these fluctuations. These results, shown in Figure 5-3, confirmed the compositional variations. A compositional map, shown in Figure 5-8, of the entire center surface was

then performed using the microprobe. The results of this analysis are not quantitative, but show variations in compositional intensity. The colors represent number of counts of the Zn spectra. The highest Zn content is represented by white. The Zn content decreases in the following order: pink, red, yellow, green and blue. The upper zone of the furnace failed during processing of this sample, leaving a quenched interface after 8.9 cm of growth. It is believed that the heater element began deteriorating several days before total failure occurred. This caused the interface to periodically translate at a faster rate, and resulted in a lower composition profile in that region.

Radial Compositional Variations

Radial variations in composition were determined by taking EDS measurements along the radius of the bisected crystal at specific distances from the tip. These measurements, combined with micrographs of the interfaces (Figures 5-9 and 5-10) taken in the microprobe with a backscatter detector, revealed that the shape of the solid-liquid interface is convex when viewed from the solid. The micrographs were taken from samples MZS-2 and MZS-5 that were quenched during growth. Radial compositional variations for each sample are shown in Figures 5-11 through 5-17.

One interesting result is that the shape of the interface changes from concave to convex in the region where the ampoule reaches full diameter. This change in shape is thought to be related to differences in the dominant methods of heat transfer in the tip region compared to the constant diameter growth region. Initially, the shape of the interface, determined from compositional variations, is concave. However, as the ampoule reaches full diameter, the interface shape becomes flat and eventually becomes slightly

convex. This can be explained by looking at the different contributions from conduction and radiation to heat transfer as shown in Table 5-1. Consideration is given only to mechanisms of heat transfer in the ampoule and alloy resulting from the thermal gradient in the region of the interface. These calculations are based on assumptions for the thermal conductivity of the liquid and solid $\text{Hg}_{1-x}\text{Zn}_x\text{Se}$ liquid as well as emissivity, as these values are not available in the literature. Heat flux from conduction is given by

$$\kappa_Q A_Q \left(\frac{\Delta T}{L} \right) + \kappa_L A_L \left(\frac{\Delta T}{L} \right) = \kappa_Q A_Q \left(\frac{\Delta T}{L} \right) + \kappa_S A_S \left(\frac{\Delta T}{L} \right), \quad (5-1)$$

where κ_Q is the thermal conductivity of the quartz, A_q is the area of the quartz, κ_S and κ_L are the thermal conductivities of solid and liquid $\text{Hg}_{1-x}\text{Zn}_x\text{Se}$, respectively, A_S and A_L are the areas of the solid and liquid $\text{Hg}_{1-x}\text{Zn}_x\text{Se}$, respectively, and $\Delta T/L$ is temperature gradient. Heat flux from radiation is given by

$$\varepsilon \varepsilon \sigma \Delta T_L (2\pi r_L L) = \varepsilon \varepsilon \sigma \Delta T_S (2\pi r_S L), \quad (5-2)$$

where ε is the emissivity, σ is Boltzmann's constant, ΔT is the difference in temperatures over length L in the solid and liquid, and r is the radius of the alloy solid and liquid.

Quartz is transparent in the infrared region and does not contribute to radiative heat transfer. In the tip region, case (a) in Figure 5-18, heat transfer is dominated by conduction through the ampoule wall, mainly because the ampoule area is large relative to the alloy area and the thermal conductivity of the quartz is probably higher than the $\text{Hg}_{1-x}\text{Zn}_x\text{Se}$. This leads to a situation where the surface of the alloy is cooler than the center, leading to a concave interface shape.

As solidification progresses in the $\text{Hg}_{1-x}\text{Zn}_x\text{Se}$ system, , the curvature of the solid-liquid interface first becomes almost flat and then changes to convex, case (b) in Figure

5-18. This interface shape in the steady state growth region is opposite of what has been observed in the $\text{Hg}_{1-x}\text{Cd}_x\text{Te}$ (Szofran and Lehoczky, 1984) and $\text{Hg}_{1-x}\text{Zn}_x\text{Te}$ (Su et al., 1993) alloys systems. Although work has been done both experimentally and mathematically to determine furnace configurations and appropriate hot and cold zone settings required to produce a convex interface, the interface shape remained concave due to the fact that there is a large change in the thermal conductivity of $\text{Hg}_{1-x}\text{Cd}_x\text{Te}$ (Holland and Taylor, 1983) and $\text{Hg}_{1-x}\text{Zn}_x\text{Te}$ (Sha et al., 1996) at the melting point. Since this convex interface has been observed in both the $\text{Hg}_{1-x}\text{Zn}_x\text{Se}$ and $\text{Hg}_{1-x}\text{Cd}_x\text{Se}$ alloy systems, it is evident that there must be a difference in the thermal conductivity of HgSe and HgTe based alloys. If the liquid and solid thermal conductivities are equal or very similar, a convex interface is expected. When the temperature at the surface temperature of the alloy is higher than the center, a convex interface results. The gap between the insulating barrier and the ampoule results in a view factor that allows radiative heating of the alloy surface from the hot zone wall. The differences in electrical properties of the HgTe and HgSe systems can be used to explain the difference in the thermal properties of this system.

Both HgSe and HgTe are considered semi-metals because they have a negative band gap. The band gap of Hg Se was measured to be -0.06 eV (Lehockzky et al., 1974), while that of HgTe was -0.303 eV (Scott, 1969). This indicates that HgSe behaves more like a metal, thus the thermal conductivity of the liquid and solid is very likely to be similar. The facts that both HgSe (Lehockzky et al., 1974) and $\text{Hg}_{1-x}\text{Zn}_x\text{Se}$ (Cobb et al., 1991) are naturally n-type and have as grown electron concentrations on the order of 10^{18}cm^{-3} , also illustrate this metal-like behavior.

The convex interface curvature observed in $\text{Hg}_{1-x}\text{Zn}_x\text{Se}$ is favorable for the growth of single crystalline material (Chang and Wilcox, 1974). Grain structure and x-ray diffraction, discussed in Chapter 4, confirmed the hypothesis that the grains nucleated at the wall or interface surface grew outward toward the wall, and terminated, resulting in growth in a singular orientation. Compositional variations in all samples led to the conclusion that all samples, grown in the Bridgman configuration, had a convex interface shape. However, for sample MZS-10, which was grown in an applied magnetic field, radial compositional variations were much smaller, indicating an almost flat interface. If the velocity of the fluid motion in the melt is larger than the growth velocity, the diffusive transfer to the interface is altered and compositional variations result. For this composition, the presence of the five tesla magnetic field was sufficient to reduce convective flow in the melt, thereby reducing radial compositional variations.

The convex interface shape is favorable for the outward growth of grains as described, however, grains can also be nucleated at the ampoule wall if nucleation sites are present. Nucleation can occur at imperfections in the ampoule wall or ampoule coating and at sites where the alloy wets the ampoule material. In these experiments, grain nucleation from the wall was observed only in the plain quartz ampoule, where evidence of wetting behavior was observed. The presence of thermal etch pits on the surface indicates that Hg vapor filled the gap between the solid and the ampoule, preventing wetting between the ampoule and alloy. A gap between the alloy and the ampoule is expected to develop, because the vapor pressure of Hg at a temperature of 1010°C is on the order of 75-100 atmospheres. Since the force due to hydrostatic pressure is approximately 0.1 atmospheres, the Hg vapor pressure pushing the melt away from the ampoule exceeds the

hydrostatic force pushing the melt against the ampoule. This reduces the nucleation potential, making nucleation of grains at the ampoule wall unlikely.

Table 5-1. Calculated contributions to heat transfer in the ampoule and alloy.

	Tip Region	Steady State Growth Region
Radiation from Liquid (W/mK)	0.36	0.48
Radiation from Solid (W/mK)	0.14	0.42
Conduction in Quartz at Liquid (W/mK)	1.32	1.62
Conduction in Quartz at Solid (W/mK)	0.84	1.47
Conduction from Liquid (W/mK)	0.26	0.54
Conduction from Solid (W/mK)	0.03	0.53

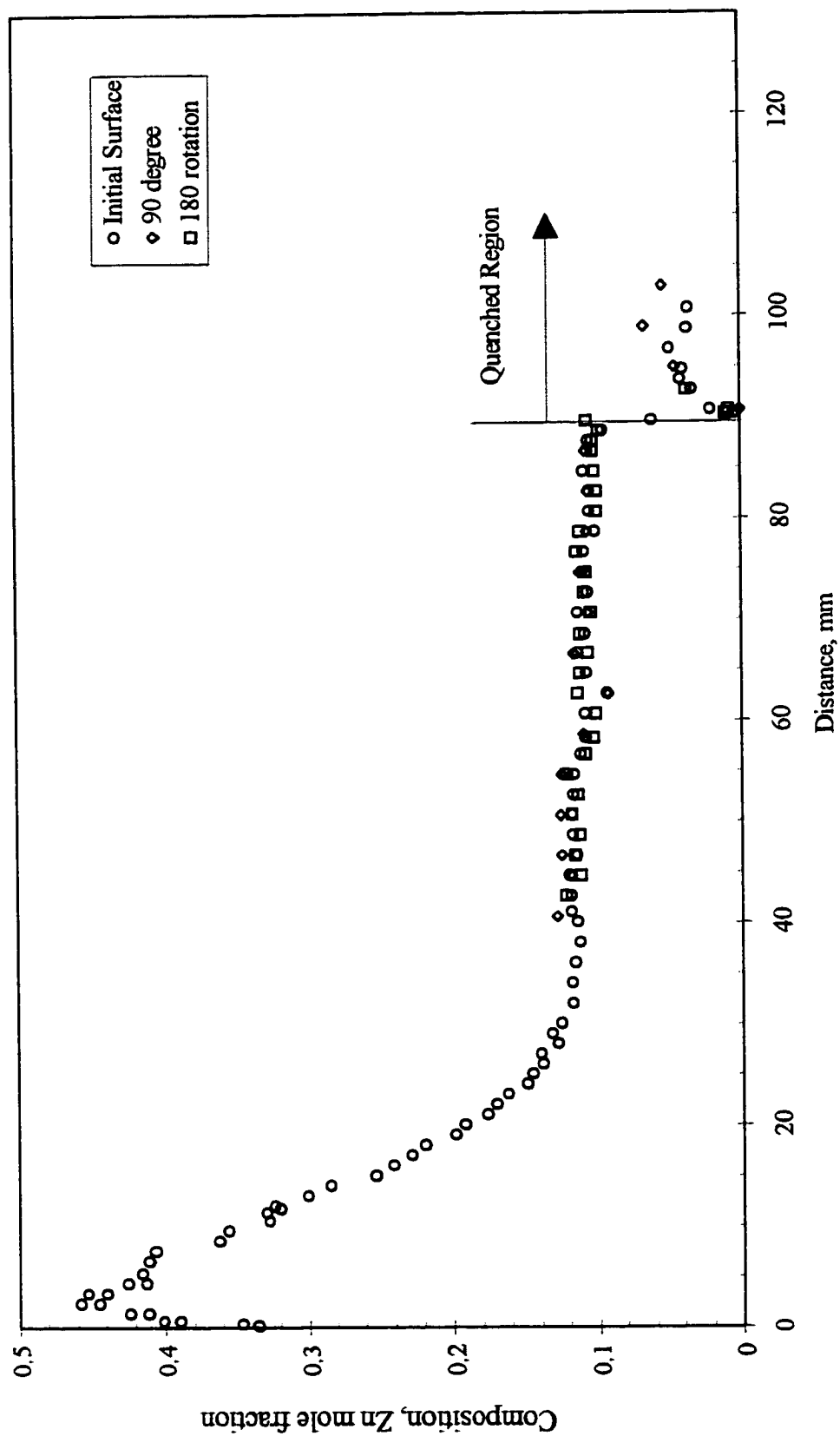


Figure 5-1. Surface composition of MZS-5 from EDS measurements at three different axial rotations.

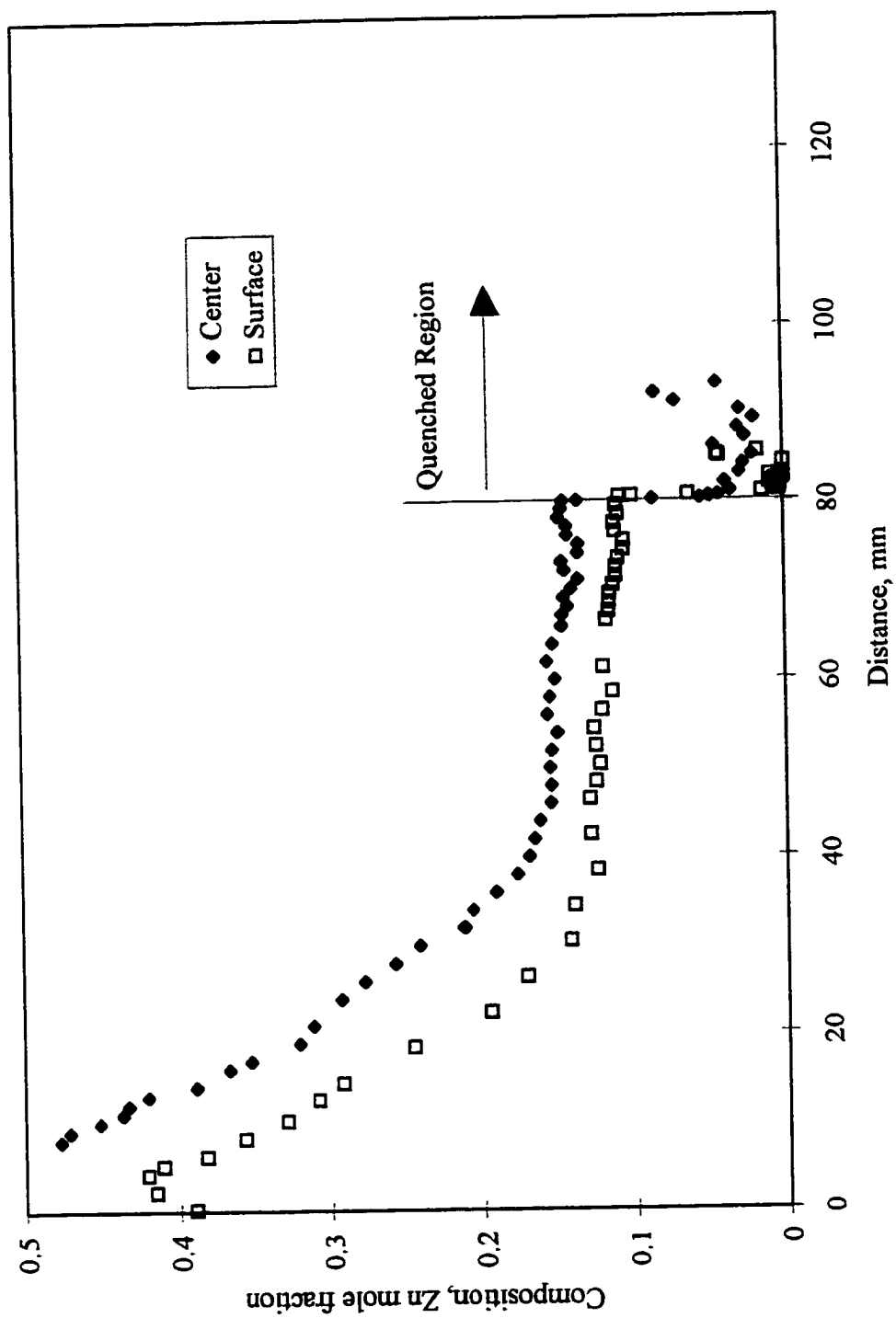


Figure 5-2, Surface and centerline composition profiles of MZS-2 from EDS measurements.

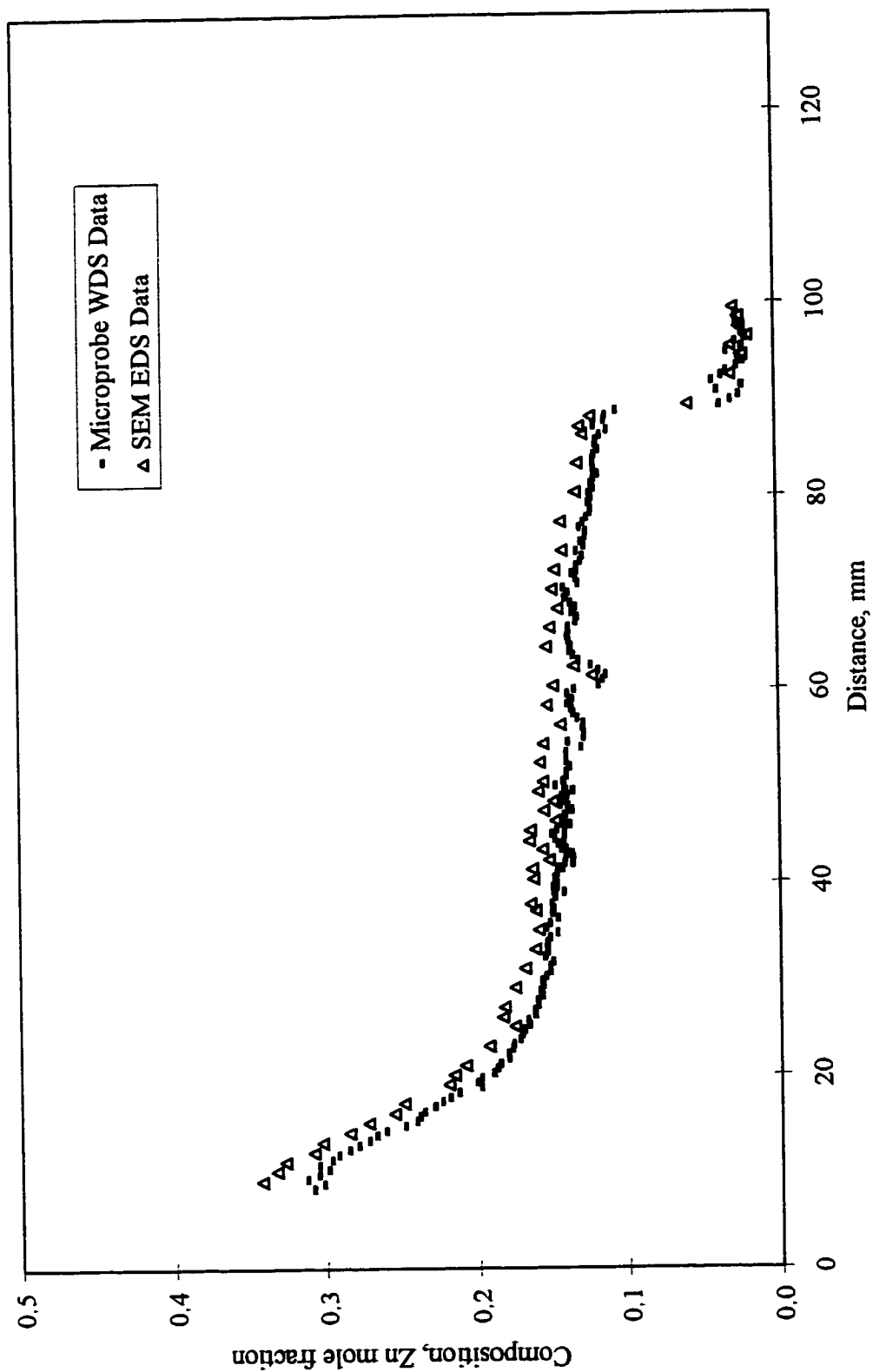


Figure 5-3. Centerline composition profiles of MZS-5 from EDS and WDS measurements.

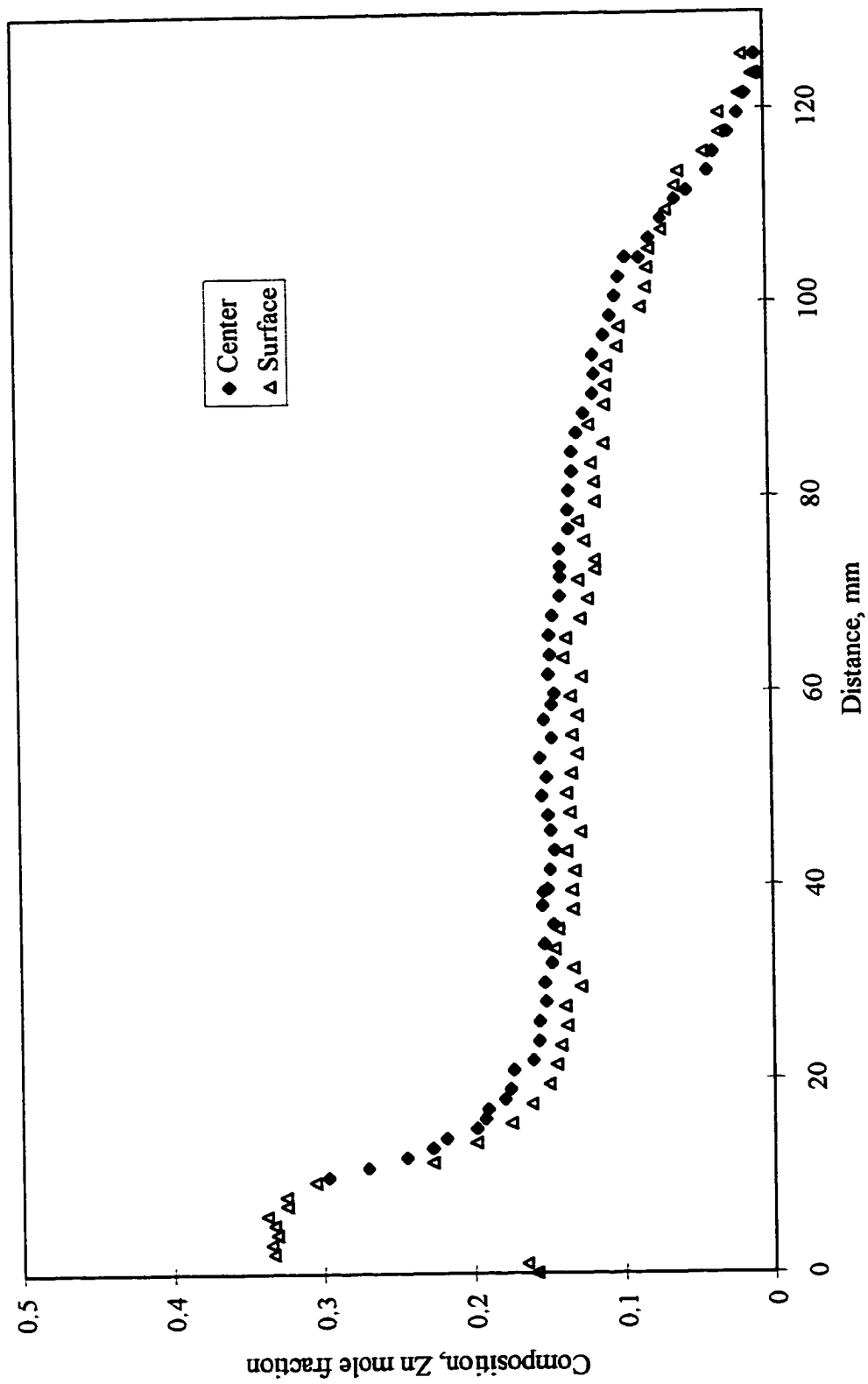


Figure 5-4. Surface and centerline composition profiles of MZS-7 from EDS measurements.

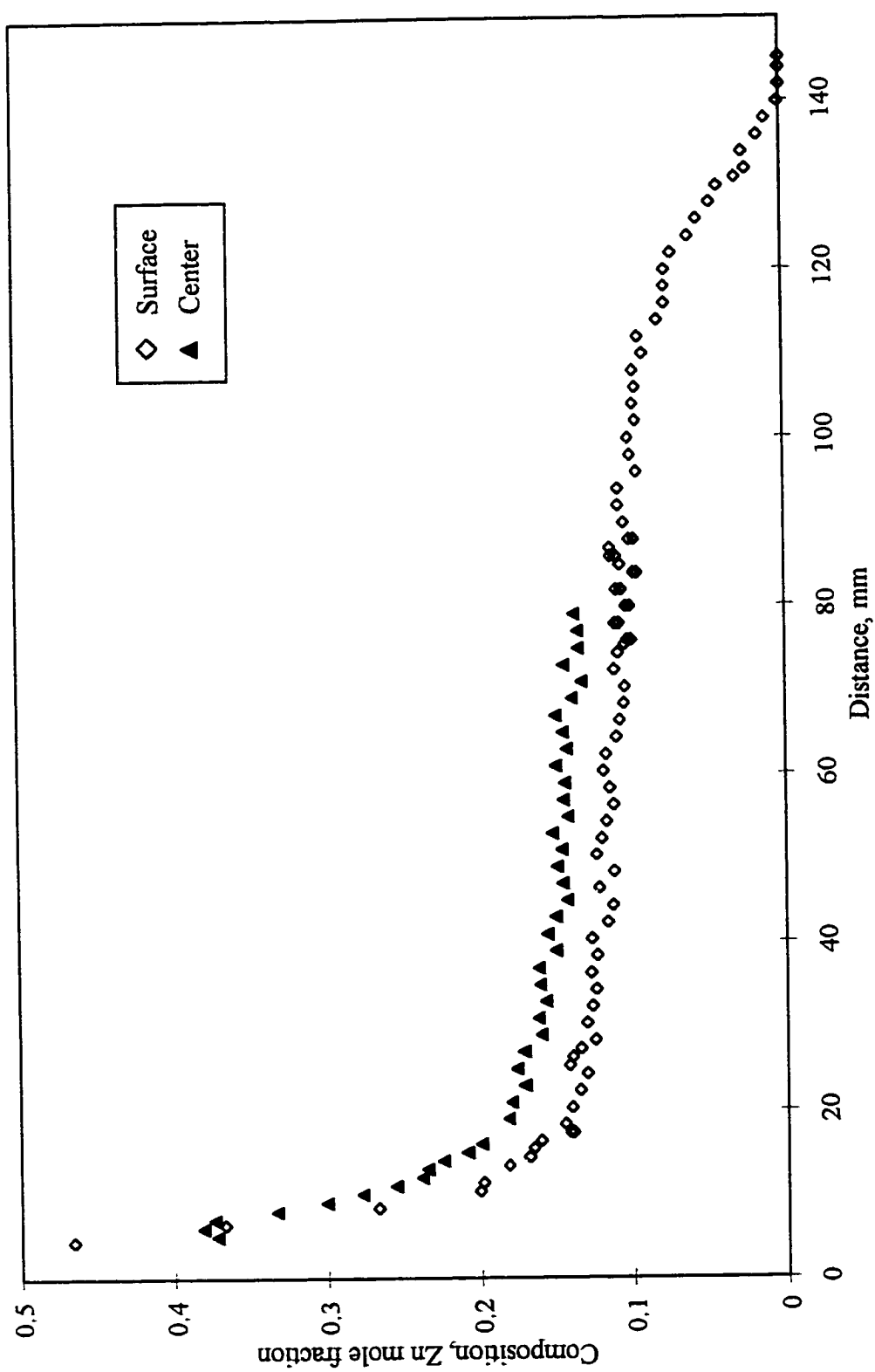


Figure 5-5. Surface and centerline composition profiles of MZS-8 from EDS measurements.

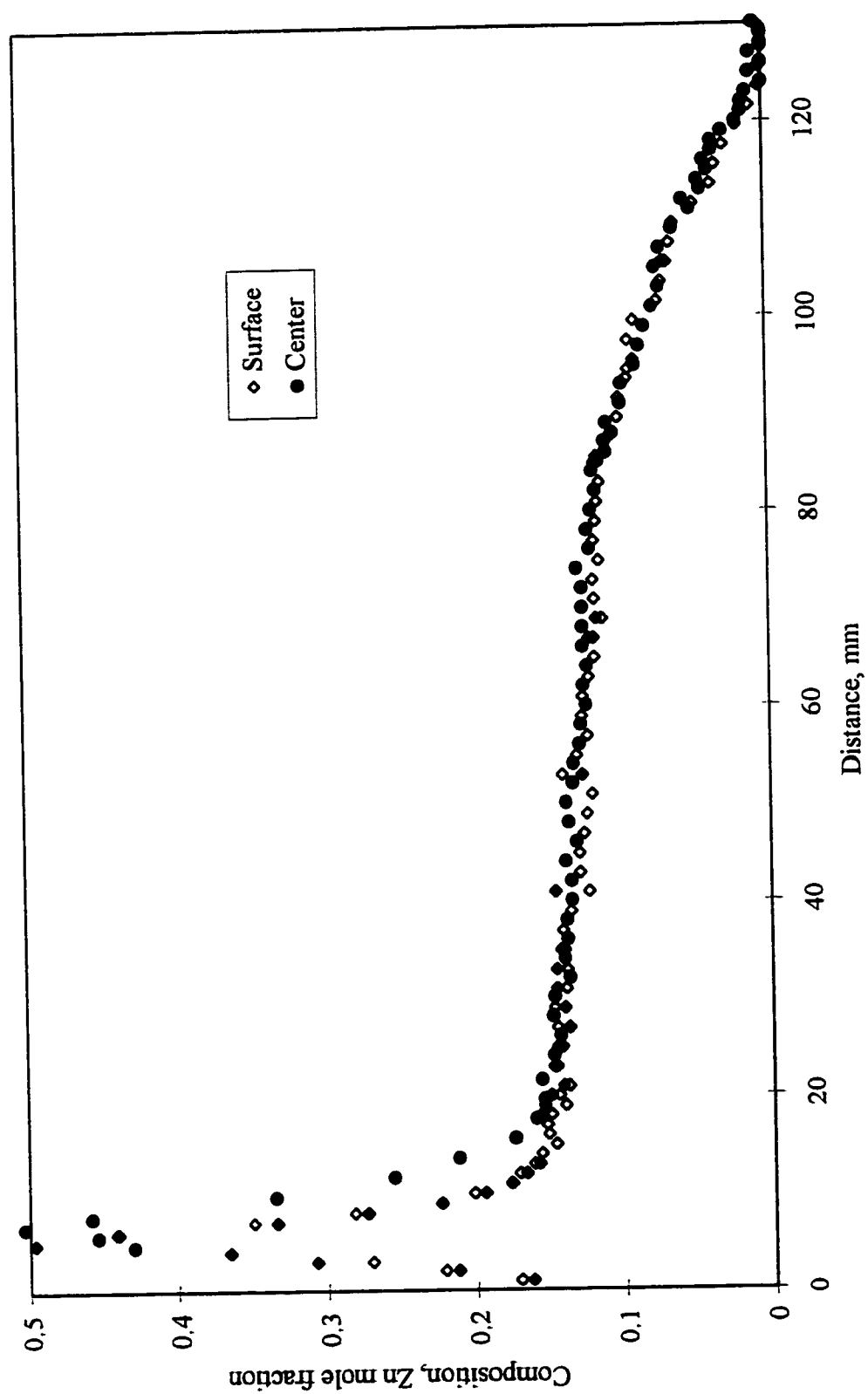


Figure 5-6. Surface and centerline composition profiles of MZS-10 from EDS measurements.

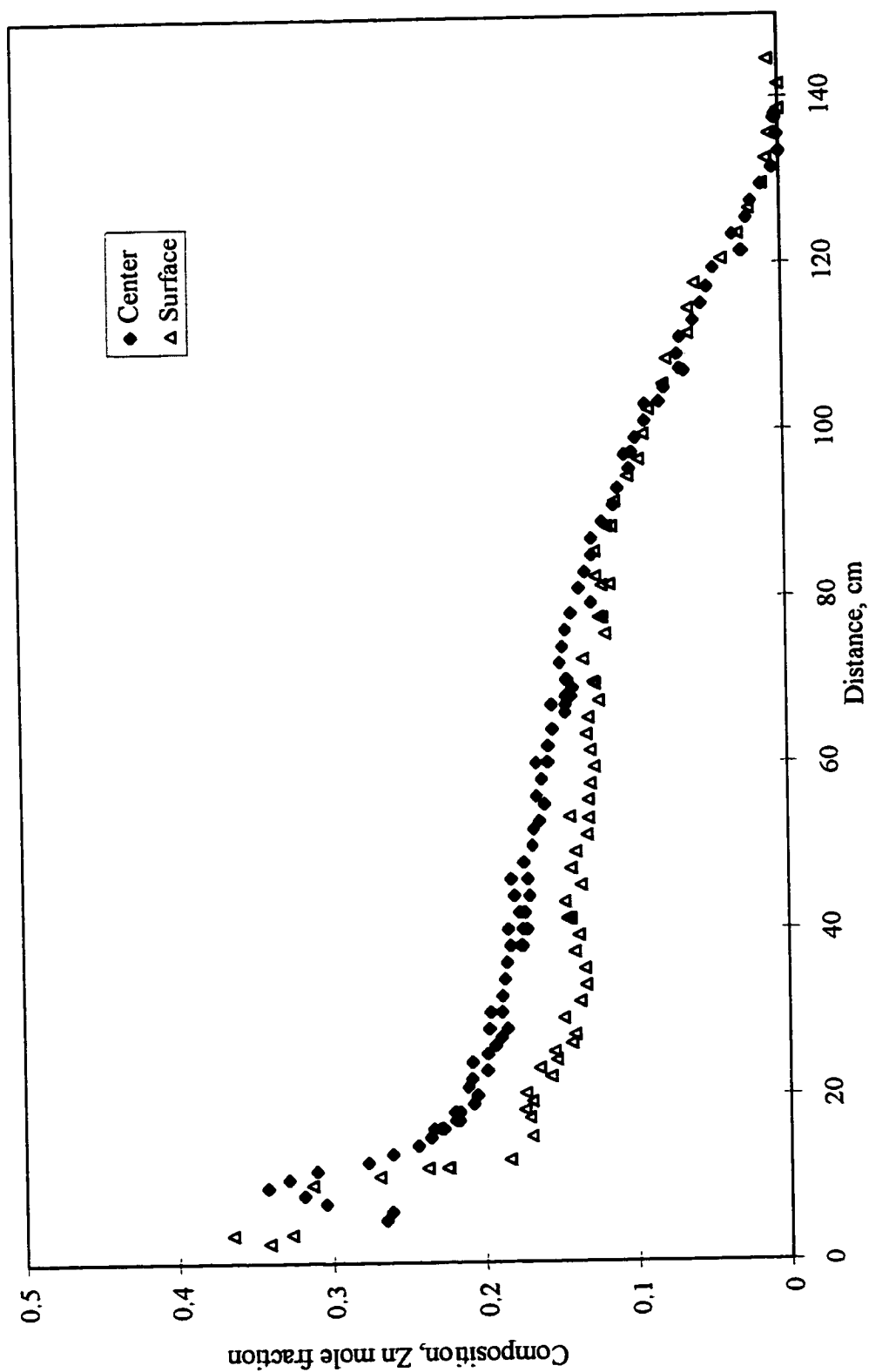


Figure 5-7. Surface and centerline composition profiles of MZS-11 from EDS measurements.

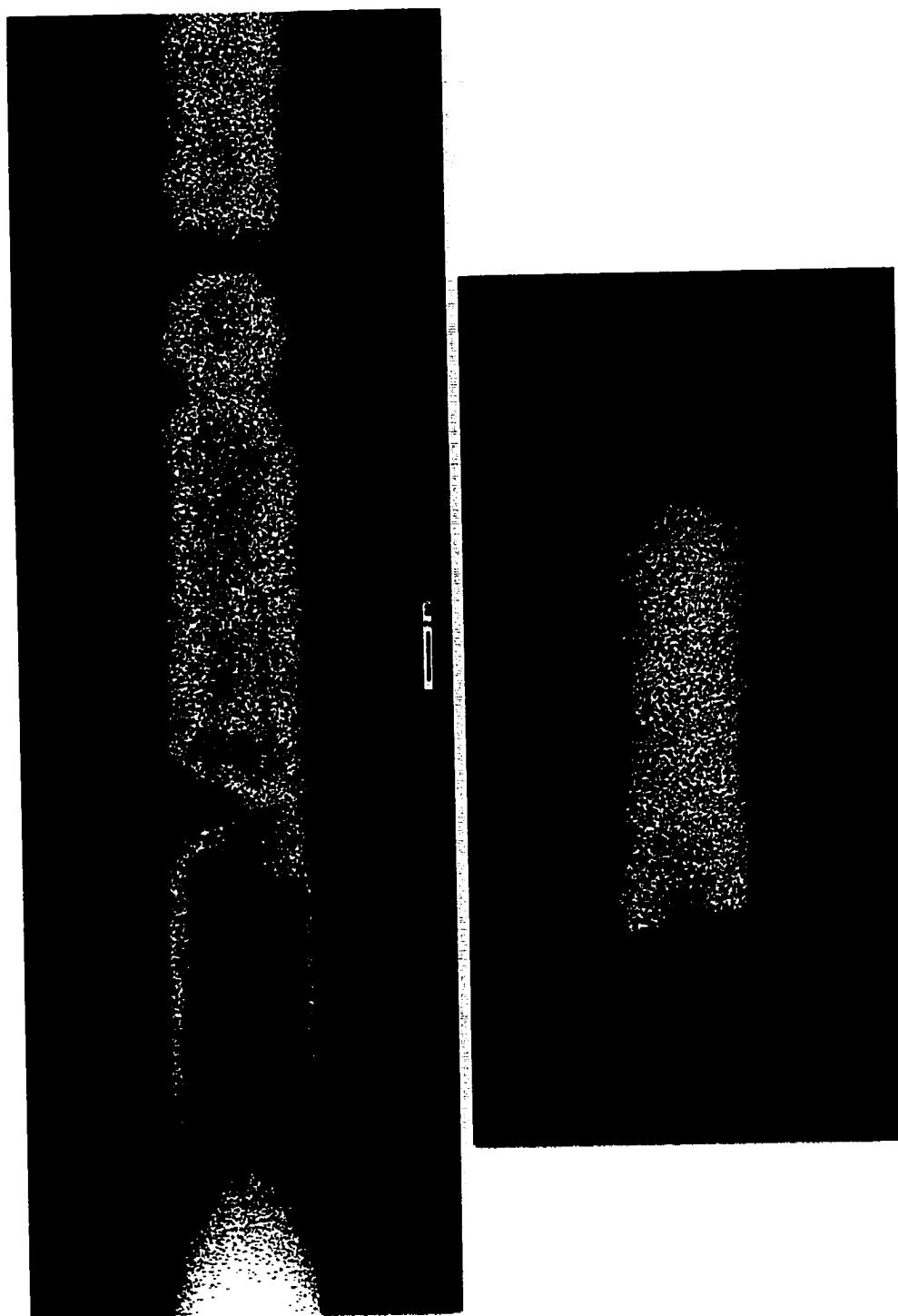


Figure 5-8. Compositional intensity of MZS-5 by microprobe mapping, showing heater power fluctuations and interface shape.
Growth direction is from left to right and top to bottom.

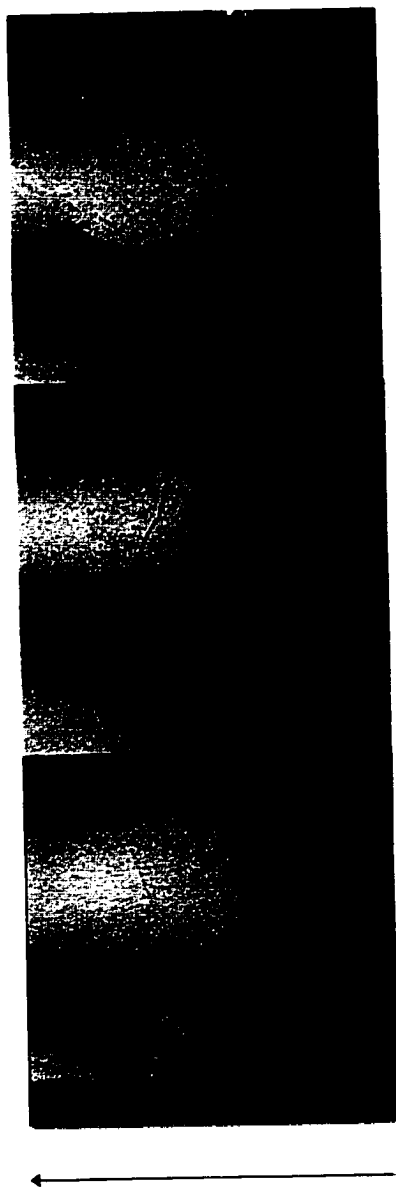


Figure 5-9. Backscatter image of quenched interface of MZS-2. Arrow indicates growth direction.

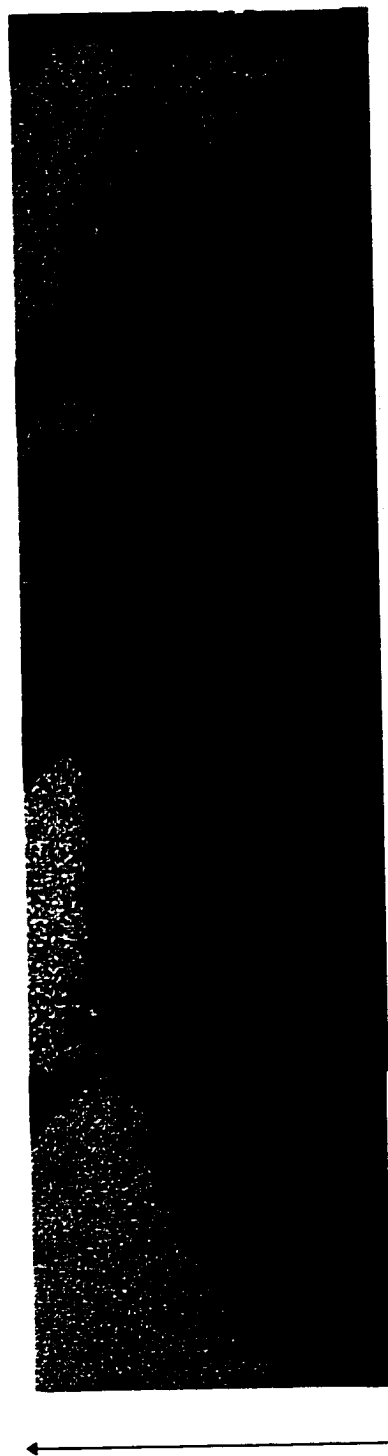


Figure 5-10. Backscatter image of quenched interface of MZS-5. Arrow indicates growth direction.

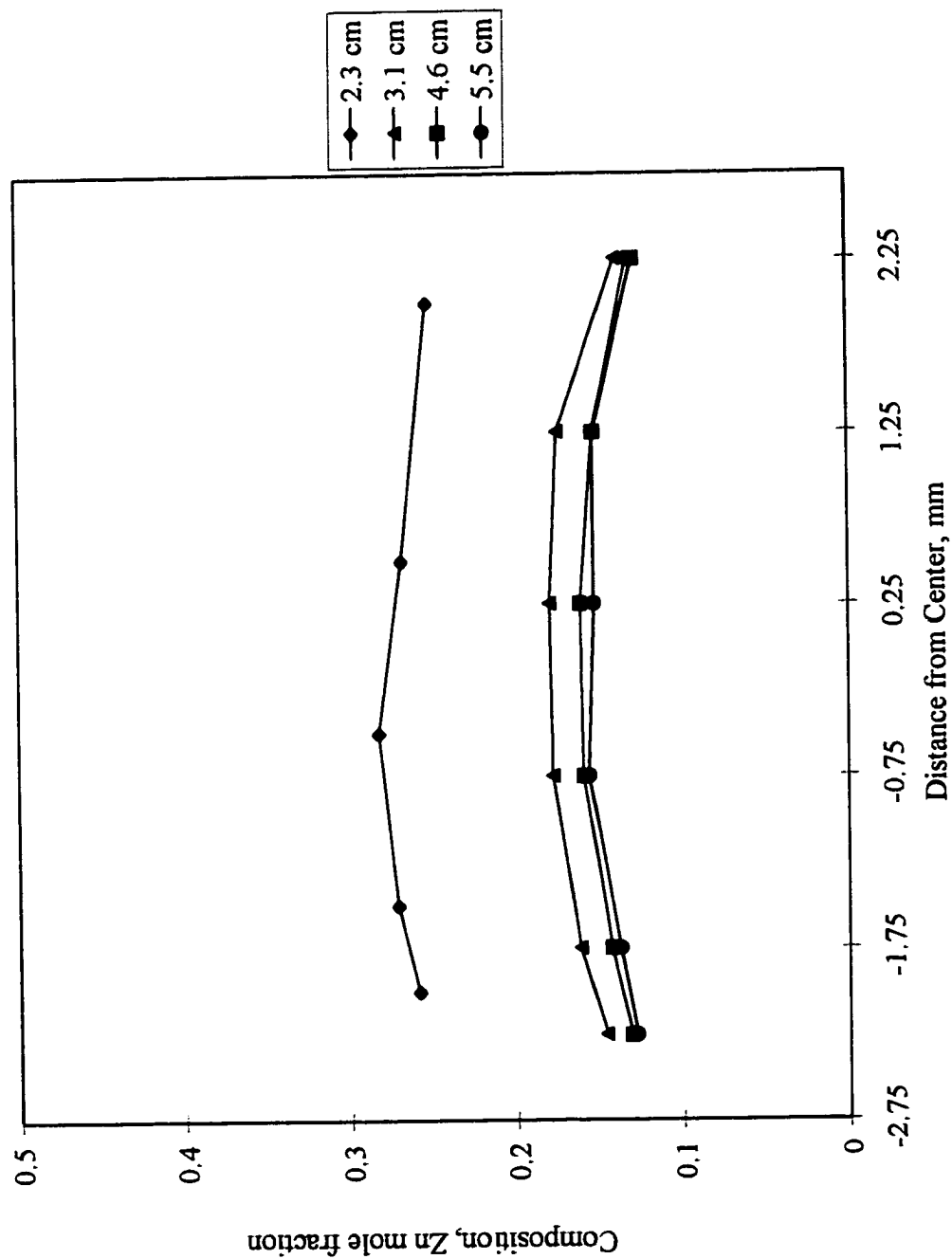


Figure 5-11. Radial composition variations by EDS in MZS-2 at stated distance from first to freeze tip.

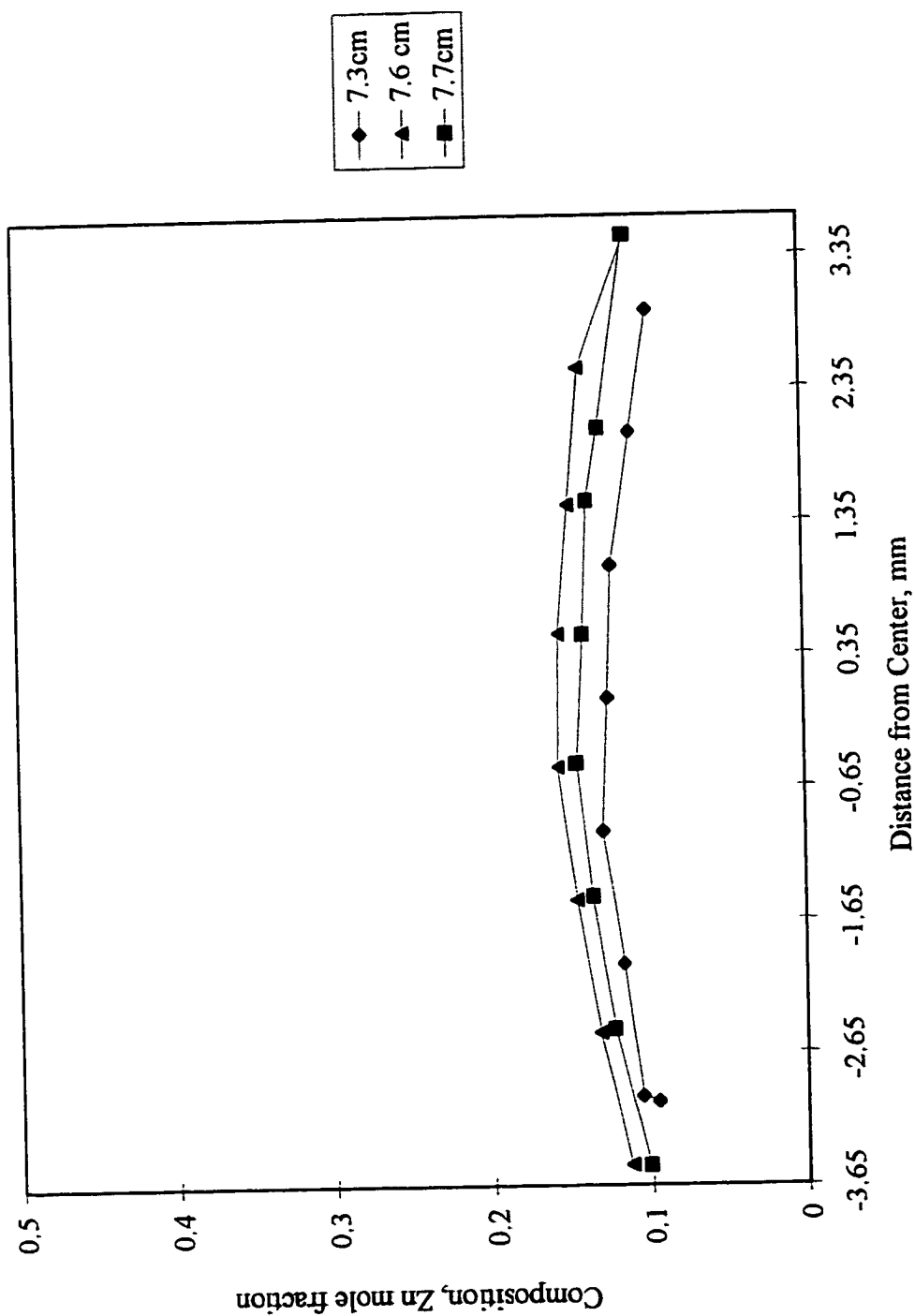


Figure 5-12. Radial composition variations by EDS in MZS-5 at stated distance from first to freeze tip.

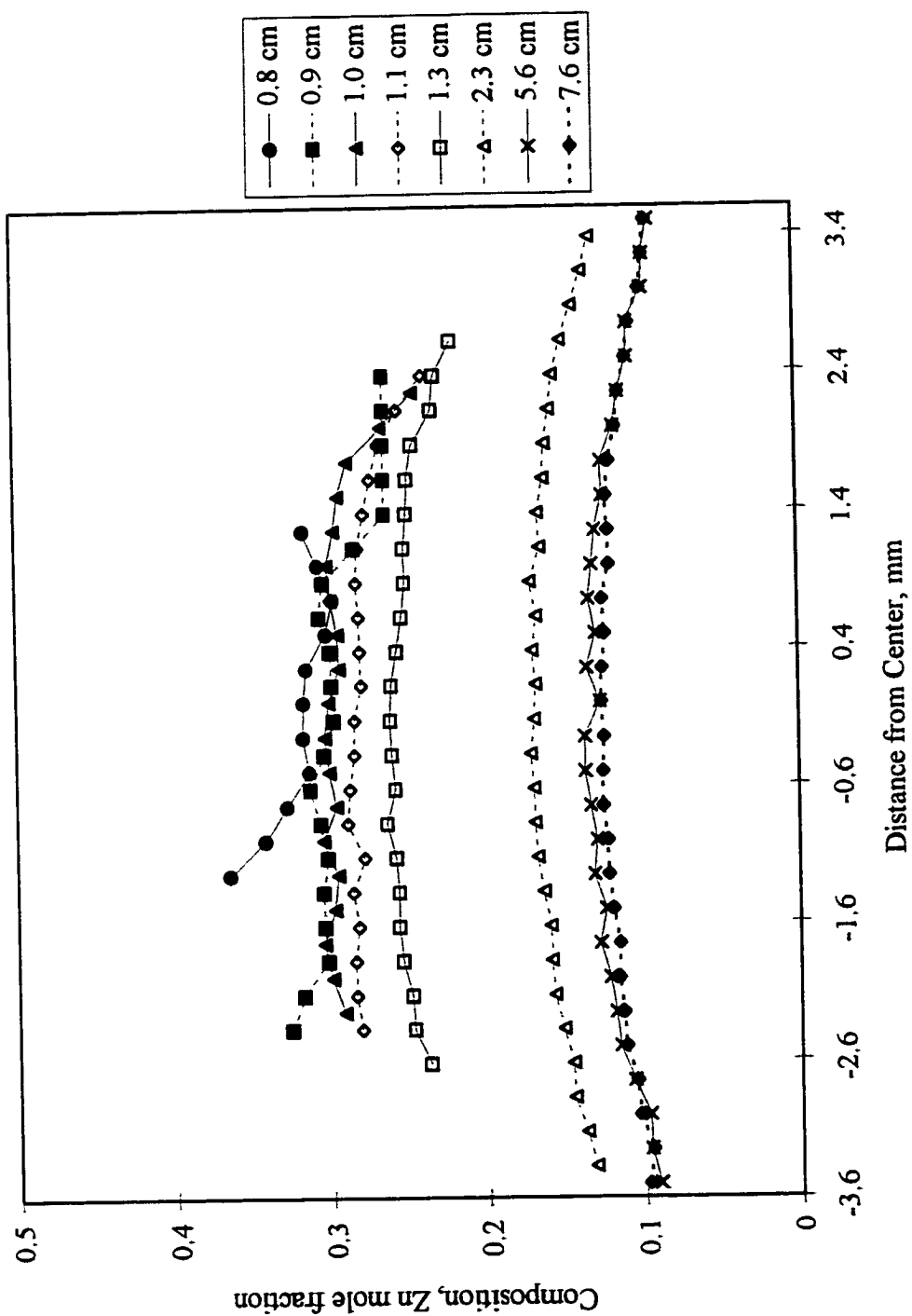


Figure 5-13, Radial composition variations by WDS in MZS-5 at stated distance from first to freeze tip.

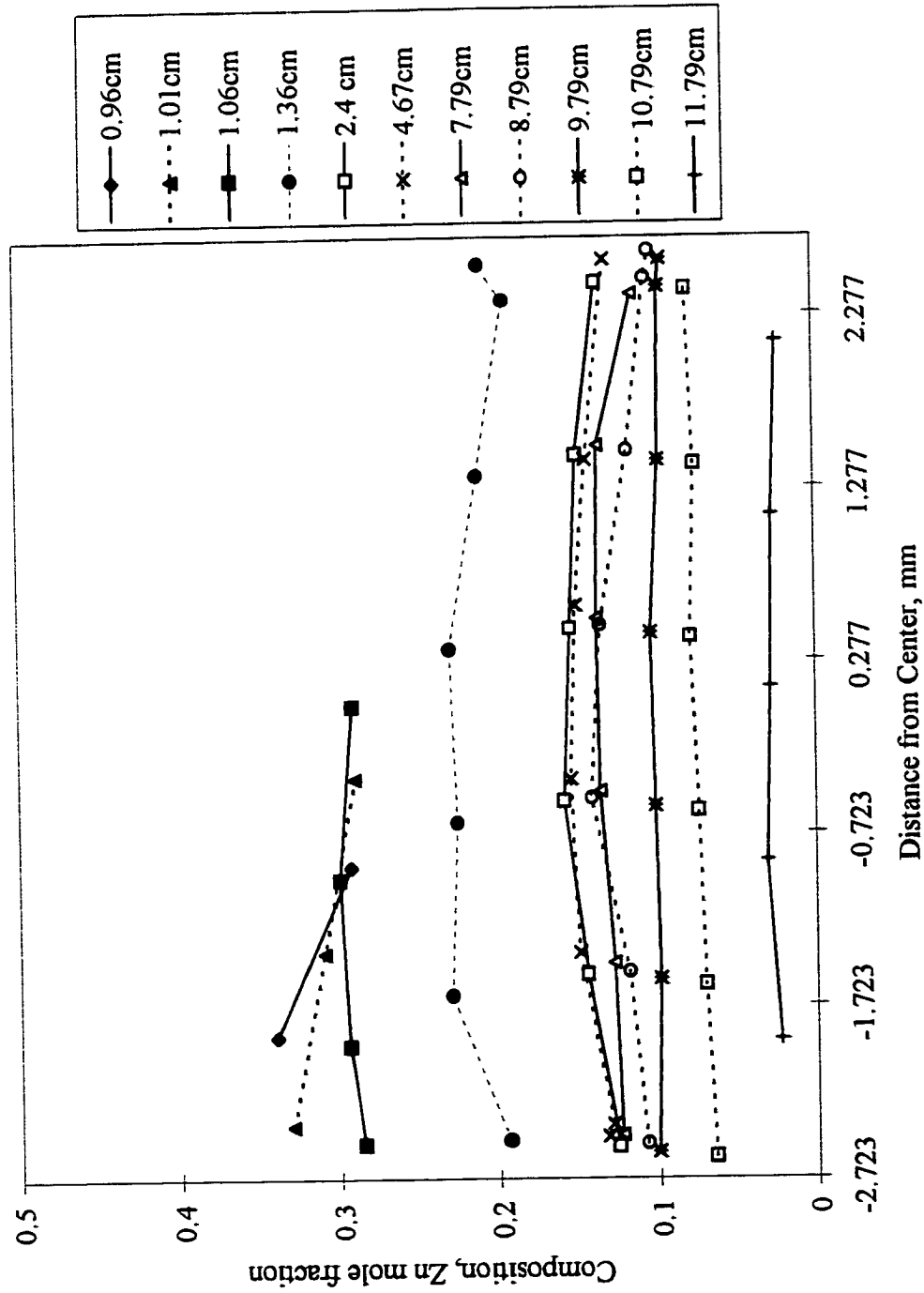


Figure 5-14. Radial composition variations by EDS in MZS-7 at stated distance from first to freeze tip.

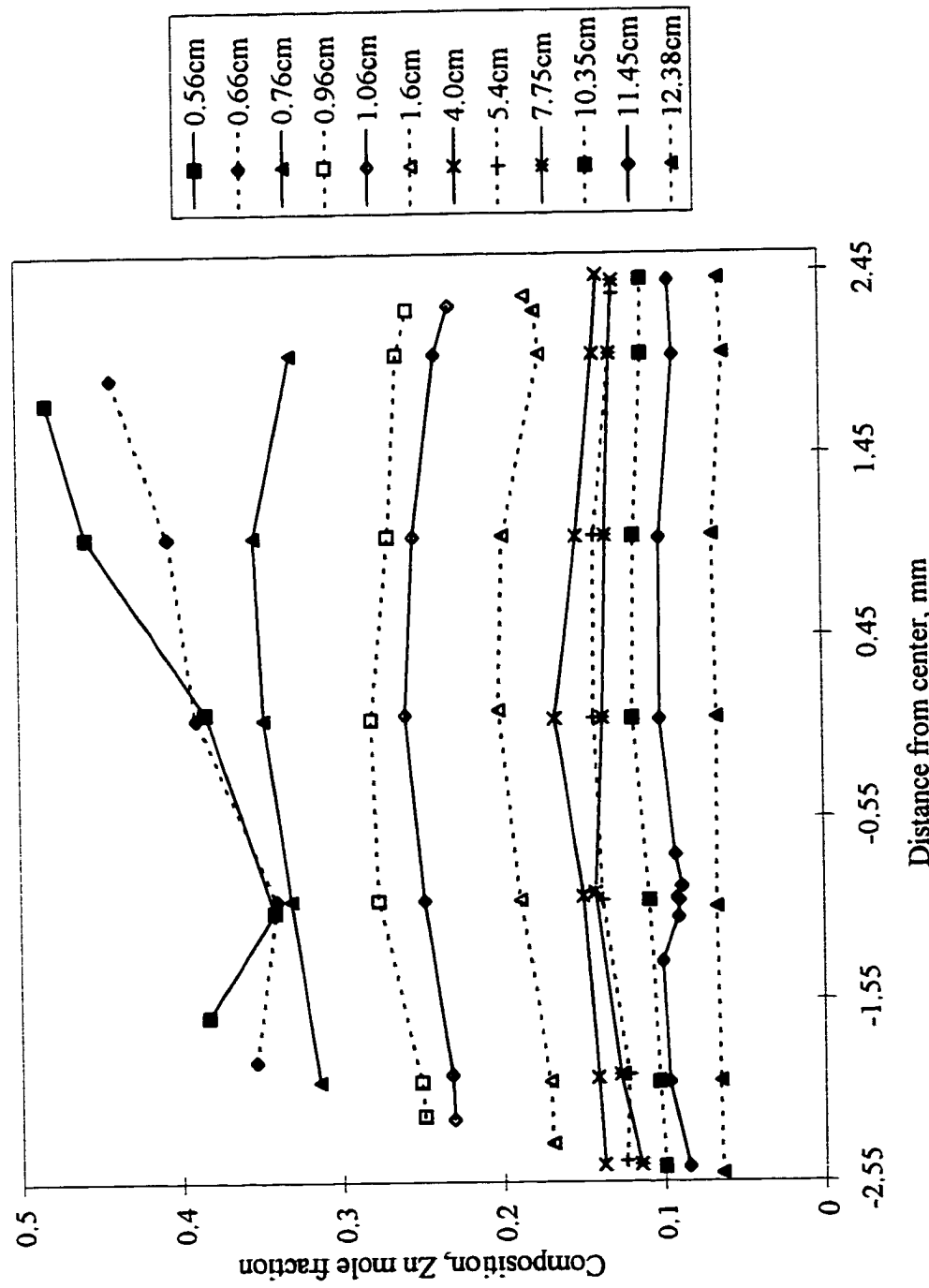


Figure 5-15, Radial composition variations by EDS in MZS-8 at stated distance from first to freeze tip.

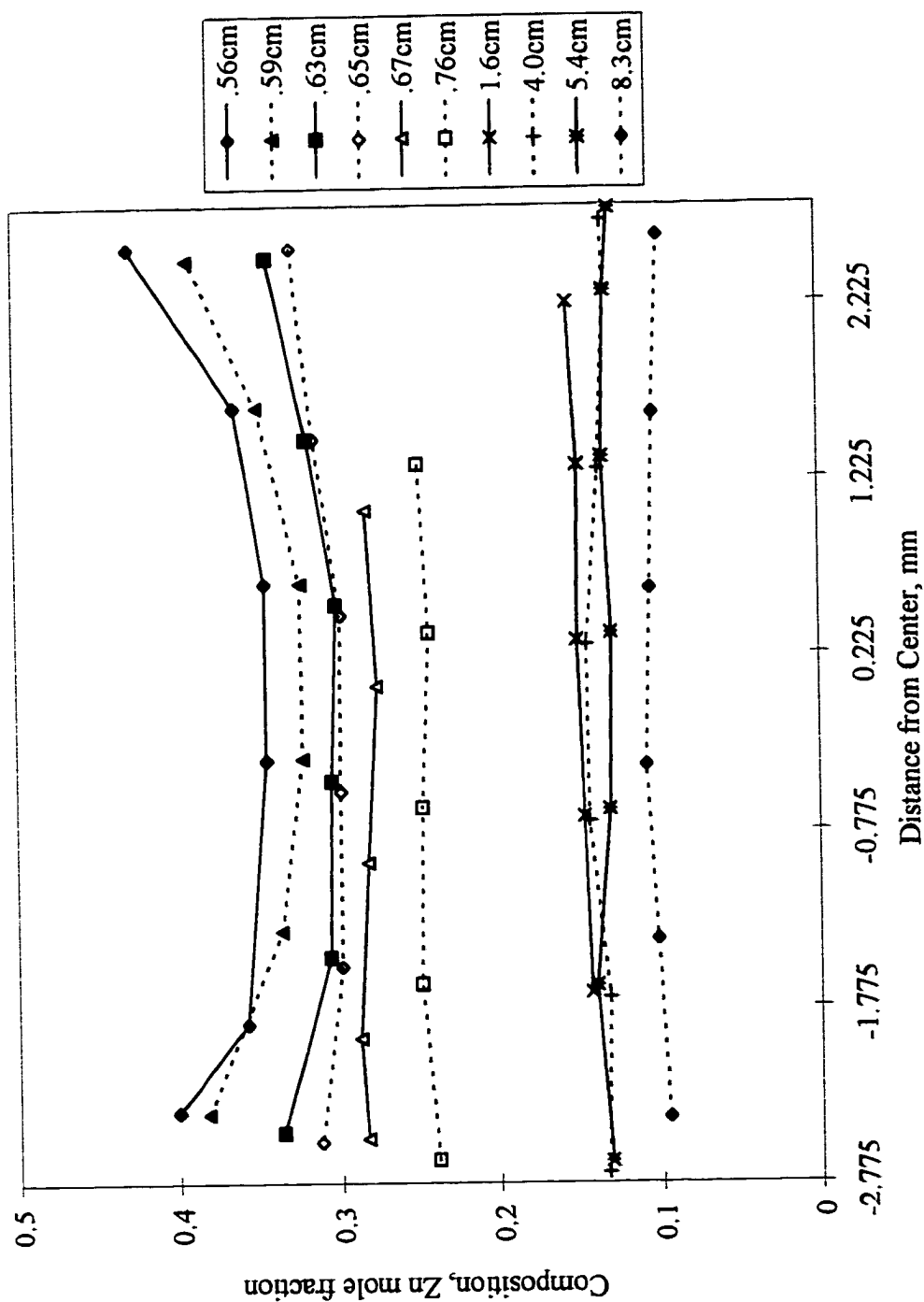


Figure 5-16. Radial composition variations by EDS in MZS-10 at stated distance from first to freeze tip.

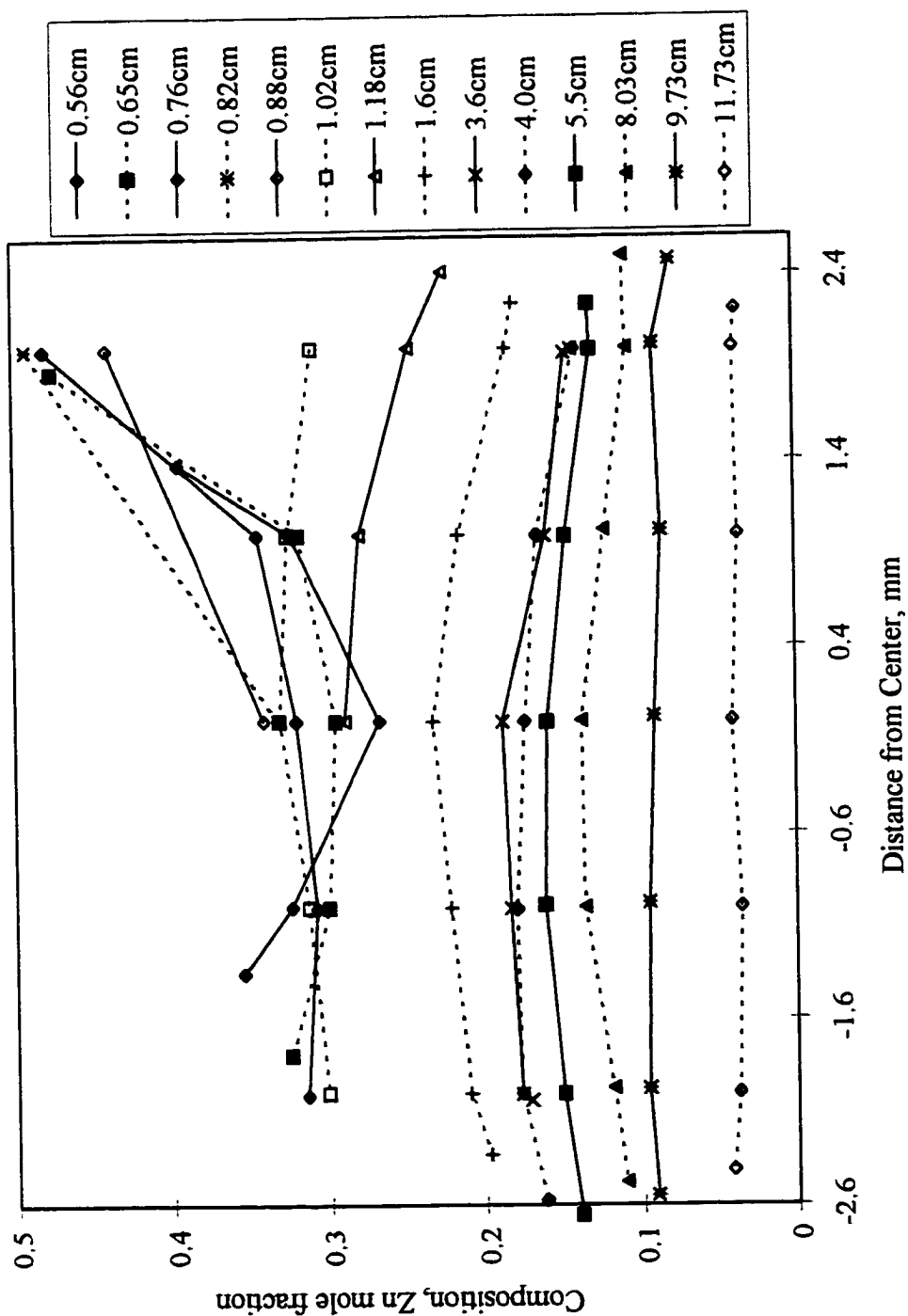


Figure 5-17. Radial composition variations by EDS in MZS-11 at stated distance from first to freeze tip.

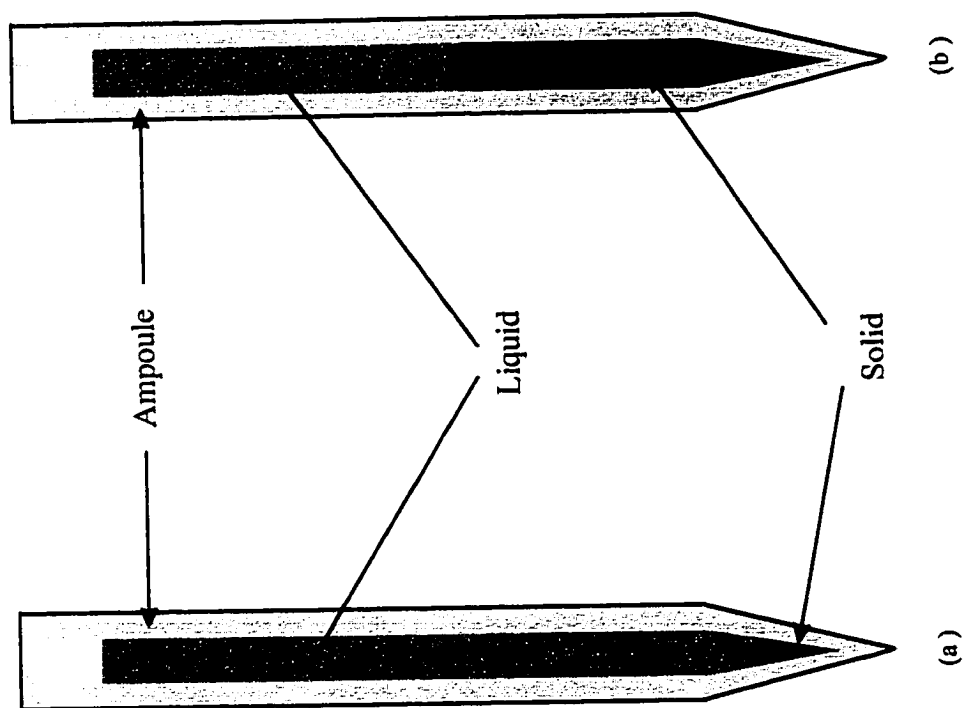


Figure 5-18. Illustration of change in shape during directional solidification: (a) tip region, (b) steady state growth.

CHAPTER 6

DISLOCATION GENERATION DURING DIRECTIONAL SOLIDIFICATION

Crystals produced by solidification from a molten liquid, generally contain significant densities of structural defects. These can include surface defects, point defects, volume defects and linear defects. Because the electrical performance of semiconductor materials is degraded by the presence of most defects, it is important to understand the relative number of these defects and how this number can be reduced by appropriate choice of processing parameters. A number of investigations in the $\text{Hg}_{1-x}\text{Zn}_x\text{Se}$ system have focused on the type and source of point defects in this system, however, no data exists on the distribution and sources of dislocations in this system. The dislocation density, based on the number of etch pits formed by chemical etching, was measured for slices taken from approximately the same distance from the first-to-freeze tip of five ingots. First, general trends in etch pit formation were documented. Then, the etch pit density in ingots with different ampoule preparation and growth environments was compared. Finally, the etch pit density was compared with similar II-VI alloys to determine if the increased bond strength due to Zn additions increased the alloy's resistance to dislocation formation.

The termination of a dislocation at a crystal surface results in an area of increased elastic energy. Chemical etchings applied to the surface result in the formation of pits because these areas of increased energy provide nucleation sites for dissolution. The

correlation between etch pits and dislocations has been used to estimate dislocation density for many years, dating back to as early as 1953 when Vogel et al. (1953) noted the one-to-one correlation in germanium.

A method for polishing and etching to reveal dislocation etch pits was developed for $\text{Hg}_{1-x}\text{Zn}_x\text{Se}$ for $x = 0.1$ alloys. Crystallographic planes of different orientation are known to respond differently to different chemical etchings. Etching some planes results in different shaped pits, and for some systems, certain crystallographic planes do not respond at all to certain etchants. To eliminate variations in etching rates and characteristics among the ingots, samples were cut along the $\{111\}$ surface.

Surface Preparation for Etch Pit Study

Each crystal ingot had previously been cut along the center axis to allow mapping of grain structure and compositional variations. Radial slices oriented to the $\{111\}$ were cut from one half of each ingot. Samples were oriented using a back reflection Laue x-ray camera and a goniometer stage. The goniometer stage was transferred to a wire saw, where samples two millimeters thick were cut from each crystal.

Oriented samples were mounted to a glass plate with CrystalBond® adhesive. Initially, damage to the surface from the cutting step was removed by grinding on 600 grit paper. Intermediate polishing was accomplished, by hand, using progressively finer diamond paste on appropriate cloths mounted to polishing wheels. Buehler nylon cloth was used for 6 μm diamond paste, followed by 3 and 1 μm paste on medium nap felt. A final polish was accomplished using a 78:19:3 solution of distilled water, colloidal silica

and sodium hyposulphate on medium-nap felt. Intermediate polishing with alumina slurries was investigated, but produced only progressively finer scratches.

Samples from each crystal were polished as described above and etched, but the etch pit size was not uniform or completely reproducible. It was discovered, when examining samples in the SEM at 70° to verify orientation by electron backscatter diffraction, that extremely fine scratches still existed on the surface. These scratches were not visible with the eye or in the SEM with the beam perpendicular to the sample surface. Eventually a procedure was developed to automate the procedure, reduce the number of required steps, and remove the final layer of mechanical damage.

Several microns were removed from the surface of each sample using a Logitech automated lapping machine with $3\mu\text{m}$ alumina slurry on a Buehler medium-nap cloth. Final chemical-mechanical polishing was performed on the same equipment but with a slurry of colloidal silica, distilled water and sodium hyposulfite as described above. Samples were removed from the glass plate, and the adhesive was removed with acetone. Samples had to be immediately immersed in isopropanol to prevent the acetone from damaging the surface finish. A final chemical polish by hand using 2% Br_2 in ethylene glycol on a medium-nap pad was required to remove all mechanical damage. Samples were rinsed in acetone, followed immediately by isopropanol and distilled water.

Selection of Appropriate Etchant

A literature search did not yield information on suitable etchings $\text{Hg}_{1-x}\text{Zn}_x\text{Se}$ alloys. Initial etchants investigated were those used to produce pits on HgSe and ZnSe binary alloys. Table 6-1 summarizes the results of various etchant compositions. Initially, the

only successful etchant was that described by Parker and Pinnel (Parker and Pinnel, 1971). Etch pits were produced at times of 7-13 minutes on the $\{111\}$ surface. The morphology of the pits was extremely rounded. Rounded etch pits have also been observed in III-V alloy systems (Sangwal, 1987). It is thought that rounded or circular etch pits are related to diffusion during the dissolution process. It has also been found that slow etchants often produce rounded pits, while fast etches produce crystallographic pits (Sangwal, 1987). The time required to produce pits with Parker's etch on $\text{Hg}_{1-x}\text{Zn}_x\text{Se}$ is considered extremely slow.

It was initially thought that an etch described by Polisar et al. (1968) destroyed the surface of the sample. The etchant was composed of 90:60:25:5 distilled water, nitric acid, hydrochloric acid, 0.1cc Br_2 in acetic acid. It was later discovered that this etchant produced a Se surface film that could be removed with 1-2 second rinse in a 2% Br_2 in methanol solution. This was followed by a brief methanol rinse, then by distilled water. The Polisar etch produced a uniform surface film at times of 1.75-2.25 minutes. The best results were achieved by immersing the sample until a uniform Se film developed over the entire surface, then removing the film. The etch pits produced by this method were triangular with slightly rounded edges.

Method for Determining Etch Pit Density

Images of each sample were taken in a SEM at a 100x magnification across the entire surface of each sample. Each image was reduced and combined to form a collage showing the overall pit distribution. A collage for each sample is shown in Figures 6-1 through 6-14. An etch pit density for each image was determined by counting the number

of etch pits and dividing by the area of the image. On images where etch pits were considerable different in size, only the largest pits with consistent size were counted. The etch density along with its location on the sample is listed for each crystal in Tables 6-2 through 6-15.

Table 6-1. Summary of etchant study.

Designation	Components	Ratio	Time/ Temperature (°C)	Results
Warekois (a) Chemical Polish HgSe	HNO ₃ :Acetic:HCl: 18 N H ₂ SO ₄	50:10:1:20	10-15 minutes/40	Rough dull finish
Warekois (b)	HCl:HNO ₃ :H ₂ O	6:2:3	2-5 minutes/25	Copper colored finish
ZnSe	Br ₂ :CH ₃ OH			Destroyed surface
ZnSe	HCl: H ₂ O			No effect
Parker	HNO ₃ : HCl: H ₂ O: 5%Br ₂ in CH ₃ OH	60:4:60:4	5-10 minute/25	Round etch pits
Polsar	H ₂ O: HNO ₃ : HCl: 0.1 cc Br ₂ in acetic	90:60:25:5	1-2.5 minutes/25	Se film removed with 5%Br ₂ in CH ₃ OH. Consistent.

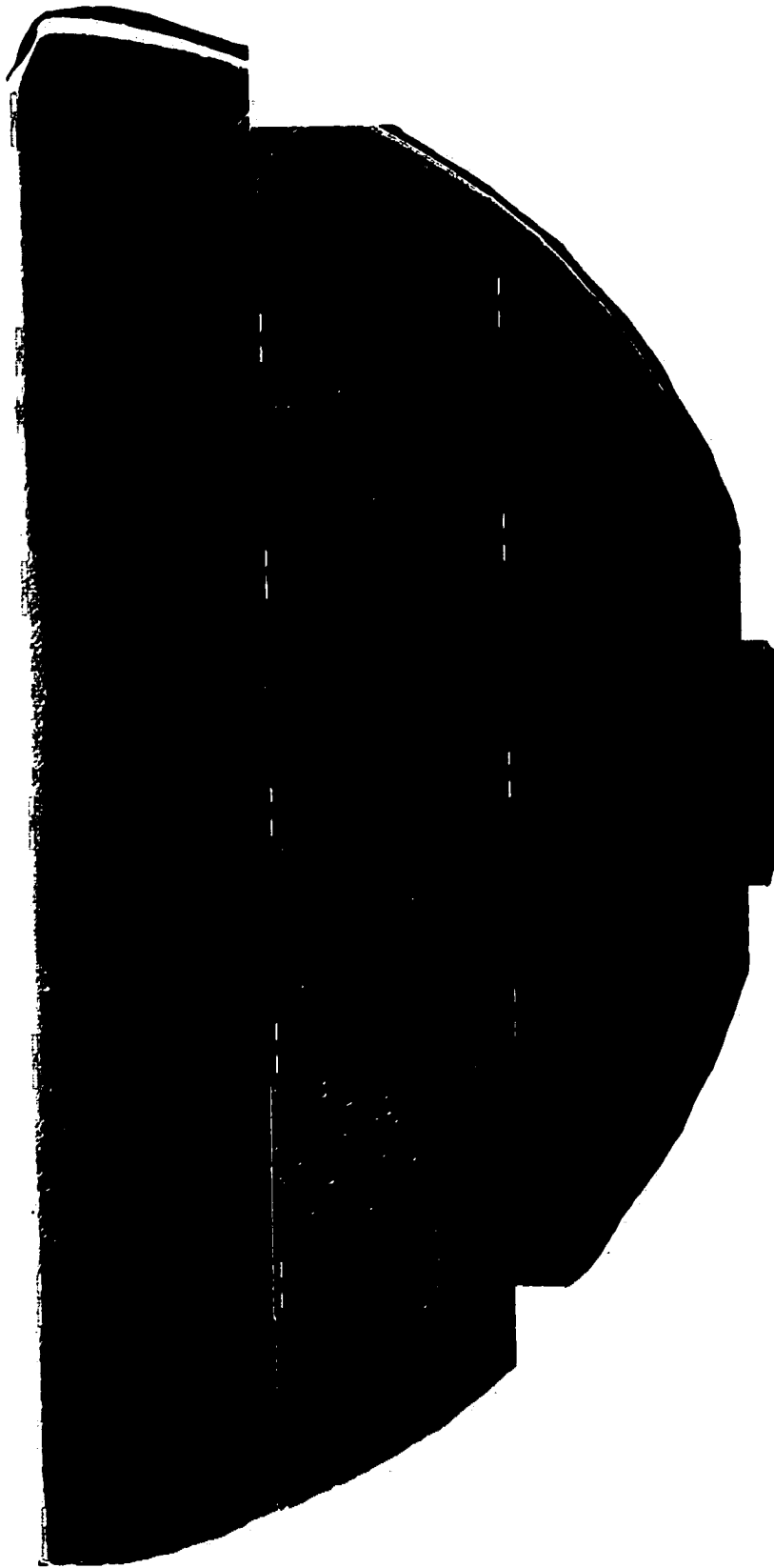


Figure 6-1. Etch pit distribution on MZS 2-1 (5.8cm).

Table 6-2. MZS 2-1 (5.8cm).

Sample Name	Location	EPD (#/cm ²)
a	top edge	3.00E+04
b	top	2.73E+04
c	top	1.50E+04
d	top	1.80E+04
e	top	1.14E+04
f	top	3.13E+04
g	top edge	8.09E+04
h	middle edge	1.01E+05
i	middle	1.22E+04
j	middle	1.15E+04
k	middle	1.05E+04
l	middle	1.64E+04
m	middle edge	1.98E+04
n	ampoule edge	7.91E+03
o	ampoule edge	1.51E+04
p	ampoule edge	9.86E+03
q	ampoule edge	7.40E+03
p2	ampoule edge	1.22E+04

Table 6-3. MZS 2-2 (5.4 cm).

Sample Name	Location	EPD (#/cm ²)
a	top edge	1.16E+04
b	top	1.10E+04
c	top	9.84E+03
d	top	1.26E+04
e	top	5.60E+03
f	top	5.18E+03
g	top edge	1.34E+04
h	middle edge	1.49E+04
i	middle	7.99E+03
j	middle	9.24E+03
k	middle	6.99E+03
l	middle	7.86E+03
m	middle edge	1.05E+04
n	middle edge	1.70E+04
o	middle 2 edge	1.28E+04
p	middle 2	1.42E+04
q	middle 2	6.24E+03
r	middle 2	8.86E+03
s	bottom edge	1.04E+04
t	bottom edge	1.37E+04
u	bottom edge	1.27E+04
v	bottom edge	2.86E+04

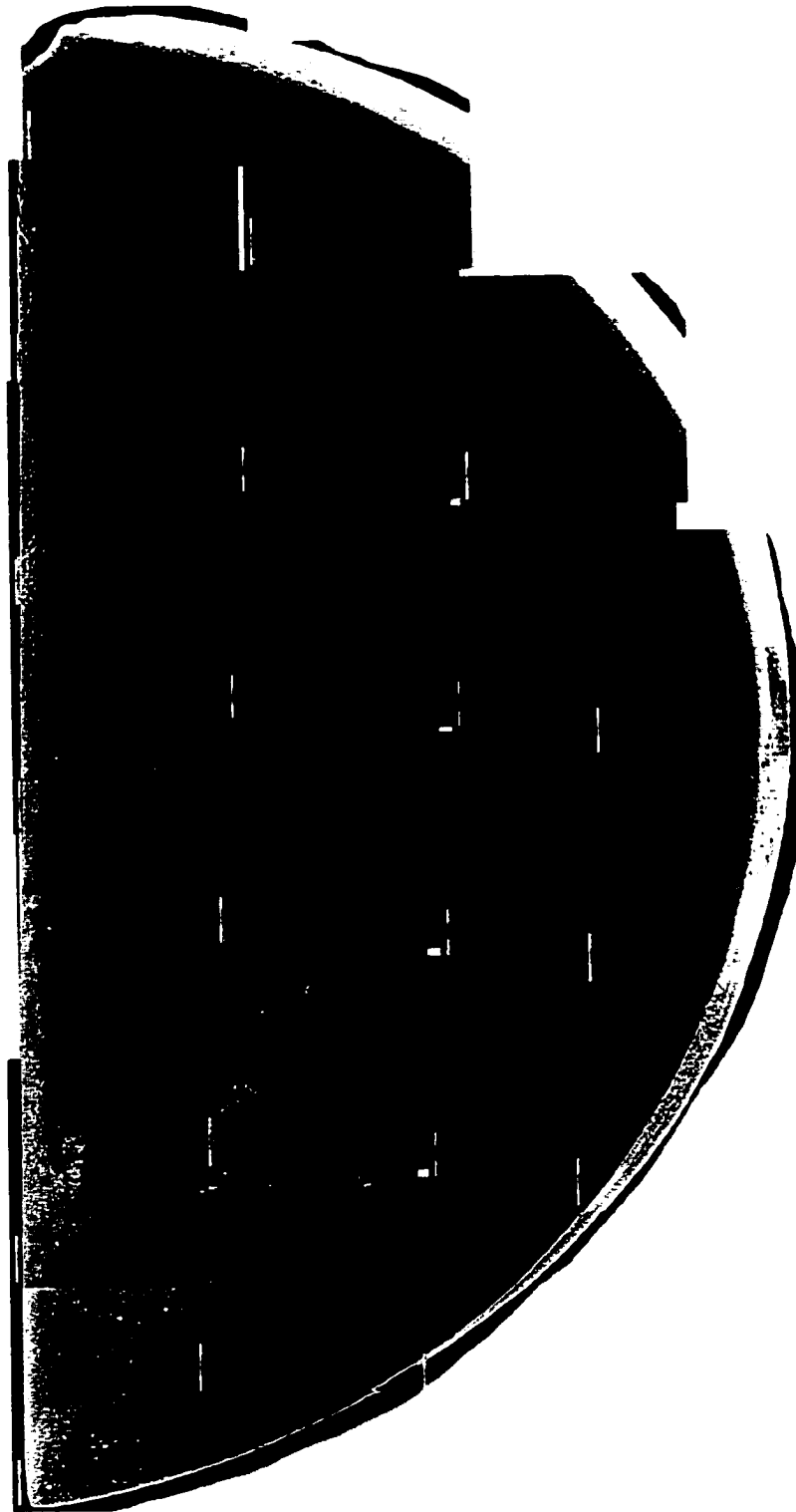


Figure 6-2. Etch pit distribution on MZS 2-2 (5.4 cm).



Figure 6-3. Etch pit distribution on MZS 2-5 (4.7cm).

Table 6-4. MZS 2-5 (4.7cm).

Sample Name	Location	EPD (#/cm ²)
a	top edge	3.38E+04
b	top	3.13E+04
c	top	2.21E+04
d	top	4.21E+04
e	top	1.48E+04
f	top	1.22E+04
g	top edge	2.80E+04
h	middle edge	8.90E+03
i	middle	6.49E+03
j	middle	6.70E+04
k	middle	8.11E+04
l	middle	8.71E+04
m	middle edge	1.65E+05
ll	middle 2 edge	1.02E+04
kl	middle 2	2.07E+04
jl	middle 2	3.55E+04
il	middle 2	9.61E+03
hl	middle 2 edge	4.62E+03
n	bottom edge	1.44E+05
o	bottom edge	5.74E+04
p	bottom edge	2.56E+04
q	bottom edge	4.71E+03

Table 6-5. MZS 5-2 (4.4cm).

Sample Name	Location	EPD (#/cm ²)
a	top edge	1.44E+04
b	top	6.40E+03
c	top	5.35E+03
d	top	4.70E+03
e	top	4.03E+03
f	top	6.86E+03
g	top	1.69E+04
h	top	
i	top	1.38E+04
j	top edge	
k	middle edge	2.13E+04
l	middle	5.24E+03
m	middle	5.62E+03
p	middle	3.75E+03
q	middle	4.24E+03
r	middle	4.62E+03
s	middle	3.75E+03
t	middle	6.37E+03
u	middle edge	1.18E+04
dd	bottom edge	1.52E+04
ee	bottom edge	1.34E+04
ff	bottom edge	5.87E+03
gg	bottom edge	4.87E+03
hh	bottom edge	4.49E+03
ii	bottom edge	4.62E+03
jj	bottom edge	8.49E+03
kk	bottom edge	8.84E+03

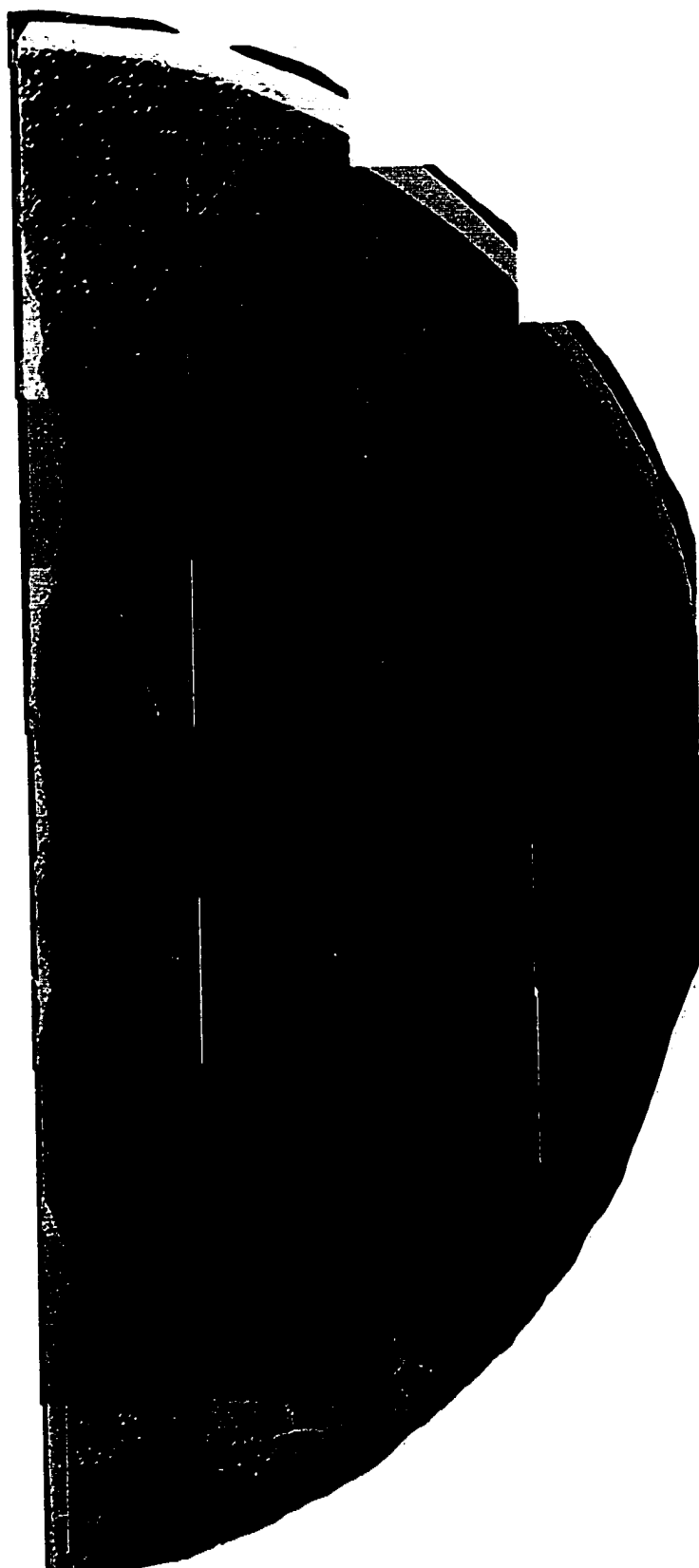


Figure 6-4. Etch pit distribution on MZS 5-2 (4.4cm).

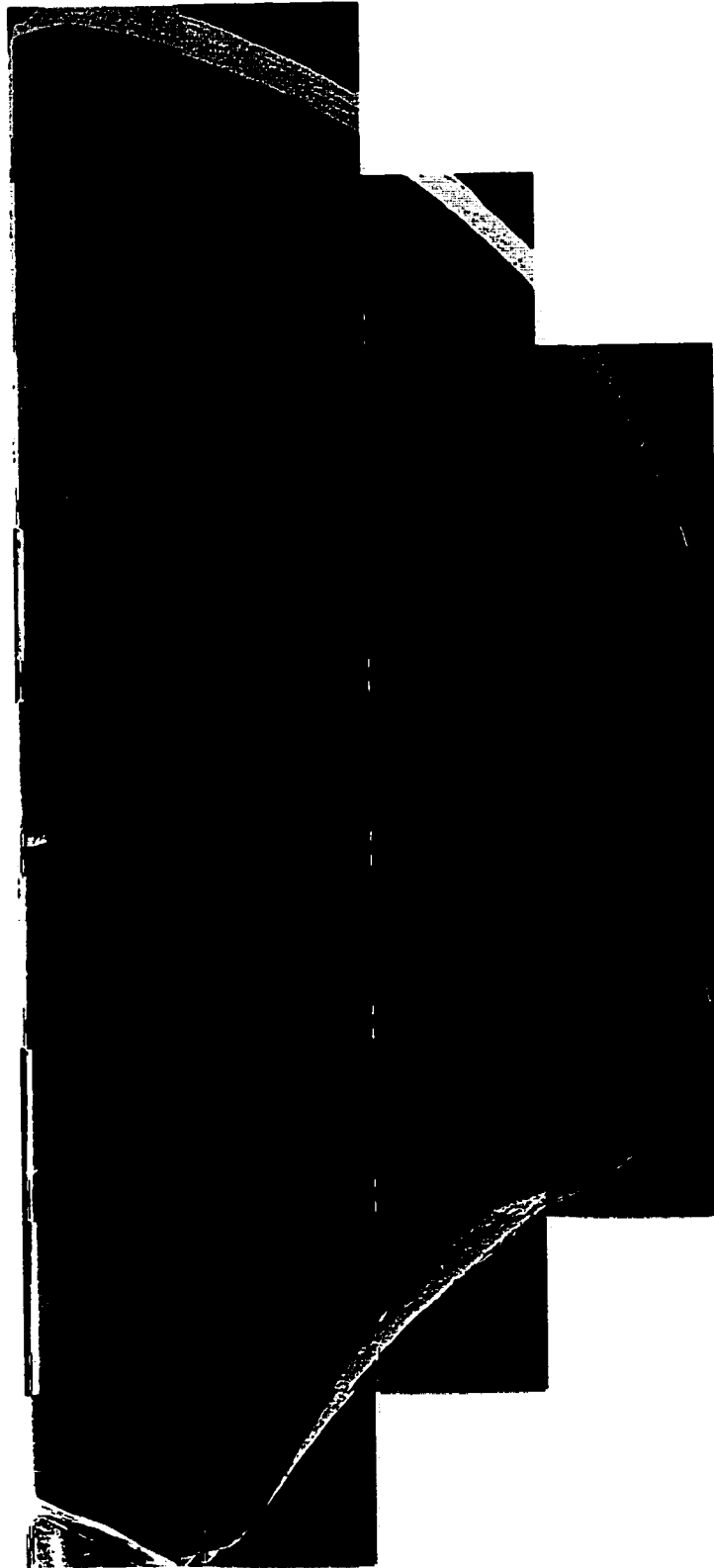


Figure 6-5. Etch pit distribution on MZS 5-5 (5.0cm).

Table 6-6. MZS 5-5 (5.0cm).

Sample Name	Location	EPD (#/cm ²)
a	top edge	
b	top	1.34E+04
c	top	1.12E+04
d	top	5.64E+03
e	top	6.83E+03
f	top	7.91E+03
g	top	4.99E+03
h	top	7.62E+03
i	top edge	3.83E+04
j	middle edge	1.61E+04
k	middle	5.24E+03
l	middle	1.75E+03
m	middle	3.62E+03
n	middle	5.74E+03
o	middle	4.87E+03
p	middle	9.74E+03
q	middle edge	2.60E+04
r	middle edge	2.92E+04
s	middle 2 edge	3.21E+04
t	middle 2 edge	5.21E+03
u	middle row 2	6.37E+03
v	middle 2	6.37E+03
w	middle 2	5.87E+03
x	middle 2	8.11E+03
y	middle 2 edge	8.15E+03
z	bottom edge	1.28E+04
aa	bottom edge	7.06E+03
bb	bottom edge	8.08E+03
cc	bottom edge	8.23E+03
dd	bottom edge	1.23E+04

Table 6-7. MZS 5-6 (5.2cm).

Sample Name	Location	EPD (#/cm ²)
a	top edge	7.78E+03
b	top	3.92E+03
c	top	2.44E+03
d	top	2.96E+03
e	top	3.99E+03
f	top	4.08E+03
g	top	2.42E+03
h	top	2.81E+03
i	top	4.85E+03
j	top edge	2.88E+04
k	middle edge	8.75E+03
l	middle	6.12E+03
m	middle	4.99E+03
n	middle	4.12E+03
o	middle	4.24E+03
p	middle	3.00E+03
q	middle	3.37E+03
r	middle	4.74E+03
s	middle edge	7.93E+03
t	middle 2 edge	3.07E+04
u	middle 2	9.45E+03
v	middle 2	4.37E+03
w	middle 2	3.87E+03
x	middle 2	4.12E+03
y	middle 2	6.62E+03
z	middle 2	7.87E+03
aa	middle 2	6.61E+03
bb	middle 2 edge	8.48E+03
cc	bottom edge	1.27E+04
dd	bottom edge	6.47E+03
ee		7.62E+03
ff		6.74E+03
gg		6.24E+03
hh	middle edge	6.66E+03
ii	bottom edge	7.20E+03
jj	bottom edge	8.76E+03
kk	bottom edge	9.43E+03
ll	bottom edge	7.88E+03

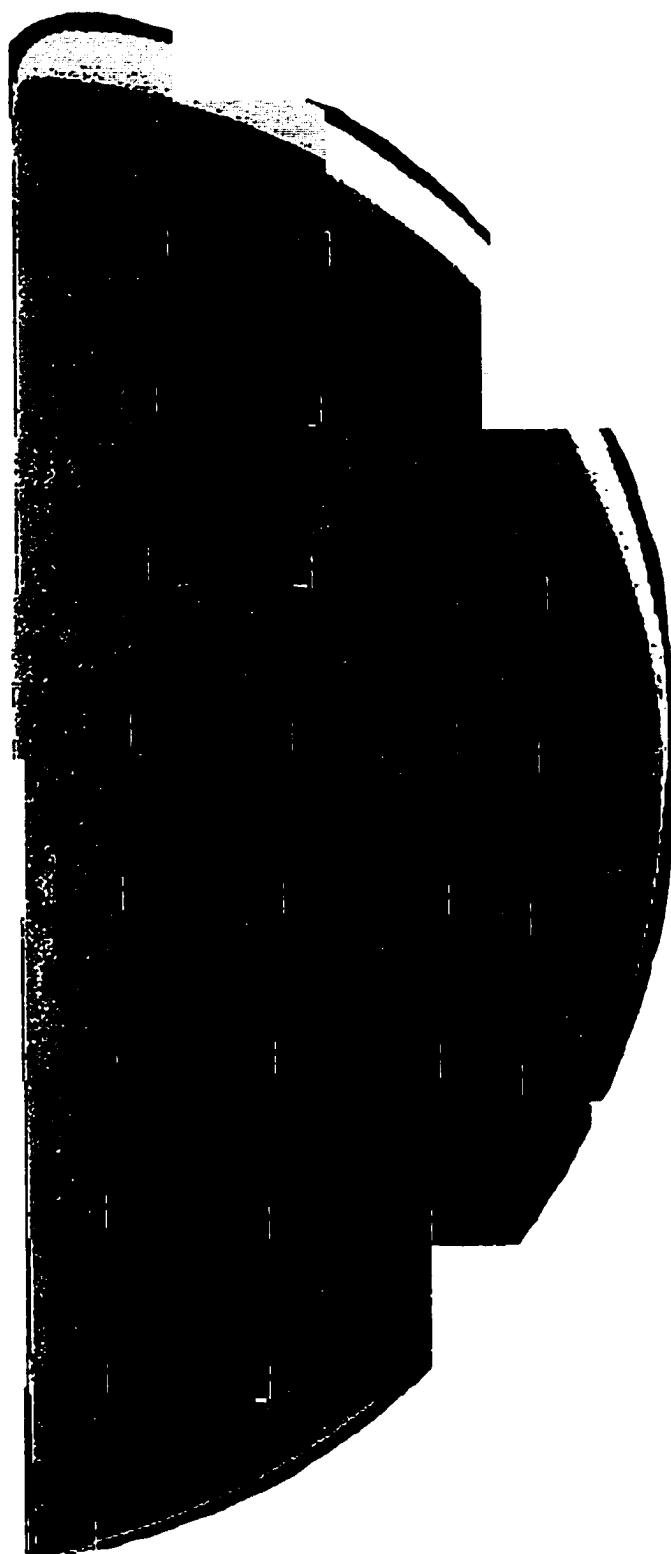


Figure 6-6. Etch pit distribution on MZS 5-6 (5.2cm).



Figure 6-7. Etch pit distribution on MZS 5-7 (5.5cm).

Table 6-8. MZS 5-7 (5.5cm).

Sample Name	Location	EPD (#/cm ²)
a	top edge	1.62E+04
b	top	5.99E+03
c	top	5.87E+03
d	top	1.27E+04
e	top	1.51E+04
f	top	8.22E+03
g	top	7.31E+03
h	top	9.00E+03
i	top edge	8.32E+03
j	middle edge	8.26E+03
k	middle	1.09E+04
l	middle	1.09E+04
m	middle	9.61E+03
n	middle	1.39E+04
o	middle	1.50E+04
p	middle	8.86E+03
q	middle	6.49E+03
r	middle edge	8.64E+03
s	middle 2 edge	9.32E+03
t	middle 2	1.84E+04
u	middle 2	1.61E+04
v1	middle 2	2.21E+04
w1	middle 2	1.89E+04
x1	middle 2	1.80E+04
y1	middle 2 edge	1.80E+04
x	bottom edge	1.45E+04
y	bottom edge	1.49E+04
z	bottom edge	1.83E+04
aa	bottom edge	2.58E+04
bb	bottom edge	1.93E+04

Table 6-9. MZS 7-1 (4.9 cm).

Sample Name	Location	EPD (#/cm ²)
a	top edge	
b	top	2.35E+03
c	top	2.88E+03
d	top	5.11E+03
e	top	4.33E+03
f	top	3.54E+03
g	top	5.25E+03
h	top	6.97E+03
i	top	1.25E+04
j	top	1.03E+04
k	top edge	1.30E+04
l	middle edge	9.35E+03
m	middle	3.00E+03
n	middle	6.24E+03
o	middle	4.37E+03
p	middle	3.62E+03
q	middle	4.99E+03
s	middle	4.87E+03
t	middle	3.50E+03
u	middle edge	7.74E+03
v	bottom edge	3.98E+03
w	bottom edge	6.80E+03
x	bottom edge	5.74E+03
y	bottom edge	4.86E+03
z	bottom edge	7.43E+03
z1	bottom edge	1.35E+04

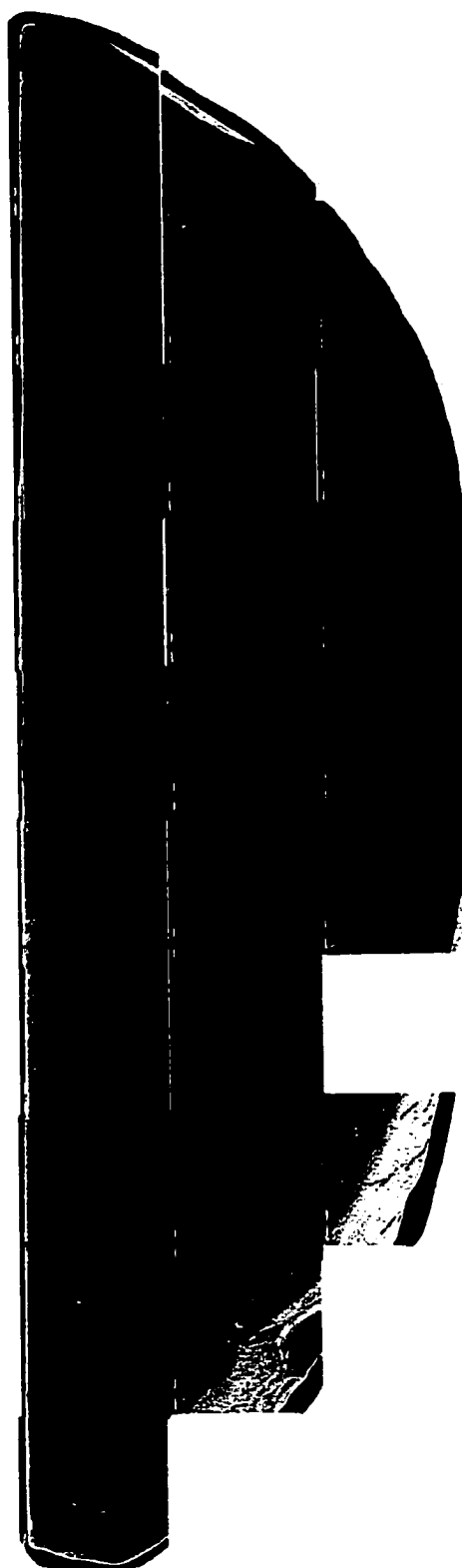


Figure 6-8. Etch pit distribution on MZS 7-1 (4.9 cm).

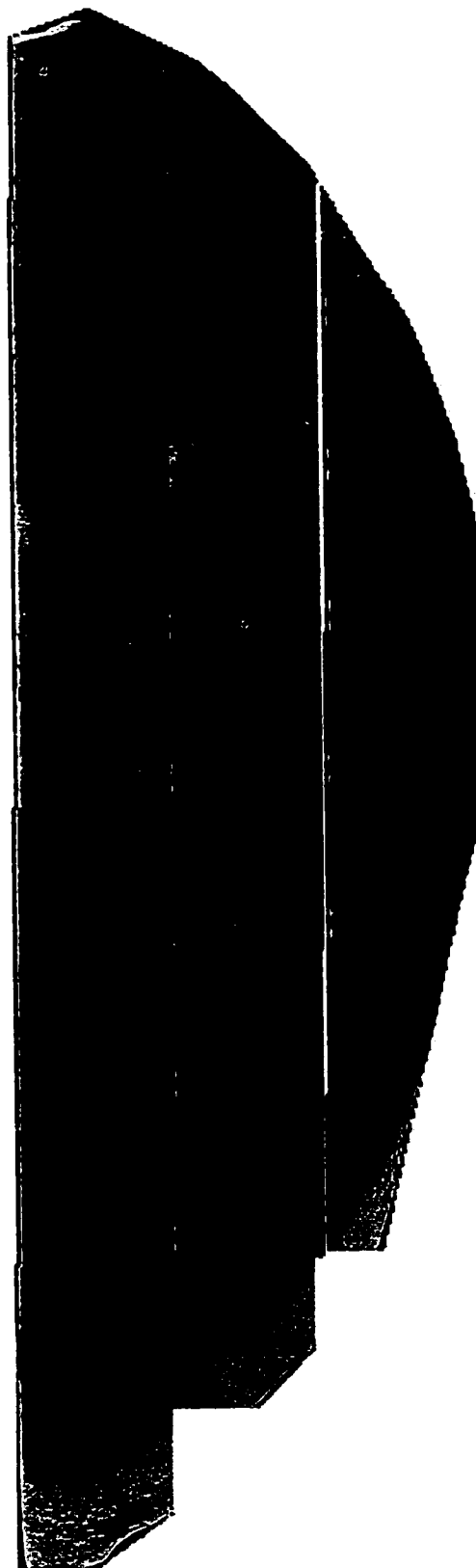


Figure 6-9. Etch pit distribution on MZS 7-2 (5.1 cm).

Table 6-10. MZS 7-2 (5.1cm).

Sample Name	Location	EPD (#/cm ²)
a	top edge	1.84E+04
b	top	2.46E+04
c	top	6.39E+03
d	top	3.24E+03
e	top	9.73E+03
f	top	4.41E+03
g	top	2.98E+03
h	top	8.58E+03
i	top	1.92E+04
j	top	1.65E+04
l	middle edge	4.36E+03
m	middle	3.75E+03
n	middle	7.74E+03
o	middle	9.11E+03
p	middle	9.49E+03
q	middle	8.49E+03
r	middle	4.12E+03
s	middle	7.62E+03
t	middle edge	1.34E+04
u	bottom edge	7.30E+03
v	bottom edge	9.02E+03
w	bottom edge	1.61E+04
x	bottom	7.81E+03
y	bottom edge	9.76E+03
z	bottom edge	5.43E+03

Table 6-11. MZS 7-5 (5.7 cm).

Sample Name	Location	EPD (#/cm ²)
b	top	1.73E+03
c	top	3.17E+03
d	top	3.75E+03
e	top	5.80E+03
f	top	9.48E+03
g	top	8.96E+03
h	top	1.29E+04
i	top	1.20E+04
j	top	2.19E+03
k	top edge	2.73E+03
l	middle edge	2.73E+03
m	middle	1.01E+04
n	middle	2.32E+04
o	middle	2.81E+04
p	middle	3.48E+04
q	middle	9.24E+03
r	middle	5.74E+03
s	middle	7.87E+03
t	middle edge	5.62E+03
u	bottom edge	1.16E+04
v	bottom edge	1.15E+04
w	bottom edge	9.72E+03
x	bottom	1.62E+04
y	bottom edge	2.01E+04
z	bottom edge	1.30E+04
z1	bottom edge	6.64E+03



Figure 6-10. Etch pit distribution on MZS 7-5 (5.7 cm).

Table 6-12. MZS 8-2 (3.7 cm).

Sample Name	Location	EPD (#/cm ²)
21	left top edge	1.50E+04
20	top edge	1.89E+04
19	top edge	2.26E+04
18	top edge	2.98E+04
17	top edge	2.03E+04
16	top edge	1.22E+04
14	left middle edge	2.60E+04
13	middle edge	1.64E+04
12	middle edge	1.39E+04
11	middle edge	1.37E+04
10	middle edge	1.28E+04
9	right middle edge	9.30E+03
6	left bottom edge	2.91E+04
5	bottom edge	1.20E+04
4	bottom edge	1.63E+04
3	right bottom edge	1.87E+04

Table 6-13. MZS 8-3 (3.9cm).

Sample Name	Location	EPD (#/cm ²)
43	left top edge	3.19E+04
42	top edge	1.97E+04
41	top edge	2.64E+04
40	top edge	2.14E+04
39	top edge	1.65E+04
38	top edge	1.80E+04
37	top edge	1.05E+04
36	right top edge	1.48E+04
35	middle edge	3.08E+04
34	middle	4.61E+04
33	middle	3.27E+04
32	middle	1.76E+04
31	middle	2.01E+04
30	right middle edge	2.28E+04
27	bottom edge	3.55E+04
26	bottom edge	2.91E+04
25	bottom edge	1.54E+04
24	bottom edge	9.99E+03

Table 6-14. MZS 10-3 (4.5 cm).

Sample Name	Location	EPD (#/cm ²)
24	left top edge	7.43E+04
23	top	3.61E+04
22	top	2.65E+04
21	top	5.23E+04
20	top	3.15E+04
19	top	3.18E+04
18	top	2.15E+04
16	left middle edge	1.07E+05
15	left edge bottom	5.70E+04
14	middle	3.21E+04
13	middle	3.22E+04
12	middle	3.22E+04
11	right middle edge	4.59E+04
10	left bottom edge	7.17E+04
6	bottom edge	1.09E+05
5	bottom edge	9.11E+04
4	bottom edge	1.09E+05
3	right bottom edge	7.80E+04

Table 6-15. MZS 10-4 (4.4 cm).

Sample Name	Location	EPD (#/cm ²)
52	top edge	9.06E+04
53	top edge	1.35E+05
54	top edge	1.61E+05
55	top edge	8.38E+04
56	top edge	1.34E+05
57	top edge	1.05E+05
58	top edge	1.07E+05
59	top edge right	7.01E+04
50	top edge left	8.63E+04
24	top	4.67E+04
23	top	8.11E+04
22	top	7.80E+04
21	top	6.65E+04
20	top	7.80E+04
19	top	1.11E+05
18	top right	1.60E+05
16	middle edge left	6.24E+04
15	middle	3.57E+04
14	middle	3.15E+04
13	middle	4.62E+04
12	middle	5.95E+04
11	middle edge right	1.13E+05
10	middle edge corner	1.73E+05
7	bottom edge left	2.16E+05
6	bottom edge	1.58E+05
5	bottom edge	1.84E+05
4	bottom edge right	2.76E+05

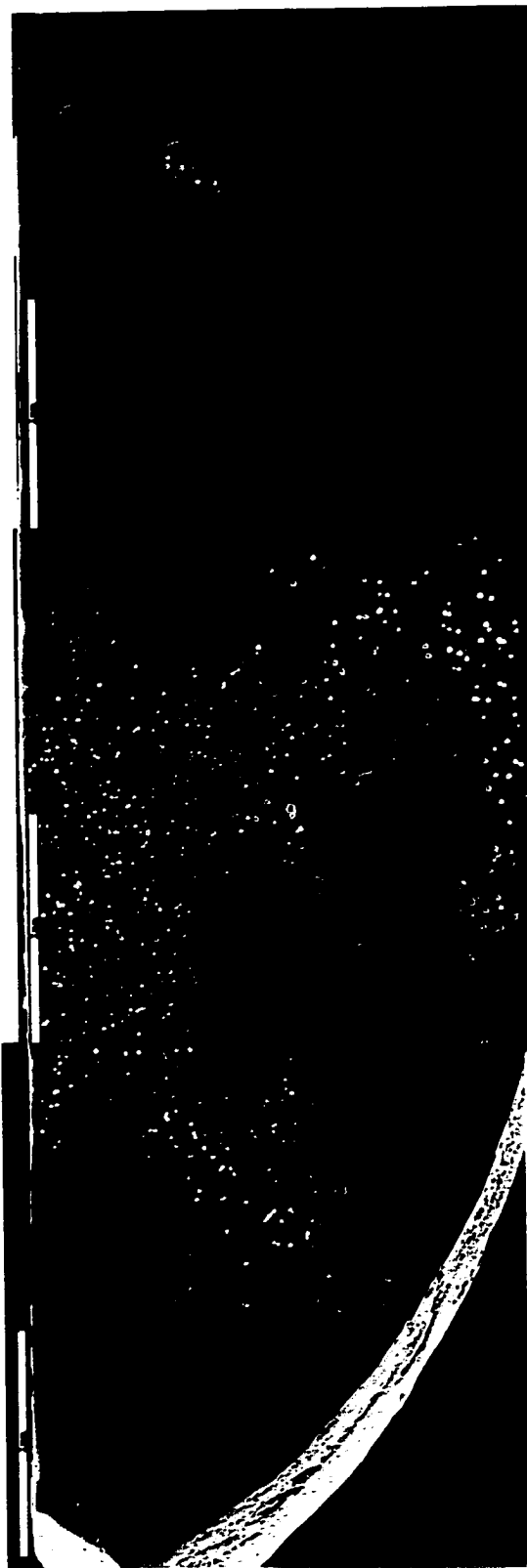


Figure 6-11. Etch pit distribution on MZS 8-2 (3.7cm).



Figure 6-12. Etch pit distribution on MZS 8-3 (3.9 cm).

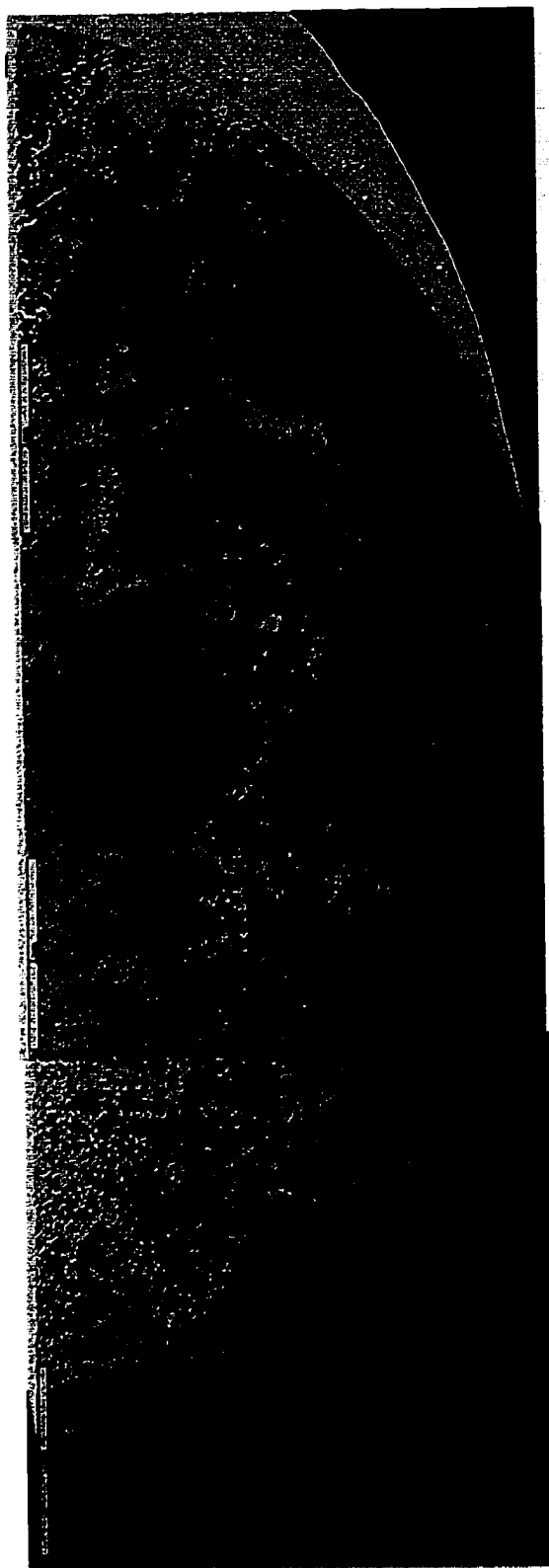


Figure 6-13. Etch pit distribution on MZS 10-3 (4.5 cm).

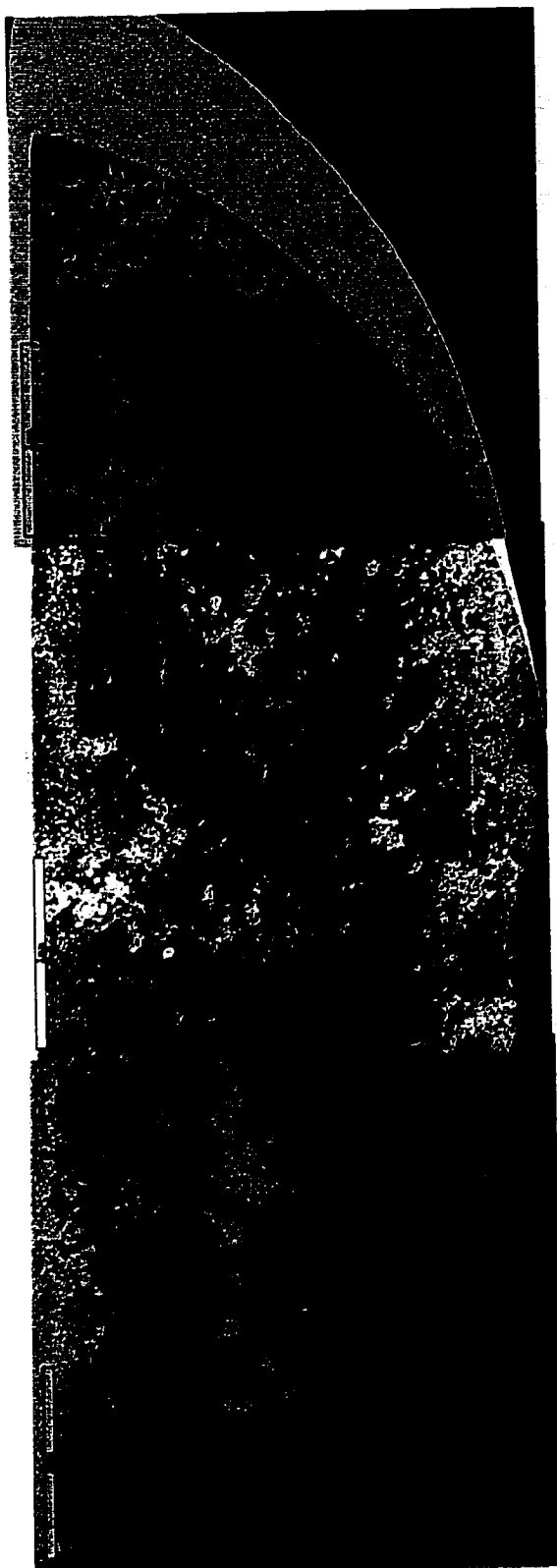


Figure 6-14. Etch pit distribution on MZS 10-4 (4.3 cm).

Origin of Dislocations during Directional Solidification

Dislocations can arise from several sources during the crystal growth process. Potential sources of dislocations include impingement of two grain of different orientation, collapse upon cooling of vacancies formed at high temperatures, thermal stresses induced by the growth process, and accommodation of lattice misfit due to concentration gradients (Nabarro, 1967). The first two mechanisms are unlikely for this material system. The favorable interface shape promotes grain growth toward the ampoule wall, so grains grow away from each other during solidification. For crystals grown from the melt, the equilibrium number of vacancies at the interface is much greater than the equilibrium number at room temperature, so a supersaturation occurs. As the alloy cools, these vacancies must either be incorporated or removed from the crystal. These vacancies can either aggregate into loops or escape the crystal by climbing into the liquid or, for small crystals, diffuse to the surface. Although there is experimental evidence of these dislocation loops, the existence of this mechanism has been questioned for normal growth conditions (Nabarro, 1967). This is probably not the primary source of dislocations in this system because the ingot diameter is small. Thermal stresses and concentration gradients are the mechanisms most likely to contribute to dislocation generation in the $\text{Hg}_{1-x}\text{Zn}_x\text{Se}$ system.

The nature of solidification from the melt of alloy systems with a large separation between the liquidus and solidus and large density differences can produce large gradients in concentration. For this alloys system, the segregation coefficient calculated from the quenched interface is approximately 5, so the composition of the first material to freeze is

higher in composition than the composition of the liquid ahead of the interface. This establishes a region ahead of the interface that is depleted of solute. Steady state is eventually established, and the composition of the solid is that of the liquid. The lattice constant for this system, however, varies linearly with composition (Kot and Simashkevich, 1964), so a change in the composition gradient requires that dislocations be formed to accommodate large misfits (Nabarro, 1967). The number of dislocations due to the stress of the compositional gradient is given by

$$\rho = \frac{1}{a^2} \frac{da}{dc_s} \delta \frac{dc_s}{dx}, \quad (6-1)$$

where a is the average lattice constant, da/dc_s is the change in lattice constant per change in composition, and $\delta(dc_s/dx)$ is the variation of the compositional gradient (Friedel, 1964). For this alloy system grown in the Bridgman-Stockbarger configuration, there are radial compositional variations due to radial temperature variations, so dislocations are expected to be generated to accommodate lattice distortion. Using the worst case compositional gradients observed for the largest diameter sample, the number of dislocations generated due to compositional variations is on the order of $10^4/\text{cm}^2$.

Thermal gradients are also imposed on the sample during the directional solidification process. The inherent nature of the solidification process induces a thermal gradient in the axial direction, and the thermal field can also vary radially, depending on the furnace characteristics. Friedel (1964) suggested that when there is a deviation from the average thermal gradient in the vicinity of the growth front, internal stresses are relieved by producing dislocations, to accommodate non-uniform thermal expansion. The dislocation density due to a variation in the thermal gradient is given by

$$\rho = \frac{1}{a} \alpha \delta \nabla T, \quad (6-2)$$

where α is the thermal expansion, a is the lattice constant, and $\delta \nabla T$ is the deviation in the thermal gradient. Small changes in the thermal gradient can introduce a significant number of dislocations, because $\alpha/a \approx 10^5/^\circ\text{cm}^2$.

There are other potential sources of dislocation formation in the crystal growth process, however, those listed above are most influenced by the nature of the material system and the growth conditions. The influence of growth conditions on dislocation densities for the $\text{Hg}_{1-x}\text{Zn}_x\text{Se}$ system is summarized in the following sections.

Effect of Ampoule Wall on Etch Pit Density

It was generally expected that a larger etch pit density would be found along the perimeter of each crystal due to interactions between the sample material and the ampoule wall. Imperfections in the ampoule wall and reactions between the alloy and the fused quartz could be nucleation sites for grain boundaries and dislocations. The differences in the thermal expansion of the ingot and the fused quartz could also induce stress into the growing crystal.

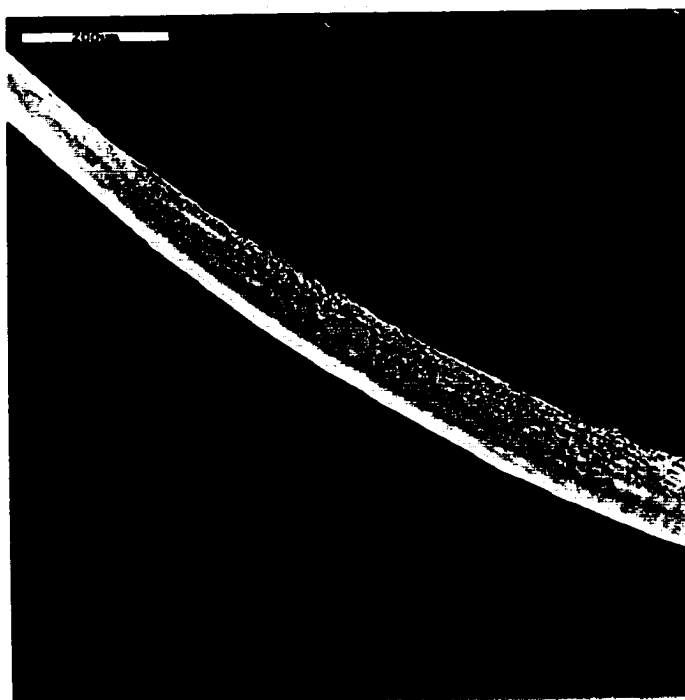
Higher dislocation densities were observed at some point along the perimeter of all ingots investigated, but a consistently higher density along all edges was not observed. Small regions along the outer surface of several samples showed a much higher density. Examples are presented in Figure 6-15 for MZS-2 and in Figure 6-16 for MZS-5. These regions are thought to be areas where the melt was attached to the surface of the ampoule wall during solidification, causing localized regions of stress. This behavior was observed, primarily, on MZS-2 and is consistent with the pictures taken of the surface prior to

characterization which indicate that there were many regions where the melt wetted the ampoule wall. An example of this behavior is shown in Figure 6-17.

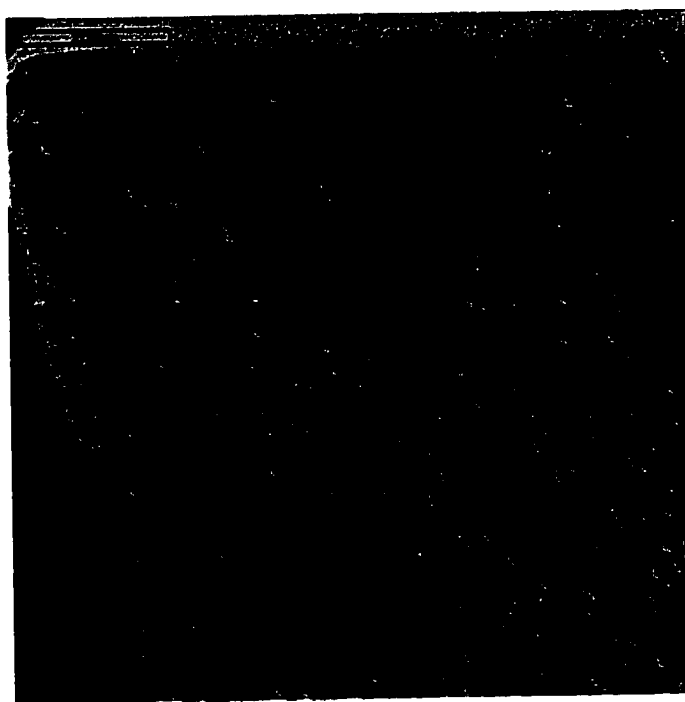
Ingot MZS-5 was grown in a 7.2 mm inner diameter ampoule that contained a graphite piece. Thermal etch pits were observed on the surface, and only one very small region of higher etch pit density was found on the edge of one radial slice from sample MZS-5. This is likely due to sticking at this point. Except for this one spot, there seemed to be no overall influence of the ampoule wall or the increased size of the ingot on the etch pit density. Etch pit densities ranged from 2.4×10^3 to $3.8 \times 10^4 \text{ cm}^{-2}$. The average etch pit density for this ingot was $1.1 \times 10^4 \text{ cm}^{-2}$, the second lowest of all ingots.

Ingot MZS-7 was grown in a 5 mm inner diameter ampoule and included a piece of graphite. This ingot moved freely in the ampoule following processing, an indication that no wetting occurred in this ingot. Slices taken from this ingot had etch pits densities ranging from 2.2×10^3 to $3.5 \times 10^4 \text{ cm}^{-2}$, with an average density of $9.0 \times 10^3 \text{ cm}^{-2}$. This ingot had the lowest average etch pit density and the density did not increase at the ampoule wall. The "W" distribution often observed in bulk grown crystals was not observed. Since the alloy apparently grew detached from the ampoule wall, the differences in thermal expansion between the alloy and ampoule did not induce stress along the ingot wall.

For crystal MZS-8, which was solidified in a 5.5 mm inner diameter ampoule coated with BN, several regions of fracture were observed on the surface. Fractured regions were not observed after 1.9 cm of growth, and regions of higher etch pit density were not observed around the edge of samples cut between 3.5 and 4.1 cm. The etch pits densities ranged from 9.3×10^3 to $3.5 \times 10^4 \text{ cm}^{-2}$. The average dislocation density,

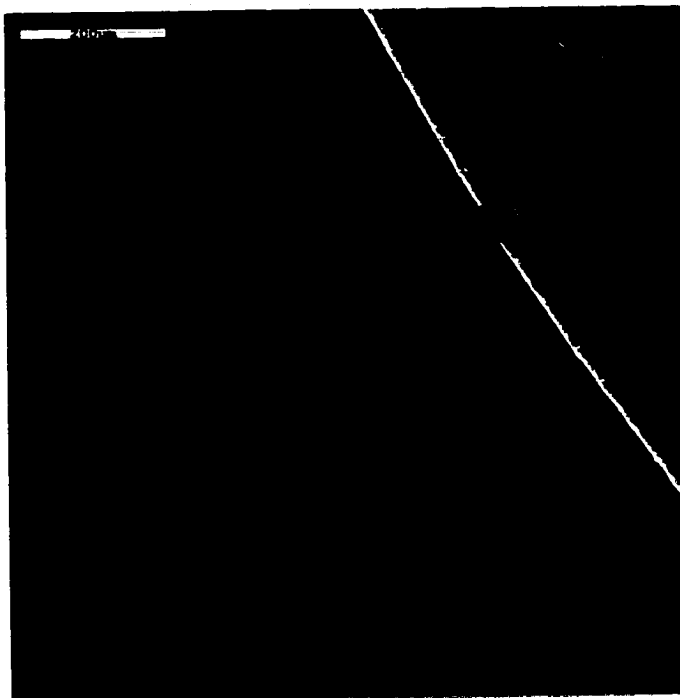


a)

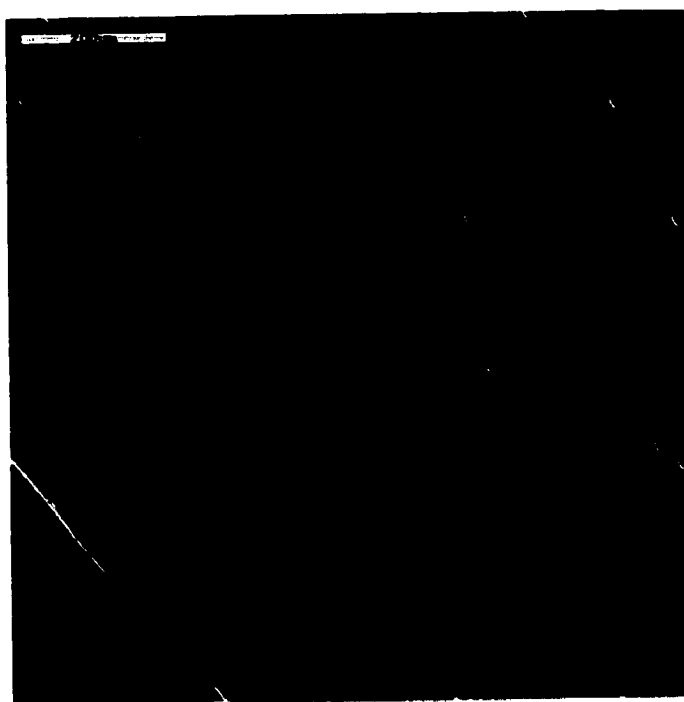


b)

Figure 6-15. Example of higher etch pit density along crystal perimeter for MZS-2:
a) MZS 2-2v, b) MZS 2-5a.

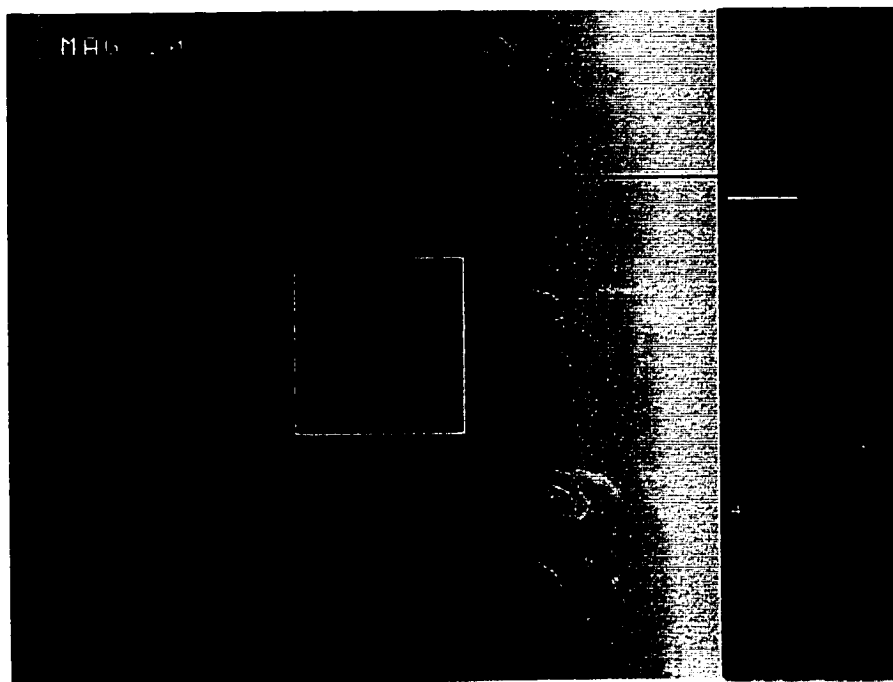


a)

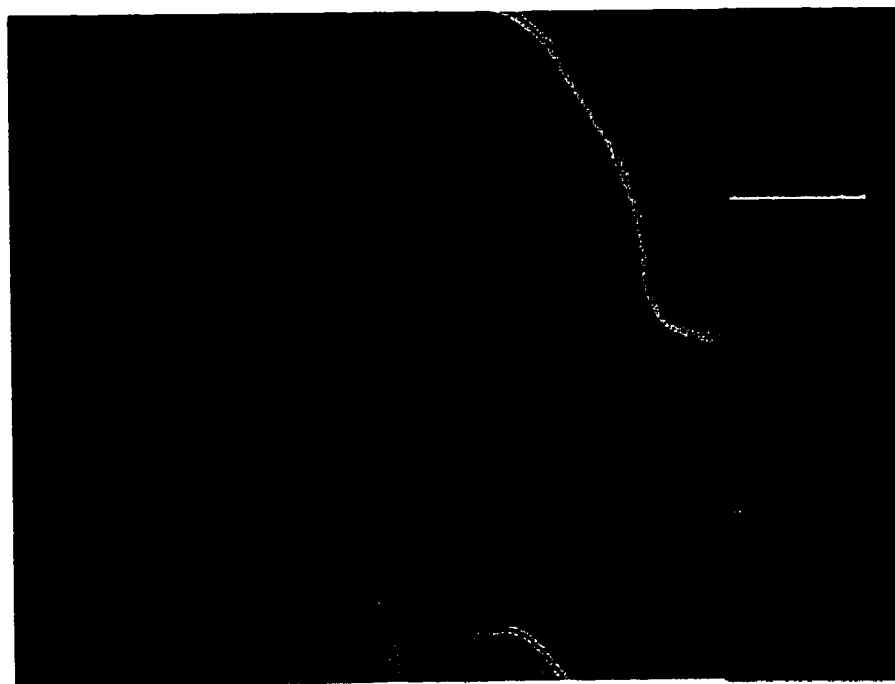


b)

Figure 6-16. Example of higher etch pit density along crystal perimeter for MZS-5:
a) MZS 5-6t, b) MZS 5-6u.



a)



b)

Figure 6-17. Example of the attached and detached solidification of the molten crystal for MZS-2: a) at 20x magnification and b) at 94x magnification.

$2.06 \times 10^4 \text{ cm}^{-2}$, was somewhat higher than observed in samples grown with a piece of graphite in the ampoule, but comparable with MZS-2 grown with no ampoule treatment. The addition of a graphite plug was more effective in reducing wetting between the ampoule and the alloy, than was the BN coating.

The dislocation densities for MZS-10, which was solidified in a magnetic field, were noticeably higher close to the ingot edge, as shown in Figure 6-18. The dislocation density along the edge was as high as $4.6 \times 10^5 \text{ cm}^{-2}$. This was the highest density measured in any other sample. Higher etch pit density was observed over the entire sample, ranging from 2.2×10^4 to $2.8 \times 10^5 \text{ cm}^{-2}$, with an average of 8.3×10^4 . Uniform thermal etch pits were observed on the ingot surface there was no evidence of wetting. This higher density was, very likely, related to the change in thermal gradient near the interface, and not due to the ampoule wall. This hypothesis is described in more detail in the next section.

Using equation 6-1, the number of dislocations expected for the $\text{Hg}_{1-x}\text{Zn}_x\text{Se}$ system due to compositional variations was calculated to be on the order of $10^4/\text{cm}^2$ for the worst case compositional gradients observed for the largest diameter sample. This is the same magnitude as observed for all the samples grown in the Bridgman-Stockbarger without an applied magnetic field.

Effect of Magnetic Field on Dislocation Density

Magnetic fields have been successfully used to reduce convective flows in the melt that can lead to compositional variations in the directional solidification of $\text{Hg}_{1-x}\text{Zn}_x\text{Te}$ (Sha et al, 1997), $\text{Hg}_{1-x}\text{Cd}_x\text{Te}$ (Watring and Lehoczky, 1996), InSb (Utech and Flemings,

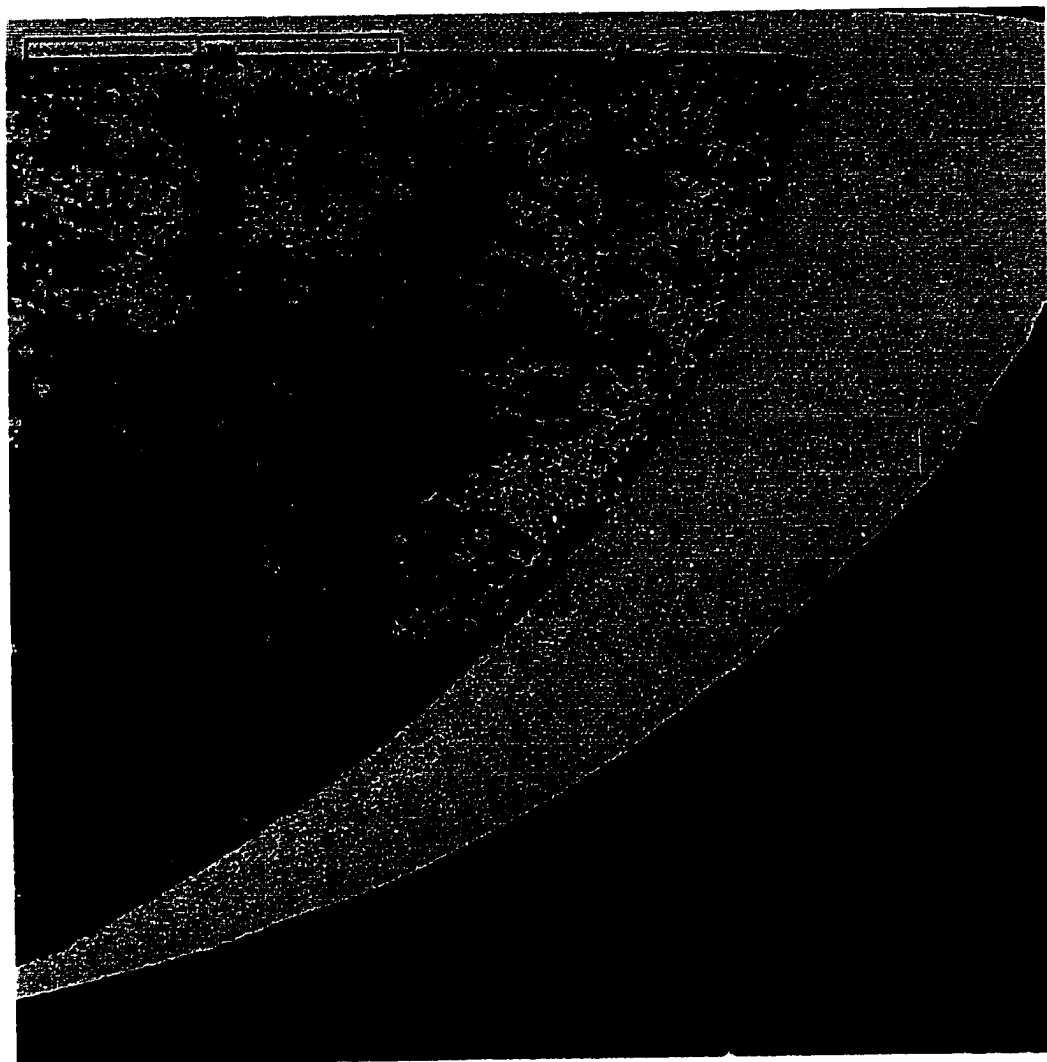


Figure 6-18. Significantly higher etch pit density observed along perimeter of MZS-10.

1966) and Ga doped Ge (Matthieson et al., 1987), and during Czochralski growth of Si (Hoshikawa, 1982) and GaAs (Terashima et al., 1984). The Lorentz force, induced by the magnetic field in electrically conductive melts, reduces the magnitude of the convective flow resulting from thermosolutal buoyancy effects (Sha et al., 1997) and can significantly reduce compositional homogeneity. Reducing compositional variations should reduce misfit dislocations.

Compositional variations were smaller in the radial direction for ingot, MZS-10, which was solidified in a 5 tesla magnetic field. Etch pit densities of slices taken from this ingot were expected to be smaller than in other ingots. However, etch pit densities in the ingot ranged from 2.2×10^4 to $2.8 \times 10^5 \text{ cm}^{-2}$, with an average density of $8.3 \times 10^4 \text{ cm}^{-2}$. This was 3-10 times higher than observed in other ingots. The thermal profile for the magnet furnace is compared with the Bridgman furnace in Figure 6-19. A large change in the thermal gradient occurs in the vicinity of the interface temperature (approximately 817°C for $x=0.10$). As noted by Nabarro (1967), even small changes in the thermal gradient can lead to significant dislocation densities due to thermal expansion effects. Using equation 6-2, the change in thermal gradient from the profile of MZS-10, and the coefficient of thermal expansion for the $\text{Hg}_{1-x}\text{Cd}_x\text{Te}$ system, the dislocation density due to the changing thermal gradient is predicted to be on the order of $10^5/\text{cm}^2$. This is along the same order of magnitude as etch pit densities observed on MZS-10. The differences in the thermal profiles occurred because even though similar hot and cold zone temperatures were used, heat pipes were not used in the magnet furnace. This caused there to be a non-linear temperature variation in the lower portion of the temperature range. This problem could be avoided in future experiments by judicious choice of zone temperatures, or incorporation of heat pipes into the configuration.

Other Considerations

Some regions of ingot MZS-5 had higher etch pit densities than expected. The upper zone of the furnace malfunctioned during growth of ingot MZS-5 and eventually

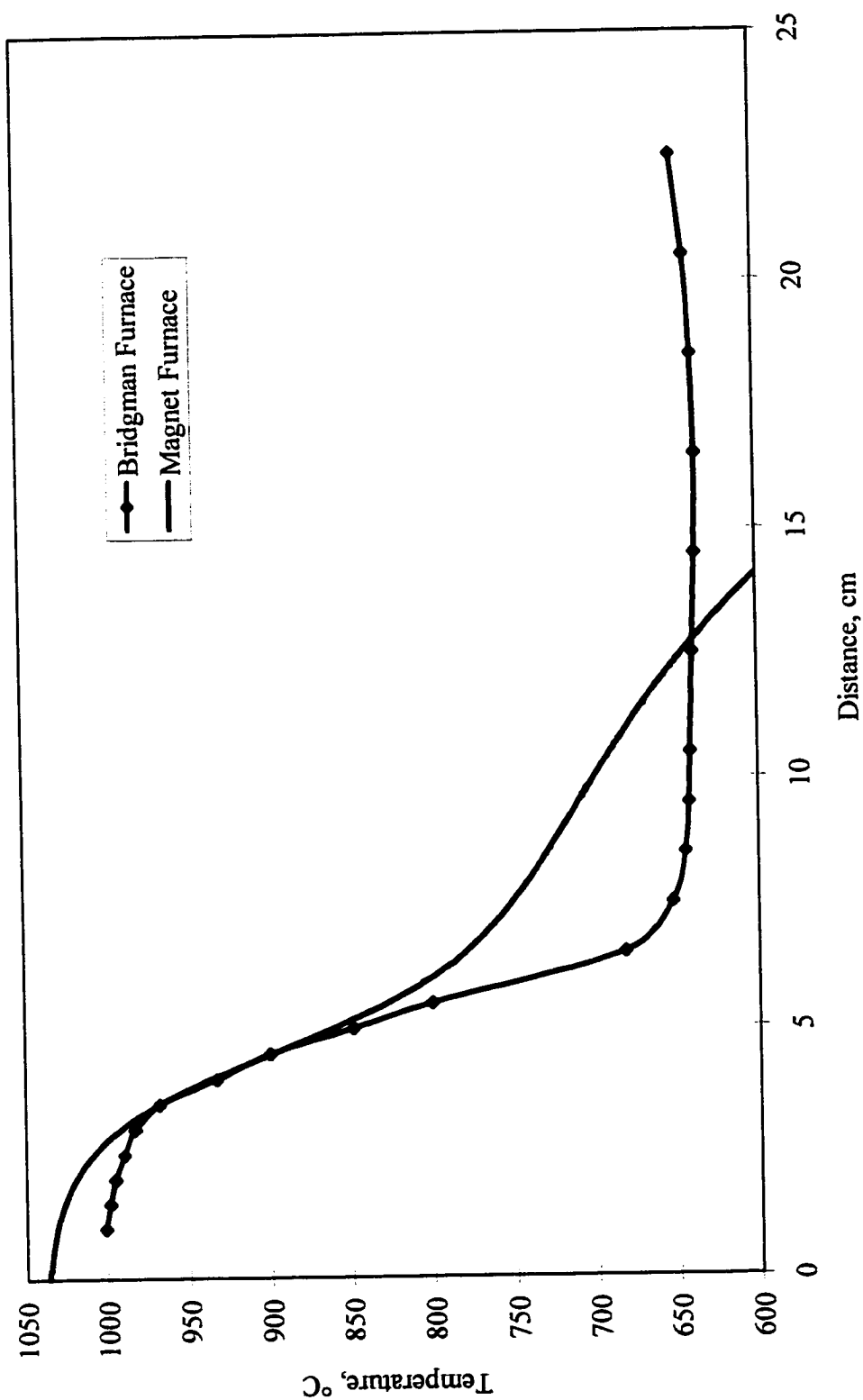


Figure 6-18. Comparison of thermal profiles for Bridgman and magnet furnaces.

lost power. Compositional variations documented in Chapter 5 at approximately 4.2, 5.5 and 6.0 cm of growth indicated there were thermal fluctuations in the upper heated zone. Higher etch pits densities were observed on sample MZS 5-7, which was cut 5.25 to 5.6 cm from the tip. This is one of the regions where compositional variations were observed, so it is likely that these dislocations were generated from the change in the thermal gradient caused by the malfunctioning heater.

Comparison of Dislocation Densities in $\text{Hg}_{1-x}\text{Zn}_x\text{Se}$ Alloys with Similar Materials

The original interest in the $\text{Hg}_{1-x}\text{Zn}_x\text{Se}$ alloy system stemmed from calculations of Sher et al. (1985) that predicted Zn additions to the HgSe lattice would result in a shorter stronger bond, thus making the lattice more stable against defect formation. The replacement of Cd with Zn in the $\text{Hg}_{1-x}\text{Cd}_x\text{Te}$ system had already been shown to improve resistance to dislocation formation (Su et al., 1988). Etch pit densities in the $\text{Hg}_{1-x}\text{Cd}_x\text{Te}$ are on the order of 10^5 to 10^6 cm^{-2} (Parker and Pinnel, 1971; private communication McKeagney). Etch pit densities for $\text{Hg}_{1-x}\text{Zn}_x\text{Te}$ grown by the Bridgman method were in the mid 10^5 cm^{-2} range (Su et al., 1988). Samples grown in a magnetic field had EPD in the low to mid 10^5 cm^{-2} . In this investigation, EPD ranged from 9.0×10^3 - $1.1 \times 10^4 \text{ cm}^{-2}$. The results show a significant reduction in the number of dislocations generated in this alloy system compared to similar II-VI Hg chalcogenides processed under similar growth conditions. These results are shown graphically in Figure 6-20.

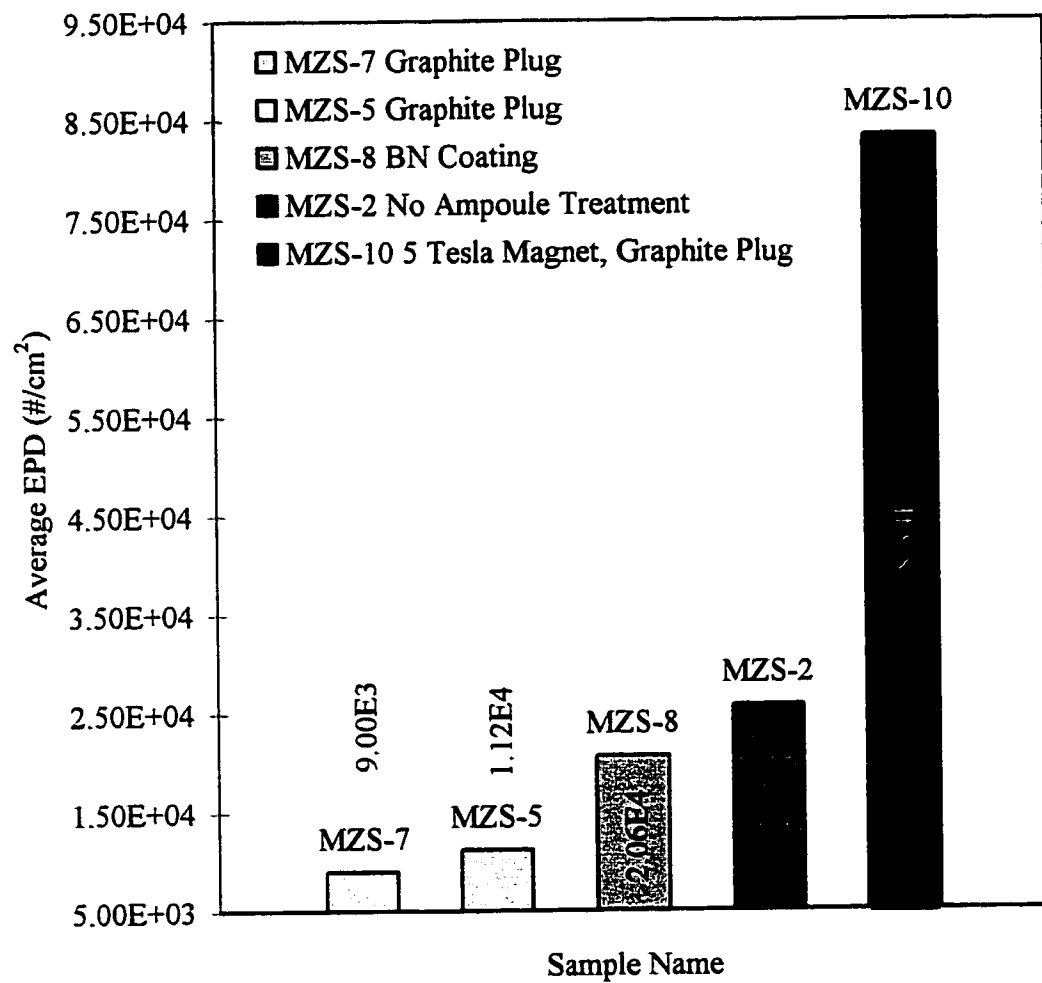


Figure 6-20. Comparison of average etch pit densities on ingots with various ampoule treatments.

CHAPTER 7 CONCLUSIONS

$\text{Hg}_{1-x}\text{Zn}_x\text{Se}$ alloys are potentially applicable for use as photoconductive detectors of electromagnetic radiation in the infrared region of the spectrum. A similar system, $\text{Hg}_{1-x}\text{Cd}_x\text{Te}$ has been used in this application for years. In many cases, usage includes long term exposure to a vacuum environment. The $\text{Hg}_{1-x}\text{Zn}_x\text{Se}$ system forms with excess electrical carriers, making it more appropriate for application in such environments. In order to produce focal plane arrays for thermal imaging, bulk single crystalline substrates with compositional homogeneity and low defect concentrations are needed. A number of investigations have reported on the electrical properties of this system, and one investigation produced epitaxial layers of $\text{Hg}_{1-x}\text{Zn}_x\text{Se}$ on GaAs. The objective of this investigation was to characterize the microstructural properties and determine whether the addition of Zn to the HgSe lattice reduced the potential for defect formation as predicted by calculations of bond strength.

An attempt was made to measure the pseudobinary phase diagram to assist in determination of appropriate growth conditions. Although experiments were fairly successful in measuring the solidus temperatures of alloys with $0.08 \leq x \leq 0.20$, the liquidus temperatures were difficult to determine. Similar difficulties had also been observed in the $\text{Hg}_{1-x}\text{Zn}_x\text{Te}$ alloy system with low concentrations of Zn (Su et al., 1996). The vapor pressure of these alloys requires the alloy to be contained in thick-walled fused quartz ampoules. This prevents the synthesized material from being rapidly quenched to

preserve compositional homogeneity in the cast alloys. The alloys were, therefore, annealed for up to 10 days to allow homogenization by diffusion in the melt. This produced slightly sharper transitions in thermal arrest curves. A high pressure furnace was constructed to measure thermal arrest curves on alloys with $x > 0.20$, but this effort was abandoned because the system lacked the required isothermal distribution. Nonetheless, enough data were obtained from these measurements to proceed with the proposed crystal growth experiments. If such experiments are repeated, samples should be rocked while melting and then quenched prior to each measurement. This should be followed by annealing just below the solidus temperature for several weeks to improve alloy homogenization.

$\text{Hg}_{1-x}\text{Zn}_x\text{Se}$ alloys with $x = 0.10$ were directionally solidified in four ampoule configurations. One ingot, MZS-10, was solidified in a magnetic field. Axial and radial compositional profiles were measured on each ingot. Axial and radial variations were similar for all ingots except MZS-10. Radial compositional variations were virtually eliminated in MZS-10. Convection in the melt ahead of the interface was significantly reduced, resulting in a reduction in thermosolutal buoyancy driven compositional redistribution. The frequency response of infrared detectors is dependent on composition, so alloy homogeneity is an essential requirement. The solidification of larger diameter ingots in a magnetic field should be further explored to ascertain the limits of magnetic field damping of convective compositional redistribution in the melt.

Two of the ingots were quenched to determine the shape of the liquid-solid interface. The shape of the interface was convex when viewed from the solid. This interface shape was highly favorable for the growth of single crystalline ingots. The initial

compositional transient contained several grains, but grain selection occurred as grains grew out toward the wall and terminated. One grain prevailed after the first few centimeters of growth, except in the ingot solidified in a magnetic field. This sample had an almost flat interface, and contained two grains until about 7 cm. These results confirmed the advantage of a slightly convex interface shape for growth of single crystals. The number of grains in a substrate limit the size and quality of a monolithic array that can be produced. The $\text{Hg}_{1-x}\text{Cd}_x\text{Se}$ alloy system can also be grown with a convex interface shape, but its electrical properties are not stable with time. Laue back-reflection x-ray diffraction confirmed the singular orientation of three of the ingots within experimental errors. White Beam Synchrotron X-ray Topography on two samples revealed that the ingots were essentially single crystals, but subgrain boundaries were detected with larger than expected misorientations. These measurements were performed in reflection mode, which is non-destructive, but measurements should also be made in transmission to explore the nature of these subgrains. This technique provides an image of individual dislocations which could be correlated with etch pit densities.

Dislocation densities for each ingot were estimated from etch pit densities measured on wafers cut from each ingot. The lowest etch pit densities were observed on the ingots grown in ampoules that included a piece of graphite. The larger diameter ingot had a slightly higher etch pit density, but the difference was probably not large enough to be considered significant. The ingots grown in the untreated ampoule and the BN coated ampoule had increased etch pit densities, presumably due to regions where the crystal wetted the ampoule wall during solidification. The highest etch pit densities were observed in the ingot grown in a magnetic field, contrary to expectations. This increase

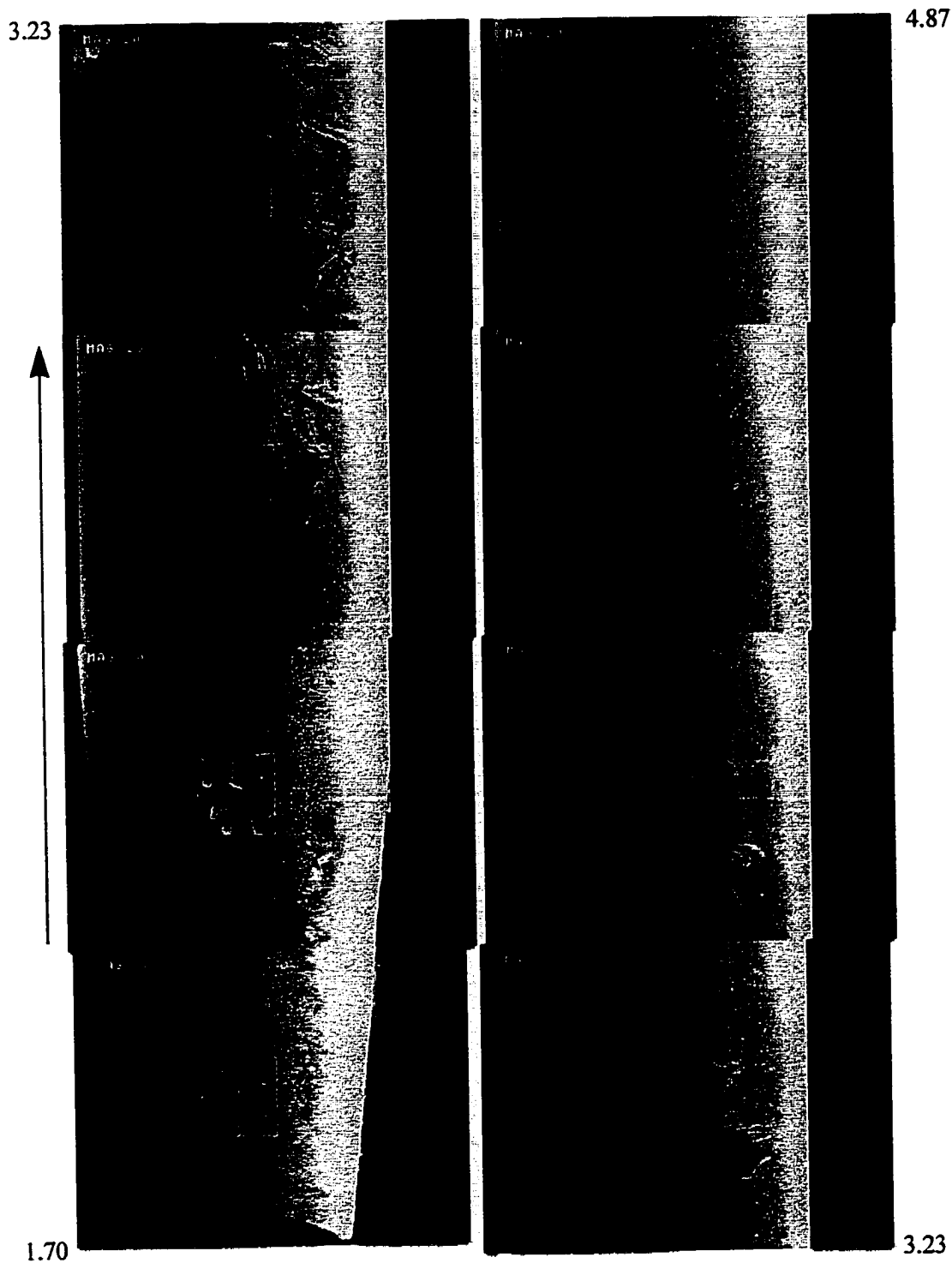
was attributed to a change in the thermal gradient near the interface temperature and not a result of the magnetic field. These results demonstrated the influence non-uniform thermal gradients have on stresses generated during solidification. In these alloys, dislocation generation was influenced more by the changing thermal gradient than by compositional variations. Future experiments should be performed to investigate the dislocation densities of an ingot grown under optimized thermal temperature gradients in an applied magnetic field.

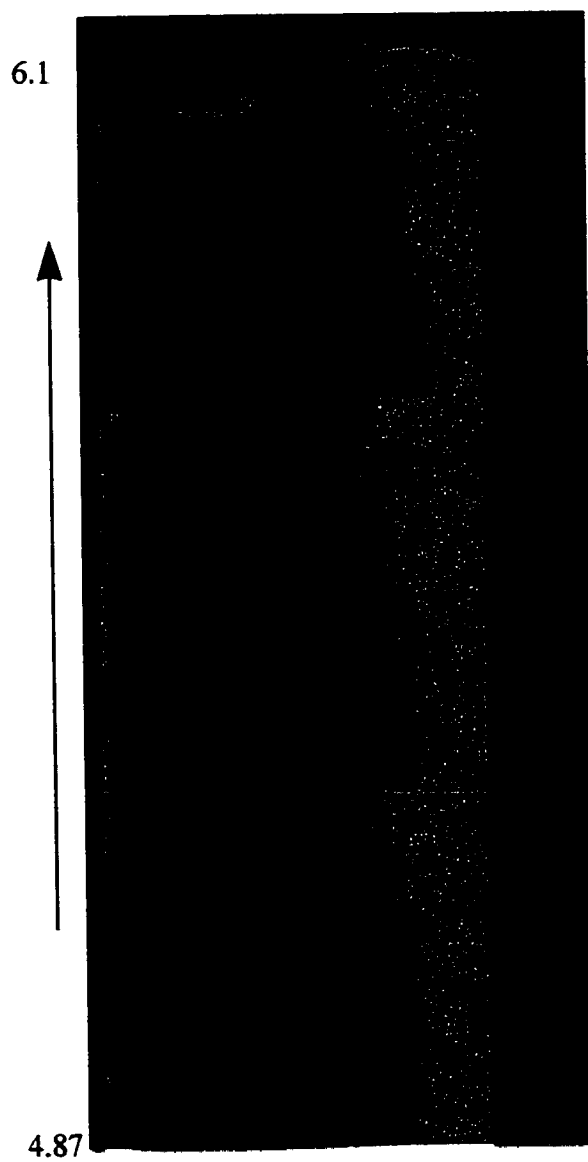
Overall dislocation densities on ingots processed with graphite were one to two orders of magnitude smaller than observed in other II-VI Hg based alloys. This confirms the prediction that Zn stabilizes the HgSe bond and thus improves the resistance to dislocation formation. Lower dislocation densities, the ability to produce compositionally homogenous single crystals, and the stability of electrical properties with time makes the $\text{Hg}_{1-x}\text{Zn}_x\text{Se}$ alloy system a viable candidate for further consideration for infrared radiation detection and imaging applications.

APPENDIX A

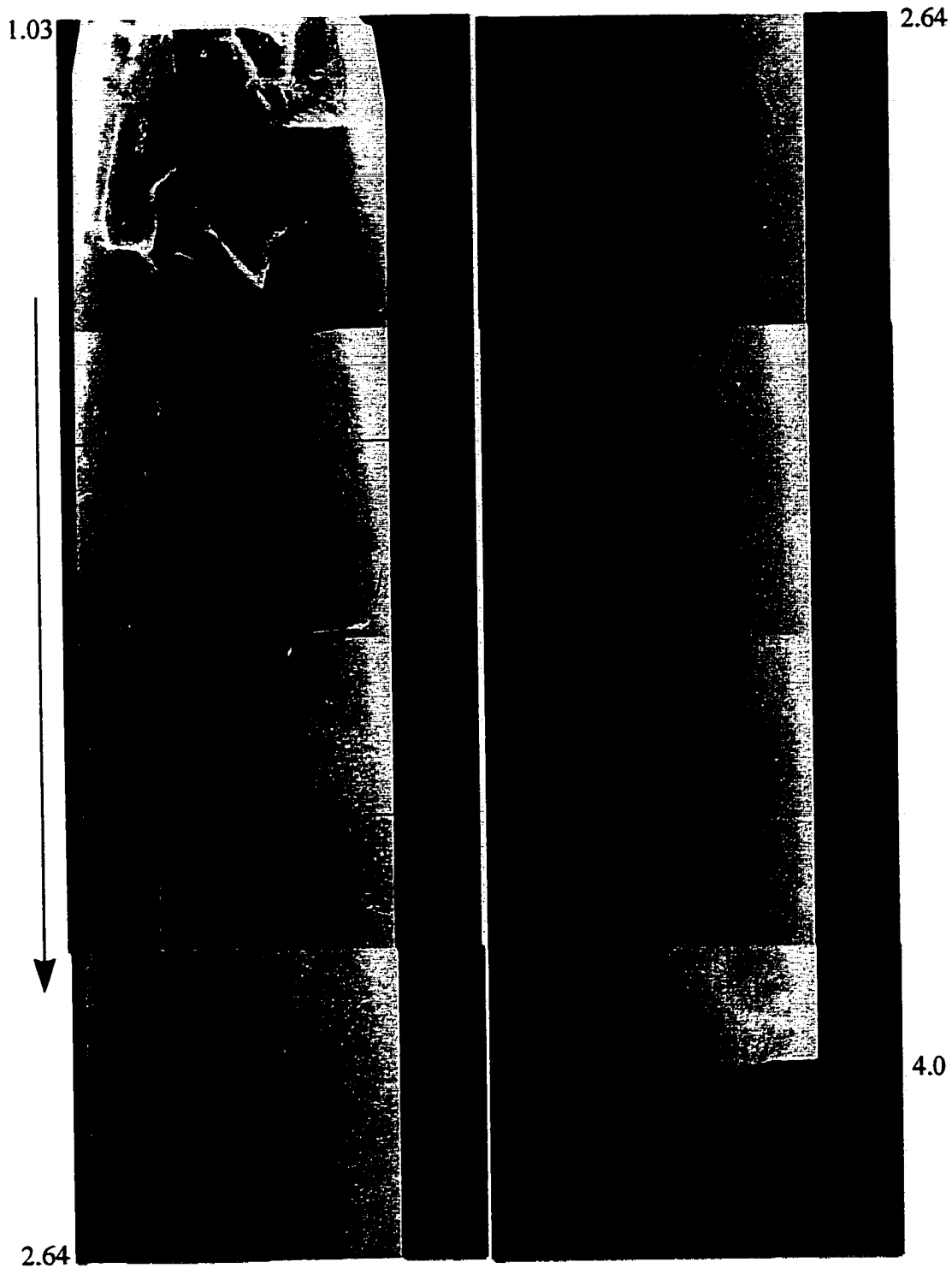
COLLAGES OF INGOT SURFACE FEATURES

COLLAGES OF INGOT MZS-2 SURFACE FEATURES





COLLAGES OF INGOT MZS-5 SURFACE FEATURES



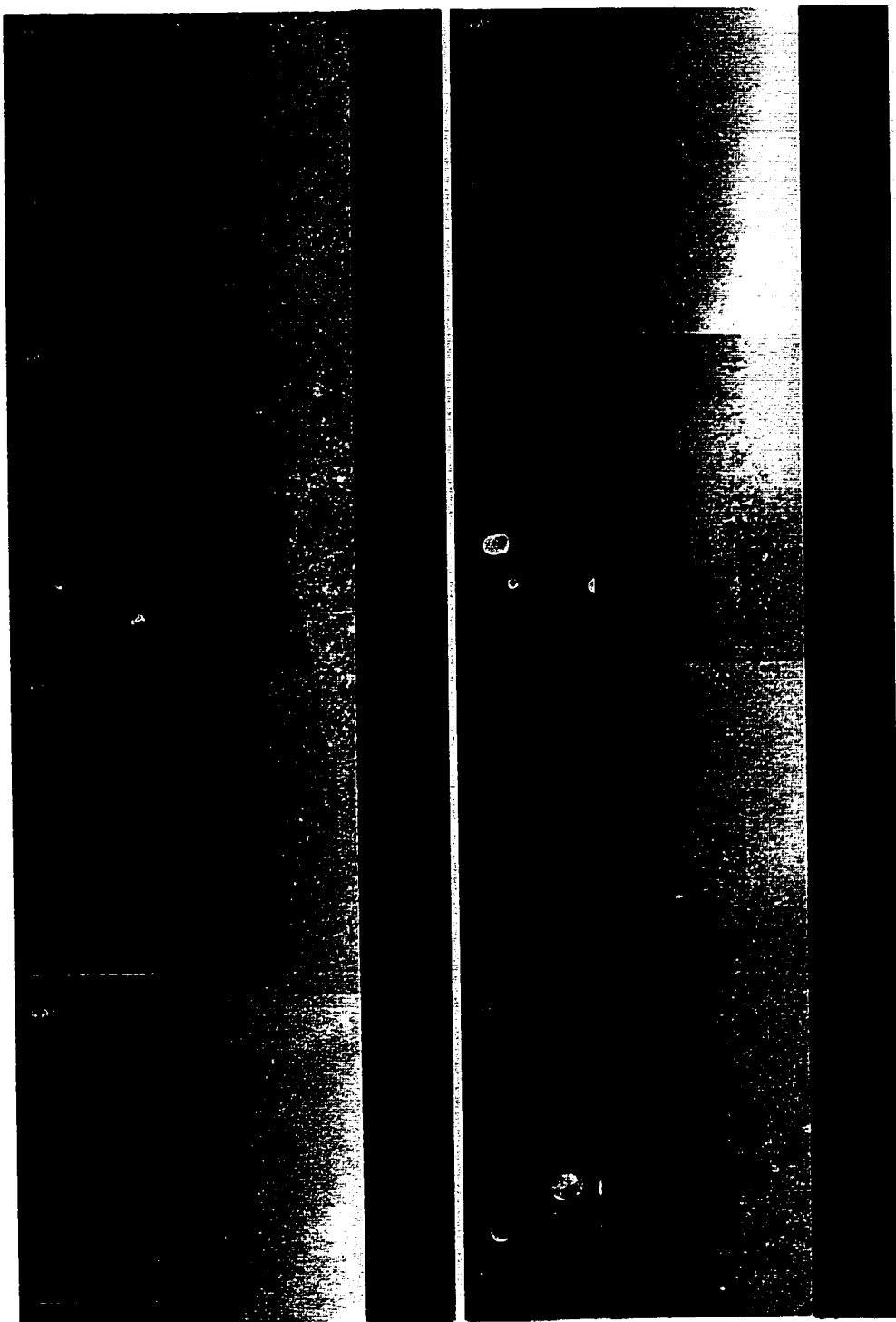
4.07

4.89

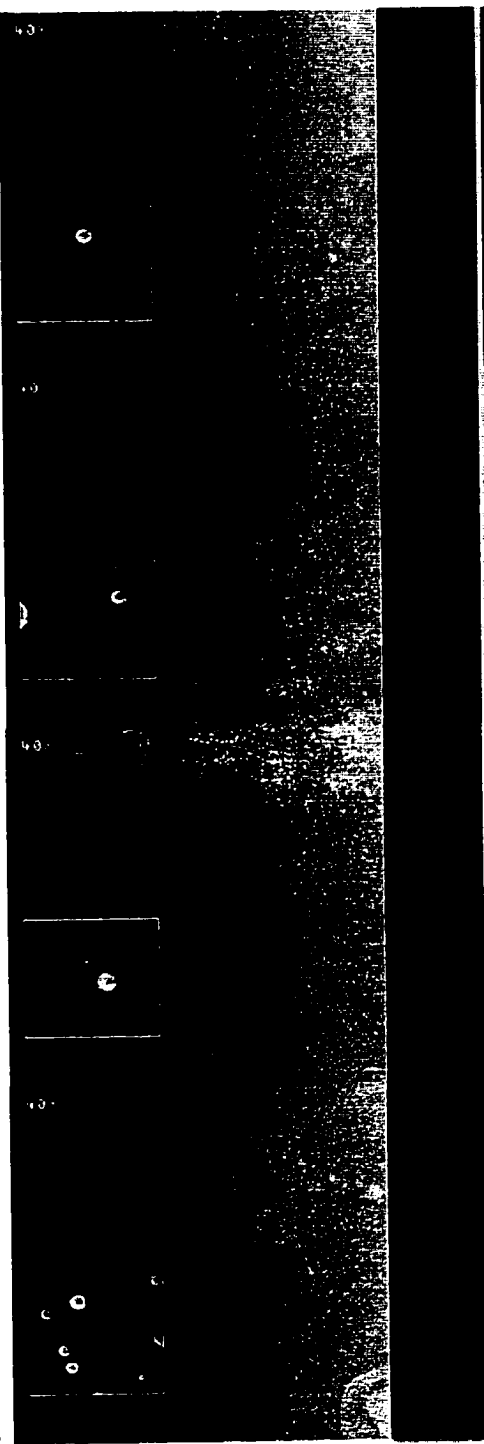


4.89

5.71

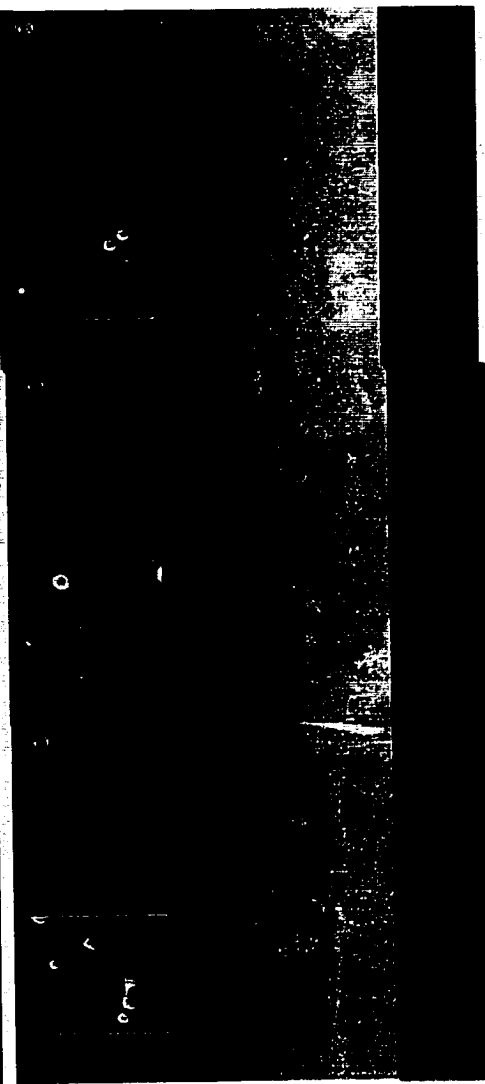


5.71



6.53

6.73



7.34

7.34

8.16



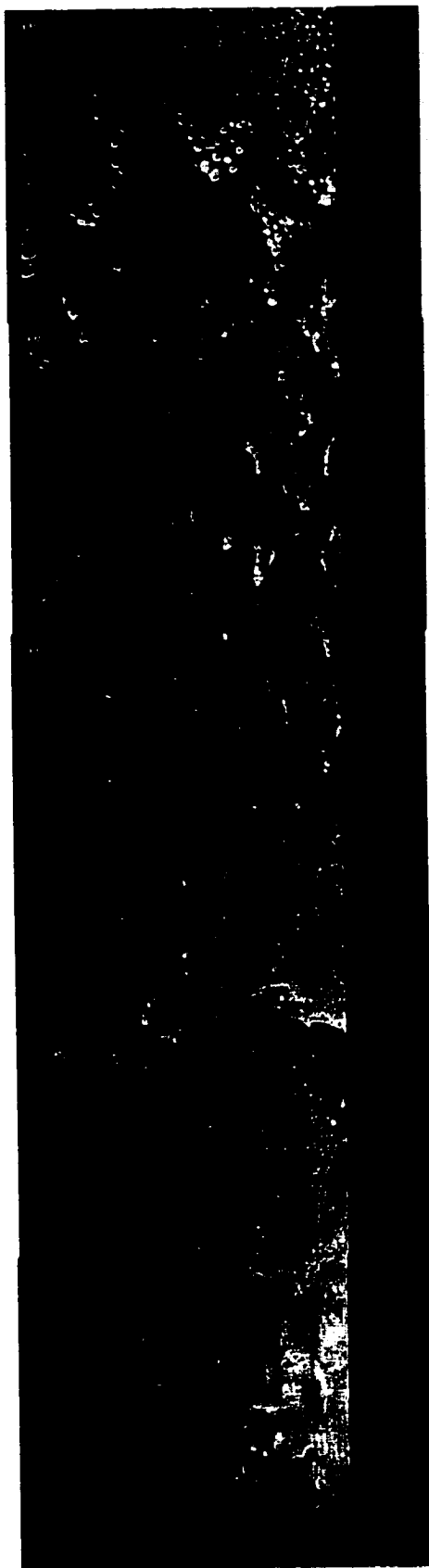
8.16

8.98

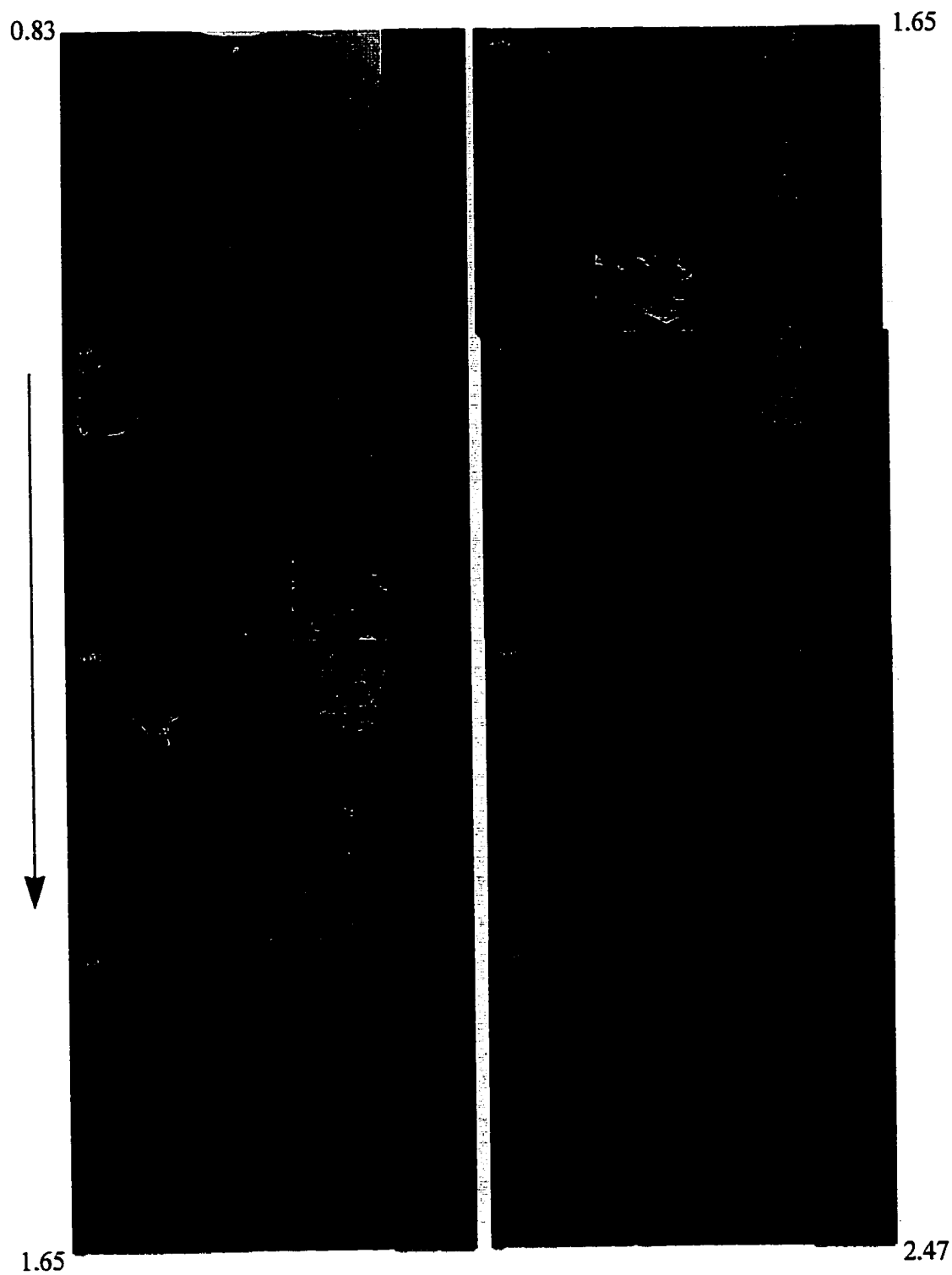
8.98



10.0



COLLAGES OF INGOT MZS-7 SURFACE FEATURES



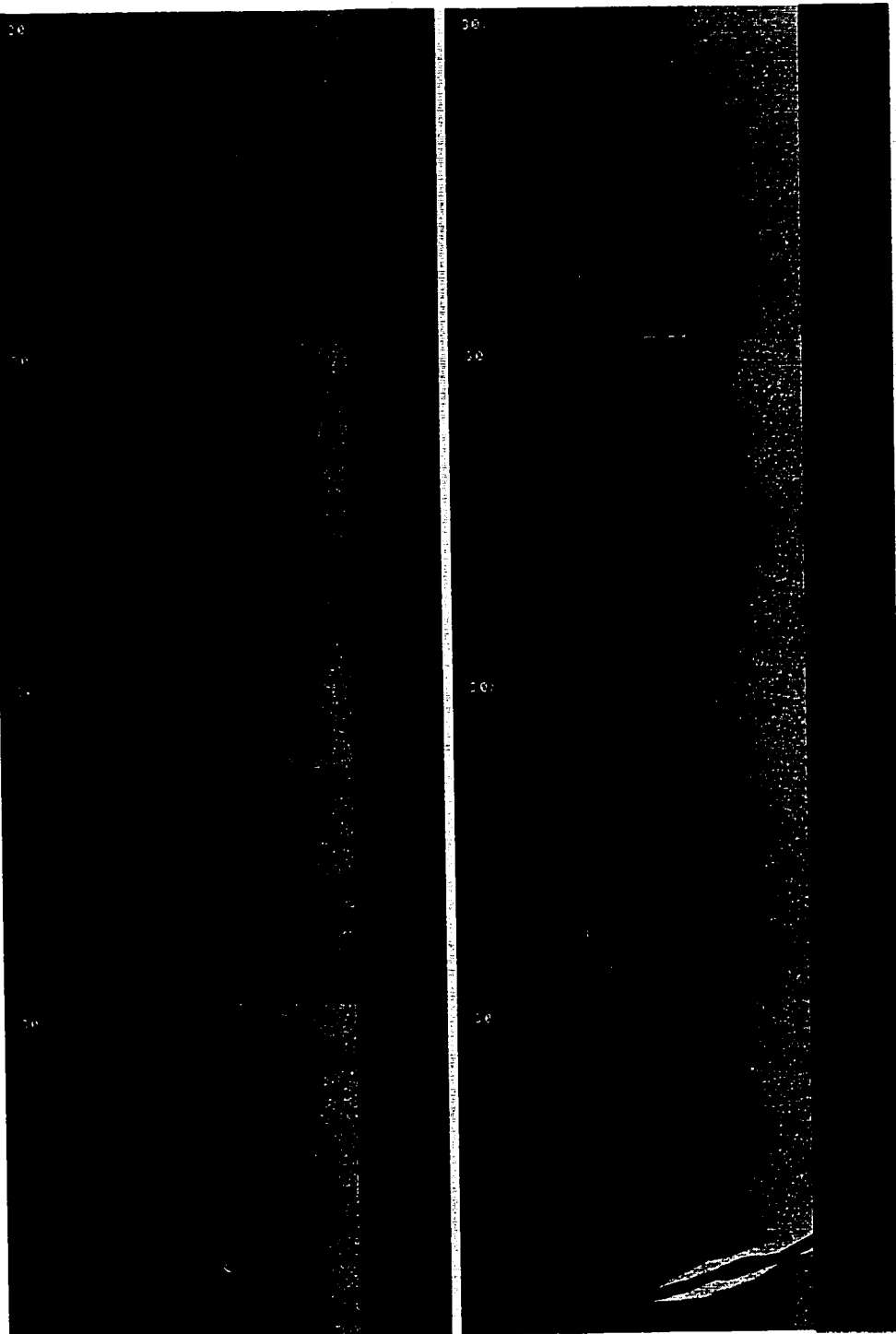
2.47

3.56



3.56

4.65



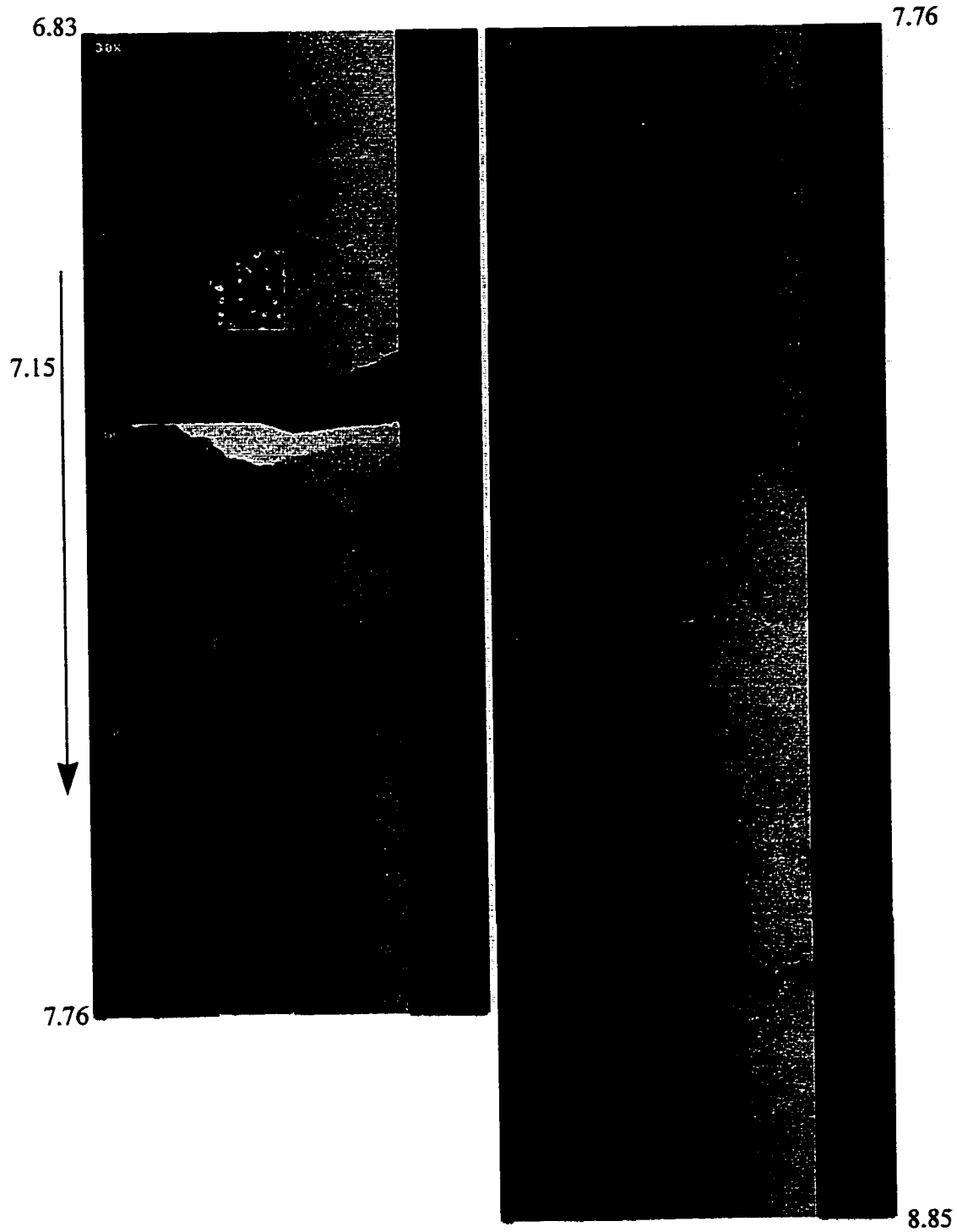
4.65

5.74



5.74

6.83



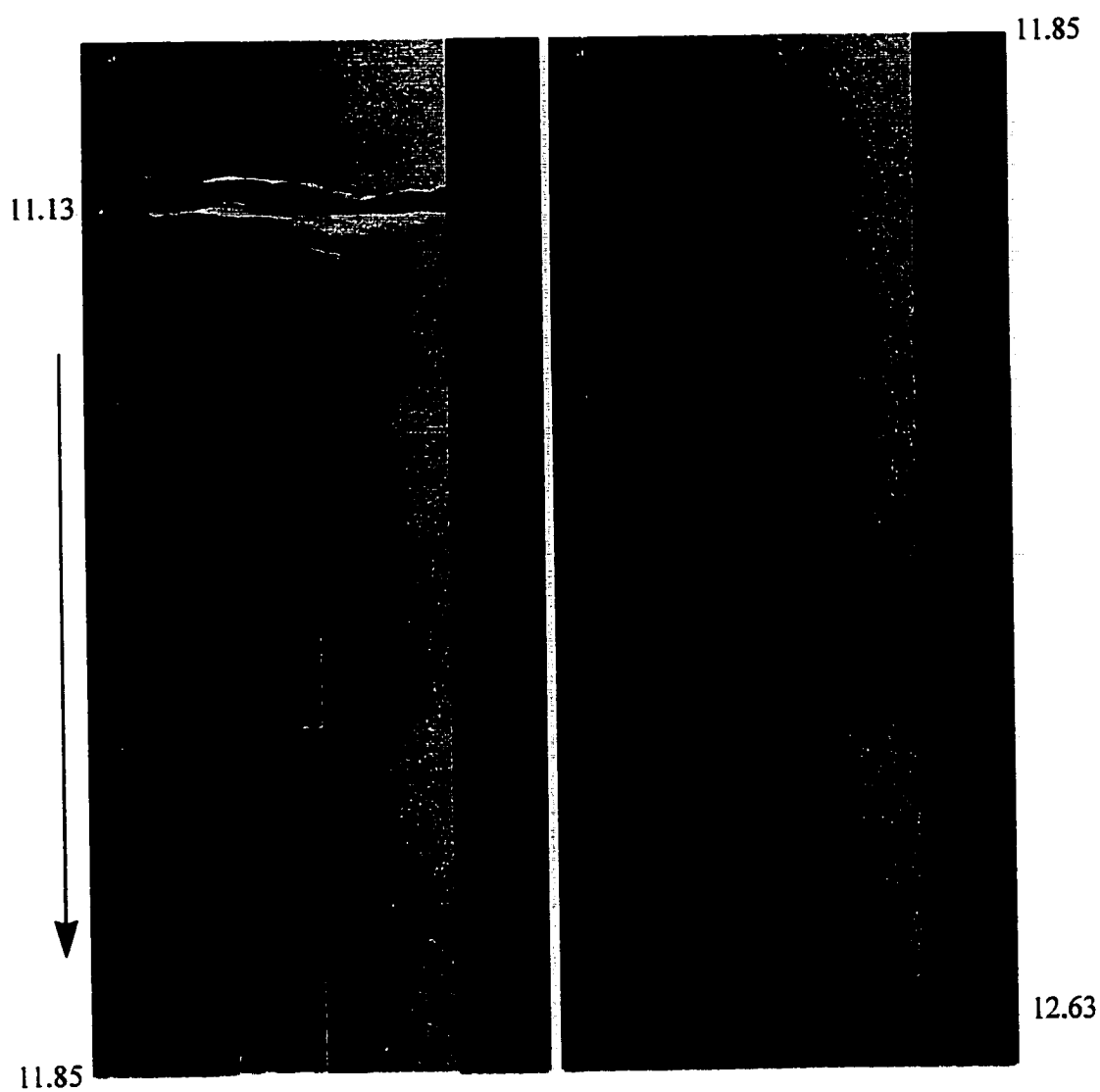
8.85

9.94

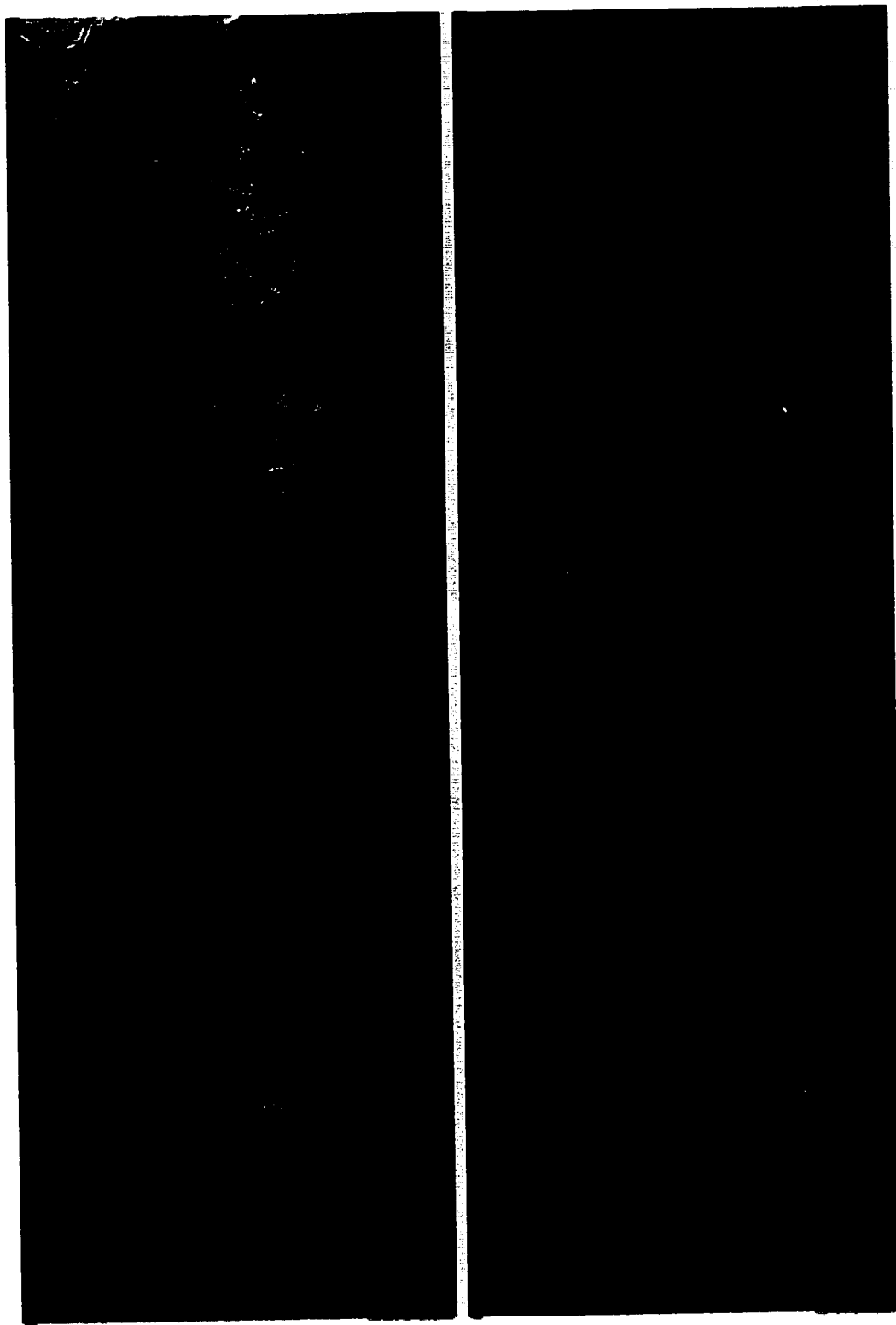


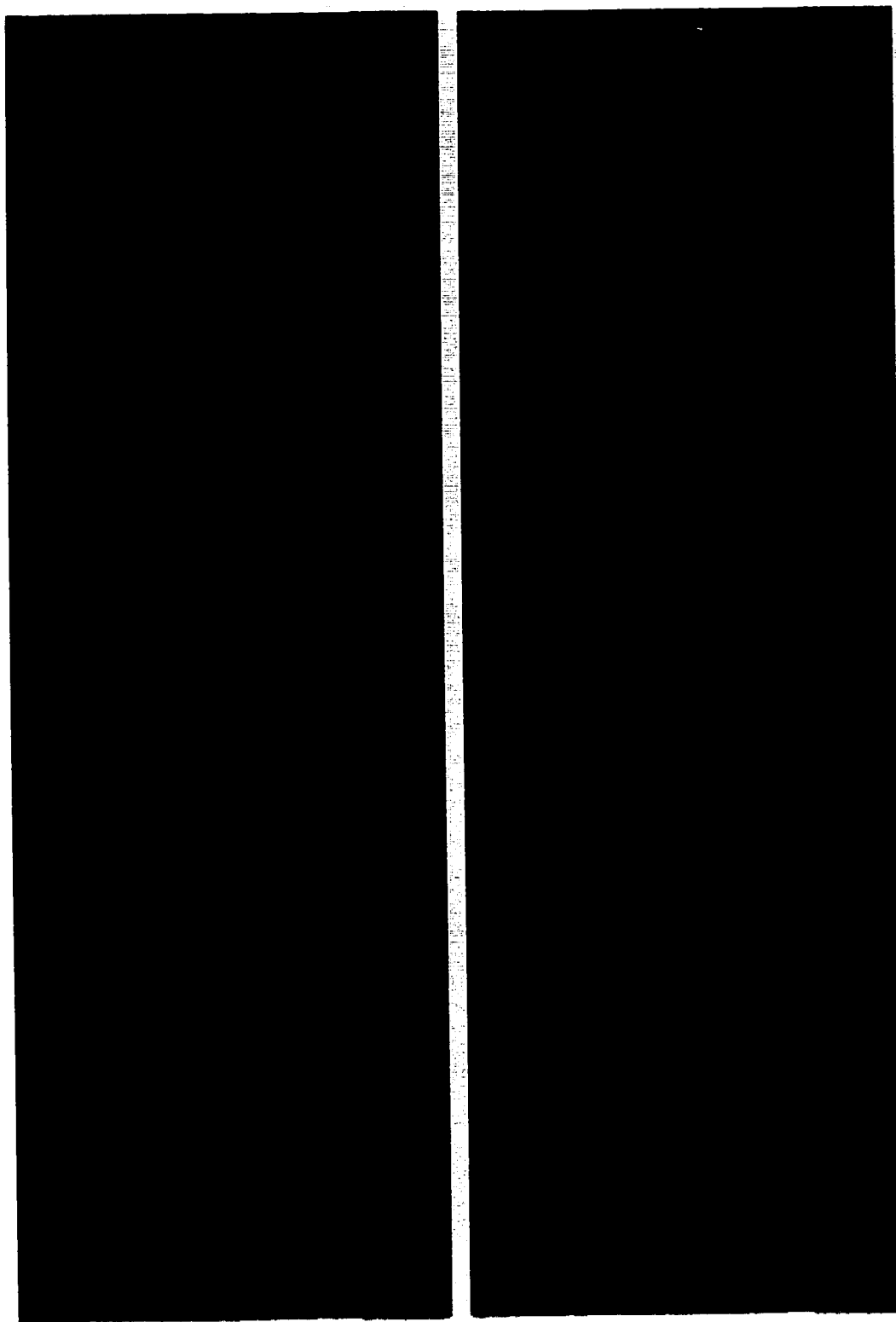
9.4

11.03



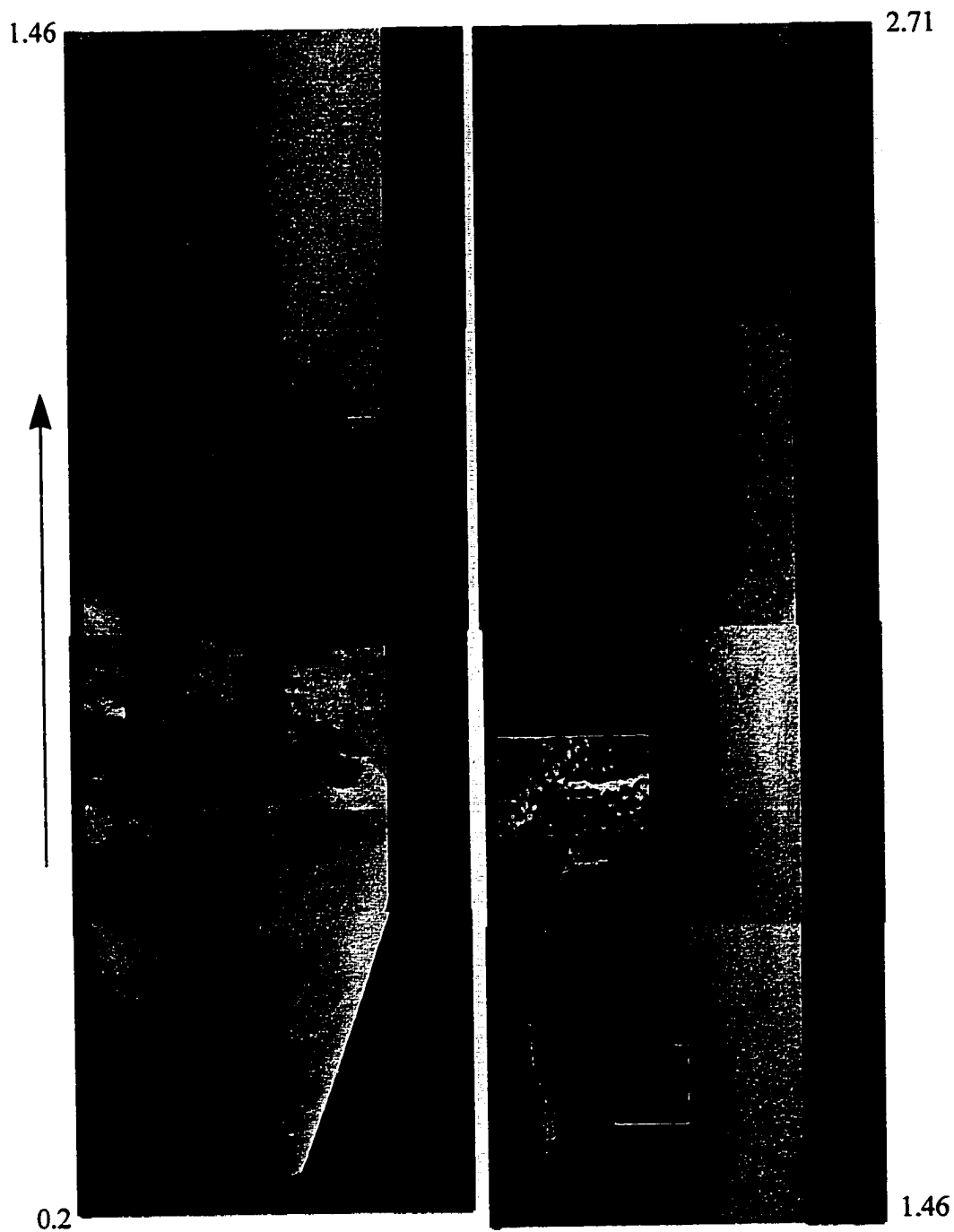
COLLAGES OF INGOT MZS-8 SURFACE FEATURES







COLLAGES OF INGOT MZS-10 SURFACE FEATURES



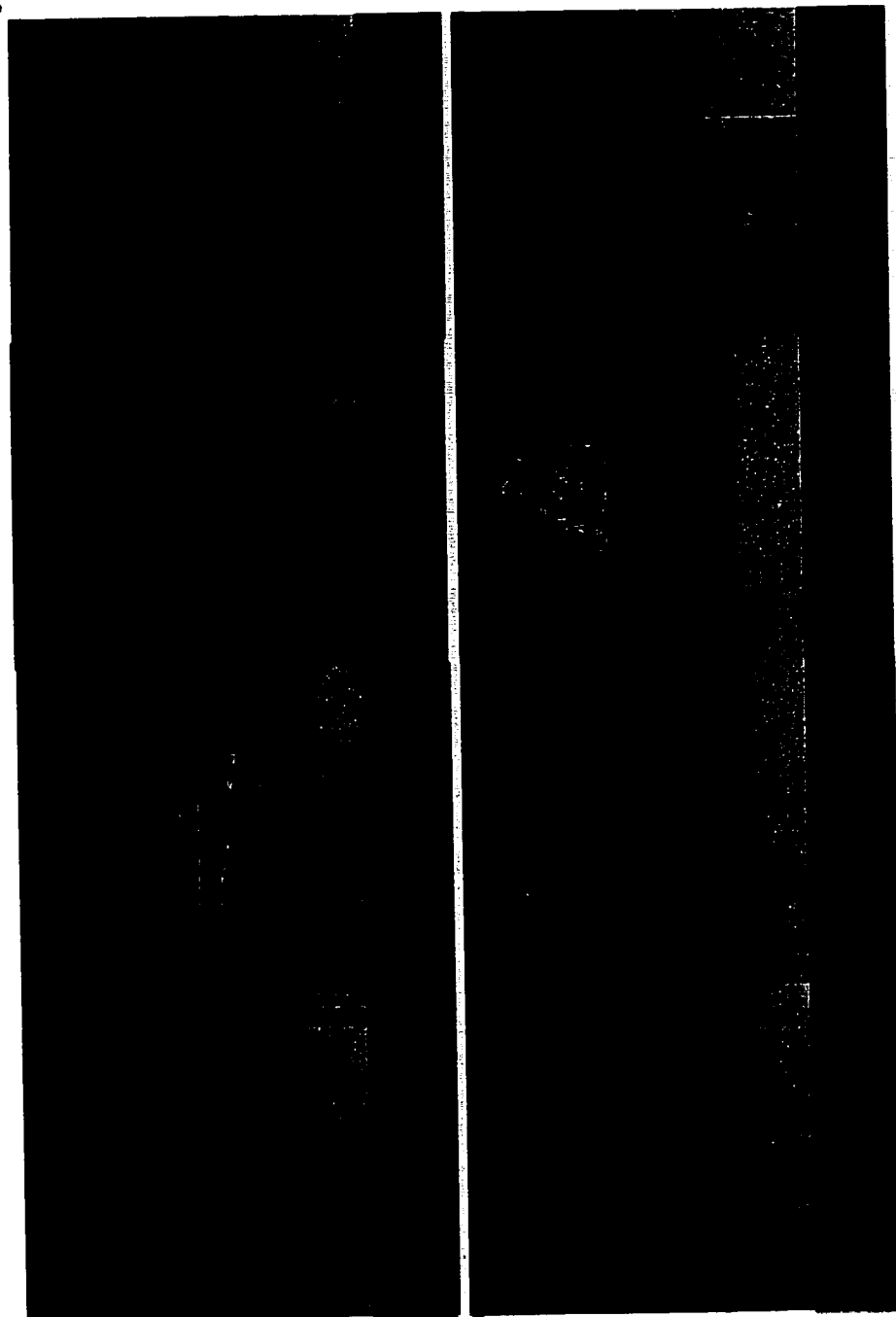
3.98

4.93



2.71

3.98



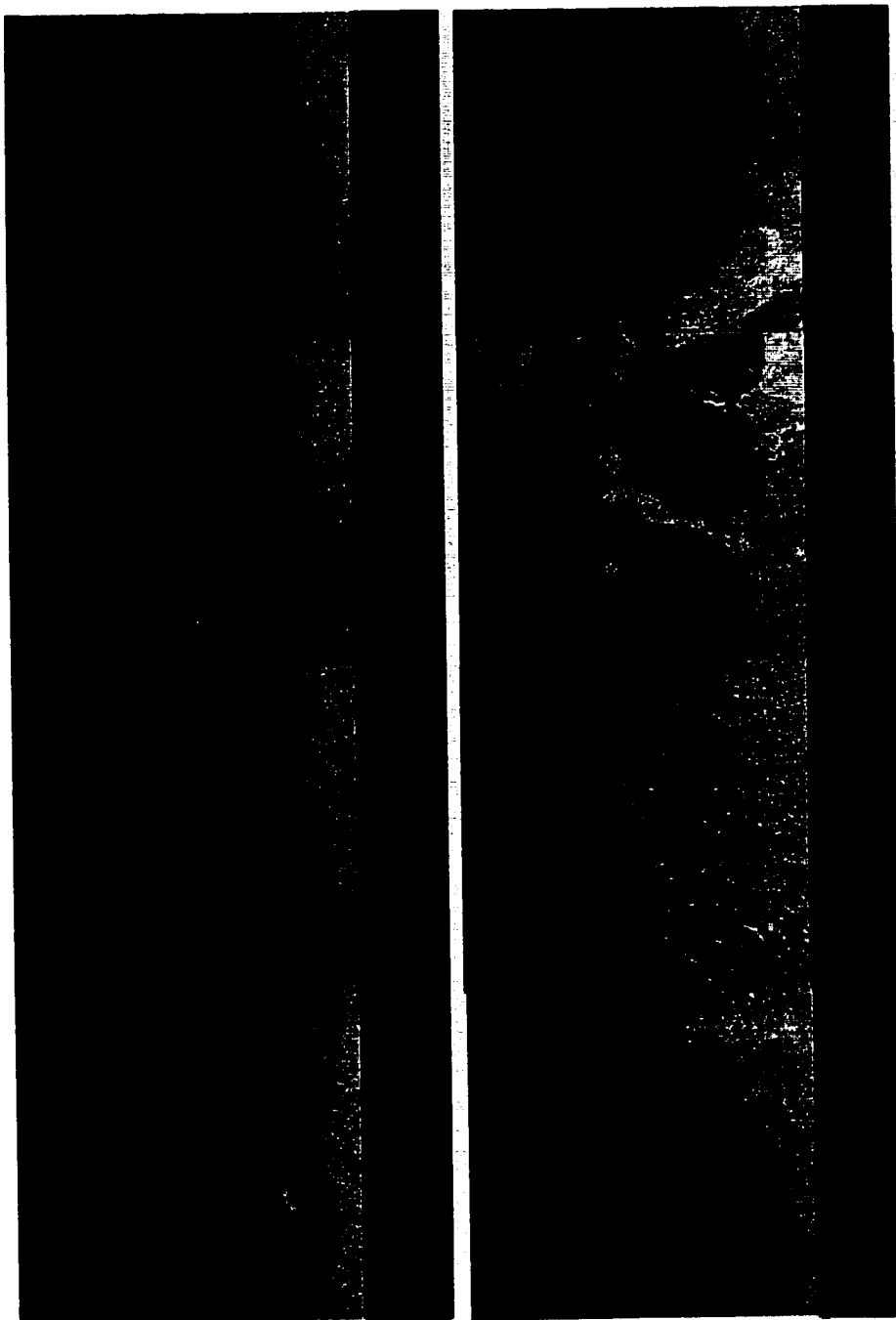
6.19

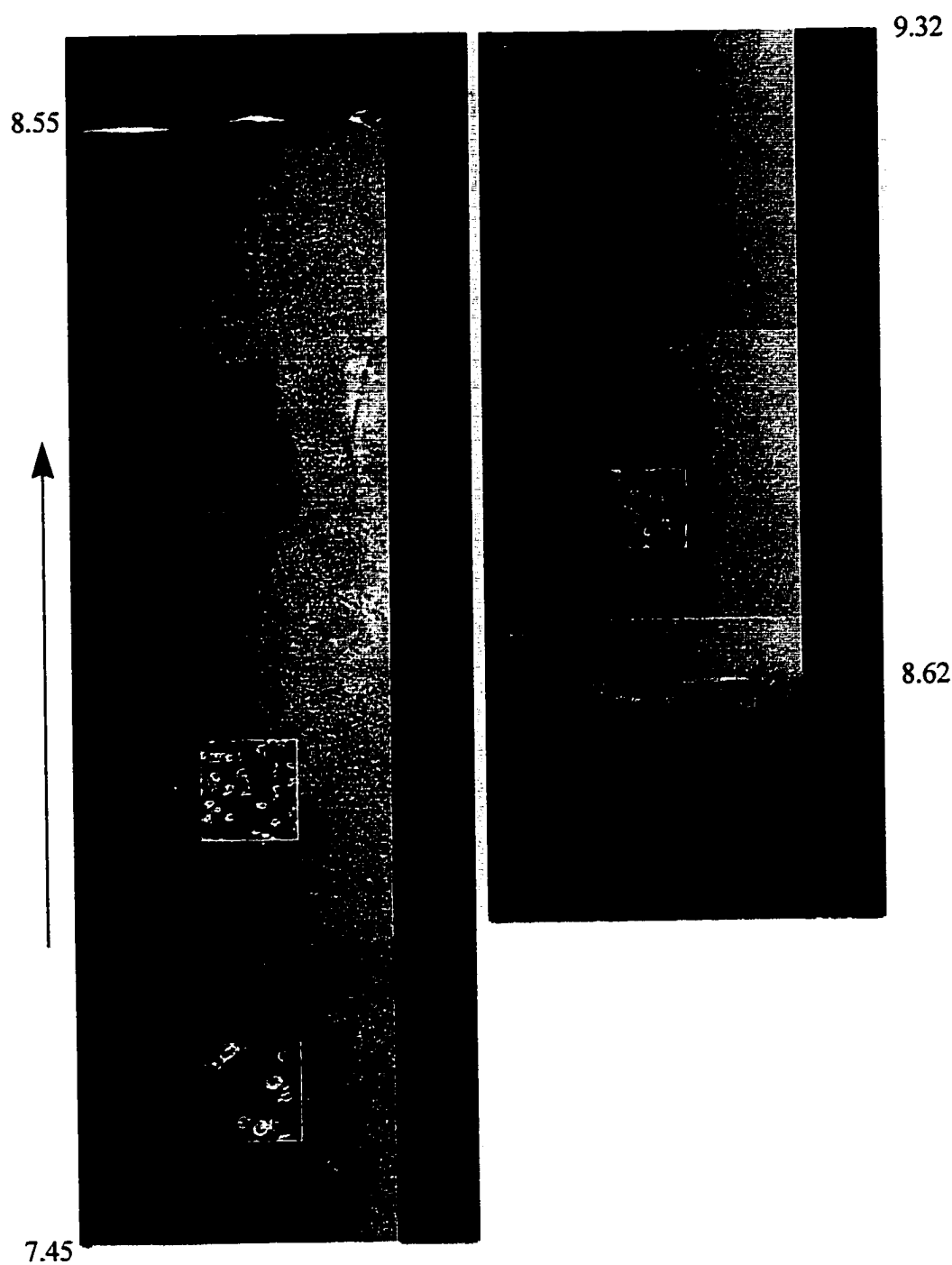
7.45



4.93

6.19





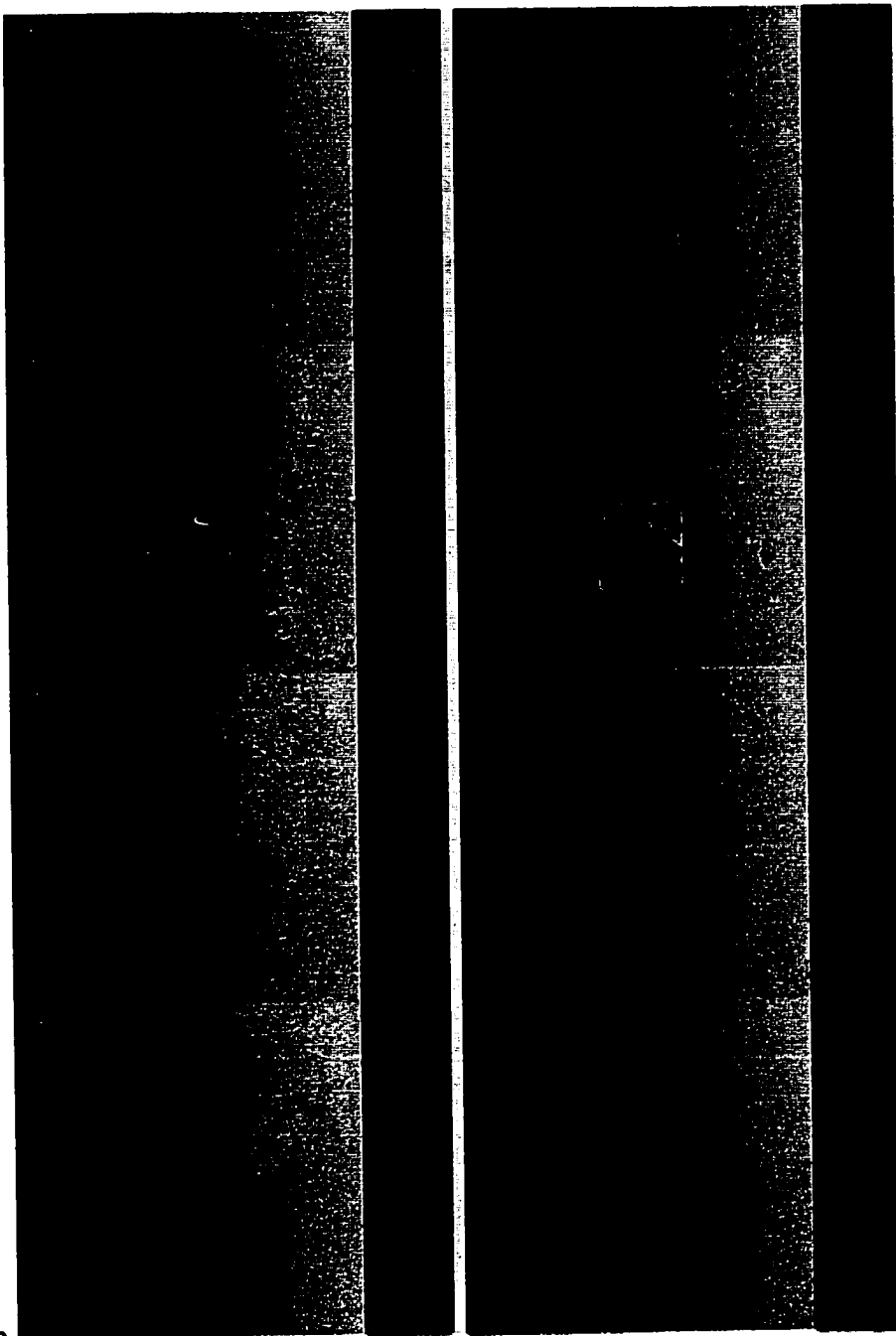
10.58

11.84



9.32

10.58

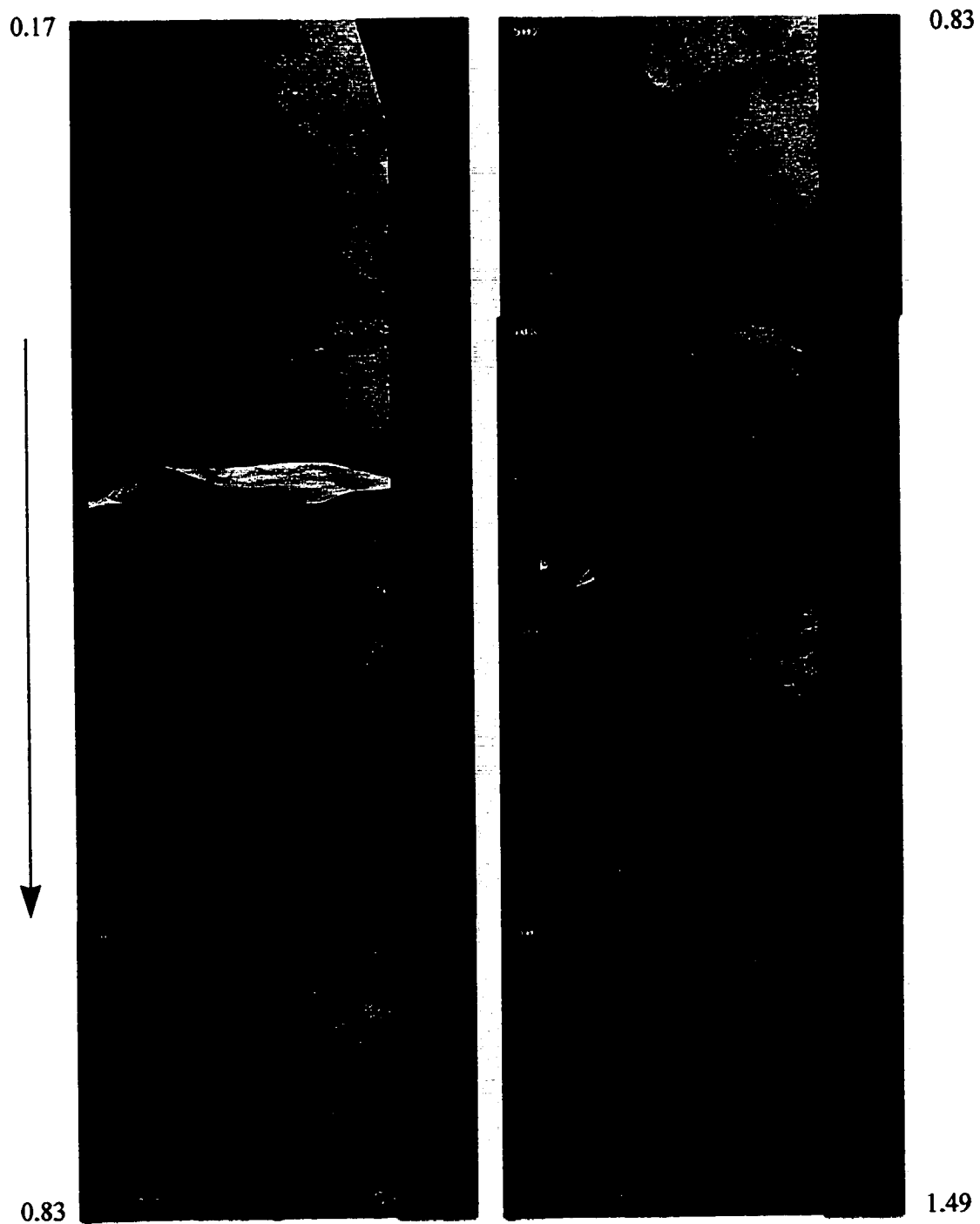


13.1



11.84

COLLAGES OF INGOT MZS-11 SURFACE FEATURES



1.49

2.15



2.15

2.80

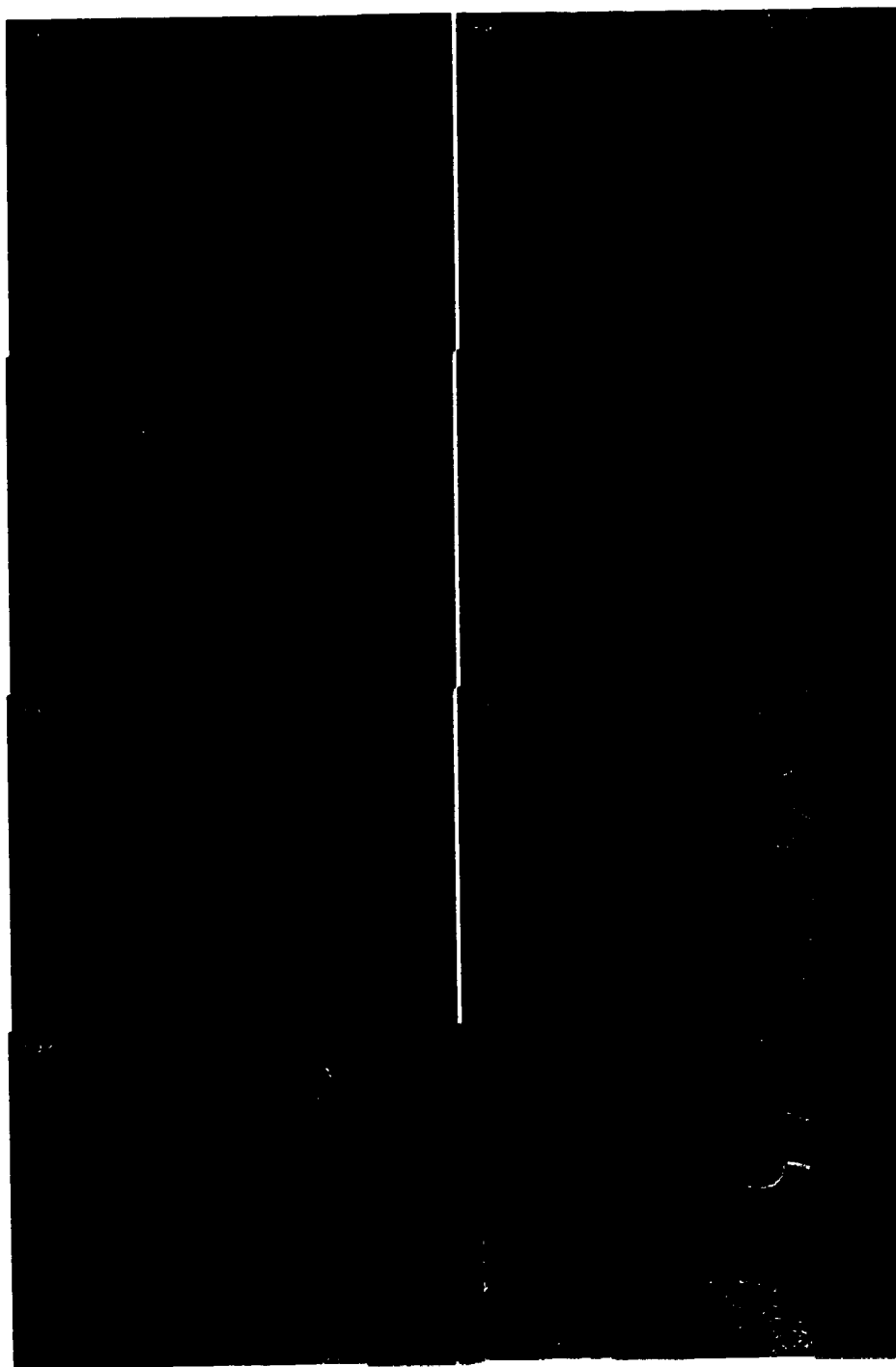
2.80

3.46



3.46

4.11



4.11

4.77



4.77

5.42

5.42

6.06



6.06

6.71

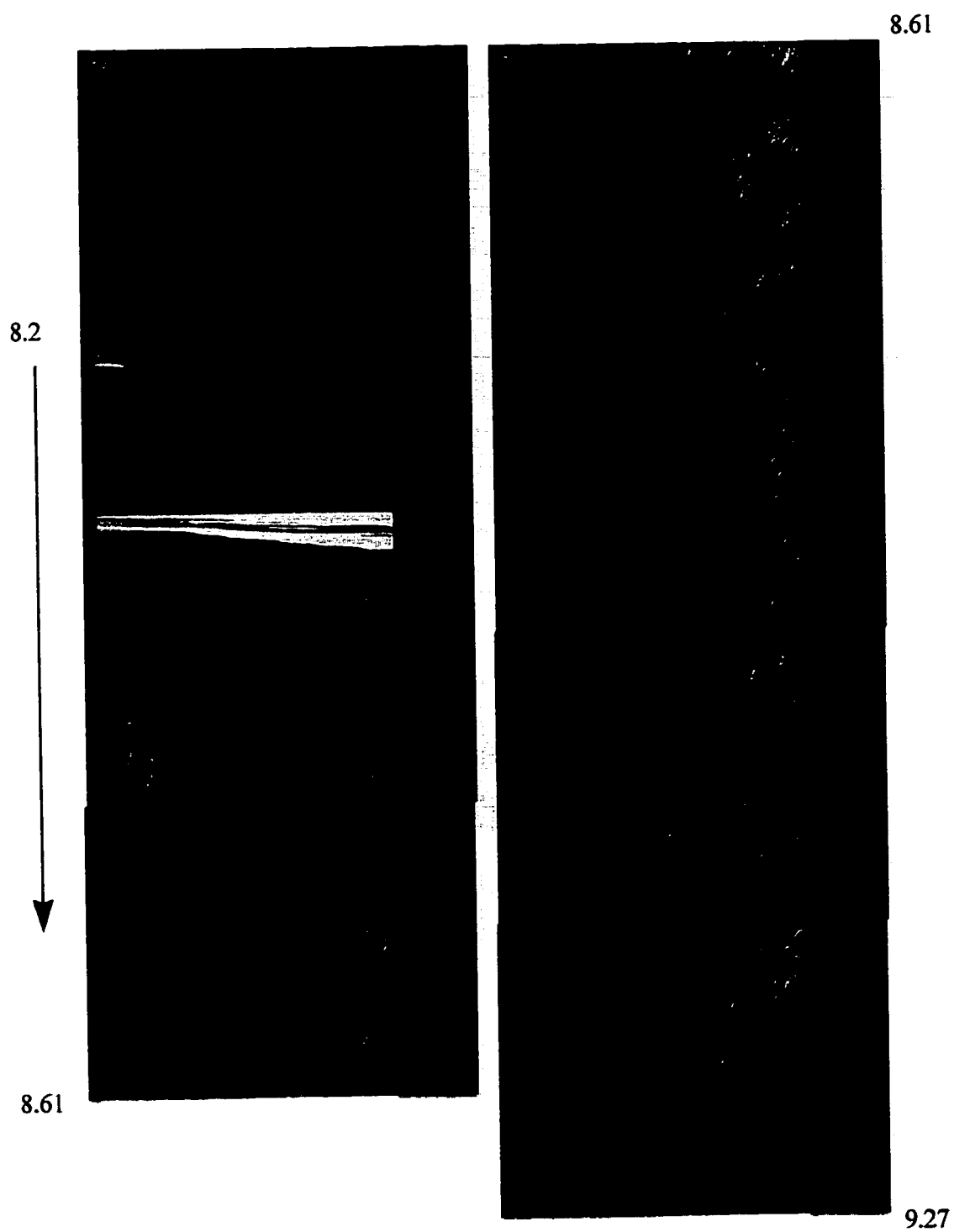
6.71

7.37



7.37

8.02



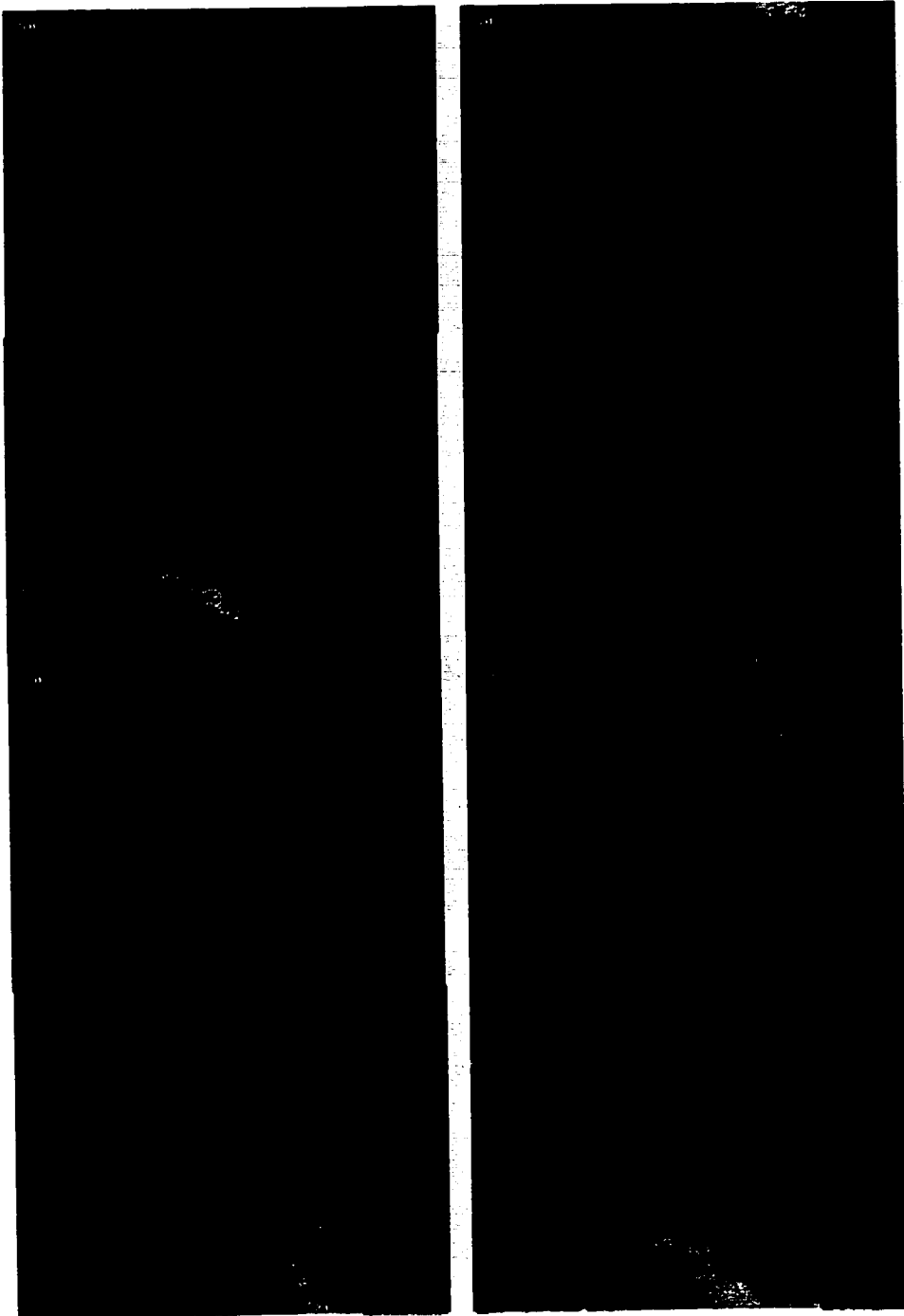
9.27

9.93



9.93

10.58



10.58

11.24



11.24

11.90

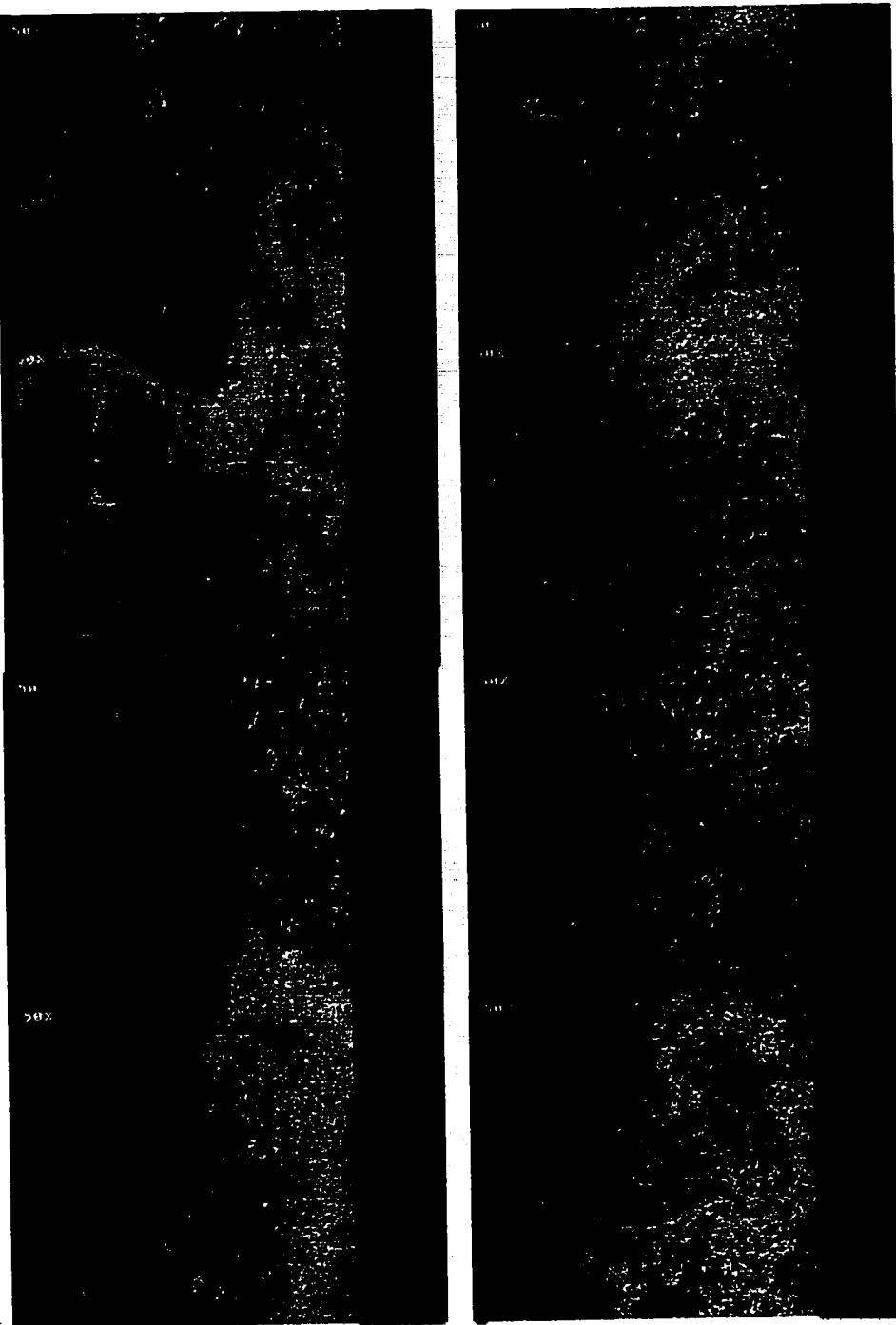
11.90

12.56



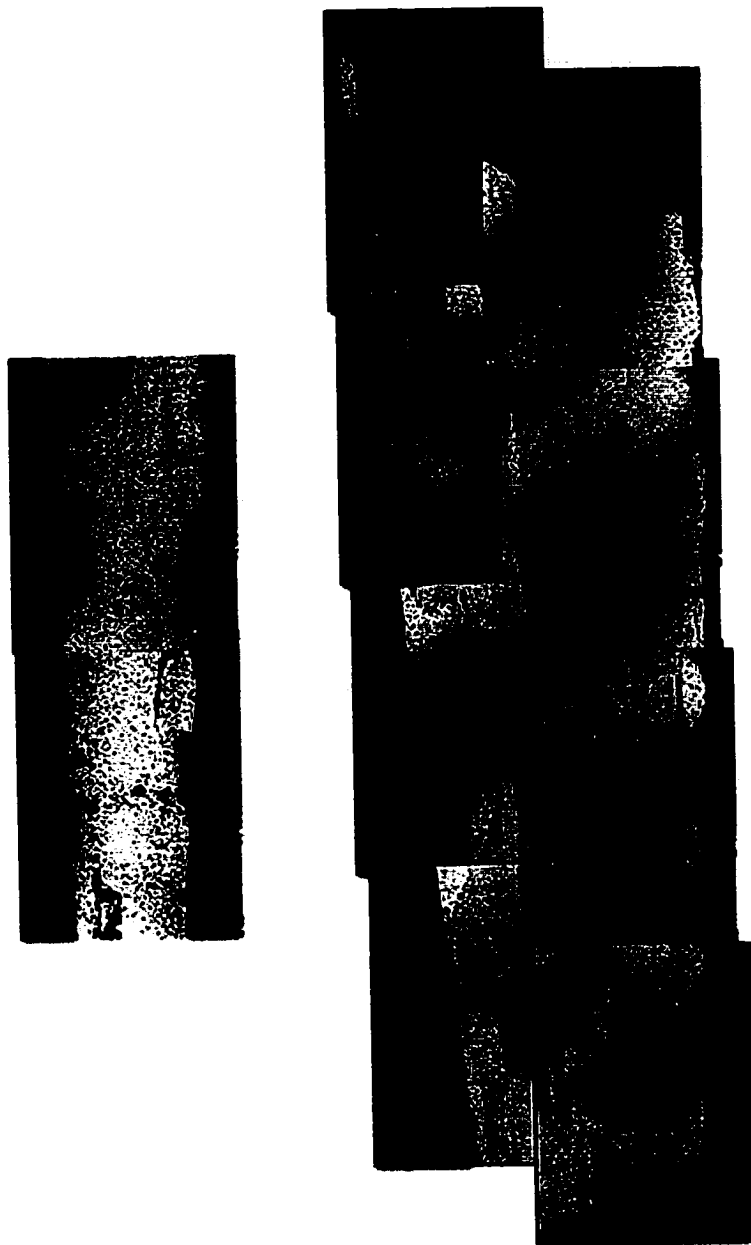
12.56

13.22

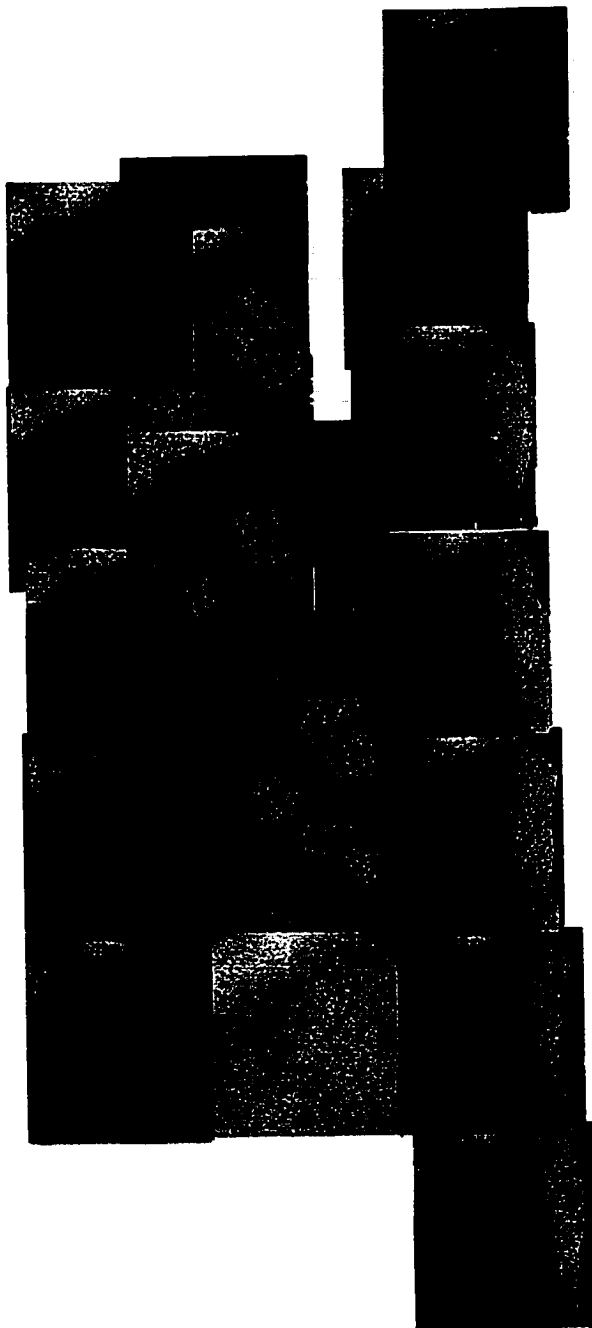


APPENDIX B

COLLAGES OF GRAIN STRUCTURE



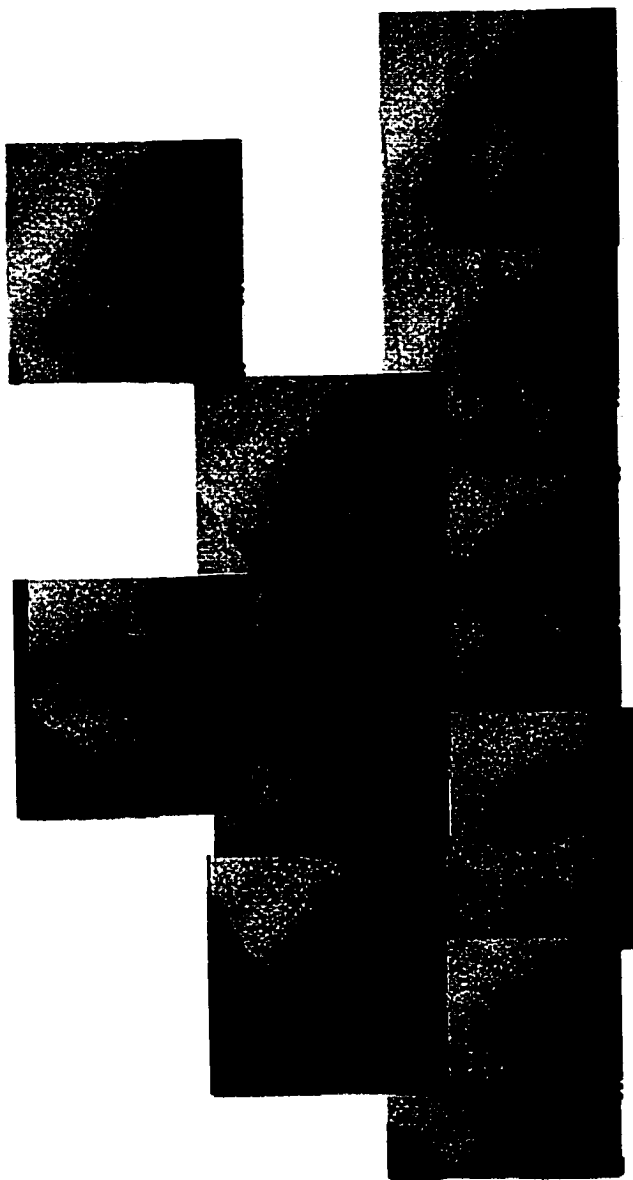
Tip of MZS-2



MZS-2



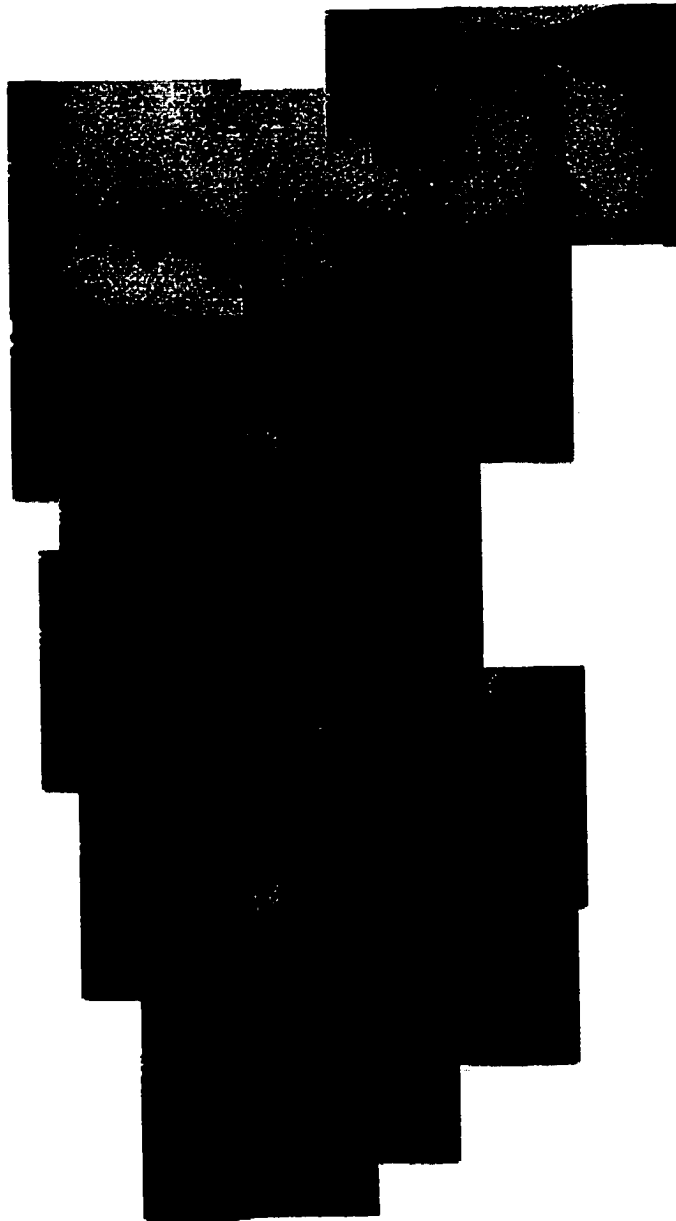
MZS-5



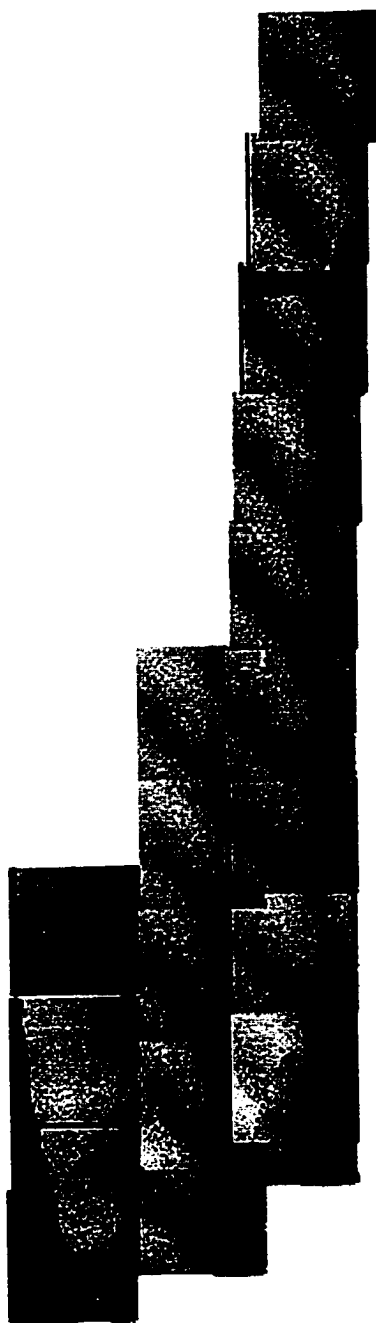
MZS-7



MZS-8



MZS-10



MZS-11

LIST OF REFERENCES

- Andrews, R. N., Walck, D., Price, M. W., Szofran, F. R., and Lehoczky, S. L., *J. Crystal Growth* 99 (1990) 717.
- Behr, S., Einfeldt, D., Hommel, C. R., Becker, G., Landwehr, and Cerva, H., *J. Crystal Growth* 159 (1996) 1123.
- Bornyk, N. M., Sokolov, A. M., Indenbaum, G. V., and Vanyukov, A. V., *Russian Metallurgy* 5 (1974) 195.
- Brebrick, R. F., and Haochieh, L., *J. Phase Equil.* 17 (1996) 495.
- Brebrick, R. F., Su, C.-H., and Liao, P.-K., in *Semiconductors and Semimetals*, eds. Willardson R. K. and Beer, A. C. (Academic, New York, 1993)
- Chang, C. E., and Wilcox, W. R., *J. Crystal Growth* 21 (1974) 135.
- Chen, A.-B., Sher, A., Spicer, W. E., *J. Vac. Sci. Technol.* A1 (1983) 1674.
- Cobb, S. D., Andrews, R. N., Szofran, F. R., and Lehoczky, S. L., *J. Crystal Growth* 110 (1991) 415.
- Cole, S., Carey, G. P., Silberman, J. A., Spicer, W. E., and Wilson, J. A., *J. Vac. Sci. Technol.* A3 (1985) 206.
- Dobrowolski, W., Galazka, R. R., Grodzicka, E., Kossut, J., and Witkowska, B., *Phys. Rev. B* 48 (1993a) 17848.
- Dobrowolski, W., Grodzicka, E., Kossut, J., and Witkowska, B., *Proceedings of the Intern. Conf. on Narrow-Gap Semiconductors - Southampton* (1992).
- Dobrowolski, W., Grodzicka, E., Kossut, J., and Witkowska B., *Semicond. Sci. Technol.* 8 (1993b) S33.
- Ehrenreich, H. and Hirth, J. P., *Appl. Phys. Letters* 46 (1985) 668.
- Einfeldt, S., Lunz, U., Heinke, H., Brecker, C. R., and Landwehr, G., *J. Crystal Growth* 146 (1995) 427.
- Ekbote, P. D., and Zope, J. K., *Indian J. Pure Appl. Phys.* 16 (1978) 103.
- Friedel, J., *Dislocations* (Pergamon, Oxford, 1964).

- Frigeri, C., Weyher, J. L., and Gall, P., *Inst. Phys. Conf. Ser. No. 117:Section 6* (1991) 353.
- Gavaleshko, N. P., Dobrowolski, W., Baj, M., Dmowski, L., Dietl, T., and Khomyak, V. V., *3rd Internat. Conf. on Physics of Narrow-Gap Semiconductors* (1977) 331.
- Gavaleshko, N. P., Gorley, P. N., Khomyak, V. V., and Shenderovskii, V. A., *Phys. Stat. Sol. (b)* 98 (1980) 463.
- Gavaleshko, N. P., Gorley, P. N., Paranachich, S. Y., Frasunyak, V. M., Khomyak, V. V., *Inorganic Materials* 19 (1984a) 298.
- Gavaleshko, N. P., and Khomyak, V. V., *Sov. Phys. Solid State* 18 (1976) 1720.
- Gavaleshko, N. P., Khomyak, V. V., Frasunyak, V. M., Paranachich, L. D., and Paranachich, S. Y., *Soviet Physics-Semiconductor* 18 (1984b) 967.
- Gavaleshko, N. P., Paranachich, S. Y., Paranachich, L. D., Khomyak, V. V., Tarasyuk, I. I., and Makogonenko, V. N., *Inorganic Materials* 21 (1986a) 971.
- Gavaleshko, N. P., Solonchuk, L. S., Khomyak, V. V., and Shenderovskii, V. A., *Sov. Phys. Solid State* 28 (1986b) 403.
- Genzel, C., Gille, P., Hähnert, I., Kiessling F. M., and Rudolph, P., *J. Crystal Growth* 101 (1990) 232.
- Guergouri, K., Triboulet, R., Tromson-Carli, A. and Marfaing, Y., *J. Crystal Growth* 86 (1988) 61.
- Hagemark, K. I., *J. Phys. Chem. Solids* 37 (1976) 461.
- Hall, E. L., and Vander Sande, J. B., *Phil. Mag* A37 (1978) 137.
- Hara, K., Machimura, H., Usri, M., Munekata, H., Kukimoto, H., and Yoshino, J., *J. Crystal Growth*, 150 (1995) 735.
- Harrison, W. A., *Electronic Structure and the Properties of Solids* (Freeman, San Francisco, 1980).
- Hirth, J. P., and Lothe, J., *Theory of Dislocations*, 2nd ed. (Wiley, New York, 1982).
- Holland, L. R., and Taylor, R. E., *J. Vac. Sci. Technol. A*1 (1983) 1615.
- Kashyap, P., Jain, M., and Sehgal, H. K., *Infrared Phys.* 30 (1990) 343.

- Kot, M. V., and Simashkevich, A. V., Acad. of Sc., USSR Bulletin - Physical Series 28 (1964) 965.
- Kot, M. V., Tryrziu, V. G., Simashkevich, A. V., Maronchuk, Y. E., and Khomyak, V. V., Soviet Physics-Solid State 4 (1962) 1128.
- Kumazaki, K., Phys. Stat. Sol. (b) 153 (1989) 751.
- Kumazaki, K., and Nishiguchi, N., Solid State Commun. 60 (1986) 301.
- Kumazaki, K., Viña, L., Umbach, C., and Cardona, M., Solid State Commun. 68 (1988) 591.
- Lehoczky, S. L., Broerman, J. G., Nelson, D. A., and Whitsett, C. R., Phys. Rev. 9 (1974) 1598.
- Lehoczky, S. L., and Szofran, F. R., Advanced Methods for Preparation and Characterization of Infrared Detector Materials, Part I, NASA CR-161598 (1980).
- Leibler, K., Girit, W., Checinski, K., Wilamowski Z., and Iwanowski, R., Phys. Stat. Sol. (b) 55 (1973) 447.
- Leute, V., and Plate, H., Ber. Bunsenges. Phys. Chem. 93 (1989) 757.
- Li, W., and Patterson, J. D., Phys. Rev B, 50 (1994) 14903.
- Li, W., and Patterson, J. D., Phys. Rev. B, 53 (1996) 15622.
- Matthieson, D. H., Wargo, M.J., Motakef, S., Carlson, D.J., Nakos, J. S., and Witt Jr., A.F., J. Crystal Growth (1987) 557.
- Mikkelsen Jr., J. C., and Boyce, J. B., Phys. Review Letters 49 (1982) 1412.
- Miller, D.J., and Koh, A. K., J. Phys. Chem. Solida. 55 (1994) 153.
- Nabarro, F. R. N., Theory of Crystal Dislocations (Oxford, London, 1967).
- Natarajan, C., Sharon, M., Lévy-Clément, C., Neumann-Spallart, M., Thin Solid Films 257 (1995) 46.
- Naumann, R. J., and Lehoczky, S. L., J. Crystal Growth 61 (1983) 707.
- Nelson, D. A., Broerman, J. G., Summers, C. J., and Nelson, C. R., Phys. Rev. B, 8 (1978) 1658.

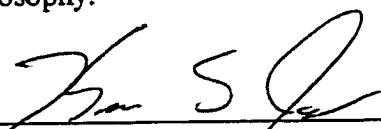
- Parker, S. G., and Pinnel, J. E., *J. Electrochem. Soc.*: SOLID STATE SCIENCE (1971) 1868.
- Patterson, J.D., and Li, W., *SPIE Vol. 2809* (1996) 78.
- Phillips, J. C., in: *Handbook on Semiconductors*, ed. Paul, W. (North-Holland, New York, 1982) 264.
- Polisar, E. L., Boinikh, N. M., Indenbaum, G. V., Vanyukov, A. V., and Shaslivin, V. P., *Izv. Vysch. Uchebn. Zaved. Fiz.* 6 (1968) 81.
- Potapov, G. A., Ponomarev, A. I., Gavaleshko, N. P., and Khomyak, V. V., *Soviet Physics-Semiconductor* 13 (1979) 517.
- Potapov, G. A., Ponomarev, A. I., Gavaleshko, N. P., and Khomyak, V. V., *Soviet Physics-Semiconductor* 14 (1980) 1383.
- Ren, J., Lansari, Y., Yu, Z., Cook, Jr., J. W., and Schetzina, J. F., *Electronic Materials* 22 (1993) 973.
- Sangwal, K., *Etching of Crystals* (North Holland, Amsteden, 1987).
- Sha, Y.-G., Su, C.-H., and Lehoczky, S. L., *J. Crystal Growth* 173 (1997) 88.
- Sher, A., Chen, A.-B., Spicer, W. E., and Shih, C.-K., *J. Vac. Sci. Technol.* A3 (1983) 105.
- Shetty, R., Wilcox, W. R., and Regel, L. L., *J. Crystal Growth* 153 (1995) 103.
- Smith, V. G., Tiller, W. A., and Rutter, J. W., *Canadian J. of Physics* 33 (1955) 723.
- Spicer, W. E., Silberman, J. A., Lindau, I., Chen, A.-B., Sher, A., and Wilson, J. A, *J. Vac. Sci. Technol.* A1 (1983) 1735.
- Steininger, J., *J. Appl. Phy.* 41 (1970) 2713.
- Strauss, A. J., and Farrell, L. B., *J. Inorg. Nucl. Chem.* 24 (1962) 1211.
- Su, C.-H., Lehoczky, S. L., and Szofran, F. R., *J. Crystal Growth* 86 (1988) 87.
- Su, C.-H., Lehoczky, S. L., Szofran, F. R., Gillies, D. C., Sha, Y.-G., Cobb, S. D., and Andrews, R. N., *Trans. Mater. Res. Soc. Jpn. A* 16 (1994) 699.
- Su, C.-H., Sha, Y.-G., Mazuruk, K., and Lehoczky, S. L., *J. Appl. Phys.* 80 (1996) 137.

- Sysoev, L. A., Raiskin, E. K., and Gurev, V. R., *Inorg. Mater.* 3 (1967) 342.
- Szofran, F. R., and Lehoczky, S. L., *J. Crystal Growth* 70 (1984) 349.
- Taguchi, T., Shirafuji, J., and Inuishi, Y., *Jpn J. Appl. Phys.* 17 (1978) 1331.
- Triboulet, R., *J. Crystal Growth* 86 (1988) 79.
- Utech, H. P., and Flemmings, M. C., *J. Applied Physics* 21 (1982) L545.
- Vogel, F. L., Pfann, W. G., Corey, H. E., and Thomas, E. E., *Phys. Rev.* 90 (1953) 489.
- Watring, D. A., and Lehoczky, S. L., *J. Crystal Growth* 167 (1996) 478.
- Yasuda, K., Iwakami, Y., and Saji, M., *J. Crystal Growth* 99 (1990) 727.
- Yu, T. C., and Brebrick, R. F., *J. Phase Equil.* 78 (1992) 476.
- Yukalov, V. I., *Phys. Rep.* 208 (1991) 395.

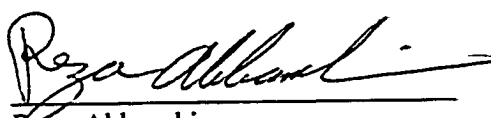
BIOGRAPHICAL SKETCH

The author was born in Birmingham, Alabama. She attended the University of Alabama at Birmingham, receiving a B.S. and M.S. in Materials Engineering in 1985 and 1987. She has been employed by the National Aeronautic and Space Administration in Huntsville, Alabama, since 1986, where she works in the Microgravity Science and Applications Division. She attended the University of Florida on a full-time study program sponsored by her employer. She received a Ph.D. in Materials Science and Engineering in 1998 from the University of Florida.

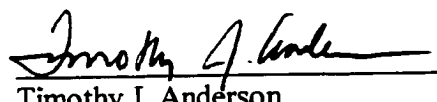
I certify that I have read this study and that in my opinion it conforms to acceptable standards of scholarly presentation and is fully adequate, in scope and quality, as a dissertation for the degree of Doctor of Philosophy.


Kevin S. Jones, Chairman
Professor of Materials Science and
Engineering


I certify that I have read this study and that in my opinion it conforms to acceptable standards of scholarly presentation and is fully adequate, in scope and quality, as a dissertation for the degree of Doctor of Philosophy.


Reza Abbaschian
Professor of Materials Science and
Engineering

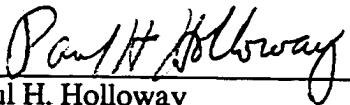
I certify that I have read this study and that in my opinion it conforms to acceptable standards of scholarly presentation and is fully adequate, in scope and quality, as a dissertation for the degree of Doctor of Philosophy.


Timothy J. Anderson
Professor of Chemical Engineering

I certify that I have read this study and that in my opinion it conforms to acceptable standards of scholarly presentation and is fully adequate, in scope and quality, as a dissertation for the degree of Doctor of Philosophy.

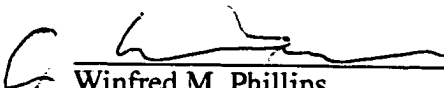

Robert T. DeHoff
Professor of Materials Science and
Engineering

I certify that I have read this study and that in my opinion it conforms to acceptable standards of scholarly presentation and is fully adequate, in scope and quality, as a dissertation for the degree of Doctor of Philosophy.


Paul H. Holloway
Professor of Materials Science and
Engineering

This dissertation was submitted to the Graduate Faculty of the College of Engineering and to the Graduate School and was accepted as partial fulfillment of the requirements for the degree of Doctor of Philosophy.

August 1998


Winfred M. Phillips
Dean, College of Engineering

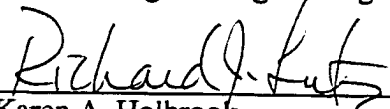
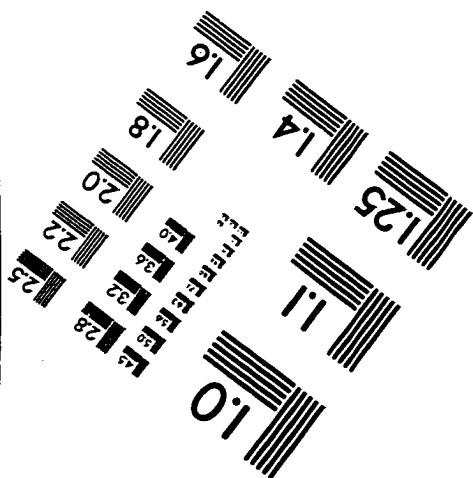
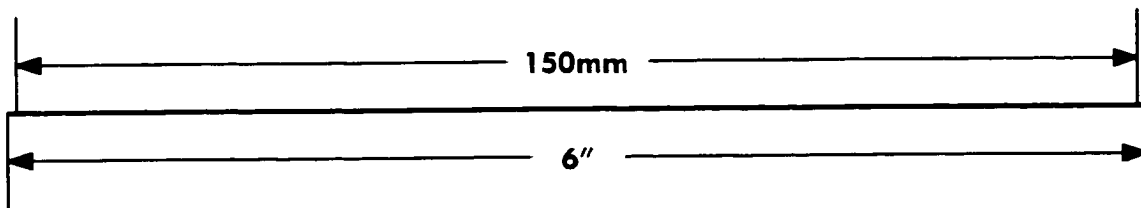
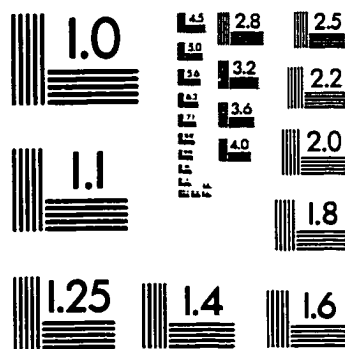
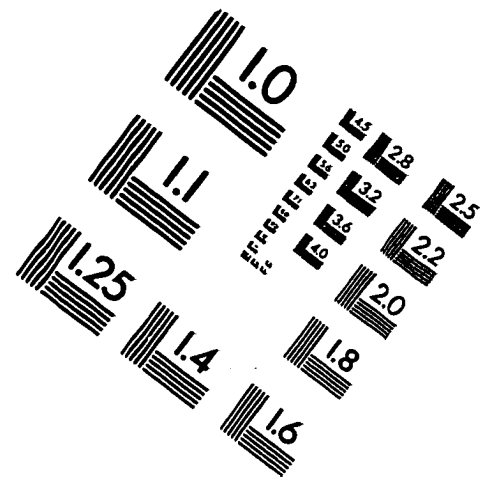
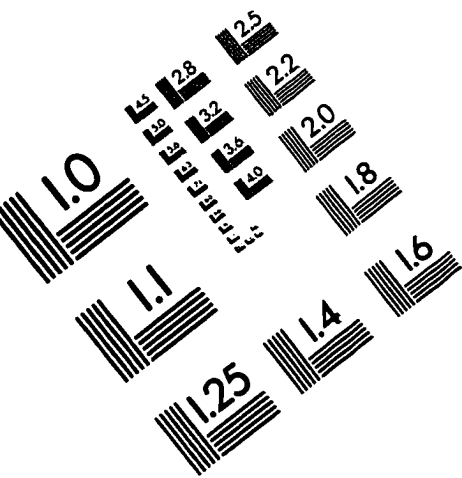

Karen A. Holbrook
Dean, Graduate School

IMAGE EVALUATION TEST TARGET (QA-3)



APPLIED IMAGE, Inc
1653 East Main Street
Rochester, NY 14609 USA
Phone: 716/482-0300
Fax: 716/288-5989

© 1993, Applied Image, Inc., All Rights Reserved

